Structural Evolution and Helium Potential of the Rukwa Rift, Tanzania

MULAYA, ERNEST,STEPHANO

How to cite:

MULAYA, ERNEST,STEPHANO (2023) *Structural Evolution and Helium Potential of the Rukwa Rift, Tanzania*, Durham theses, Durham University. Available at Durham E-Theses Online: http://etheses.dur.ac.uk/15172/

Structural Evolution and Helium Potential of the Rukwa Rift, Tanzania

---

Ernest Stephano Mulaya

Supervisors

Prof. Jon Gluyas (Durham University)

Prof. Ken McCaffrey (Durham university)

Prof. Chris Ballentine (University of Oxford)

A thesis submitted for the degree of Doctor of Philosophy

Department of Earth Sciences

United Kingdom

2023

Table of Contents

List of Figures

List of Tables

List of Appendix

Abstract

The Rukwa Rift is regarded as example of active continental rifting with complex structure patterns associated with significant helium occurrences. Gas composition data in the Rukwa Rift Basin indicate high radiogenic helium content ~ 10% which is far above the economic threshold of 0.3%. Unlocking helium resources is critical as the current global society faces a significant shortage of helium supply.

An integrated study of geological, geochemical and structural evidence such as 2-D seismic data, Digital Elevation Model (DEM) and wells data from the Rukwa Rift Basin has been used to define the evolution and timing of structural patterns within two structural domains: Domains A (north) and B (south). These structural domains are separated by the Saza Shear Zone (SSZ) which controls the oblique divergent effects of the Rukwa Rift. We demonstrate how these structures control the distribution of potential helium traps and reservoirs quality, average porosity and permeability ranges (c. 26-30% and 272.7- 660.6 mD) respectively. Most of sites with high helium concentrations occur along deep-rooted fault systems which suggest the possibility of such faults being the main migration conduits of helium from the Precambrian basement rocks.

The Rukwa Rift has high heat flow ~64-99 mW/m^2 and a high probability of helium charge from the surrounding crustal rocks in the region with flux capability of ∽22 x 10^{-6} mol $^4He/m^2$ yr. We argue that it is not the extreme thermal conditions which matters for the release of radiogenic helium as long as they are above closure temperature for common helium-retentive minerals. Generally, these findings provide both qualitative and quantitative insight into assessment of helium resource potential.

About the author

Ernest Mulaya is a PhD student sponsored by UK Commonwealth Scholarship Commission (CSC) with grant **TZCA-2019-133**. The project is a follow up of a major recent discovery of helium made in the Rukwa Rift during 2015 by a team led by Prof. Jon Gluyas (Durham University) and Prof. Chris Ballentine (Oxford University) under research programme sponsored by Statoil (now Equinoir). This was followed by research plans designed to understand the helium system in the Earth's crust of which partly, Ernest's research is based.

Ernest is also a member of academic staff at the School of Mines and Geosciences of the University of Dar es Salaam in Tanzania. During high school studies he specialized in Economics, Geography and Advanced Mathematics thereafter joined the University of Dar es Salaam in Tanzania to pursue Bachelor of Science in Geology (First Class Honours). After undergraduate studies, Ernest served as exploration geologist for the Africa Barrick Gold Exploration Ltd, a subsidiary under Barrick Gold Corporation, the second-largest gold mining company in the world with its headquarters in Toronto, Ontario Canada. Before joining Durham University, Ernest attended Norwegian University of Science and Technology (NTNU) in Norway to pursue MSc. Petroleum Geoscience specializing in petrophysics hence adding on his exciting scale of experiences and exposures in earth sciences.

Declaration

I hereby declare that this thesis is the result of my own work except where acknowledged. It has never been submitted to any other university or anywhere else for the same or any other award. No portion of the work in this thesis has been submitted in support of an application for the same or another degree or qualification at any other university or institute of learning.

Data availability statement

The data that support the findings of this study are available from Tanzania Petroleum Development Corporation (TPDC). Restrictions apply to the availability of these data, which were used under license for this study. Data are available from the author(s) with the permission of Tanzania Petroleum Development Corporation (TPDC).

Copyright Statement

Acknowledgement

I would like to sincerely thank my supervisory team; Prof. Jon Gluyas, Prof. Ken McCaffrey, Dr. Thomas Phillips (Durham University) and Prof. Chris Ballentine (University of Oxford) for their all sorts of unwavering support, guidance, constructive criticism and discussion towards achievement of this study. I was privileged that our relationship was not strictly academic, they always treated me as a good friend and a colleague, which I'm immensely grateful! *'Asante sana'!*

Many thanks to the Review Committee team for my PhD progress at Durham Earth Science Department including Prof. Andy Aplin, Dr. Richard Walters (now working with KPMG) and Prof. Bob Holdsworth. Their positive comments and scrutiny as an oversight mechanism of my academic progress gave me new impetus to work even harder and achieve more results. Gary Wilkinson is thanked for helping me with GIS and software issues including installations and troubleshooting. I also owe huge thanks to Professor Evelyne Mbede from the University of Dar es salaam for her mentorship and tireless support towards linking my research findings into use by the government of Tanzania.

My sincere heartfelt gratitude goes to the United Kingdom Commonwealth Scholarship Commission (CSC) for the fully bursary offer to pursue this study and to my family too. The University of Dar es salaam in Tanzania is thanked for granting me a study leave and keeping my job. Furthermore, I extend my thanks to Tanzania Petroleum Development Corporation (TPDC) and the Petroleum Upstream Regulatory Authority (PURA) for providing me with seismic dataset. **European Aid/135375/L/Act/Tz** is thanked for partly funding the petrophysical analysis (Chapter 3) at the University of Aberdeen in 2017 on samples collected in the field by Cassy Mtelela.

Special thanks to my wife Gloria and our wonderful children, Erin (daughter) and Espen (son); and my father Stephano for their patience, prayers, love and encouragement throughout my PhD journey.

To my friends Faustine Matiku, Mukakaro Charles, Raphael Menda, Gerald Mrema Remidius Mwema and Rockyus Kerenge, many thanks for the natter, social charts and nostalgic conversation. Massive thanks to my primary school teachers including Magero Misana, Daudi Mafwiri, Harrison Justine, Chausiku Maonyesho, Heri Mujungu and Amond Gunje (R.I.P), During my early age at primary school, these teachers gave me amazing support, unforgettable confidence and most importantly they repeatedly said *'Ernest you are a genius'!* A voice that still dwells in me so powerfully.

Finally, but not least, I dedicate this thesis to my late mum (Helen), late grandma (Nyamchele) and late grandpa (Mulaya) for inspiring and jump-starting my curiosity during early childhood towards who I'm today. Hopefully I would have made them super proud. May their souls continue resting in peace!

Chapter 1: General introduction

1.1 Introduction and research context

The Rukwa Rift is located within the western arm of the East African Rift System (EARS) southwest of the Tanzania Craton (Chorowicz, 2005; Saria et al., 2014; Wedmore et al., 2021; Fig. 1.1). Within this rift, the Rukwa Rift Basin (RRB) exhibits structural patterns from the influence of polyphase tectonic regimes from the Palaezoic, Mesozoic and Cenozoic Eras (Ebinger, 1989; Sander & Rosendahl, 1989; Mulaya et al., 2022). The RRB is bordered by two faults, the NW-trending Lupa Fault to the east and the Ufipa Fault to the west which are broadly collinear with the general rift trend (Mulaya et al., 2022; Fig. 1.1). The stratigraphic sequences in the RRB include three major sedimentary packages overlying Precambrian basement namely, the Permian Karoo Supergroup, the Red Sandstone Group (Cretaceous and Oligocene) and the Lake Beds Group (Miocene-Pleistocene) (Quennell et al., 1956; Wescott et al., 1991; Morley et al., 1992; Wopfner, 1993; Mtelela et al., 2016).

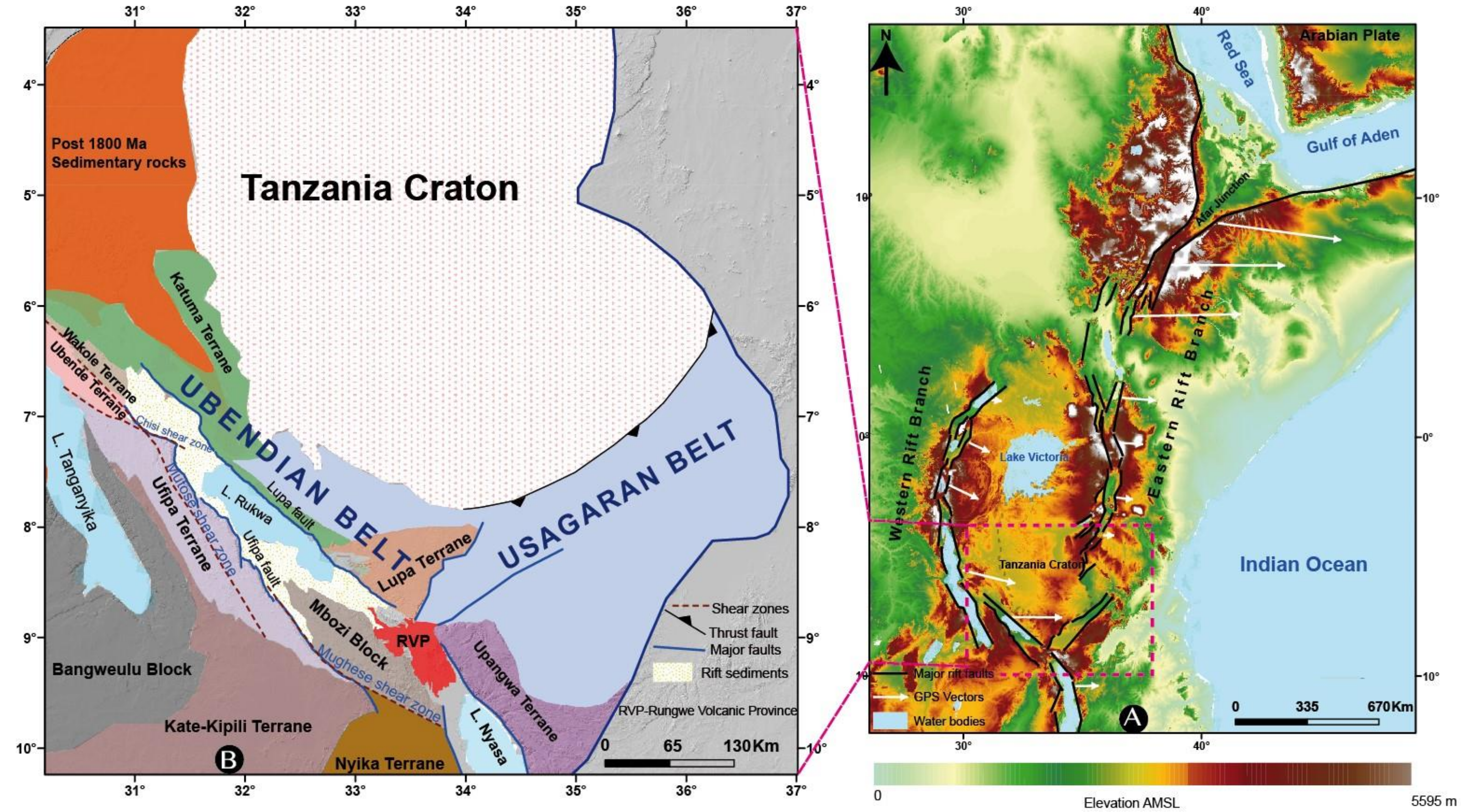

Fig. 1.1. (A) Shaded relief of the Eastern and Western branches of the EARS showing major rift faults mapped on color-coded TanDEM-X 90m data. The GPS vectors from the geodetic measurement show relative rate of extension and direction extracted from Saria et al., 2014. (B) Regional tectonic map superimposed on hill shaded TanDEM-X 90m data showing Precambrian terranes, shear zones and structures surrounding the Rukwa Rift within the Ubendian mobile belt southwestern of the Tanzania Craton (modified after Theunissen et al., 1996; Lemna et al., 2019; Heilman et al., 2019; Mulaya et al., 2022).

Synthesis of the RRB in the recent past was focused on increasing understanding of the basin in relation to hydrocarbon prospectivity, although drilling program of the two wells; Ivuna-1 and Galula-1 resulted as dry wells (Morley et al, 1992, Mtelela et al., 2017). Most recent research has documented a huge concentration of helium ~10% advecting with nitrogen as a carrier gas in thermal springs (Barry et al., 2013; Danabalan et al., 2017). Unlike conventional extraction of commercial helium in the world which occurs as a co-product of natural gas, the RRB represents a hydrocarbon free prospect for helium (Danabalan et al., 2022). The radiogenic helium diffuses into the overlying sediments of the RRB and originates from the surrounding Archean-aged Tanzania Craton and Precambrian basements (Danabalan, 2017). The migration of the deep entrapped helium is triggered by recent tectonic and volcanic activity associated with the East African Rift System (Barry et al., 2013; Danabalan et al, 2017). All these factors make the Rukwa Rift an ideal location to examine and analyse the helium potentials of Tanzania. However, definitive geological settings in the subsurface where helium accumulates and occurs remains challenging. This thesis focuses on the following main aims;

(1) To demonstrate the evolution and geometry of the structural patterns in space and time in relation to helium accumulation potential in the RRB.
(2) To describe the spatio-temporal variation of depocenter morphology and reconstruct the tectonic processes with general implications for helium reservoirs distribution in the RRB.
(3) To quantify the timing of accumulation in RRB and mass balance between ^{4}He efflux and production potential of each tectonic terrane in the region.
(4) To compare geological conditions for helium play elements at the Rukwa Rift with other areas around the world that have similar geologic setting.

1.2. Why is helium useful?

Helium is the second element on the periodic table with unique properties such as its extremely low boiling point, non-flammability, small molecular size, and superfluid properties enabling diverse and specialized applications (Broadhead, 2005; Danabalan et al., 2017). Apart from the common use in party balloons and making a squeaky voice, helium is used to achieve superconductivity in MRI machines in hospitals and CERN's Large Hadron Collider. Other diverse applications include welding, semiconductor and optical fibre manufacturing, leak detection, lifting and development of the new applications in computer hard drives and hybrid air vehicles (Broadhead, 2005; Chaudhuri et al., 2015). For instance in the USA, helium is used for magnetic resonance imaging, 30%; lifting gas, 17%; analytical and laboratory applications, 14%; welding, 9%; engineering and scientific applications, 6%; leak detection and semiconductor manufacturing, 5% and various other minor applications, 14% (USGS, 2020; USGS 2022). Despite these important applications, some of them without substitutability, the global supply of helium has been dwindling year after year putting the world community under pressure to look for further discoveries. A significant quantity of gas is potentially generated radiogenically from the oldest rocks (e.g. Precambrian aged rocks) containing uranium and thorium elements (Danabalan, 2017).

1.3 Global overview of helium demand and supply

The total helium reserves and resources of the world are estimated to be ~40 billion cubic meters (1.439 trillion cubic feet) with 25% in Qatar, 22% in USA, Algeria 21%, Russia, 17%; Canada, 5%; China, 3% and the rest of the world ~7%. (USGS, 2022). The entire global helium industry relies on production of up to ca. 160 million cubic meters from just few sites including the US (48%), Qatar (32%), Algeria (9%), Australia, 3%; and the rest of the share from Russia, Canada and Poland; all originating from serendipitous discoveries when exploring and producing petroleum (Danabalan et al., 2017; USGS, 2020).

Shockingly, the current global consumption is approximately 170 million cubic meters per year outstripping the current production (Helium-One, 2023). In parallel with the dwindling supply, the unit price (US$ per thousand cubic feet) has risen by over 100% in the past decade with the estimated price for private industry's Grade-A helium up to ca. $7.57 per cubic meter ($210 per thousand cubic feet) in 2019 (USGS, 2020).

1.4 History of helium exploration in Tanzania

In Tanzania, helium gas was first documented during the colonial era particularly in Lake Balangida up to 3.7% v/v (James, 1953), Lake Manyara 5.7% v/v (Kent, 1942), and Utimbaru fault thermal springs including Majimoto 17.5% v/v and Mananka 9.3% (James, 1957; Morgan 1958). Notably, the colonial exploration in 1958 involved drilling up to 800 ft at Majimoto by the United Kingdom Atomic Energy Authority (UKAEA) which was analysed by the Government Chemist Lab, London (Morgan 1958; James, 1967). In all these areas, helium was associated with thermal springs seeping to the surface.

Post-colonial studies include Rukwa Basin 4.2% v/v (James, 1967) and recent findings in the same basin have documented up to 10% v/v (Barry et al., 2013; Danabalan, 2017). These concentrations are significant and put Tanzania on a global map of high potential for helium exploration.

1.5 Thesis outline

This section provides a brief outline and content overview for chapter 1-6. Each chapter (Chapter 2-5) is independent with a self-standing introduction, methodology, results, discussion and conclusions. Therefore chapters 2-5 represent either a manuscript ready for publication or one paper that has already been published (Mulaya et al., 2022).

1.5.1 Chapter 1- General introduction

This chapter gives introductory information, overview of regional geologic setting of the study area and general research context. It also gives account on rationale for the project, highlight the uses of helium and its economic implications in a wider perspective.

1.5.2 Chapter 2- Structural geometry and evolution of the Rukwa Rift Basin, Tanzania: Implications for helium potential

This chapter integrates well-tied 2D seismic reflection data, field observations and satellite imagery interpretations to provide a detailed description and illustration of the rift geometry and structural styles. We investigate how the evolution of these structures has influenced stratigraphic distribution and occurrence of helium resource within the RRB. This chapter has been published in the Basin Research journal (Doi: https://doi.org/10.1111/bre.12646).

1.5.3 Chapter 3- Seismic stratigraphic framework, dispersal of depocenters and helium reservoirs in the Rukwa Rift Basin

In this chapter, we present new isopach maps, isochron maps and petrophysical data to describe the distribution of helium reservoirs in the RRB in space and time. The spatio-temporal variations of depocenter morphology for each rifting episodes are illustrated hence providing insights into proportions of accommodation space and sediment accumulations which have wider implications for helium occurrences. The petrophysical parameters (grain density, porosity, and permeability) are analysed to assess the quality of potential helium reservoirs to increase the chance of economic success.

1.5.4 Chapter 4 - Heat flow as a catalyst for radiogenic helium release in the East Africa Rift System

This chapter gives a detailed account of mass balance calculations for the helium production potential and explores chances of accumulation in the RRB. Statistical approaches are applied to geochemical data observed in thermal springs and recorded heat flow to provide insights into the timescale of helium production, release and a possible timing of accumulation surge in the RRB.

1.5.5 Chapter 5 - Assessing helium potential from geothermally active settings

This chapter reviews the play elements for generation, migration and accumulation potential in the Rukwa Rift and other provinces in the world with particular focus on the Bakreswar-Tantloi province (India) and the Yellowstone province (USA). Published datasets are collated and analysed in ArcGIS database to map common geological conditions towards assessing helium prospectivity.

1.5.6 Chapter 6 - Conclusions and future research

This chapter provides a synthesis of the main findings and conclusions from the preceding chapters and recommend on the future work.

References

Barry, P. H., Hilton, D. R., Fischer, T. P., De Moor, J. M., Mangasini, F., & Ramirez, C., 2013. Helium and carbon isotope systematics of cold "mazuku" CO2 vents and hydrothermal gases and fluids from Rungwe Volcanic Province, southern Tanzania Chemical Geology, 339, 141-156. https://doi.org/10.1016/j.chemgeo.2012.07.003

Broadhead, R.F., 2005. Helium in New Mexico—geologic distribution, resource demand, and exploration possibilities. *New Mexico Geology*, *27*(4), pp.93-100.

Chaudhuri, H., Sinha, B. and Chandrasekharam, D., 2015. Helium from geothermal sources. *Proc World Geotherm Congr*.

Chorowicz, Jean, 2005. "The East African rift system". Journal of African Earth Sciences. **43** (1): 379–410. https://doi.org/10.1016/j.jafrearsci.2005.07.019.

Danabalan, D., Gluyas, J.G., Macpherson, C.G., Abraham-James, T.H., Bluett, J.J., Barry, P.H. and Ballentine, C.J., 2022. The principles of helium exploration. *Petroleum Geoscience*, *28*(2), pp.petgeo2021-029.

Danabalan, D., 2017. Helium: Exploration Methodology for a Strategic Resource. PhD Thesis, Durham University.

Ebinger, C.J., 1989. Tectonic development of the western branch of East African rift system. Geol. Soc. Am. Bull. 101, 885-903. https://doi.org/10.1130/0016-7606(1989)101%3C0885:TDOTWB%3E2.3.CO;2

Heilman, E., Kolawole, F., Atekwana, E. A., & Mayle, M., 2019. Controls of basement fabric on the linkage of rift segments. *Tectonics,* 38, 1337–1366. https://doi.org/10.1029/2018TC005362.

Helium-One., 2023 https://www.helium-one.com/helium-market/ accessed on 9th January 2023

Kent, P.E. (1942). A note on Pleistocene deposits near lake Manyara, Tanganyika. Geol.Mag.Vol.79

James, T.C.,1953. Niobium, salt and natural gas deposits in Northern province Tanganyika. Records of the Geological Survey of Tanganyika. Vol.III

James, T.C., 1957. Occurrences of helium-bearing gases in Musoma and North Mara District, Lake Province. Rec. Geol. Surv. Tanganyika, 7, 1957 (1959), 66-71.

James, T. C., 1967. Thermal springs in Tanzania. *Institution of Mining and Metallurgy*.

Kilembe, E. A., & Rosendahl, B. R. ,1992. Structure and stratigraphy of the Rukwa rift. *Tectonophysics*, *209*(1-4), 143-158.

Lemna, O. S., Stephenson, R., & Cornwell, D. G. (2019). The role of pre-existing Precambrian structures in the development of Rukwa RiftBasin, southwest Tanzania. Journal of African Earth Sciences, 150, 607–625.

https://doi.org/10.1016/j.jafrearsci.2018.09.015

Morgan, D.A.O., 1958. Report on helium investigation at Majimoto, Tanganyika. Unpublished report by U.K.A.E.A

Morley, C.K., Cunningham, S.M., Harper, R.M. and Wescott, W.A., 1992. Geology and geophysics of the Rukwa rift, East Africa. *Tectonics*, *11*(1), pp.69-81.

Mtelela, C. (2016). Sedimentology and stratigraphy of the late Cenozoic Lake beds succession, Rukwa Rift Basin, Tanzania: implications for hydrocarbon prospectivity (Doctoral dissertation, James Cook University). https://researchonline.jcu.edu.au/47290/

Mtelela, C., Roberts, E.M., Hilbert-Wolf, H.L., Downie, R., Hendrix, M.S., O'Connor, P.M. and Stevens, N.J., 2017. Sedimentology and paleoenvironments of a new fossiliferous late Miocene-Pliocene sedimentary succession in the Rukwa Rift Basin, Tanzania. *Journal of African Earth Sciences*, *129*, pp.260-281.

Mulaya, E., Gluyas, J., McCaffrey, K., Phillips, T. and Ballentine, C., 2022. Structural geometry and evolution of the Rukwa Rift Basin, Tanzania: Implications for helium potential. *Basin Research*, *34*(2), pp.938-960.

Quennell, A.M., McKinlay, A.C. and Aitken, W.G., 1956. Summary of the geology of Tanganyika, part 1. *Geological Surv. Tanganyika Mem*, *126*.

Sander, S. and Rosendahl, B.R., 1989. The geometry of rifting in Lake Tanganyika, east Africa. *Journal of African Earth Sciences (and the Middle East)*, *8*(2-4), pp.323-354.

Saria, E., Calais, E., Stamps, D. S., Delvaux, D., & Hartnady, C. J. H. , 2014. Present-day kinematics of the East African Rift. Journal of Geophysical Research: Solid Earth, 119, 3584–3600. https://doi.org/10.1002/2013JB010901.

Theunissen, K., Klerkx, J., Melnikov, A., & Mruma, A. (1996). Mechanisms of inheritance of rift faulting in the western branch of the East African Rift. Tanzania. Tectonics, 15(4), 776–790. https://doi.org/10.1029/95TC0 3685

USGS,2020. United States Geological Survey, Mineral Commodity Summaries, January 2020

USGS,2022. United States Geological Survey, Mineral Commodity Summaries, January 2022

Wedmore, L.N., Biggs, J., Floyd, M., Fagereng, Å., Mdala, H., Chindandali, P., Williams, J.N. and Mphepo, F., 2021. Geodetic constraints on cratonic microplates and broad strain during rifting of thick Southern African lithosphere. *Geophysical Research Letters*, *48*(17), p.e2021GL093785. https://doi.org/10.1029/2021GL093785.

Wescott, W.A., W.N. Krebs, D.W. Englehardt, and S.M. Cunningham, 1991, New biostratigraphic age dates from the Lake Rukwa basin in western Tanzania: AAPG Bulletin, v.75, p. 1255–1263.

Wopfner, H., 1993. Structural development of Tanzanian Karoo basins and the break-up of Gondwana. In *Gondwana symposium* (pp. 531-539).

Chapter 2: Structural Geometry and Evolution of the Rukwa Rift Basin, Tanzania: Implications for Helium Potential

(A paper published in the Basin Research Journal, Doi: https://doi.org/10.1111/bre.12646).

Structural Geometry and Evolution of the Rukwa Rift Basin, Tanzania: Implications for Helium Potential

Ernest Mulaya[1,2], Jon Gluyas[2], Ken McCaffrey[2], Tom Phillips[2], Chris Ballentine[3]

[1]School of Mines and Geosciences, University of Dar es Salaam, P.O. Box 35052, Dar es Salaam, Tanzania.

[2]Department of Earth Sciences, Durham University, Durham, UK, DH1 3LE.

[3]Department of Earth Sciences, University of Oxford, Oxford, UK, OX1 3AN.

Ernest Mulaya (Corresponding author); Email: ernest.s.mulaya@durham.ac.uk

Abstract

The Rukwa Rift Basin, Tanzania is regarded as a modern example of cratonic rift zone despite complex polyphase extensional and episodic inversion structures. We interpret 2D seismic reflection data tied to wells to identify and describe structures controlling stratigraphic sequences (Late Carboniferous to Pleistocene) in two main segmented Rukwa Rift domains, A and B, which are controlled by the Chisi and Saza shear zones. Fault geometry and stratal patterns are illustrated in relation to their kinematic interaction with folds. Fold structures reflect both extensional and compressional deformation and were mapped with a particular interest for their helium potential. We illustrate fault bend folds, fault propagation folds and fault propagation monoclines that are related to extension events. Folds related to compression exhibit various structural styles reflecting at least two phases of episodic and widespread inversion. Firstly, Early Jurassic inversion phase which involved multi-faulted anticlines in the Karoo strata. Secondly, a mild and widespread inversion structures during the Pleistocene which are characterized by both symmetrical and asymmetrical anticlines styles. Taken together, the extensional and compressional fold structures, stratal juxtapositions and unconformities define stratigraphic packages that are widely distributed in the Rukwa Rift Basin and form potential subsurface traps for helium-nitrogen rich gases, from which some seep to the surface, evidently documented in thermal springs

across the region.

Keywords: Rukwa Rift Basin; rift border faults; inversion styles; fault rotated fold styles; thermal springs; helium-nitrogen gases

2.1 Introduction

The Rukwa Rift Basin (RRB) is located within the western arm of the East African Rift System (EARS) near an intersection of the Victoria-Nubia-Rovuma-San tectonic plates (Chorowicz, 2005; Saria et al., 2014; Stamps et al., 2018; Wedmore et al., 2021; Fig. 2.1A-B). This basin has an axial length of ca. 300 km, widening from 40 to 80 km progressively towards the southeast (Fig. 2.1B). The RRB records multiple stages of tectonic rifting from the Palaezoic, Mesozoic and Cenozoic (Ebinger, 1989; Morley, 1989; Sander & Rosendahl, 1989; Roberts et al., 2012; Fig. 2.2). Previous authors have suggested that this rift basin is a reactivated system of Neoproterozoic sinistral shear zones within the NW-trending Paleoproterozoic Ubende belt on the western margin of the Archean-Tanzanian Craton (e.g. Quennell et al., 1956; Wescott et al., 1991; Lenoir et al., 1994; Delvaux et al., 1992; Morley et al., 1992; Theunissen et al., 1996). These earlier studies based on limited datasets inferred a number of tectonic extension directions for the Rukwa Rift which fall into three end-member models - NW-SE, NE-SW and E-W directions (e.g. Chorowicz and Mukonki, 1980; Ebinger, 1989; Sander and Rosendahl 1989; Morley et al., 1992; Mbede, 1993; Wheeler and Rosendahl, 1994; Delvaux et al., 2012). However, the recent published geodetic data observation, Kostrov summation analyses of local teleseismic earthquake data and source mechanisms for stress inversion, indicate present-day E-W extension rates ca. 2.26 mm y^{-1} (Delvaux and Barth, 2010; Saria et al., 2014; Stamps et al., 2018; Lavayssière et al., 2019). First-motion focal mechanism solutions for earthquakes reveal deformation from normal dip slip to strike slip on steep nodal planes (≥45°) with modal depths of 25–35 km (e.g. Delvaux et al., 2010; Lavayssière et al., 2019). Yet critical questions remain regarding the spatial and temporal distribution and evolution of structures, their kinematic interpretations and which have profound implications for helium potential at kilometer-scale depths within unconformably-bound synrift sedimentary packages.

Geochemical studies of surficial seepages of thermal springs and soils in the RRB have recently confirmed that they contain up to 10% helium by volume, with nitrogen dominating as a carrier gas (James, 1967a; James, 1967b; Barry et al., 2013; Danabalan, 2017). It is worth noting that such high concentrations of helium are exceptional in nature and substantially above the commonly accepted concentration of 0.3% for economically viable extraction of helium (Danabalan, 2017). Unlike the conventional helium occurrences associated with hydrocarbon in many places, the RRB presents a 'pure play' prospect where radiogenic helium is associated with nitrogen and carbon dioxide gases (e.g. Danabalan, 2017). The radiogenic helium, transported into the overlying sediments of the RRB, is inferred to originate from the surrounding Archean-aged Tanzania Craton or underlying Proterozoic basement (e.g. Holland et al., 2013; Warr et al., 2018). The release of the deep helium from its source is hypothesised to have been enhanced by recent tectonic and volcanic activity associated with the Cenozoic East African Rift System (Barry et al., 2013; Danabalan, 2017). All these factors make the RRB an ideal location to examine how the structural heterogeneities formed during the evolution of the RRB contribute to its helium potential.

This study integrates well-tied 2D seismic reflection data, field observations and satellite imagery interpretations to address the question of how the rift geometry and structural styles have influenced basin stratigraphic distribution and helium potential for the RRB.

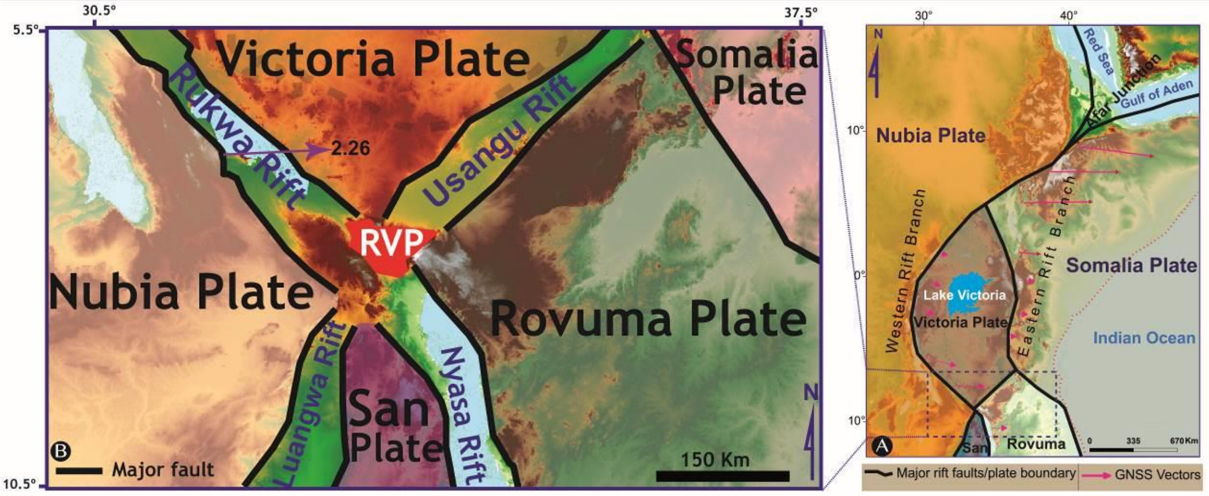

Fig. 2.1. (A) Map showing the tectonic configuration and boundaries of the major plates i.e. the Nubia and Somalia plates and microplates including San, Victoria and Rovuma plates. The GPS vectors from the geodetic measurement (pink arrows) show relative rate of extension and direction extracted from Saria et al. (2014) along the Eastern and the Western branches of the EARS mapped on color-coded TanDEM-X 90m data (Fernandes et al., 2004; Saria et al., 2014; Stamps et al., 2018; Daly et al., 2020; Wedmore et al., 2021). (B) Close up map showing regional configuration of the tectonic plates and major rifts forming plate boundaries, superimposed on color-shaded terrain map. RVP=Rungwe Volcanic Province.

2.2 Regional geologic and tectonic setting

2.2.1 Geology, tectonic terranes and shear zones

The RRB lies within the NW-trending Paleoproterozoic Ubendian orogenic belt at the southwestern margin of Tanzania between the Tanzanian Craton and the Archean-Paleoproterozoic Bangweulu Block (Kilembe and Rosendahl, 1992). The basin is surrounded by uplifted Paleoproterozoic basement that comprises mainly granulite and amphibolite facies metamorphic rocks with granitic intrusions (Daly, 1988; Kilembe and Rosendahl, 1992; Delvaux et al., 2012; Fritz et al., 2013). These basement units are subdivided into eight terranes, which are separated by ductile shear zones. These terranes include; Katuma, Lupa, Upangwa, Mbozi, Kate-Kipili, Ufipa, Wakole and Ubende Terranes (Boniface et al., 2012; Fig. 2.3A). These Precambrian terranes surrounding the RRB reveals three dominant lineament orientations of NW-SE, NNW-SSE and NNE-SSW (Fig. 2.3A).

The major shear zones in the Ubendian orogenic belt include; the Mughese shear zone, the Mutose shear zones, the Chisi shear zone and the Saza shear zone (Mnali, 1999; Boniface et al., 2012; Fig. 2.3A). Notably the Chisi shear zone, which defines a suture, marks the edge of the Ubendian orogenic belt and separates the Archaean to Paleoproterozoic Bangweulu cratonic block from the Archean Tanzania Craton (Boniface et al., 2012; Delvaux et al., 2012; Heilman et al., 2019). These tectonic terranes and shear zones significantly influence the geometry and syn-rift sediment distribution within the RRB, which we discuss in this study.

2.2.2 East Africa Rift System

The current tectonic setting of the N-S trending East African Rift System (EARS) extends from the Afar depression in Ethiopia through eastern Africa, stretching to the Southwest Indian Ridge i.e. at the junction with the Antarctic plate (e.g. Saria et al., 2014; Stamps et al., 2018; Fig. 2.1A). The EARS forms a divergent plate boundary mainly between the Nubian and the Somalian tectonic plates from which strains are accommodated along the Victoria, Rovuma, San and Lwandle subplates (Fernandez et al., 2004; Saria et al., 2014; Stamps et al., 2018; Daly et al., 2020; Wedmore et al., 2021). The EARS initiation dates back to the early Miocene and exhibit various active faulted-basins, frequent seismicity and volcanic centers (Ebinger, 2005; Saria et al., 2014). The EARS bifurcates into the Eastern and Western rift branches influenced by several zones of inherited basement fabrics (Daly et al., 1989; Theunissen et al., 1996; Chorowicz, 2005; Fig. 2.1A). The Western branch exhibits several rifts occupied by large, mainly deep lakes from north to south including Lakes Albert, Edward, Kivu, Tanganyika, Rukwa and Nyasa (Malawi) and it continues to the Indian Ocean (Saria et al., 2014; Katumwehe et al., 2015; Lemna et al., 2019). The Rukwa Rift is located between the Victoria and Nubia plate near the intersection of the Victoria-Nubia-Rovuma- San plates (Fig. 2.1B).

2.2.3 Generalized stratigraphy of the Rukwa Rift Basin (RRB)

The stratigraphic sequences in the RRB include three major sedimentary packages overlying Precambrian basement namely: the Karoo Supergroup, the Red Sandstone Group and the Lake Beds Group (Quennell et al., 1956; Wescott et al., 1991; Morley et al., 1992; Mtelela, 2016; Fig. 2.2). The Karoo Supergroup comprises the Late Carboniferous to Permian units that lie unconformably on Precambrian Basement (Kilembe and Rosendahl, 1992; Morley et al., 1999b; Fig. 2.2). The Red Sandstone Group unconformably overlies the Karoo Supergroup and is divided into two formations including the Cretaceous fluviatile Galula Formation, and the Oligocene Nsungwe Formation composed of mainly quartzose and richly fossiliferous fluvial-lacustrine sandstone sequences (Roberts et al., 2010; Mtelela et al., 2017; Widlansky et al., 2018). Finally, the uppermost strata consist of Late Miocene-Pleistocene Lake Beds Group which comprises two subdivisions including the Late Miocene-Pliocene Malangali Formation and the Pleistocene Ilasilo Formation (Hilbert-Wolf et al., 2017; Mtelela et al., 2017; Fig. 2.2). The uppermost strata contain records of the modern tectonic development of the EARS and associated extensive influence from the Rungwe Volcanic Provinces (RVP) (Ebinger et al., 1989; Wescott et al., 1991; Mtelela, 2016; Lawrence et al., 2021).

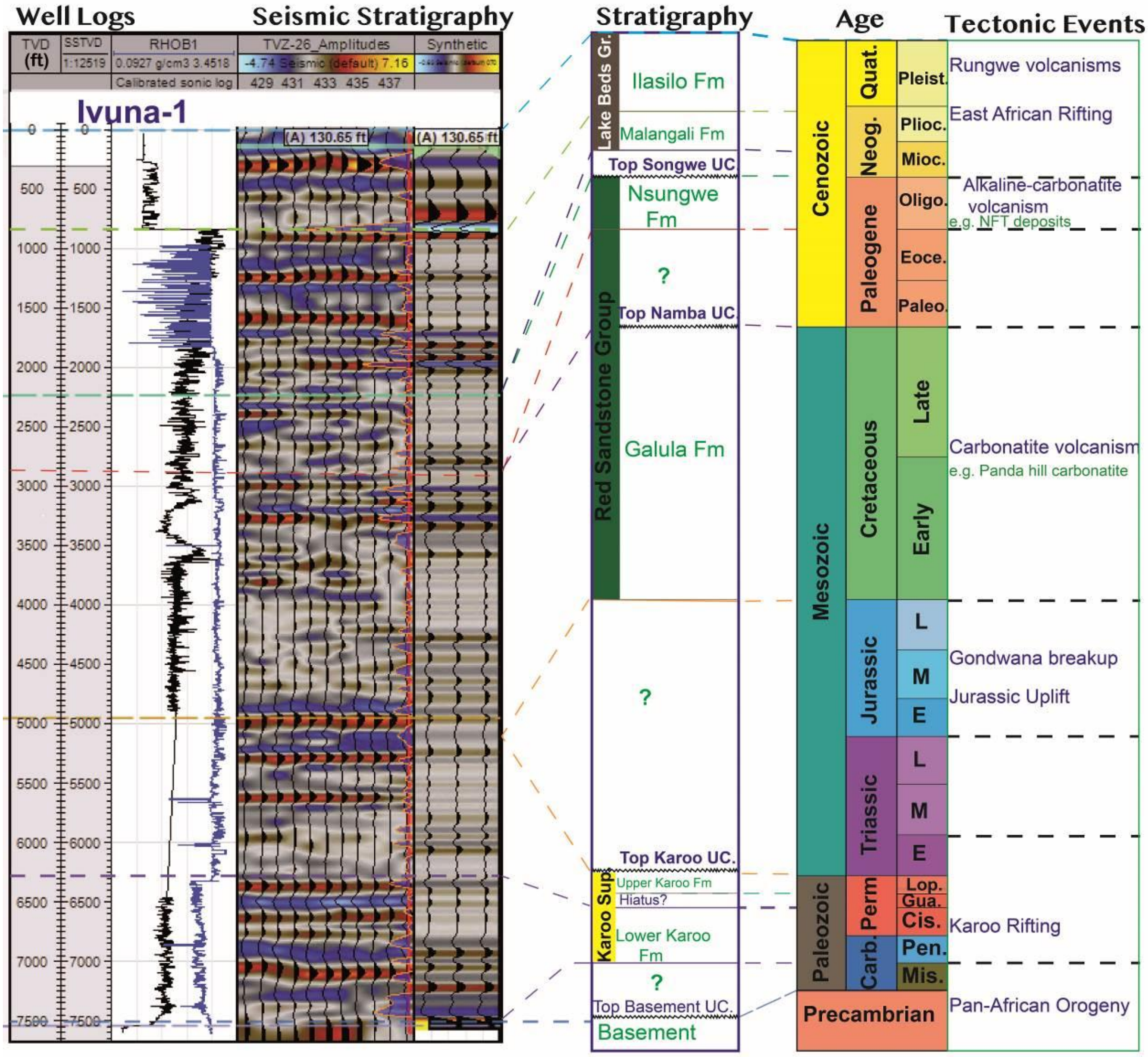

Fig. 2.2. Generalized stratigraphy of the Rukwa Rift Basin correlated with the major regional tectonic events, Formations (Fm), Unconformities (UC) and a synthetic seismogram generated from well logs i.e. the bulk density and acoustic logs tied to seismic section (TVZ-26). Stratigraphic data (well tops information) from the geological report are correlated with high amplitude seismic horizons, hence providing confidence and control during interpretation. The ages of key horizons are constrained using previous work by Mtelela, (2016); Hilbert-Wolf et al., 2017; Lawrence et al., 2021 and references therein. Sup = Supergroup; Gr = Group; NFT = Nsungwe Formation Tuffs.

2.3.0 Methods and datasets

In this study the results from borehole-constrained 2D seismic reflection data, Digital Elevation Model (DEM) data and fieldwork are integrated to document structural and stratigraphic evolution of the RRB. This combined approach provides insights into the geometric and physiographic distribution of faults, stratigraphic units and their spatial relationships to rift-related structures (e.g. Hayward and Graham, 1989; Morley et al., 1999b; Turner and Williams, 2004; Phillips et al., 2020; Gluyas and Swarbrick 2021).

2.3.1 Datasets

2.3.1.1 Digital Elevation Models (TANDEM-X 90m data)

We compiled TanDEM-X 90m (TerraSAR-X add-on for Digital Elevation Measurements) data, which were acquired by the German Aerospace Center (DLR) in partnership with Airbus Defence and Space between 2010 and 2015 (Rizzoli et al., 2017). These data are products of an Earth observation radar mission consisting of a Synthetic Aperture Radar (SAR) interferometer (Wessel, 2016). The acquisition involved the separation between two identical satellites by 120 m to 500 m to create a 3D map of the Earth's land surfaces (Zink et al., 2014; Wessel, 2016). The TanDEM-X 90 m data provides a global Digital Elevation Model (DEM) with a 0.4 arcseconds (12 m) horizontal spatial resolution, and pixel spacing of 3 arcseconds corresponding to approximately 90 m at the equator, which is ideal for the purpose of this study (Zink et al., 2014; Wessel, 2016; Rizzoli et al., 2017).

2.3.1.2 Seismic and borehole data

The 2D seismic data used in this study were acquired by American Oil Company (AMOCO), Pecten, and Petrofina under a production sharing agreement with the Tanzania Petroleum Development Corporation (TPDC) in the 1980’s while exploring for hydrocarbons in the area (Kilembe and Rosendahl, 1992; Morley et al., 1992). A land seismic program of 840 km was recorded with 64 - fold coverage using LRS 309 vibrators by Western Geophysical and 1610 km with 48 - fold acquired by Seiscom

Delta in the Lake Rukwa (Morley et al., 1992), which occupies almost a half of the ca. 5800 km^2 depression formed adjacent to the Lupa Fault (see Appendix 1). The survey included a total of ca. 2450 km of 2D seismic lines spaced between 2.5-5.0 km apart stored in SEG-Y format. This operation resulted in the drilling of two dry wells namely Ivuna-1 and Galula-1, to depths of 7600 ft. (2317 m) penetrating the basement and 5000 ft. (1524 m) respectively (Wescott et al., 1991; Morley et al., 1992; Table 2.1). The two wells yielded wireline logs and formation tops data that are used to constrain the mapped seismic horizons (Fig. 2.2).

The seismic data are presented in Two Way Travel time (TWT). They are displayed with SEG reverse polarity, such that a downward increase in acoustic impedance is represented by a trough (blue) whereas a downward decrease in acoustic impedance is represented by a peak (red) reflection event on a seismic profile (Avseth et al., 2010). The seismic data are characterized by continuous and distinct medium to high energy events, however some places show low energy discontinuous and chaotic reflections with significantly degraded image quality. Thus, the datasets are in places of good quality and optimal to ca. 6000 ms TWT depth to the Precambrian Basement, whereas in other areas the image quality is poor thus compromising the image resolution. The variability of the resolution across the dataset is reflected in some of the maps and seismic sections presented in this study.

2.3.2 Methods

2.3.2.1 Lineament mapping

Examination of the TanDEM-X 90 m derived hill shade and color-coded aspect maps enabled networks of topographic lineaments to be mapped. The lineaments were mapped to show the current spatial relationship between the traced structures and the distribution of thermal springs across the region which provides fundamental constraints on the fluid flow. Multiple directions of these lineaments are assumed to depict fault systems, fracture zones, mineral fabric orientations, and striking dyke structures or shear zones (e.g. Kervyn et al., 2006; Smets et al., 2016; Fig. 2.3). Using the shaded relief maps, topographic lineaments were identified and traced in ArcGIS software and calibrated by the existing field maps (e.g. Kervyn et al., 2006). The geometry of mapped lineaments was analysed using Stereonet™ software based on algorithms illustrated by Allmendinger et al. (2013). Nevertheless, there are a number of caveats which concern the validity of this methodology and misinterpretation cannot be totally excluded. Some minor faults might be missed entirely due to small displacement and limited resolution to map structures from synrift outcrops.

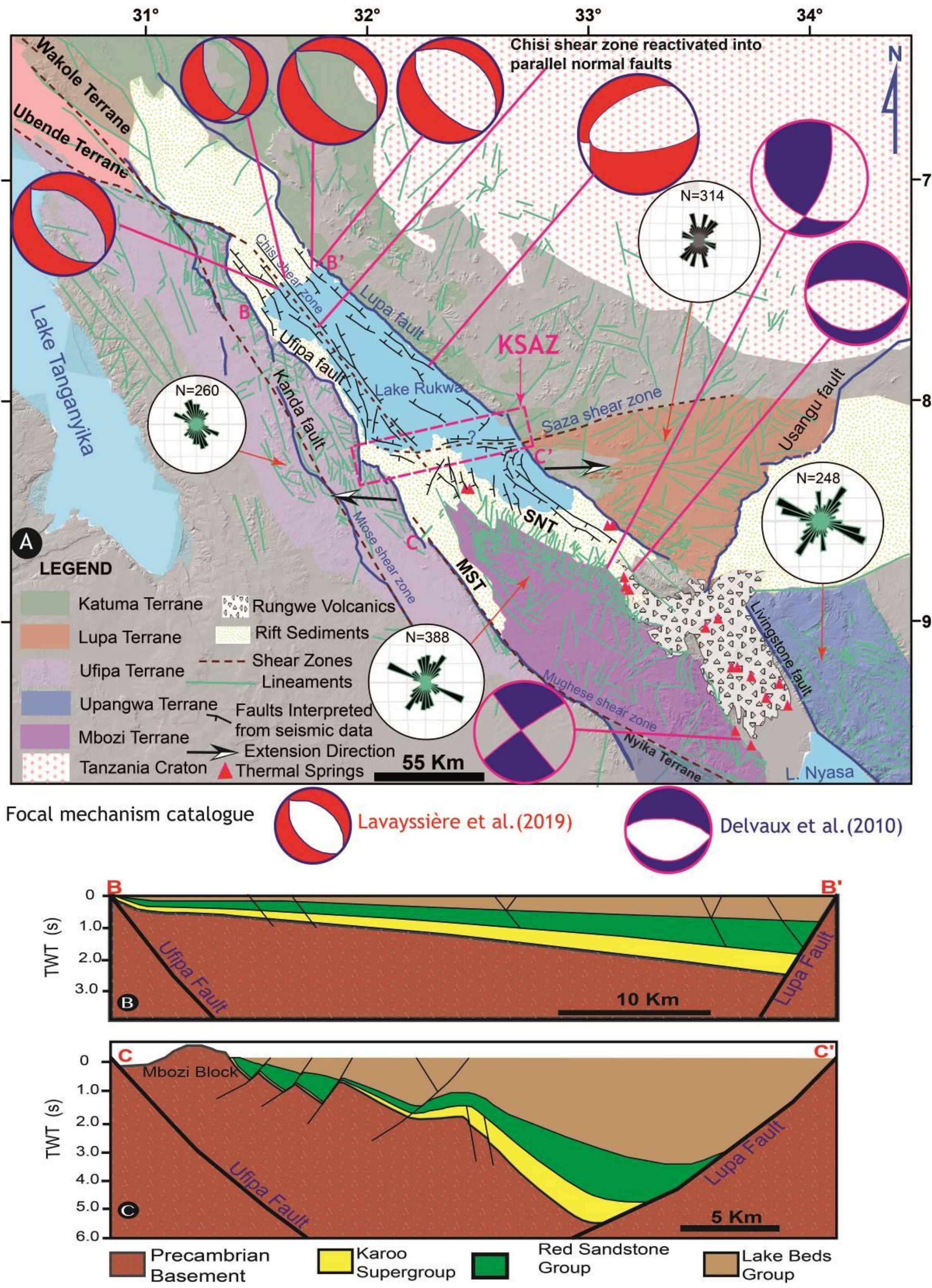

Fig. 2.3. (A) Map showing the Precambrian terranes surrounding the Rukwa Rift Basin with rose diagrams that summarise the main lineaments trends showing NW-SE, NNW-SSE and NNE-SSW directions, mapped on hill shade images. The intrabasinal faults are interpreted from seismic data. The Mbozi Block bifurcates the

basin into the Musongano trough (MST) to the West and the Songwe sub-basin (SNT) to the east. Note the shear zones separating different terranes i.e. Mughese, Mtose, Chisi and Saza shear zones (e.g. Mnali, 1999; Heilman et al., 2019; Lemna et al., 2019; Kolawole et al., 2021). Note the Saza shear zone lies sub-parallel to the extension direction and perpendicular to the Chisi shear zone. Cross sections (B-B′ and C-C′) show the general basin geometry in Domain A and B respectively, separated by the Kwera-Saza Accommodation Zone (KSAZ) (see Fig. 2.4 for domain locations).

2.3.2.2 Seismic data interpretation

Both seismic and well data were uploaded to Schlumberger's Petrel Software™ version 2018. The seismic data interpreted on an interactive workstation provide snapshots and important constraints on the subsurface potential for helium resources the RRB. Before interpretation, quality control of the seismic sections and horizons was performed using synthetic seismograms and lithological logs to tie the stratigraphic data to the seismic reflection data (Roe et al., 1996; Fig. 2.2). During interpretation the major stratigraphic top reflectors were identified on a well-constrained 2D seismic image and picked based on borehole data and checkshot surveys from the Ivuna-1 well (Fig. 2.2). Four major seismic sequences were identified and interpreted corresponding to the Precambrian basement, Karoo Supergroup, Red Sandstone Group and Lake Beds sequences. The major seismic reflectors confining the stratigraphic sequences were mapped across the data coverage and the approximate depths shown in TWT. Consequently, time-thickness maps derived from major strata were generated using a convergent interpolation algorithm embedded in Petrel software.

Table 2.1. Well tops and the lithological boundaries extracted from drilling and geological report with End of Hole (E.O.H) (Morley et al., 1992; Roe et al., 1996).

Well Name	**Top Horizon**	**Depth (ft)**
Ivuna-1 (E.O.H=7600 ft)	Top Nsungwe Formation	2233
	Top Upper Karoo Formation	4950
	Top Precambrian Basement	7540
Galula-1 (E.O.H=5000 ft)	Top Nsungwe Formation	5000

2.4.0 Results

2.4.1 Rift geometry, physiography and stratigraphy

Major fault networks in the RRB consist of two border faults, the NW-trending Lupa Fault to the east and the Ufipa Fault to the west which are broadly collinear with the general rift trend and extend up to c. 350 km and c. 400 km respectively (Fig. 2.3A-C; Fig. 2.4). The Lupa Fault terminates abruptly in the northwest and becomes buried in the Rungwe volcanic province in the southeast and thus it is no longer visible at the surface (Fig. 2.3A). To the west and southwest the RRB is bordered by the NW-trending Ufipa Fault, which abuts the Chisi shear zone in the northwest (Kervyn et al., 2006, Heilman et al., 2019; Fig. 2.3A; Fig. 2.4).

Intrabasinal faults are characterized by km-scale normal faults, which are either parallel to border faults or exhibit NNE-SSW and NNW-SSE orientations (Fig. 2.3A-C; Fig. 2.4). The spatial and temporal variation of the border faults, shear zones and the intrabasinal fault networks exert control over synrift sedimentary packages and stratigraphic distribution in the RRB (e.g. Fig. 2.3A-C). Based on these structural patterns, we have divided the RRB into two structural domains; namely Domain A and Domain B (Fig. 2.4).

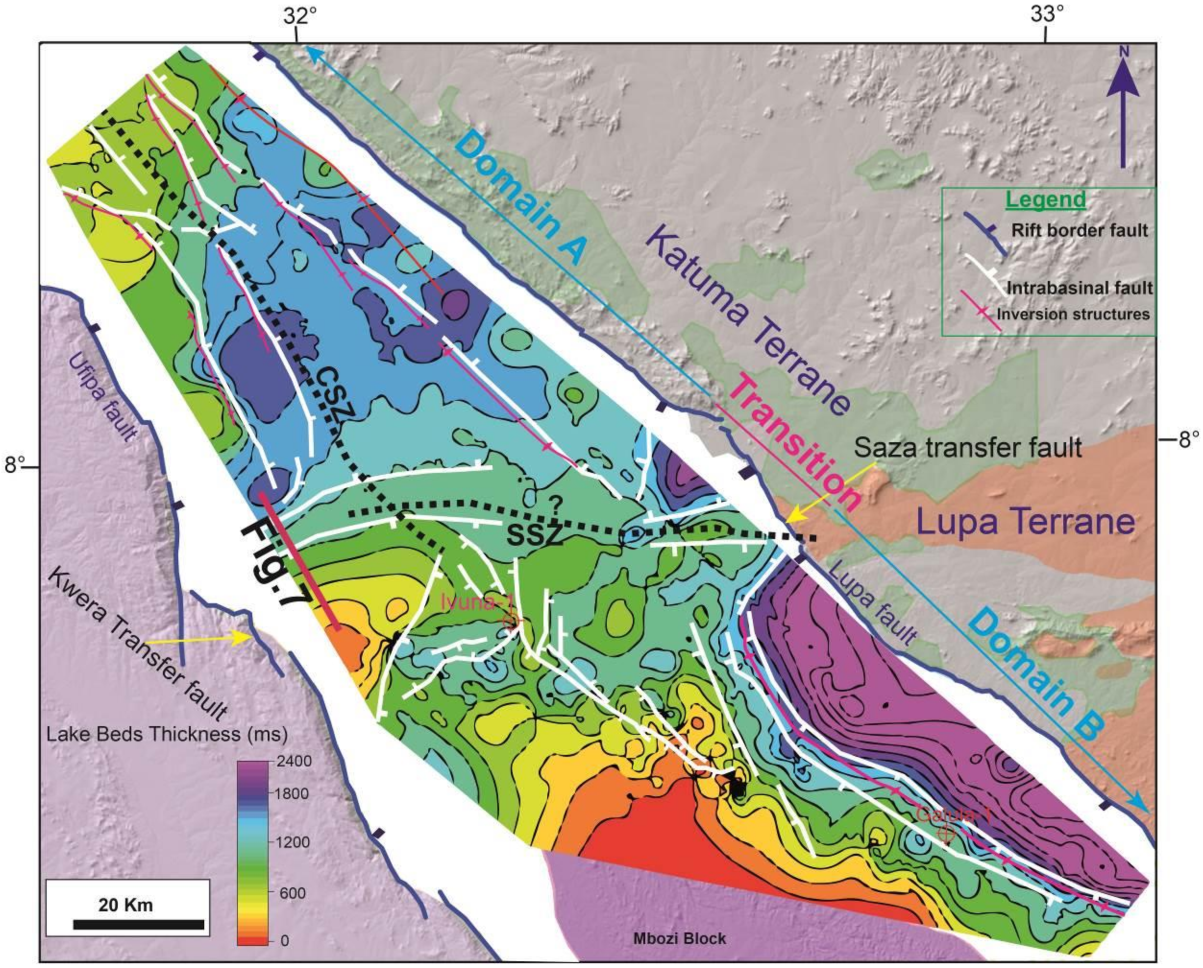

Fig. 2.4. Time-thickness map for the Lake Beds Group superimposed on hill shaded map and interpreted structures showing intrabasinal faults, distribution of inversion structures and depocenters segmented into Domain A and B. Note the WNW-ESE – striking faults perpendicular to the Chisi Shear Zone (CSZ) and sub-parallel to the Saza Shear Zone (SSZ).

2.4.1.1 Domain A - Steep faults and gently-dipping synrift package wedge

Domain A extends northwestward from the northern end of the Mbozi Block (Fig. 2.4). In this domain, the Lupa Fault exhibits planar geometry at all mapped depths (Fig. 2.5A). Within 5 - 10 km of the Lupa Fault, the RRB is characterized by steeply NE-dipping antithetic normal faults whereas in the middle of basin it is dominated by steeply dipping conjugate faults between which strata are mildly folded (Fig. 2.5A). Further to the west of the RRB, steeply dipping normal faults, that are synthetic faults to the Ufipa Fault, dominate and are aligned with the Chisi shear zone (Fig. 2.3A; Fig. 2.4).

The RRB in Domain A is characterized by gently dipping synrift stratal wedges that show overall thickening to c. 3500 ms TWT towards the Lupa Fault in a region covering the entire basin north of the Mbozi Block (Fig. 2.5A). In this domain the Karoo Supergroup and the Red Sandstone Group exhibit a progressively thickening wedge morphology that dips gently towards the Lupa Fault whereas the Lake Beds strata are relatively shallowly dipping and display constant thickness of c. 1600 ms TWT. Generally, the synrift strata range between 2500 and 3500 TWT ms, and are considerably thinner than the equivalent units in Domain B (Fig. 2.5A; Fig. 2.6).

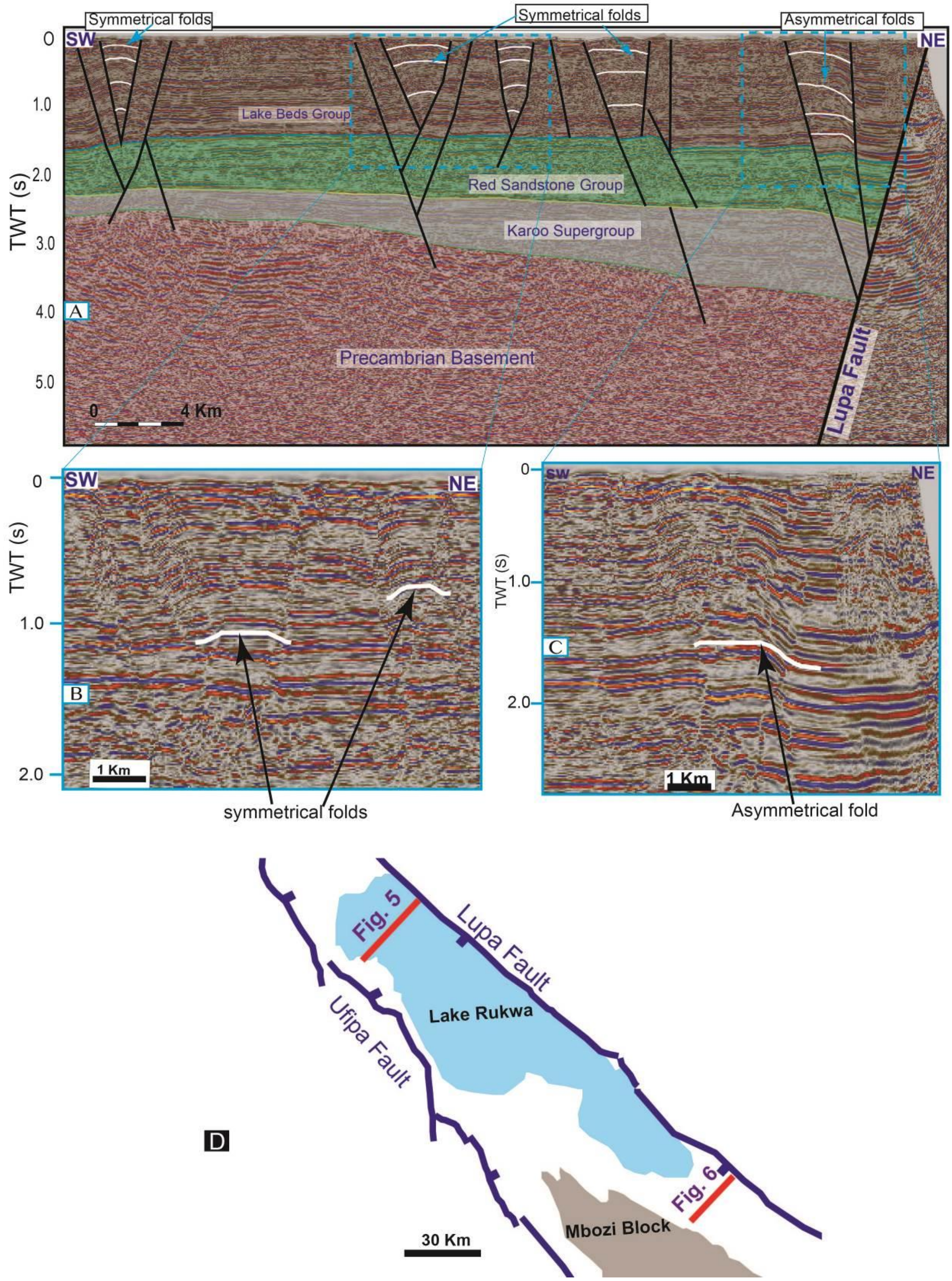

Fig. 2.5. (A) Geoseismic sections interpreted within Domain A characterized by uniformly steep Lupa Fault and, asymmetrical and symmetrical folds. (B) Seismic section showing symmetrical folds (white curves) bounded by steeply dipping

conjugate normal faults in the middle and western part of the basin. (C) Seismic section showing symmetrical folds (white curve) associated with the antithetic faults within proximity of c. 5 - 10 km from the Lupa Fault (D) Sketch map showing the location of seismic lines illustrated in Figs. 2.5 & 2.6 in relation to the position of the Lake Rukwa (See also Fig. 2. 9A for map location).

2.4.1.2 Domain B - Rotated faults and steep synrift package wedge

In Domain B, the Lupa Fault dips more steeply than in Domain A in the upper section and more gently in the lower section (Fig. 2.6). In the middle of the basin c. 25 km from the Lupa Fault, we map a major intrabasinal rotated fault with a general NW-strike and SW-dip extending through the entire Domain B (cf. Fig. 2.4 to see map extent). This fault exhibits a curvilinear pattern in map-view and rotational geometry in cross section (Fig. 2.4; Fig. 2.6). Adjacent to the Mbozi Block, Domain B is characterized by predominantly NNW-SSE and NNE-SSW striking faults/lineaments, which extend into the Mbozi Block and the RRB (Fig. 2.3A).

The geometry of the RRB in Domain B is that of a classical half-graben in which the sedimentary packages thicken and dip towards the Lupa Fault (Fig. 2.6). The basin thickness varies from zero across the uplifted Mbozi block and the Ufipa Fault in the southwest thickening to 6000 ms TWT adjacent to the Lupa Fault. The synrift sedimentary packages in this domain are generally thicker than their coeval packages within Domain A (Fig. 2.5A; Fig. 2.6). Notably the Karoo Supergroup in this domain exhibits two distinctly different seismic characters and structural styles. The lower part of the Karoo sequences sequence is highly faulted, whilst the upper sequence remains relatively undeformed (Fig. 2.6). A high-amplitude seismic reflector, which separates the upper and lower sequences, exhibits distinct continuity across the basin (Fig. 2.6). Based on these seismic signatures observed in Domain B, we divide the Karoo Supergroup into two subdivisions, herein named the Upper Karoo Formation and Lower Karoo Formation. These distinct intervals most likely record the Karoo Supergroup deposition between late Carboniferous

(Pennsylvanian) – Permian (Cisuralian) and late Permian (Lopingian) respectively with a hiatus that is possibly Guadalupian age (cf. Delvaux, 2001; Mtelela et al., 2017; Hilbert-Wolf et al., 2017; Widlansky et al., 2018; Fig. 2.2; Fig. 2.6).

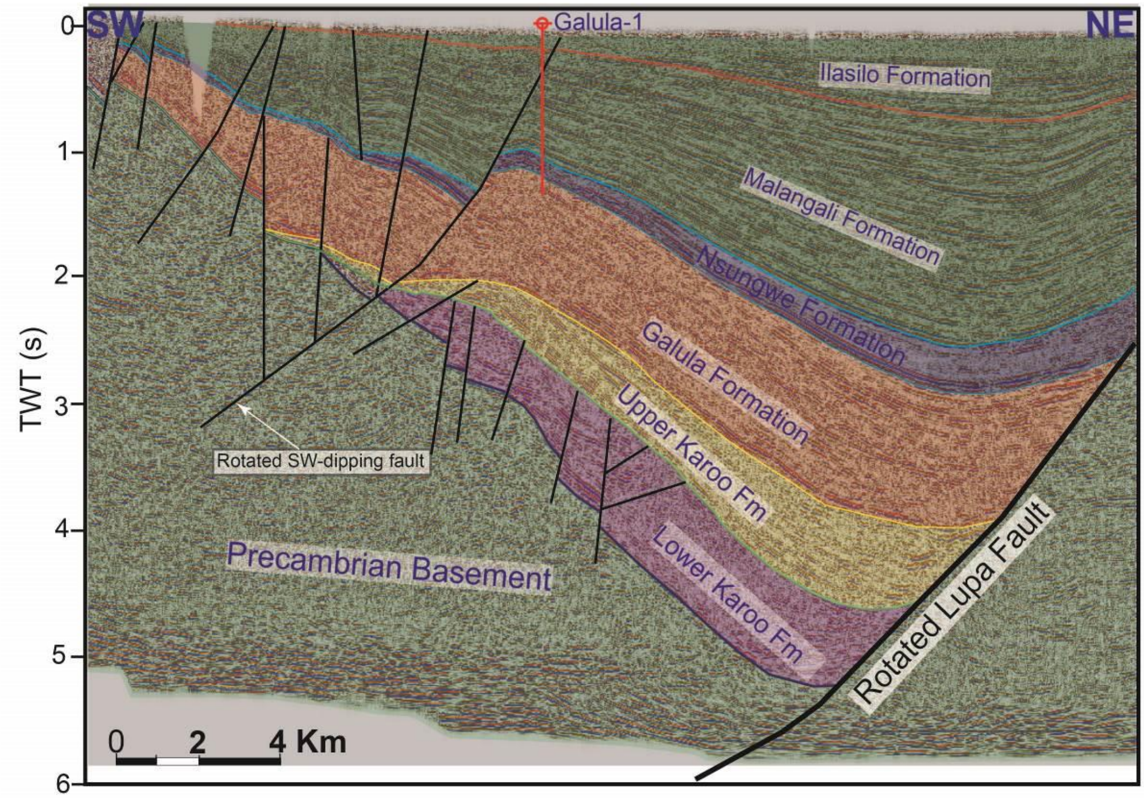

Fig. 2.6. Geoseismic section through Domain B of the RRB showing the temporal stratigraphic distribution of a typical half-graben geometry. The synrift sediment packages dip steeply towards the rotated Lupa Fault and thin up to surface on top of the uplifted Mbozi block. Note the Lower Karoo Formation characterized by basement-rooted faults, which are truncated at top Lower Karoo horizon (see Fig. 2.5D & 2.9A for map location).

2.4.1.3 Border fault segmentation and transfer zones

The Lupa and the Ufipa faults exhibit discrete ca. 25 km and 20 km length border fault segments respectively located approximately at 8° S which we name the Saza and Kwera transfer faults (Fig. 2.4). By transfer fault we refer to a dip-slip fault segment between two major border fault segments, which have slightly different displacement and geometry components i.e. a transitional zone of deformational strain from fault to fault (e.g. Walsh and Watterson, 1989). These structures bound a region that we have named the Kwera - Saza Accommodation Zone (KSAZ) (Fig. 2.3A). The transfer fault segment separates the border faults into northern and southern segments and acts as a transition zone between Domain A and B (Fig. 2.3A; Fig. 2.4). These transfer segments are separated from the main border fault segments by a gap of up to ca. 3 - 5 km at both ends of the fault traces (Fig. 2.4). The surface trace of these fault segments is characterized by a deviation from the main NW-SE trend of border faults to the NNW-SSE and WNW-ESE along the Lupa and the Ufipa Fault respectively (Fig. 2.4). These segments are possibly associated with a relay ramp (cf. Gawthorpe et al., 1990; Gawthorpe and Hurst 1993).

The time-structural map reveals that, the KSAZ is characterized by sediment accumulation minima and ESE-trending normal faults (Fig. 2.4). Notably across the KSAZ we see a transition zone separating the contrasting stratigraphic packages in Domain A and B along the strike length (cf. section 2.4.1.1 and 2.4.1.2; Fig. 2.4). West of the RRB, the stratigraphy across the KSAZ is characterized by a topographic basement high associated with uplift, erosion surfaces and truncation of Karoo strata (Fig. 2.7A-B).

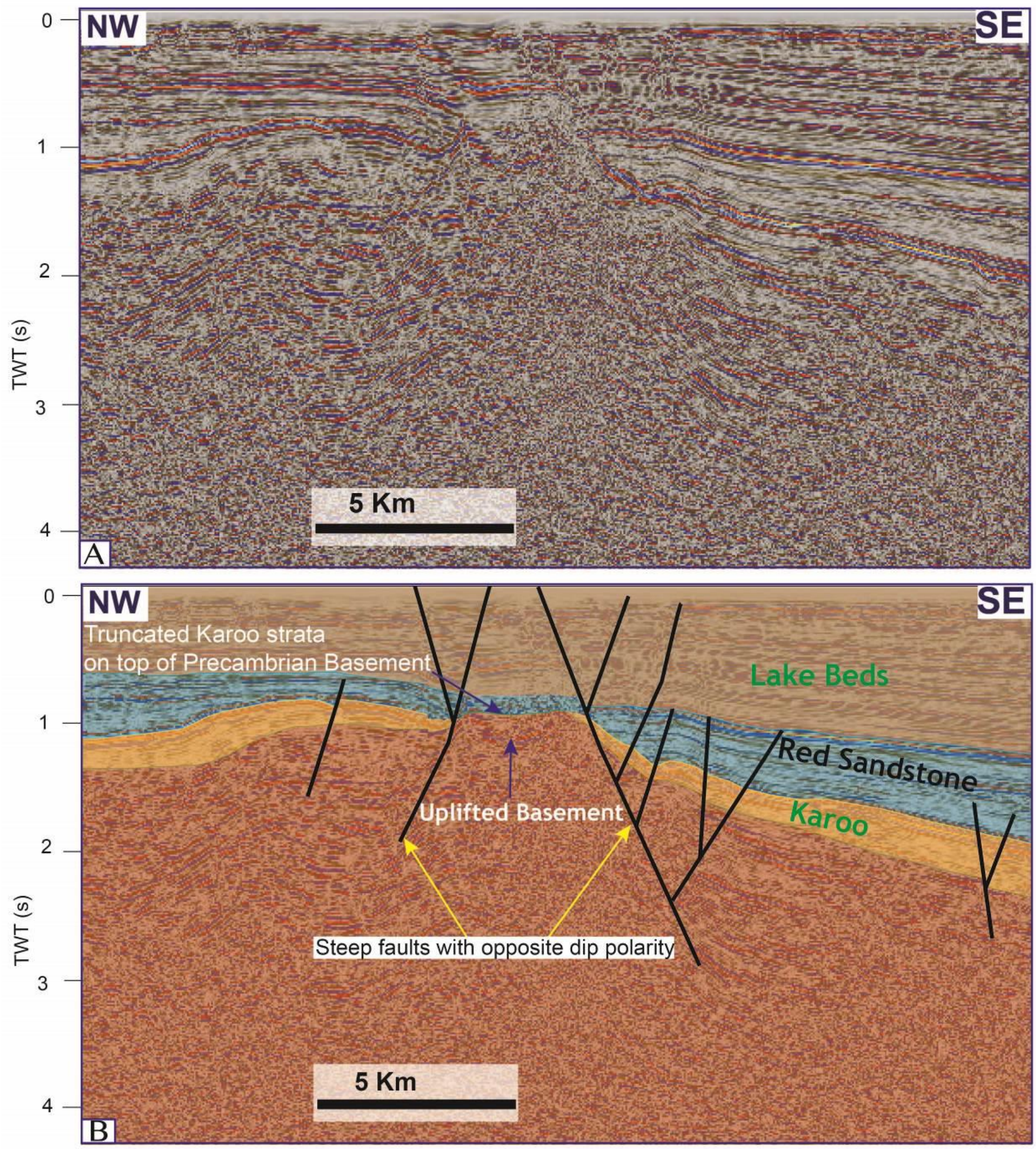

Fig. 2.7. (A) Uninterpreted seismic section. (B) Interpreted geosection illustrating the topographic basement high, truncation of Karoo strata and unconformity associated with strong amplitude response. Note the NE trending fault (NW and SE-dipping) is located adjacent to Kwera relay ramp (see Fig. 2.4 and Fig. 2.9A for map view and location).

2.4.2 Fault control on thermal springs and helium seeps

Thermal springs which are associated with helium in the RRB are mainly controlled by border faults and intrabasin fault networks (e.g. Figs. 2.8A-C). The intrabasin faults traced particularly at the northern end of the Mbozi Block in the Itumbula and Ivuna areas consist of a series of isolated faulted blocks and rotated sedimentary wedges (Figs. 2.8A-B). The Karoo and the Red Sandstone sequences are juxtapositioned along NW-SE and NNW-SSE striking normal faults associated with throws up to 630 ms TWT (Fig. 2.8B). These strata show significant thickness increase between 430 and 710 ms TWT towards the SW - dipping normal faults set (Fig. 2.8B).

Field observations reveal numerous sites which exhibit thermal springs with significant helium concentration in the RRB (e.g. Fig. 2.8A; Table 2.2). These thermal springs are distributed adjacent to the northern end of the Mbozi Block and along the Lupa Fault (Fig. 2.8A). Notably, in the vicinity of the Itumbula and Ivuna areas, surface manifestations reveals that the thermal springs with gas are bubbling into the salt pan at the boundary between the Precambrian basement and the synrift sediments (e.g. Figs. 2.8B-C). The combined seismic cross-sectional views and surface manifestation of thermal springs from the Ivuna and Itumbula sites reveal that these fluids emanate from both NW-SE and NNW-SSE striking faults and at the lithological contact between the sedimentary units and the Precambrian basement (e.g. Figs. 2.4 & 2.8B-C). The geochemical analysis of fluid samples from these two sites in particular, show low $^3He/^4He$ ratios and high radiogenic helium concentration between 2% and 5% v/v associated with high nitrogen gas up to 96% (Danabalan, 2017; Table 2.2). The abundance of radiogenic helium concentrations in this part of the RRB confirms that the source rock is crystalline basement which is rich in helium producing minerals, i.e. uranium and thorium.

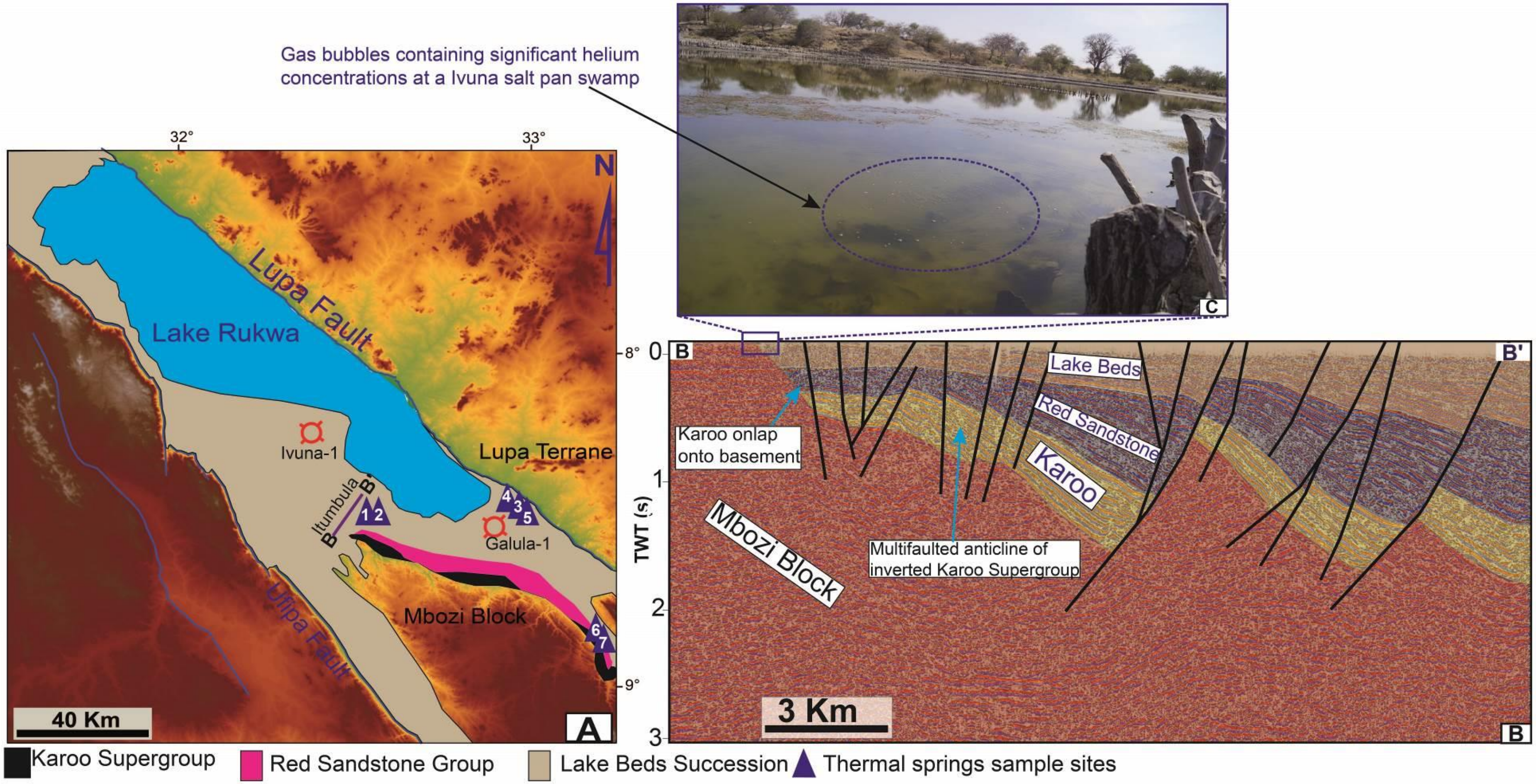

Fig. 2.8. (A) A map showing location of thermal springs in the basin, lithology distribution after Mtelela, (2016) and 2D seismic section trace in vicinity of Ivuna and Itumbula shown by the purple line B - B′. (B) A series of rotated faulted blocks associated with

strata juxtaposition of both Karoo and Red Sandstone. Note the inverted Karoo Supergroup at SW end. (C) A photo showing bubbles of nitrogen dominated helium-rich rich gas from Ivuna salt pan associated with thermal saline surface seeps. The photo was taken viewing north adjacent to basement outcrops. The location of the cross section is shown by the purple line B-B′ and sample sites for helium shown in triangular blue symbols numbered from 1-7 in Fig. 2.8A (see geochemical details for each site in Table 2.2).

Table 2.2. Sample sites showing nitrogen and radiogenic helium concentrations. The $^{3}He/^{4}He$ ratios from samples are normalised to the atmospheric $^{3}He/^{4}He$ ratio of 1.4 x 10^{-6} (designated as 1 Ra). These results were also extracted from Danabalan, (2017) (see Fig. 2.8A for sample sites locations).

Sample site	^{4}He concentration (cm^{3} STP) (x 10^{-2})	N_2 concentration (cm^{3} STP)	$^{3}He/^{4}He$ (Ra)	References
1. Ivuna	2.5	0.96	0.18	Barry et al. (2013)
2. Itumbula	4.2	0.96	-	James, (1967a)
3. Lupa	0.005	-	3.45	Barry et al. (2013)
4. Lupa	0.02	-	3.75	James, (1967a)
5. Lupa	0.001	-	1.21	James, (1967a)
6. Songwe	-	-	1.19	Barry et al. (2013)
7. Songwe	-	-	3.61	Barry et al. (2013)

2.4.3 Fold structures and styles

The RRB exhibits various fold styles, which are collocated with the normal faults and are widely distributed across Domain A and B. In Domain A, two sets of folds are identified associated with ca. 10% of the faults within the Lake Beds sequences (Fig. 2.5A); The first fold set consists of symmetrical fold structure mapped between high angle conjugate normal faults (Fig. 2.5B). The second set is characterized by asymmetrical folds of stratigraphy in the hanging wall of normal faults that are antithetic to the Lupa Fault (Fig. 2.5C).

In Domain B, the Red Sandstone and Lake Beds sequences are deformed by asymmetric folds in the immediate hanging wall of the Lupa Fault in the southeast part of the basin (Fig. 2.9A-B). These folds verge towards the hanging wall of the Lupa Fault with fold axis roughly striking WNW-ESE. The amplitudes of these folds progressively decrease upwards to zero from a maximum of 140 ms at a depth of 3000 ms TWT (Fig. 2.9B). The Lupa Fault shows a relatively steeply dipping upper segment and a gently dipping lower segment while the folded strata dip toward the fault (Fig. 2.9B). We interpret these structures as fault bend folds formed as a passive response to the hanging wall moving past the dip change inflection point on the

Lupa fault at depth.

Proximal to the northern end of the Mbozi Block, the folds exhibit amplitudes ca. 60 ms TWT and wavelength c. 3.5 km and are associated with the upward termination of normal faults, i.e. they exhibit upward transition from faulting to folding (Fig. 2.9C). Within these faults, the synrift strata show sagging in the hanging wall synformal structure, most likely due to differential compaction and loading, i.e. variation of thickening and thinning affecting both the Oligocene Nsungwe Formation and the lower Lake Beds sequences (Late Miocene-Pliocene Malangali Formation) (e.g. Mtelela et al., 2017; Hilbert-Wolf et al., 2017; Fig. 2.9C). The synkinematic wedges and onlaps indicate that these folds initiated in the Oligocene (c. 25-26 Ma) and deformation continued until the Pleistocene (c. 2.6 Ma?) (cf. Roberts et al., 2012; Hilbert-Wolf et al., 2017). We interpret these structures as fault propagation folds formed above the tip of propagating blind normal faults. The combination of progressive fault propagation, displacement, folding and sedimentation produce a rotation of the wedge-shaped sedimentary packages, which thicken towards the hanging wall of the intrabasin faults.

Furthermore, in the middle of the basin within Domain B, sedimentary units older than the Lake Beds sequences at depths below 1.0 s TWT are folded with alternating anticlines in the footwall and synclines in the hanging wall of a major SW-dipping fault (Fig. 2.9D). We infer that the SW-dipping fault created an upward widening zones of distributed monoclinal flexural deformation (trishear) which were later breached by the faults (Fig. 2.9D). In the Lake Beds sequences only the lower most units are rotated and constantly dip away from the master faults as a result of fault propagation (Fig. 2.9D). In contrast, the uppermost sequences of the Lake Beds exhibit locally uplifted strata relative to the adjacent block and show a compressional phase (Fig. 2.9D). We interpret these extensional structures as fault-propagation monoclines.

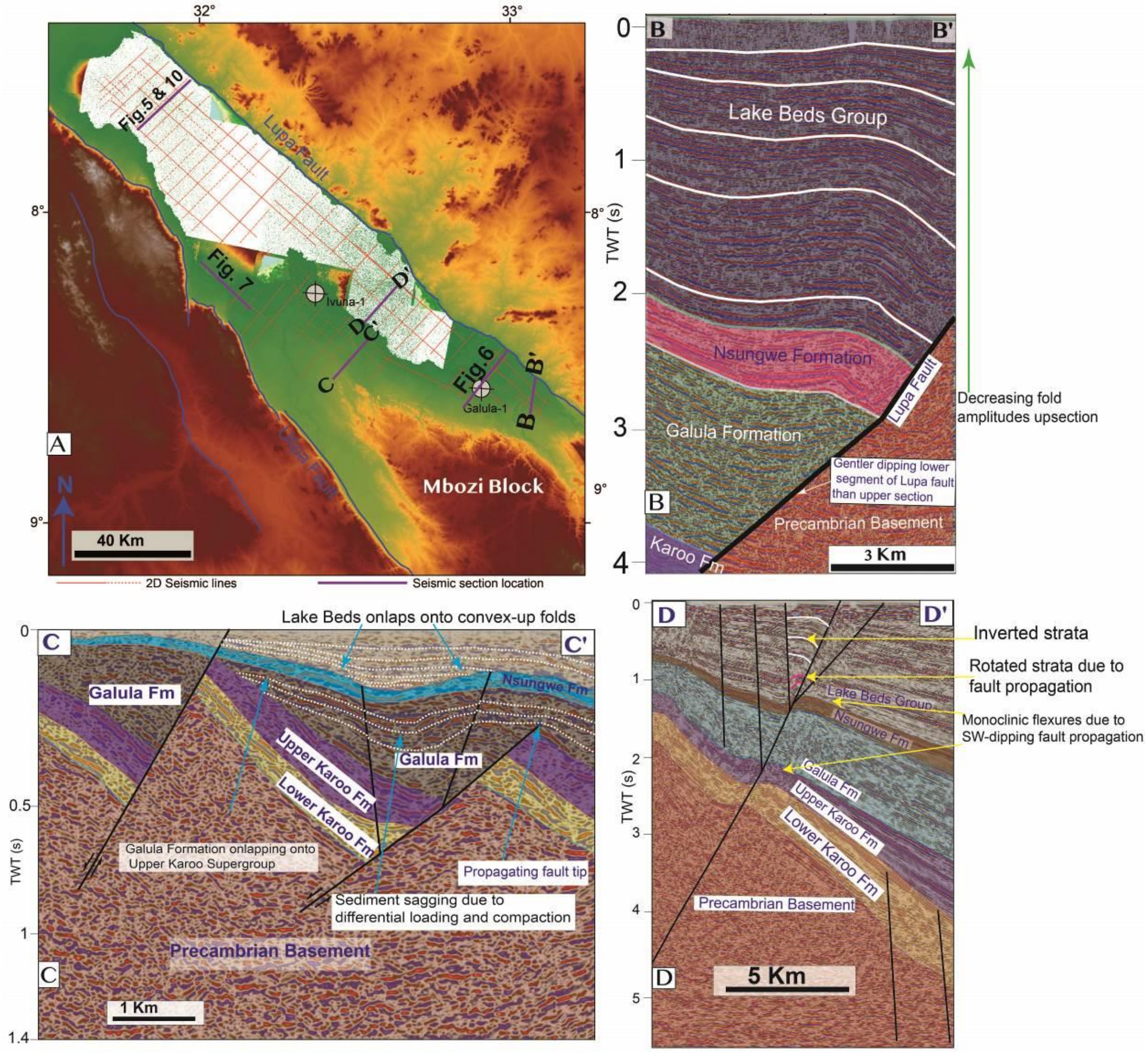

Fig. 2.9. (A) A map showing the surface location of the interpreted seismic sections indicated by purple thick lines. (B) Geoseismic section showing the fault bend folds as a passive response due to bending/rotation in the geometry of the Lupa Fault. (C) Interpreted seismic section showing faulted block rotation and fault propagation folds. Note the syn-kinematic record of onlaps in the Lake Beds sequences and propagating fault tip in the NE end, buried due to high sedimentation rate. (D) Breached fault propagation monocline with anticline in the footwall and syncline in the hanging wall. Note the rotated Lake Beds strata in the lower section due to space accommodation during fault propagation whereas the uppermost strata are inverted.

2.4.4 Inversion phases and styles

The diagnostic features and extent of inversion structures are mapped and described in the context of potential traps for a helium-rich gas phase. The description is based on genetic mechanisms and kinematic relationships between faults and fold systems (e.g. Withjack et al., 2002).

We mapped a Karoo-aged inversion phase characterized by open and low amplitude (up to c. 150 ms), anticlines involving several faults (cf. Fig. 2.8B). These structures are located in the southwest of the basin adjacent to the Ufipa Fault and the northern end of the Mbozi Block (cf. Fig. 2.8A). The anticlines involving Karoo sequences are inverted and the SW limb onlaps onto the Mbozi Block (Fig. 2.8B). These inversion structures are mapped within the Karoo strata and are overlain by Cretaceous Red Sandstone sequences (Fig. 2.8B). The seismic data suggest that the inversion phase occurred after the deposition of the last Karoo sediment and just before the first sediment deposition of the Red Sandstone Group during the Cretaceous. Based on this evidence, we infer that, these multifaulted anticlines represent an inversion phase that was active during the Middle Mesozoic, possibly in the Early Jurassic.

The younger inversion structures in the RRB are recorded only in the Lake Beds sequences and occur in two styles (Fig. 2.10A). Firstly, asymmetrical anticlines, which have a relatively steeper forelimb, that verge towards the hanging wall of adjacent NE - dipping faults (Fig. 2.10A). These structures occur in the antithetic faults to the Lupa Fault (Fig. 2.10A). The fold axes are sub-parallel to the Lupa Fault striking NW - SE. They extend remarkably parallel to the Lupa border fault with amplitudes that ranges between 100 - 150 ms within Domain A (Fig. 2.4; Fig. 2.10A).

The second inversion style is characterized by anticlines that form symmetric boxfold geometries with low-amplitudes 80 - 120 ms TWT (Fig. 2.10A). These anticlines appear as fault - parallel symmetrical folds of synrift units between steeply dipping conjugate normal faults (Fig. 2.10A-B). They form away from the main Lupa Fault and are traceable along strike in both Domains A and B (Fig. 2.4). The synkinematic strata mapped in the uppermost part of the Lake Beds sequences reveal that these structures formed due to mild, but widespread inversion during the latest Pleistocene age (Fig. 2.10B).

2.5.0 Discussion

2.5.1 Rift geometry and structural patterns

Our results suggest that the RRB exhibits a gently dipping sedimentary wedge and typical half graben geometries in Domain A and B respectively, consisting of tectonically controlled synrift sedimentary units with maximum sediment thickness recorded for each sequence adjacent to the Lupa Fault (cf. Fig. 2.5A; Fig. 2.6). The half-graben geometry in Domain B is thus partly similar to results of Rosendahl et al. (1986) and Ebinger, (1989). The overall geometry suggests that both Karoo and post-Karoo extensional strains were partitioned between Domain A and B (Figs. 2.3A & 2.4). In Domain A the extensional strains were accommodated by the Lupa Fault and the Chisi shear zone which most likely accommodated the formation of parallel synthetic normal faults to the Ufipa Fault (Figs. 2.3A & 2.4). In Domain B, the Lupa Fault dominated the strain localization while the possible position of the southern termination of the Chisi shear zone (cf. Heilman et al., 2019; Lemna et al., 2019; Figs. 2.3A & 2.4) appears to have accommodated strains along rotated faulted blocks on the western side of the RRB (see Fig. 2.9C). This spatial arrangement implies that the Chisi shear zone crosscuts the Saza shear zone almost perpendicularly and implies the latter is sub-parallel to the RRB extension direction (cf. Figs. 2.3A & 2.4). We infer that the Saza shear zone extends into the RRB and continues sub-parallel to KSAZ (Figs. 2.3A) and ESE-striking faults (see Figs. 2.3A & 2.4). The Saza shear zone possibly provided an earlier strain shadow (cf. Reilly et al., 2017; Phillips et al., 2020) which inhibited an even distribution of regional stresses between the two structural domains, hence partitioning the extension rate and strains i.e. simultaneously higher extension and strain rate in Domain B than A.

In addition, the difference in the two structural domains may be attributable to segmentation and growth of the Lupa Fault (e.g. Withjack et al., 2002). The spatial distinctness of stratigraphy for each major unit in the two depocenters may be due to existence of a large axial supply of sediment from the southeast where the nearest depocenter in Domain B became completely infilled before Domain A became progressively infilled (e.g. Withjack et al., 2002). Alternatively the differences may be attributable to climatic variation, lateral facies and provenance changes (cf. Mtelela et al., 2016).

Based on the present relative spatial position of the fault segments and their alignment along strike of the border faults i.e. inline versus en echelon segments (see Fig. 2.4), we infer that the Saza transfer fault segment most likely suggests a 'hard linkage' formed between two synthetic fault segments whose tips are offset. The Kwera transfer fault suggests a 'soft linkage' between overlapping discrete en-echelon normal fault segments (e.g. Nelson et al., 1992; Peacock and Parfitt, 2002; Delvaux et al., 2012; Zwaan et al., 2016; Heilman et al., 2019). A key observation is that no inversion structures are observed adjacent to the transfer faults or within the KSAZ (cf. Figs. 2.3A & 2.4). This suggests that this area formed a strain shadow, as commonly observed in transfer zones (e.g. Schlische, 1991; Lambiase and Bosworth 1995; McLeod et al., 2000). Similar features are identified in the Taranaki Basin, Farsund Basin, Gulf of Evvia and Gulf of Suez where the rift is divided into several depocenters separated by polarity changing transfer zones (e.g. Gawthorpe et al., 1990; Reilly et al., 2017; Phillips et al., 2020).

The overall deformation and structural patterns in the Rukwa Rift suggest oblique stresses dominated the extension in the Rukwa Rift in an ESE-WNW orientation (Fig. 2.3A). The mapped fault obliquity, orientations and patterns i.e. both the Karoo and post-Karoo faults, which largely penetrate the crystalline basement, would most likely occur when there was a pre-existing basement faults that were reactivated in an oblique divergent sense (cf. Peace et al., 2018; Figs. 2.3A & 2.4). However, the seismicity and geodetic observation reveal a complex kinematic interplay of the Nubia-Somalia-Rovuma-San plates near the Rukwa Rift (e.g. Saria et al., 2014; Stamps et al., 2018; Daly et al., 2020). These tectonic plates and associated rift interactions may equally account for the temporal and spatial variations of the local resultant stresses in the Rukwa Rift, thus influencing the deformation described in this study (e.g. Walsh et al., 2001; Reilly et al., 2017; Fig. 2.3A).

2.5.2 Fault rotated fold styles

The occurrences of rotated fault propagation folds in the RRB suggest strain accommodation at the fault tip within the overlying synrift sedimentary package (e.g. Mitra, 1990; Fig. 2.11A-B). In the hanging wall of the normal faults, these sedimentary packages show rotational kinematics, most likely amplified by high rate of extension and folding above the uplifted footwall (e.g. Ravnås and Bondevik, 1997; Fig. 2.11A-B). These fold styles are most likely controlled by the presence of rheologically weak strata possibly pressurized shales in a stratigraphy, which impede direct strain accommodation during upward fault propagation (cf. Mitra, 1993; Couples et al., 1998; Withjack and Schlische, 2006; Ford et al., 2007; Hardy, 2018). We infer that the burial of a fault propagation tip implies that the sedimentation rate outpaced the incremental accommodation space generation during the Cretaceous - Pleistocene (e.g. Withjack et al., 2002; Fig. 2.11B).

In contrast to fault propagation folds discussed above, the fault propagation monoclines most likely reflect relatively slower rate of fault propagation with respect to the rate of fault displacement in asymmetrical trishear zones (cf. Jin and Groshong, 2006). Consequently, the fault propagation partitions the deformation into multilayer buckling, kink-band migration and limb rotations to form a wide monoclinal fold (cf. Mitra, 1990; Withajack et al., 1990; Hardy and McClay, 1999; Ferrill et al., 2004; Fig. 2.9D).

We hypothesize that for generation of fault bend folds in the RRB, fault initiation could have occurred at different depths and finally linking up i.e. deep - rooted basement faults system which are gently dipping, linked up with the steeper faults in the overlying synrift strata both propagating upward at different rates (e.g. Fig. 2.11C-D). The Earthquake data from the Rukwa Rift indicate that the ruptures occur at varied depths between 25 and 35 km (Delvaux and Barth, 2010; Craig et al., 2011; Lavayssiere et al., 2019) thus, faults initiating at various depths could have merged, most likely the Ubendian shear zone in the underlying basement accelerating a more rotational fault geometry which we observe in Domain B (e.g. Osagiede et al., 2020; Fig. 2.11C-D). The fault bend geometries may trigger a reverse frictional drag as a passive response of synrift strata, which amplify folding in the hanging wall of the Lupa Fault (cf. Mitra, 1993; Withjack et al., 2002; Fig. 2.9B; Fig. 2.11D).

2.5.3 Inversion styles, mechanisms and timing

The earliest inversion structures mapped in the RRB exhibit multifaulted anticlines (Fig. 2.8B). We determine that this inversion affected only the Karoo Supergroup and the seismic data reveal that it occurred during Middle Mesozoic, possibly Early Jurassic times (cf. Fig. 2.8B). This phase was therefore before the deposition of the earliest Cretaceous Red Sandstone Group and just after the deposition of the Karoo Supergroup. We infer that, inversion was most likely attributable to compressional pulse associated with uplift during initiation of Gondwana rifting (e.g. Wopfner, 1993). This evidence precludes the argument that the transpressional inversion occurred during early Mesozoic as suggested by Delvaux et al. (2012).

The youngest inversion in the RRB was mild due to the absence of noticeable complete reversal of neither original normal faults displacement nor significant decrease in normal fault offsets. The synkinematic records observed suggest short-lived inversion phase during the Pleistocene affected the Lake Beds sequences in the uppermost stratigraphy (Fig. 2.10B). We infer that the variation of asymmetric and symmetric folds styles within both Domains A and B can be explained by the temporal and spatial variation of mechanical properties of the stratigraphy and strain accommodation across the RRB (e.g. Withjack et al., 2002).

Our observations show that inversion anticlines are not uniformly distributed across the basin, with a significant absence of these structures in some areas and along other similar faults (cf. Fig. 2.4). Based on this observation, we suggest that, there may be strain shadows between faults and that the geometry of some faults acted as a buttress to far field regional and other resultant local forces where inversion only occurred on the larger and least geometrically complex segments of faults. (e.g. Walsh et al., 2001; Reilly et al., 2017; Phillips et al., 2020). Alternatively, the absence of inversion in some places may partly be attributable to steep dips, short wavelength folds and high density faulting not visible in 2D seismic reflection data (e.g. Morley et al., 1999a).

Within the EARS, such as the Lotikipi basin and the Anza Graben in Kenya, mild inversion occurred during the late Miocene-Pleistocene and has been linked to ridge push and spreading in the Red Sea and Gulf of Aden (Bott, 1991; Bosworth, 1992; Morley, 1999; Wescott et al., 1999). The spreading in the Red Sea and Gulf of Aden seems too remote to have been influenced the local strains in the Rukwa Rift and the whole Western branch of the EARS, rather we infer that this could possibly be explained by kinematic interactions of the Nubia-Victoria-Rovuma-San plates and associated tectonic boundaries occupied by rifts particularly the South Tanganyika, the North Malawi and the Southwestern (Luangwa) rifts (e.g. Saria et al., 2014; Lavayssière et al., 2019; Daly et al., 2020; Wedmore et al., 2021). These tectonic plates and associated rifts interaction could have induced a new stress regime and/or rotation leading to the inversion structures described in this study (e.g. Fig. 2.4). An alternative near-field mechanism is that inversion resulted from variation of resultant local strains on intrabasinal faults and complex inherited fabrics due to the multiphase tectonic history (e.g. Turner and Williams, 2004). A final possibility is the presence of East African mantle plumes and localized magmatic pulses in the Rungwe Volcanic Province (Nyblade and Robinson, 1994), which are often associated with thermo-kinematic anomalies and might have induced local strain fields and rotation in the Rukwa Rift (cf. Negredo et al., 1995; Ziegler et al., 1995; Hansen and Nielsen, 2003). Further work is required to understand the mechanical and rheological complexities involved in these mechanisms, at the moment it is difficult to discern an exclusive single factor which caused inversion and explains its distribution particularly in the RRB.

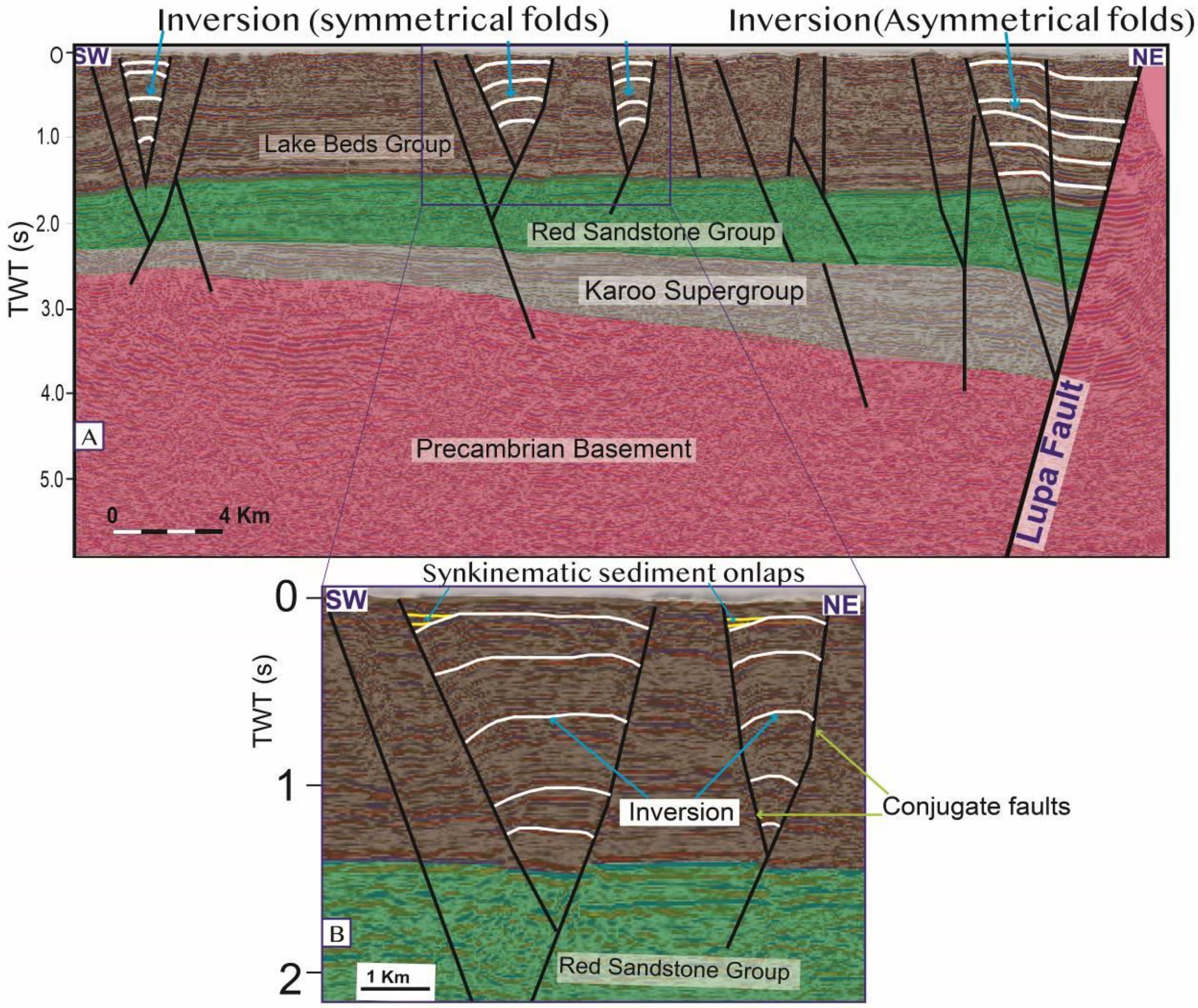

Fig. 2.10. (A) Interpreted geoseismic section illustrating inversion styles i.e symmetrical and asymmetrical anticline inversion within steeply dipping faults. (B) Close up of interpreted seismic section showing symmetrical folds inversions styles between the high angle faults. Note the synkinematic sediment onlaps revealing the timing of inversion (Pleistocene age). (See Fig. 2.9A for map location).

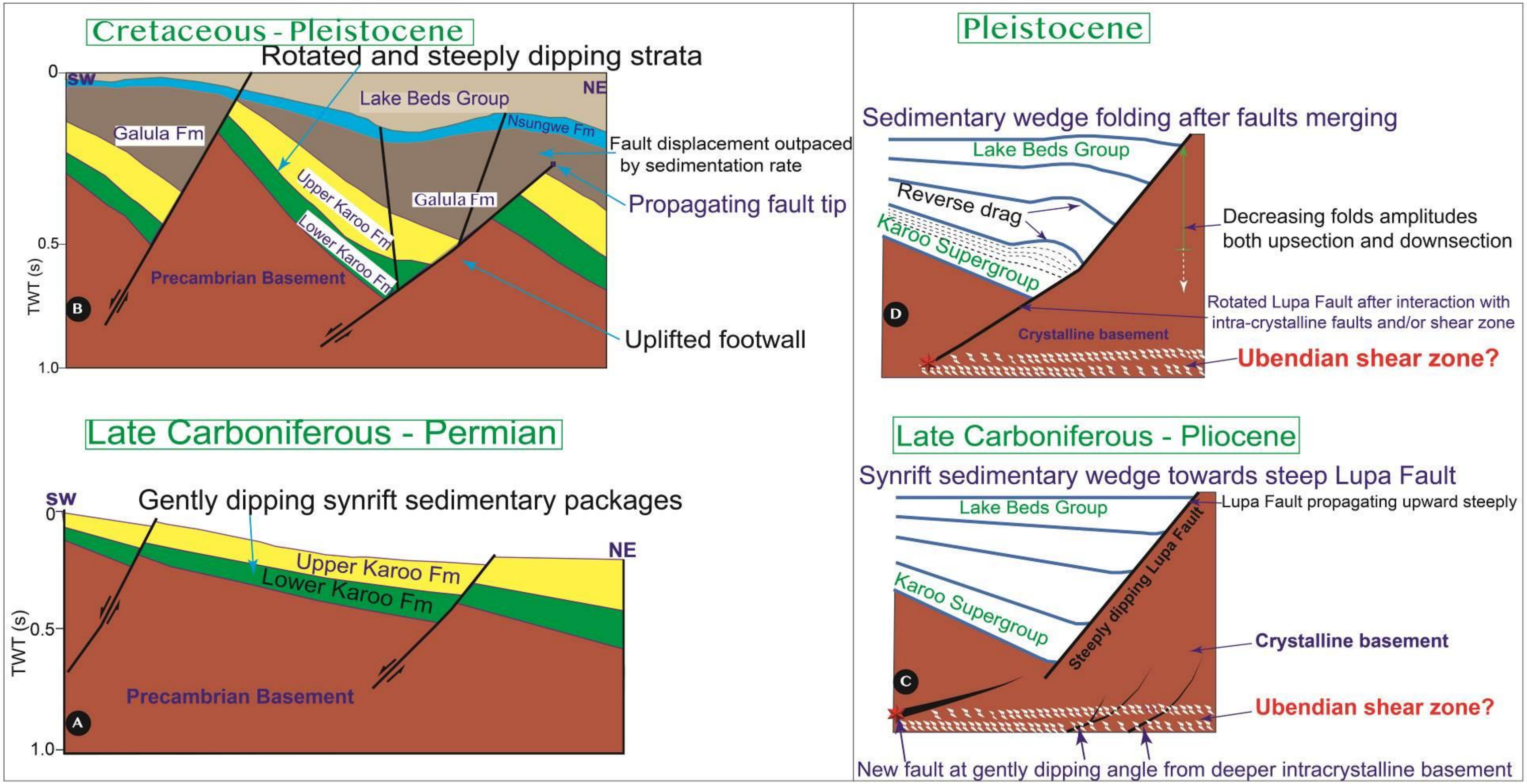

Fig. 2.11 (A) Geological section showing gently dipping synrift sedimentary packages created during Late Carboniferous to Permian times. (B) Fault propagation folding and strata rotation amplified by folding and high extension rate during Cretaceous-Pleistocene. (C) Deeper gently-dipping fault and shallower steeply-dipping Lupa fault both propagating upward at different rates.

(D) Merging of newly forming faults from crystalline basement which propagates upward interacting with a shallower propagating Lupa Fault resulting into fault bend and reverse drag of strata to form folds in the hanging wall.

2.5.4 Helium potential in the Rukwa Rift Basin

The Precambrian Basement beneath the RRB and the surrounding terranes are composed of mainly granitoids, gneisses and granulites which are rich in helium producing minerals, i.e uranium and thorium, and provide potential source rocks for radiogenic ^{4}He (Danabalan, 2017; Fig. 2.12A-D). An enhanced expulsion of ^{4}He and associated gases, such as nitrogen, is most likely triggered regionally by the onset of East African mantle plume activity and related rifting (e.g. Nyblade and Robinson, 1994; Ebinger and Sleep, 1998; Danabalan et al., 2021). The structural data presented here suggest that basement rooted faults trending NNW-SSE, NNE-SSW, NW-SE are linked to interconnected basement structures including Ubendian shear zones (e.g. Fig. 2.11D). The faults, fractures, shear zones, lithological contacts, porous and permeable strata are likely to provide the main conduits for migration of helium-nitrogen rich seeps in the RRB (cf. Fig. 2.3A; Fig. 2.8B; Fig. 2.11D; Fig. 2.12A-F). Notably the helium prospects in the RRB are preferentially located adjacent to both the Mbozi and the Lupa Terranes and exhibit a dense and deep - rooted structural heterogeneity, reactivated by polyphase tectonics (cf. Fig. 2.8B; Fig. 2.11A-B). Many other thermal springs sites are devoid of significant radiogenic helium concentration (e.g. Barry et al., 2013), possibly due to lack of fluid connectivity spatially, i.e. hydrothermal circulation of fluid carrying radiogenic helium and variability of crustal-scale open-system behaviour (e.g. Lowenstern et al., 2014).

Similar to hydrocarbon systems, the potential traps for helium in the RRB are either stratigraphic, structural or a combination of both (e.g. Gluyas and Swarbrick 2021). Potential stratigraphic traps in the RRB may include juxtaposition of the Karoo sequences leading to wedge truncation against the uplifted Precambrian Basement sealed by unconformity (cf. Fig. 2.7A-B; Fig. 2.8B). Within Domain B, the Upper Karoo Formation, Galula Formation and the Nsungwe Formation have been documented to comprise mainly sandstones with porosity between 16% and 28% (Roberts et al., 2010; Mtelela, 2016) hence they present potential reservoirs for helium accumulations (Fig. 2.12E). These strata exhibit extension related anticlines bound by unconformities (e.g. Fig. 2.2), which may provide an effective trap and seal (Fig. 2.12E).

The Lake Beds strata comprise siliciclastic sandstones with c.16% porosity (Mtelela et al., 2016), and thus may present fairly good reservoirs while the inversion anticlines identified in this interval may provide effective traps (Fig. 2.12E). Notably, shales and carbonates that have been documented in the Lake Beds strata (Mtelela, 2016) imply the presence of effective seals for helium. Analogue basins containing similar inversion anticlines, stratigraphy, and with proven recent hydrocarbon discoveries in the East African Rift System are the Albertine Graben in Uganda and the Turkana Basin (Kenya) (Morley et al., 1999a; Tiercelin et al., 2012; Abeinomugisha and Kasande, 2012). However, given the small atomic radius of helium (e.g. Danabalan et al., 2021) and multiphase deformation, these helium traps may be at a greater risk of leakage and equally give rise to the surficial thermal springs rich in helium which are observed in the RRB (Fig. 2.8B-C; Fig. 2.12A).

The source of high nitrogen associated with helium-rich fluids in the RRB is still unclear. In this study we infer that previously documented organic rich shale and liptinite rich coals in the K2 unit in the Karoo Supergroup (Wescott et al., 1991; Kilembe and Rosendahl, 1992) might have undergone thermogenic reaction enhanced by rifting and volcanic activity (e.g. Snyder et al., 2003; Williams et al., 1992). These events possibly resulted in nitrogen accumulations during the Cretaceous and Oligocene carbonatite volcanism and the recent Cenozoic Rungwe volcanism. During the catagenesis stage (80°-120°C), the thermogenic changes in the basin cause high NH_4^+ in pore fluids and substitution in potassic minerals i.e illites (Hunt, 1979; Paxton, 1984; Williams et al., 1992; Lawrence et al., 2021). This catagenesis stage coincides with the closure temperature of some helium retentive minerals e.g. apatite and hematite (Danabalan et al., 2021), which can possibly mix with nitrogen rich-carrier fluid and migrate with pristine ^4He from the crystalline basement into the Rukwa synrift strata (e.g. Fig. 2.12A-F). Depending on the reaction kinematics and bulk mineralogy, the NH_4^+ rich fluids may undergo anaerobic ammonia oxidation (anammox) enroute to surface to produce nitrogen gas (e.g. Williams et al., 1992; Strous et al., 1999). However, these inferences need to be tested by isotopic studies. Further from the highlands of the Rungwe volcanic centers, the admixture of hydrothermal fluids, meteoric water and mantle derived ^3He, provide the main advection recharge in the region and may dissolve other components i.e ^4He, carbonates enroute to relatively lowland Rukwa Rift Basin hence leading to binary mixture signatures for ^4He and ^3He across the region (Fig. 2.12A-F).

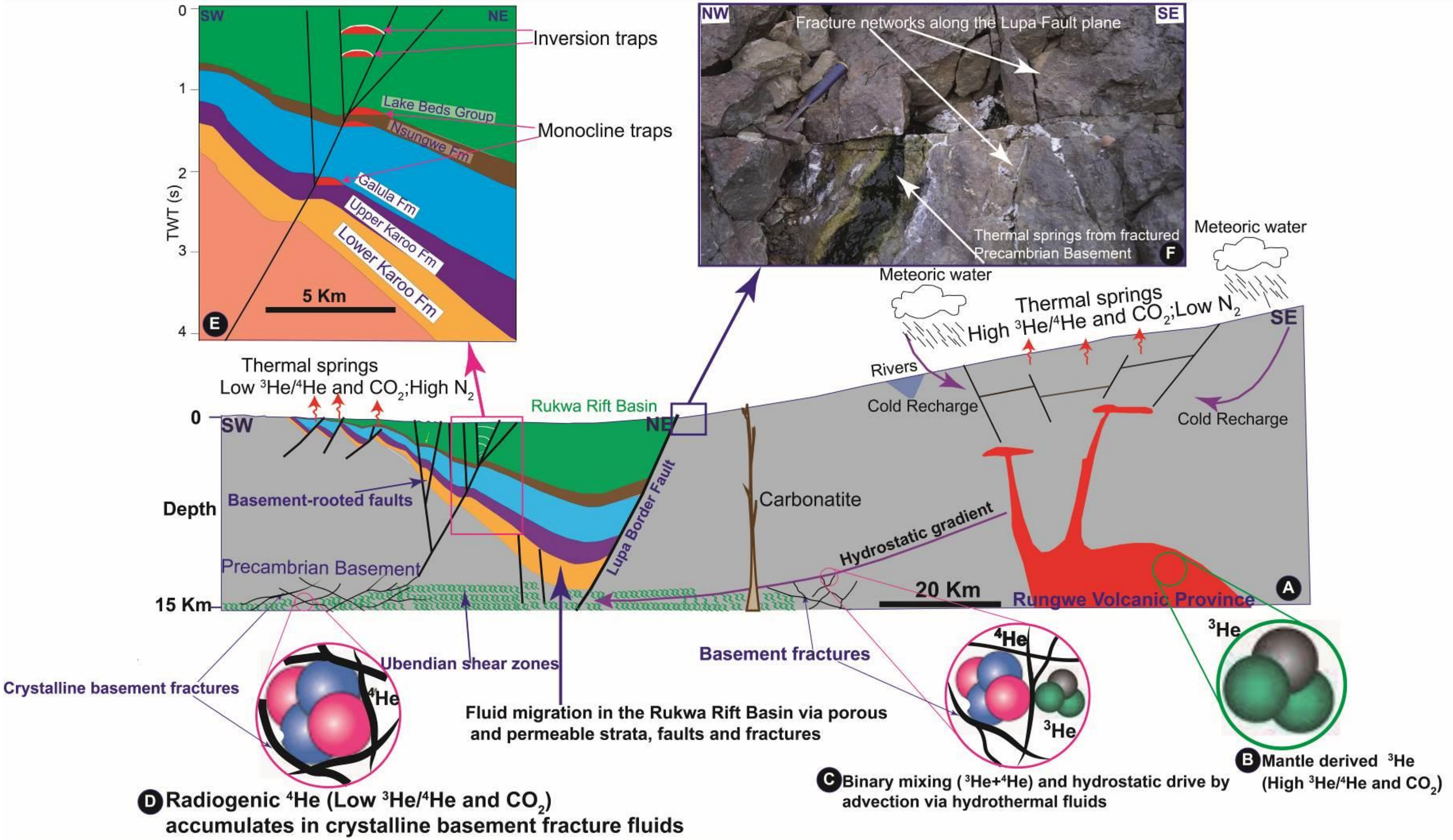

Fig. 2.12. (A) Cross section showing the generalized thermal fluid system associated with helium in the Rukwa Rift Basin. (B) Mantle derived ^{3}He associated with high CO_2 outgassing from the Rungwe Volcanic Province (Barry et al., 2013; Danabalan, 2017).

(C) Secondary migration involving binary mixing between a pure crustal end member and a mantle end member i.e. high ^4He concentrations, associated high N_2 concentrations and low $^3He/^4He$ ratios (predominantly crustal input) whereas closer to the Rungwe Volcanic Province high CO_2, low N_2, low ^4He and high $^3He/^4He$ ratios (mantle input) observed by Barry et al. (2013) and Danabalan, (2017). (D) Primary migration of ^4He involving diffusion from helium producing minerals at elevated temperature above the closure temperature and interconnected fractures due to overpressure (Warr et al., 2018; Danabalan et al., 2021). (E) Potential traps for helium involving inverted Lake Beds strata and relatively older monocline traps sealed by unconformities. (F) A photo taken facing NE at the Lupa Fault showing that the thermal spring systems clearly follow the lithology contacts, faults and fracture network systems.

2.6.0 Conclusions

From this study we conclude;

- The overall deformation in the Rukwa Rift largely localizes on NW-striking border faults, intrabasinal faults (with NNE, NW and NNW-trends), shear zones and transfer zones. These structures accommodate ESE-WNW directed oblique divergence and they exert control on accommodation space and occurrences of thermal springs rich in helium-nitrogen that are manifest at the surface regionally.
- The RRB exhibits a gently dipping wedge to a typical half-graben geometry containing synextensional sedimentary packages up to a maximum thickness of 6000 ms TWT. Within these sedimentary packages a series of anticline structures, mapped stratal juxtaposition and stratigraphic-unconformity are widely distributed in the basin, and provide potential subsurface traps for helium-rich fluids.
- The RRB exhibits both extensional and compressional fold styles i.e. fault bend folds, fault propagation folds and fault propagation monocline which are collocated with the normal faults and are widely distributed within Domain A and B.
- The RRB exhibit two phases of inversion which resulted in different fold styles in the RRB; the first produced multifaulted anticlinal Karoo inversion during the Early Jurassic and the second was a mild and widespread inversion during the Pleistocene which gave rise to both symmetrical and asymmetrical open anticlines.
- The crystalline basement provides the source rocks for the radiogenic helium while nitrogen is derived from thermogenic reaction of organic rich shale and liptinite rich coals, enhanced by rifting and associated volcanic activity.

Acknowledgements

This work was funded by United Kingdom Commonwealth Scholarship Commission, the results of which is part of the first author's PhD study at Durham University. Tanzania Petroleum Development Corporation (TPDC) is thanked for providing the dataset. Authors are extending their gratitude to anonymous reviewers for critical reviews that significantly enhanced the output of this study.

References

Abeinomugisha, D. and Kasande, R., 2012. Tectonic control on hydrocarbon accumulation in the intracontinental Albertine Graben of the East African rift system. AAPG International Conference and Exhibition, Cape Town, South Africa, October 26-29, 2008.

Allmendinger, R. W., Cardozo, N. C., and Fisher, D., 2013. Structural Geology Algorithms: Vectors & Tensors: Cambridge, England, Cambridge University Press, 289 pp.

Avseth, P., Mukerji, T. and Mavko, G., 2010. Quantitative seismic interpretation: Applying rock physics tools to reduce interpretation risk. Cambridge university press.

Barry, P. H., Hilton, D. R., Fischer, T. P., De Moor, J. M., Mangasini, F., & Ramirez, C., 2013. Helium and carbon isotope systematics of cold "mazuku" CO2 vents and hydrothermal gases and fluids from Rungwe Volcanic Province, southern Tanzania Chemical Geology, 339, 141-156. https://doi.org/10.1016/j.chemgeo.2012.07.003.

Boniface, N., Schenk, V., and Appel, P., 2012. Paleoproterozoic eclogites of MORB-type chemistry and three Proterozoic orogenic cycles in the Ubendian Belt (Tanzania): Evidence from monazite and zircon geochronology, and geochemistry. Precambrian Research, 192,16–33 https://doi.org/10.1016/j.precamres.2011.10.007.

Bosworth, W., 1992. Mesozoic and early Tertiary rift tectonics in East Africa. *Tectonophysics*, *209*(1-4), pp.115-137.

Bott, M.H.P., 1991. Ridge push and associated plate interior stress in normal and hot spot regions. *Tectonophysics*, *200*(1-3), pp.17-32.

Chorowicz, J. and Mukonki, M.B., 1980. Lineaments anciens, zones transformantes recentes et geotectoniques des fosses dans l'est African, d'après la teledetection et la microtectonique: Museum Royal Africa Central, Tervuren, Belgium. Department of Geology and Mineralogy Annual Report, pp. 143–146.

Chorowicz, Jean, 2005. "The East African rift system". Journal of African Earth Sciences. **43** (1): 379–410. https://doi.org/10.1016/j.jafrearsci.2005.07.019.

Couples, G.D., Lewis, H. and Tanner, P.G., 1998. Strain partitioning during flexural-slip folding. Geological Society, London, Special Publications, 127(1), pp.149-165. https://doi.org/10.1144/GSL.SP.1998.127.01.12

Craig, T.J., Jackson, J.A., Priestley, K. and McKenzie, D., 2011. Earthquake distribution patterns in Africa: their relationship to variations in lithospheric and geological structure, and their rheological implications. *Geophysical Journal International*, *185*(1), pp.403-434.

Daly, M.C., Green, P., Watts, A.B., Davies, O., Chibesakunda, F. and Walker, R., 2020. Tectonics and landscape of the Central African Plateau and their implications for a propagating Southwestern Rift in Africa. *Geochemistry, Geophysics, Geosystems*, *21*(6), p.e2019GC008746.

Daly, M. C, 1988. Crustal shear zones in central Africa—A kinematic approach to Proterozoic tectonics. Episodes, 11(1), 5–11. https://doi.org/10.18814/epiiugs/1988/v11i1/003.

Daly, M.C., Chorowicz, J., Fairhead, J.D., 1989. Rift basin evolution in Africa: the influence of reactivated steep basement shear zones. Geological Society, London, Special Publications 44, 309. https://doi.org/10.1144/GSL.SP.1989.044.01.17.

Danabalan, D., 2017. Helium: Exploration Methodology for a Strategic Resource. PhD Thesis, Durham University.

Danabalan, D., Gluyas, J., Macpherson, C.G, Abraham-James, T.H, Bluett, J.J, Barry, P.H, and Ballentine, C.J, 2021. Principles of Helium Exploration. *Petroleum Geoscience* (In press).

Delvaux, D., Levi, K., Kajara, R., & Sarota, J., 1992. Cenozoic paleostress and kinematic evolution of the Rukwa–North Malawi rift valley (East African Rift System). Bulletin des Centres de Recherche Exploration-Production ElfAquitaine, 16, 383–406.

Delvaux, D., 2001. Karoo rifting in western Tanzania: precursor of Gondwana break-up. *Contributions to geology and paleontology of Gondwana in honor of Helmut Wopfner: Cologne, Geological Institute, University of Cologne*, pp.111-125.

Delvaux, D. and Barth, A., 2010. African stress pattern from formal inversion of focal mechanism data. *Tectonophysics*, *482*(1-4), pp.105-128.

Delvaux, D., Kervyn, F., Macheyeki, A. S., & Temu, E. B., 2012. Geodynamic significance of the TRM segment in the East African Rift (W-Tanzania): Active tectonics and paleostress in the Ufipa plateau and Rukwa basin. Journal of Structural Geology, 37, 161–180. https://doi.org/10.1016/j.jsg.2012.01.008.

Delvaux, D., Kraml, M., Sierralta, M., Wittenberg, A., Mayalla, J.W., Kabaka, K., Makene, C. and GEOTHERM Working Group, 2010. Surface Exploration of a Viable Geothermal Resource in Mbeya Area, Sw Tanzania. Part I: Geology of the Ngozi-Songwe Geothermal System.

Ebinger, C.J., 1989. Tectonic development of the western branch of East African rift system. Geol. Soc. Am. Bull. 101, 885-903. https://doi.org/10.1130/0016-7606(1989)101%3C0885:TDOTWB%3E2.3.CO2.

Ebinger, C.J., Deino, A.L., Drake, R.E. and Tesha, A.L., 1989. Chronology of volcanism and rift basin propagation: Rungwe volcanic province, East Africa. *Journal of Geophysical Research: Solid Earth*, *94*(B11), pp.15785-15803. https://doi.org/10.1029/JB094iB11p15785.

Ebinger, C., and N. H. Sleep.,1998. Cenozoic magmatism in central and east Africa resulting from impact of one large plume, Nature, 395, 788-791.

Ebinger, Cynthia, 2005. "Continental break-up: The East African perspective". Astronomy and Geophysics. 46 (2): 2.16–2.21. https://doi.org/10.1111/j.1468-4004.2005.46216.x.

Fernandes, R.M.S., Ambrosius, B.A.C., Noomen, R., Bastos, L., Combrinck, L., Miranda, J.M. and Spakman, W., 2004. Angular velocities of Nubia and Somalia from continuous GPS data: implications on present-day relative kinematics. *Earth and Planetary Science Letters*, *222*(1), pp.197-208.

Ferrill, D.A., Morris, A.P., Sims, D.W., Waiting, D.J., Hasegawa, S., 2004. Development of synthetic layer dip adjacent to normal faults. In: Sorkhabi, R., Tsuji, Y. (Eds.), Faults, Fluid Flow, and Petroleum Traps American Association of Petroleum Geologists Memoir. American Association of Petroleum Geologists, Tulsa, OK, USA, pp. 125–138. DOI:10.1306/1033720M853133.

Ford, M., De Veslud, C.L.C. and Bourgeois, O., 2007. Kinematic and geometric analysis of fault-related folds in a rift setting: The Dannemarie basin, Upper Rhine Graben, France. Journal of Structural Geology, 29(11), pp.1811-1830. https://doi.org/10.1016/j.jsg.2007.08.001.

Fritz, H., Abdelsalam, M., Ali, K. A., Bingen, B., Collins, A. S., Fowler, A. R., et al. (2013). Orogen styles in the East African Orogen: Areview of the Neoproterozoic to Cambrian tectonic evolution. Journal of African Earth Sciences, 86, 65–106. https://doi.org/10.1016/j.jafrearsci.2013.06.004.

Gawthorpe, R.L., Hurst, J.M. and Sladen, C.P., 1990. Evolution of Miocene footwall-derived coarse-grained deltas, Gulf of Suez, Egypt: implications for exploration. *AAPG bulletin*, *74*(7), pp.1077-1086.

Gawthorpe, R.L. and Hurst, J.M., 1993. Transfer zones in extensional basins: their structural style and influence on drainage development and stratigraphy. *Journal of the Geological Society*, *150*(6), pp.1137-1152. https://doi.org/10.1144/gsjgs.150.6.1137.

Gluyas, J.G. and Swarbrick, R.E., 2021. *Petroleum geoscience*. John Wiley & Sons.

Jin, G. and Groshong Jr, R.H., 2006. Trishear kinematic modeling of extensional fault-propagation folding. *Journal of Structural Geology*, *28*(1), pp.170-183. https://doi.org/10.1016/j.jsg.2005.09.003.

Hansen, D.L. and Nielsen, S.B., 2003. Why rifts invert in compression. *Tectonophysics*, *373*(1-4), pp.5-24. https://doi.org/10.1016/S0040-1951(03)00280-4.

Hardy, S., 2018. Coupling a frictional- rifts invert in compression cohesive cover and a viscous substrate in a discrete element model: First results of application to thick-and thin-skinned extensional tectonics. *Marine and Petroleum Geology*, *97*, pp.32-44. https://doi.org/10.1016/j.marpetgeo.2018.06.026.

Hardy, S., McClay, K., 1999. Kinematic modeling of extensional fault propagation folding. Journal of Structural Geology 21, 695–702. https://doi.org/10.1016/S0191-8141(99)00072-3

Heilman, E., Kolawole, F., Atekwana, E. A., & Mayle, M., 2019. Controls of basement fabric on the linkage of rift segments. *Tectonics,* 38, 1337–1366. https://doi.org/10.1029/2018TC005362.

Hayward, A. B., and Graham, R. H., 1989. Some geometrical characteristics of inversion. *Geological Society, London, Special Publications*, *44*(1), 17-39. https://doi.org/10.1144/GSL.SP.1989.044.01.03.

Hilbert-Wolf, H., Roberts, E., Downie, B., Mtelela, C., Stevens, N.J. and O'Connor, P., 2017. Application of U–Pb detrital zircon geochronology to drill cuttings for age control in hydrocarbon exploration wells: A case study from the Rukwa Rift Basin, Tanzania. *AAPG Bulletin*, *101*(2), pp.143-159.

Holland, G., Lollar, B. S., Li, L., Lacrampe-Couloume, G., Slater, G. F., & Ballentine, C. J., 2013. Deep fracture fluids isolated in the crust since the Precambrian era. *Nature*, *497* (7449), 357.

Hunt, J. M., 1979. Petroleum Geochemistry and Geology. W. H. Freeman.

James, T. C.,1967a. Thermal springs in Tanzania. *Institution of Mining and Metallurgy*, Transactions/Section B (Applied Earth Science) 76, B1–B18 *in* Macheyeki, A. S., Delvaux, D., De Batist, M., & Mruma, A. (2008). Fault kinematics and tectonic stress in the seismically active Manyara–Dodoma Rift segment in Central Tanzania–Implications for the East African Rift. *Journal of African Earth Sciences*, *51*(4), 163-188.

James, T. C., 1967b. Thermal springs in Tanzania – discussions and conclusions. *Institution of Mining and Metallurgy*, Transactions/Section B (Applied Earth Science) 76, B168–B174 *in* Macheyeki, A. S., Delvaux, D., De Batist, M., & Mruma, A. (2008). Fault kinematics and tectonic stress in the seismically active Manyara–Dodoma Rift segment in Central Tanzania–Implications for the East African Rift. *Journal of African Earth Sciences*, *51*(4), 163-188.

Katumwehe, A. B., Abdelsalam, M. G., & Atekwana, E. A., 2015. The role of pre-existing Precambrian structures in rift evolution: The Albertine and Rhino grabens, Uganda. Tectonophysics, 646, 117–129. https://doi.org/10.1016/j.tecto.2015.01.022.

Kervyn, F., Ayub, S., Kajara, R., Kanza, E., & Temu, B., 2006. Evidence of recent faulting in the Rukwa rift (West Tanzania) based on radar interferometric DEMs. *Journal of African Earth Sciences*, *44*(2), 151-168. https://doi.org/10.1016/j.jafrearsci.2005.10.008.

Kilembe, E. A., & Rosendahl, B. R., 1992. Structure and stratigraphy of the Rukwa rift. *Tectonophysics*, *209*(1-4), 143-158.

Kolawole, F., Phillips, T.B., Atekwana, E.A. and Jackson, C.A.L., 2021. Structural inheritance controls strain distribution during early continental rifting, Rukwa Rift. *Frontiers in Earth Science*, p.670. https://doi.org/10.3389/feart.2021.707869

Lambiase, J.J. and Bosworth, W., 1995. Structural controls on sedimentation in continental rifts. *Geological Society, London, Special Publications*, *80*(1), pp.117-144. https://doi.org/10.1144/GSL.SP.1995.080.01.06.

Lawrence, L., Spandler, C., Roberts, E.M. and Hilbert-Wolf, H.L., 2021. Mineralogy and origin of the alkaline Nsungwe Formation tuffs of the Rukwa Rift Basin, southwestern Tanzania. *Lithos*, *380*, p.105885.

Lavayssière, A., Drooff, C., Ebinger, C., Gallacher, R., Illsley-Kemp, F., Oliva, S.J. and Keir, D., 2019. Depth extent and kinematics of faulting in the southern Tanganyika rift, Africa. *Tectonics*, *38*(3), pp.842-862.

Lemna, O. S., Stephenson, R., & Cornwell, D. G., 2019. The role of pre-existing Precambrian structures in the development of Rukwa RiftBasin, southwest Tanzania. Journal of African Earth Sciences, 150, 607–625.

Lenoir, J.L., Liégeois, J.P., Theunissen, K. and Klerkx, J., 1994. The Palaeoproterozoic Ubendian shear belt in Tanzania: geochronology and structure. *Journal of African Earth Sciences*, *19*(3), pp.169-184.

Lowenstern, J.B., Evans, W.C., Bergfeld, D. and Hunt, A.G., 2014. Prodigious degassing of a billion years of accumulated radiogenic helium at Yellowstone. *Nature*, *506*(7488), pp.355-358.

Mbede, E.I., 1993. Tectonic development of the Rukwa Rift basin in SW Tanzania (Vol. 152). Fachber. Geowiss., TU Berlin.

Mitra, S., 1990. Fault-propagation folds: geometry, kinematic evolution, and hydrocarbon traps. *AAPG bulletin*, *74*(6), pp.921-945.

Mitra, S., 1993. Geometry and kinematic evolution of inversion structures. *AAPG Bulletin*, *77*(7), pp.1159-1191. https://doi.org/10.1306/BDFF8E2A-1718-11D7-8645000102C1865D.

McLeod, A.E., Dawers, N.H. and Underhill, J.R., 2000. The propagation and linkage of normal faults: insights from the Strathspey–Brent–Statfjord fault array, northern North Sea. *Basin Research*, *12*(3-4), pp.263-284. https://doi.org/10.1111/j.1365-2117.2000.00124.x.

Mnali, S.R., 1999. Palaeoproterozoic felsic magmatism and associated gold-quartz vein mineralization in the western part of the Lupa goldfield, south-western Tanzania. Unpublished PhD thesis, University of Dar es Salaam, Tanzania, 198 p.

Morley, C. K., R. M. Harper and S. T. Wigger., 1999a. Tectonic Inversion in East Africa, in C. K. Morley ed., Geoscience of Rift Systems – Evolution of East African Rift System: AAPG studies in Geology No. 44, p. 193-210.

Morley, C.K., R.A. Day, R. Lauck, R. Bosher, D.M. Stone, S.T. Wigger, W.A. Wescott, D. Haun, N. Bassett, and W. Bosworth., 1999b. Geology and Geophysics of the Anza Graben, in C.K. Morley ed., Geoscience of Rift Systems—Evolution of East Africa: *AAPG Studies in Geology* No. 44, p. 67–90.

Morley, C.K., Cunningham, S.M., Harper, R.M. and Wescott, W.A., 1992. Geology and geophysics of the Rukwa rift, East Africa. *Tectonics*, *11*(1), pp.69-81.

Morley, C.K., 1989, Extension, detachments, and sedimentation in continental rifts (with particular reference to East Africa): Tectonics, v. 8, p. 1175–1192.

Morley, C.K. ed., 1999. *Geoscience of rift systems: evolution of East Africa* (No. 44). Amer Assn of Petroleum Geologists.

Mtelela, C., Roberts, E.M., Hilbert-Wolf, H.L., Downie, R., Hendrix, M.S., O'Connor, P.M. and Stevens, N.J., 2017. Sedimentology and paleoenvironments of a new fossiliferous late Miocene-Pliocene sedimentary succession in the Rukwa Rift Basin, Tanzania. *Journal of African Earth Sciences*, *129*, pp.260-281.

Mtelela, C., 2016. Sedimentology and stratigraphy of the late Cenozoic lake beds succession, Rukwa Rift Basin, Tanzania: implications for hydrocarbon prospectivity (Doctoral dissertation, James Cook University). https://researchonline.jcu.edu.au/47290/.

Mtelela, C., Roberts, E.M., Downie, R. and Hendrix, M.S., 2016. Interplay of structural, climatic, and volcanic controls on late quaternary lacustrine–deltaic sedimentation patterns in the Western Branch of the East African Rift System, Rukwa Rift Basin, Tanzania. *Journal of Sedimentary Research*, *86*(10), pp.1179-1207.

Negredo, A.M., Fernandez, M. and Zeyen, H., 1995. Thermo-mechanical constraints on kinematic models of lithospheric extension. *Earth and Planetary Science Letters*, *134*(1-2), pp.87-98. https://doi.org/10.1016/0012-821X(95)00107-N.

Nelson, R.A., Patton, T.L. and Morley, C.K., 1992. Rift-segment interaction and its relation to hydrocarbon exploration in continental rift systems (1). *AAPG bulletin*, *76*(8), pp.1153-1169. https://doi.org/10.1306/BDFF898E-1718-11D7-8645000102C1865D.

Nyblade, A.A. and Robinson, S.W., 1994. The African superswell. *Geophysical research letters*, *21*(9), pp.765-768.

Osagiede, E.E., Rotevatn, A., Gawthorpe, R., Kristensen, T.B., Jackson, C.A. and Marsh, N., 2020. Pre-existing intra-basement shear zones influence growth and geometry of non-colinear normal faults, western Utsira High–Heimdal Terrace, North Sea. *Journal of Structural Geology*, *130*, p.103908.

Paxton, S. T., 1984. Occurrence and distribution of am- monium illite in the Pennsylvania, U.S.A. coal fields and proposed relationship to thermal maturity. Geol. Soc. Am. Abstr. Prog. 16,620.

Peace, A., McCaffrey, K., Imber, J., van Hunen, J., Hobbs, R. and Wilson, R., 2018. The role of pre-existing structures during rifting, continental breakup and transform system development, offshore West Greenland. *Basin Research*, *30*(3), pp.373-394. https://doi.org/10.1111/bre.12257.

Peacock, D.C.P., Parfitt, E.A., 2002. Active relay ramps and normal fault propagation on Kilauea Volcano, Hawaii. Journal of structural geology 24, 729e742. https://doi.org/10.1016/S0191-8141(01)00109-2.

Phillips, T., Jackson, C. A. L., and Norcliffe, J., 2020. Pre-inversion normal fault geometry controls inversion style and magnitude, Farsund Basin, offshore southern Norway. *Solid Earth*. https://doi.org/10.5194/se-11-1489-2020.

Quennell, A.M., McKinlay, A.C. and Aitken, W.G., 1956. Summary of the geology of Tanganyika, part 1. *Geological Surv. Tanganyika Mem*, *126*.

Ravnås, R., & Bondevik, K.,1997. Architecture and controls on Bathonian–Kimmeridgian shallow-marine synrift wedges of the Oseberg–Brage area, northern North Sea. *Basin Research*, *9*(3), 197-226.

Reilly, C., Nicol, A. and Walsh, J., 2017. Importance of pre-existing fault size for the evolution of an inverted fault system. *Geological Society, London, Special Publications*, *439*(1), pp.447-463. https://doi.org/10.1144/SP439.2.

Rizzoli, P., Martone, M., Gonzalez, C., Wecklich, C., Tridon, D.B., Bräutigam, B., Bachmann, M., Schulze, D., Fritz, T., Huber, M. and Wessel, B., 2017. Generation and performance assessment of the global TanDEM-X digital elevation model. *ISPRS Journal of Photogrammetry and Remote Sensing*, *132*, pp.119-139. https://elib.dlr.de/113892/.

Roberts, E.M., Stevens, N.J., O'Connor, P.M., Dirks, P.H.G.M., Gottfried, M.D., Clyde, W.C., Armstrong, R.A., Kemp, A.I.S. and Hemming, S., 2012. Initiation of the western branch of the East African Rift coeval with the eastern branch. *Nature Geoscience*, *5*(4), pp.289-294.

Roberts, E.M., O'Connor, P.M., Stevens, N.J., Gottfried, M.D., Jinnah, Z.A., Ngasala, S., Choh, A.M. and Armstrong, R.A., 2010. Sedimentology and depositional environments of the Red Sandstone Group, Rukwa Rift Basin, southwestern Tanzania: New insight into Cretaceous and Paleogene terrestrial ecosystems and tectonics in sub-equatorial Africa. *Journal of African Earth Sciences*, *57*(3), pp.179-212. https://doi.org/10.1016/j.jafrearsci.2009.09.002.

Roe, E., Dypvik, H. and Kilembe, E., 1996. Sedimentological analysis of the logs and cuttings from the wells Ivuna #1 and Galula #1, the Rukwa Rift valley, Western Tanzania- A progress report (Unpublished).

Rosendahl, B.R., Reynolds, D.J., Lorber, P.M., Burgess, C.F., McGill, J., Scott, D., Lambiase, J.J. and Derksen, S.J., 1986. Structural expressions of rifting: lessons from Lake Tanganyika, Africa. *Geological Society, London, Special Publications*, *25*(1), pp.29-43.

Sander, S. and Rosendahl, B.R., 1989. The geometry of rifting in Lake Tanganyika, east Africa. *Journal of African Earth Sciences (and the Middle East)*, *8*(2-4), pp.323-354.

Saria, E., Calais, E., Stamps, D. S., Delvaux, D., & Hartnady, C. J. H. , 2014. Present-day kinematics of the East African Rift. Journal of Geophysical Research: Solid Earth, 119, 3584–3600. https://doi.org/10.1002/2013JB010901.

Schlische, R.W., 1991. Half-graben basin filling models: new constraints on continental extensional basin development. *Basin Research*, *3*(3), pp.123-141. https://doi.org/10.1111/j.1365-2117.1991.tb00123.x.

Smets, B., Delvaux, D., Ross, K.A., Poppe, S., Kervyn, M., d'Oreye, N. and Kervyn, F., 2016. The role of inherited crustal structures and magmatism in the development of rift segments: Insights from the Kivu basin, western branch of the East African Rift. *Tectonophysics*, *683*, pp.62-76.

Snyder, G., Poreda, R., Fehn, U. and Hunt, A., 2003. Sources of nitrogen and methane in Central American geothermal settings: Noble gas and 129I evidence for crustal and magmatic volatile components. *Geochemistry, Geophysics, Geosystems*, *4*(1), pp.1-28.

Stamps, D.S., Saria, E. and Kreemer, C., 2018. A geodetic strain rate model for the East African Rift System. *Scientific reports*, *8*(1), pp.1-9. DOI:10.1038/s41598-017-19097-w

Strous, M., Fuerst, J.A., Kramer, E.H., Logemann, S., Muyzer, G., van de Pas-Schoonen, K.T., Webb, R., Kuenen, J.G. and Jetten, M.S., 1999. Missing lithotroph identified as new planctomycete. *Nature*, *400*(6743), pp.446-449.

Theunissen, K., Klerkx, J., Melnikov, A., & Mruma, A., 1996. Mechanisms of inheritance of rift faulting in the western branch of the East African Rift, Tanzania. *Tectonics*, *15*(4), 776-790. https://doi.org/10.1029/95TC03685.

Tiercelin, J.J., Thuo, P., Potdevin, J.L. and Nalpas, T., 2012. Hydrocarbon prospectivity in Mesozoic and early–middle Cenozoic rift basins of central and northern Kenya, Eastern Africa. DOI:10.1306/13351553M1001742.

Turner, J.P. and Williams, G.A., 2004. Sedimentary basin inversion and intra-plate shortening. *Earth-Science Reviews*, *65*(3-4), pp.277-304.

Walsh, J.J. and Watterson, J., 1989. Displacement gradients on fault surfaces. *Journal of Structural Geology*, *11*(3), pp.307-316.

Walsh, J.J., Childs, C., Meyer, V., Manzocchi, T., Imber, J., Nicol, A., Tuckwell, G., Bailey, W.R., Bonson, C.G., Watterson, J. and Nell, P.A., 2001. Geometric controls on the evolution of normal fault systems. *Geological Society, London, Special Publications*, *186*(1), pp.157-170. https://doi.org/10.1144/GSL.SP.2001.186.01.10.

Warr, O., Lollar, B.S., Fellowes, J., Sutcliffe, C.N., McDermott, J.M., Holland, G., Mabry, J.C. and Ballentine, C.J., 2018. Tracing ancient hydrogeological fracture network age and compartmentalisation using noble gases. *Geochimica et Cosmochimica Acta*, *222*, pp.340-362.

Wedmore, L.N., Biggs, J., Floyd, M., Fagereng, Å., Mdala, H., Chindandali, P., Williams, J.N. and Mphepo, F., 2021. Geodetic constraints on cratonic microplates and broad strain during rifting of thick Southern African lithosphere. *Geophysical Research Letters*, *48*(17), p.e2021GL093785. https://doi.org/10.1029/2021GL093785.

Wescott, W.A., S.T. Wigger, D.M. Stone, and C.K. Morley., 1999, Geology and Geophysics of the Lotikipi Plain, in C.K. Morley ed., Geoscience of Rift Systems—Evolution of East Africa: *AAPG Studies in Geology No*. 44, p. 55–65.

Wescott, W.A., W.N. Krebs, D.W. Englehardt, and S.M. Cunningham, 1991, New biostratigraphic age dates from the Lake Rukwa basin in western Tanzania: AAPG Bulletin, v.75, p. 1255–1263.

Wessel, B., 2016. TanDEM-X Ground Segment DEM Products Specification Document. Technical Note 3.1, German Aerospace Center (DLR). https://tandemx-science.dlr.de/

Wheeler, W.H. & Rosendahl, B.R., 1994. Geometry of the Livingstone Mountains Border-fault, Nyasa (Malawi) Rift, East Africa.Tectonics, 13, 303-312. https://doi.org/10.1029/93TC02314.

Widlansky, S.J., Clyde, W.C., O'connor, P.M., Roberts, E.M. and Stevens, N.J., 2018. Paleomagnetism of the Cretaceous Galula Formation and implications for vertebrate evolution. *Journal of African Earth Sciences*, *139*, pp.403-420.

Williams, L.B., Wilcoxon, B.R., Ferrell, R.E. and Sassen, R., 1992. Diagenesis of ammonium during hydrocarbon maturation and migration, Wilcox Group, Louisiana, USA. *Applied Geochemistry*, *7*(2), pp.123-134.

Withjack, M.O., Schlische, R.W. and Olsen, P.E., 2002. Rift-basin structure and its influence on sedimentary systems. DOI: 10.2110/pec.02.73.0057.

Withjack, M.O. and Schlische, R.W., 2006. Geometric and experimental models of extensional fault-bend folds. *Geological Society, London, Special Publications*, *253*(1), pp. 285-305. https://doi.org/10.1144/GSL.SP.2006.253.01.15.

Wopfner, H., 1993. Structural development of Tanzanian Karoo basins and the break-up of Gondwana. In *Gondwana symposium* (pp. 531-539).

Ziegler, P.A., Cloetingh, S. and van Wees, J.D., 1995. Dynamics of intra-plate compressional deformation: the Alpine foreland and other examples. *Tectonophysics*, *252*(1-4), pp.7-59. https://doi.org/10.1016/0040-1951(95)00102-6.

Zink, M., Bachmann, M., Brautigam, B., Fritz, T., Hajnsek, I., Moreira, A., Wessel, B. and Krieger, G., 2014. TanDEM-X: The new global DEM takes shape. *IEEE Geoscience and Remote Sensing Magazine*, *2*(2), pp.8-23.

Zwaan, F., Schreurs, G., Naliboff, J. and Buiter, S.J., 2016. Insights into the effects of oblique extension on continental rift interaction from 3D analogue and numerical models. *Tectonophysics*, 693, pp.239-260. https://doi.org/10.1016/j.tecto.2016.02.036.

Chapter 3: Seismic stratigraphic framework, dispersal of depocenters and helium reservoirs in the Rukwa Rift Basin

(A manuscript to be submitted in the Tectonophysics Journal)

Seismic stratigraphic framework, dispersal of depocenters and helium reservoirs in the Rukwa Rift Basin

Ernest Mulaya[1,2], Jon Gluyas[2], Ken McCaffrey[2], Thomas Phillips[2], Chris Ballentine[3], Evelyne Mbede[1], Cassy Mtelela[1]

[1]School of Mines and Geosciences, University of Dar es Salaam, P.O. Box 35052, Dar es Salaam, Tanzania.

[2]Department of Earth Sciences, Durham University, Durham, UK, DH1 3LE.

[3]Department of Earth Sciences, University of Oxford, Oxford, UK, OX1 3AN.

Ernest Mulaya (Corresponding author)

Email: ernest.s.mulaya@durham.ac.uk

Abstract

The classical half-graben geometry of the Rukwa Rift Basin (RRB) reflects overall maximum sediment accumulation adjacent to the border fault (Lupa Fault) via a basin history that comprised multiple local depocenters. In this study, laboratory-cored samples, 2D seismic reflection data, Digital Elevation Model (DEM) and well data are integrated to map the distribution of sediment accumulation. This enables us to document the change in morphology of depocenters and reservoir quality during each rifting phase from the Late Palaeozoic to the Late Cenozoic Era. The isochron and time-thickness maps reveal that the Rukwa Rift Basin experienced a shift in depocenter location and progressive strata dispersal in space and time during each of the rifting phases since the early Karoo-aged rifting. The distribution of depocenters is defined by topographic highs related to footwall uplift during a multiphase rifting history that modulated the deposition, differential erosional patterns, drainage system and sediment routing in the RRB. We illustrate that the depocenters to the south of the Saza shear zone might have been isolated initially during Karoo rifting, contiguous during Cretaceous and possibly linked into a single main depocenter during the latter stages of rifting (Late Miocene -Pleistocene). These

results provide insights into proportions of accommodation space and sediment accumulations which have wider implications for the distribution of helium reservoirs. Petrophysical parameters (grain density, porosity, and permeability) are analysed to assess the quality of potential helium reservoirs to add value on chance of economic success. The main helium reservoir potential is represented by sandstone sequences mainly in the Karoo and Red Sandstone formations. Petrophysical analyses of these sandstone sequences show anomalously high porosity and permeability ranges which are c. 26-30% and 272.7-660.6 mD respectively.

3.1 Introduction

The Rukwa Rift Basin (RRB), Tanzania is a structurally controlled intracontinental rift exhibiting half graben geometry and an uplifted footwall in the west arm of the East African Rift System (EARS) (Rosendahl et al., 1986; Ebinger, 1989; Schlische, 1991; Chorowicz, 2005; Mulaya et al., 2022; Fig. 3.1). Like many other cratonic rifts, the RRB exhibits large- to small-scale structures such as crustal-scale inherited faults and shear zones that have controlled sediment accommodation space and distribution (Mulaya et al., 2022). The distribution of syntectonic sedimentary sequences in the basin controls potential reservoirs for helium accumulation (Mulaya et al., 2022; Danabalan et al., 2022). Tectonically, this region has been affected by Paleozoic to Cenozoic rifting cycles that were influenced by the reactivation of the NW - trending Palaeoproterozoic Ubende mobile belt (e.g. Wescott et al., 1991; Delvaux et al., 1992; Morley et al., 1992; Lenoir et al., 1994; Theunissen et al., 1996; Katumwehe et al., 2015; Mtelela, 2016).

The RRB is considered a new frontier for helium exploration in the region (e.g. Danabalan, 2017; Danabalan et al., 2022; Mulaya et al., 2022). The basin is estimated to contain a probable reserve of c. 138 Billion Cubic Feet (BCF) (Helium-One, 2019).

These findings have kindled interest in helium exploration and further academic research in the basin. Previous studies in the RRB focused on describing general tectonic activities, rift geometry and their implications for hydrocarbon and helium potential (Mbede, 1993; Delvaux et al., 2012; Mtelela, 2016; Mtili et al., 2021; Mulaya et al., 2022). This work provides crucial insights into the structural evolution and architecture of the Rukwa Rift Basin and the western branch of the East African Rift Systems (EARS). Of equal importance, detailed stratigraphic and sedimentological analysis of the RRB and related depositional processes and systems show that potential fluid reservoirs are distributed throughout the whole stratigraphic sequence in units such as the Karoo Supergroup, the Red Sandstone Group and the Lake Beds Group (e.g. Quenell et al., 1956; Wescott et al., 1991; Morley et al., 1992; Wheeler and Karson, 1994. Mtelela, 2016; Roberts et al., 2010; Hilbert-Wolf et al., 2017; Mtelela et al., 2017; Widlansky et al., 2018). Nonetheless, a detailed understanding of the tectonostratigraphic evolution and the temporal-spatial variation of depocenters that formed the potential helium reservoirs in the RRB remain of utmost importance.

Assessing a basin's helium potential, in common with hydrocarbon resource assessment, requires understanding of rifting phases, rift basin evolution and reservoir quality (e.g. Nelson et al., 1992; Gluyas and Swarbrick, 2021; Danabalan et al., 2022; Mulaya et al., 2022). Unlike hydrocarbon systems, however, helium occurrences require longer time scale to enable stable and significant volume of crust rich in uranium and thorium to release sufficient quantity and accumulate helium. The expulsion of helium from basement source rocks and subsequent migration into sedimentary strata for storage is controlled by a significant change in thermal gradient facilitated by a carrier fluid via hydraulic conduits (Danabalan et al., 2022). In basins such as the RRB with few well data and sparse coverage of 2D seismic reflection data and a known complex tectonic history (e.g. Morley et al., 1992; Chorowicz, 2005; Mulaya et al., 2022) an advance in our understanding of tectonostratigraphic evolution can provide a pivotal insight into its helium resource potential. In this contribution we present new isopach maps, isochron maps, petrophysical data and interpret 2D seismic sections to describe the spatio-temporal variation of depocenter morphology and reconstruct the tectonic processes with general implications for helium reservoirs distribution and quality. We unveil how each rifting cycle affected physiographic distribution and sediment accommodation and created potential for helium reservoirs occurrences in the RRB.

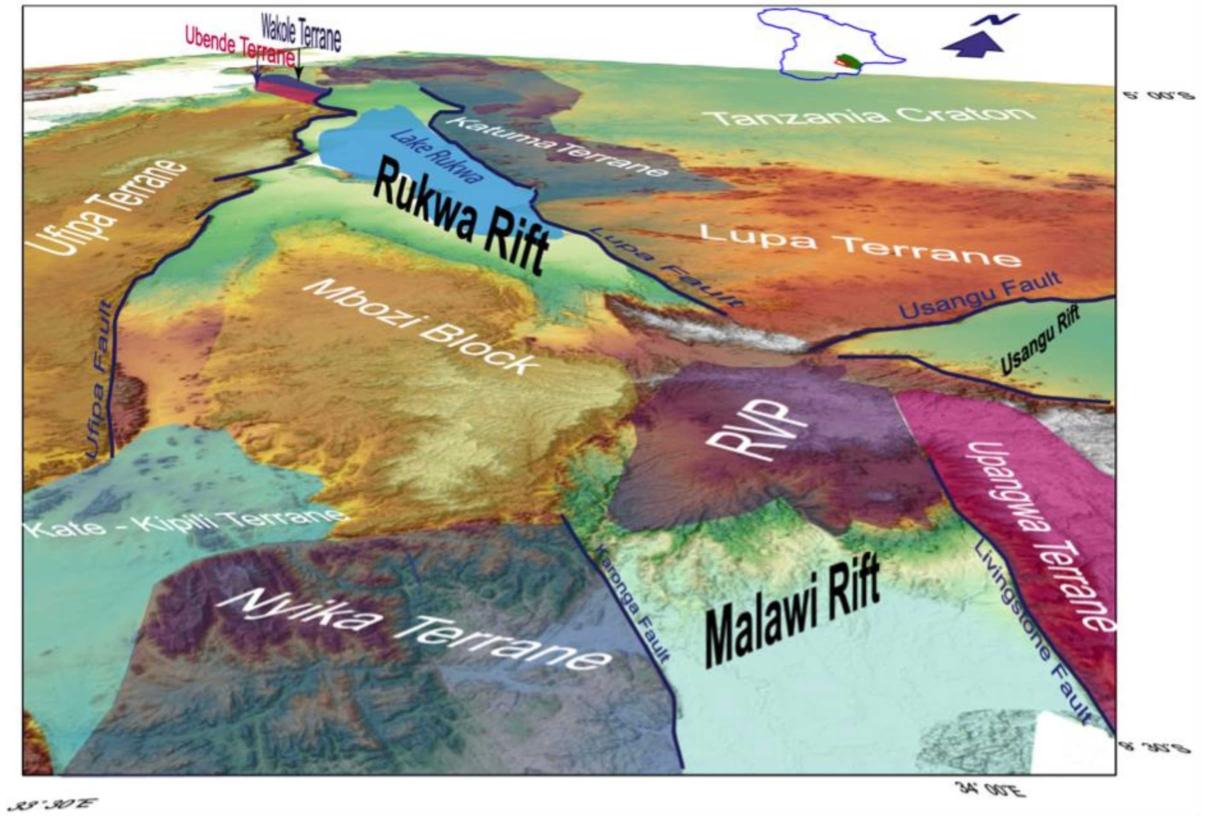

Fig. 3.1. 3-D Tectonic map superimposed on hill shaded relief of TanDEM-X 90 m showing Precambrian terranes, major rifts and structures surrounding the Rukwa Rift Basin within the Ubendian mobile belt in the southwest of Tanzania Craton. Note the major rifts intersect at the Rungwe Volcanic Province (RVP).

3.2.0 Geologic setting

The RRB lies within the NW-trending Paleoproterozoic Ubendian orogenic belt and is surrounded by Precambrian terranes (e.g. Kilembe and Rosendahl, 1992; Fig. 3.1). The RRB is the product of at least three rifting phases which mainly includes Karoo rifting, post-Karoo rifting and Late Cenozoic rifting recorded in synrift strata (Ebinger, 1989; Morley, 1989; Mulaya et al., 2022). Stratigraphically, the synrift packages are subdivided into the Late Carboniferous–Permian-aged Karoo Supergroup, the Cretaceous/Oligocene-aged Red Sandstone Group and Late Miocene to Plio-Pleistocene-aged Lake Beds Group (Quennell et al., 1956; Wescott et al., 1991; Morley et al., 1992; Roberts et al., 2010; Mtelela, 2016; Fig. 3.2a-b).

Lithostratigraphically, the Karoo Supergroup is composed of conglomerate, sandstone, shale/mudstone and liptinitic rich coal of the K2 unit (Kilembe and Rosendahl, 1992; Morley et al., 1992). The Red Sandstone Group is characterized by fluvial-lacustrine cross-bedded micaceous sandstone and minor shale interbeds (Dypvik et al., 1990; Kilembe and Rosendahl, 1992; Roberts et al., 2010; Mtelela, 2016). The Lake Beds Group includes both fluviatile and a profundal lacustrine system dominated by unconsolidated alluvium, siliciclastic- and volcanoclastic-dominated strata and mudstone with intercalated volcanic ash (Kilembe and Rosendahl, 1992; Roberts et al., 2010; Mtelela, 2016).

Recent analysis of geodetic, seismic and earthquake datasets indicate a present-day E-W to WNW-ESE extension direction, with predominantly normal faults controlling the stratigraphic distribution (Delvaux and Barth, 2010; Saria et al., 2014; Stamps et al., 2018; Lavayssière et al., 2019; Mulaya et al., 2022).

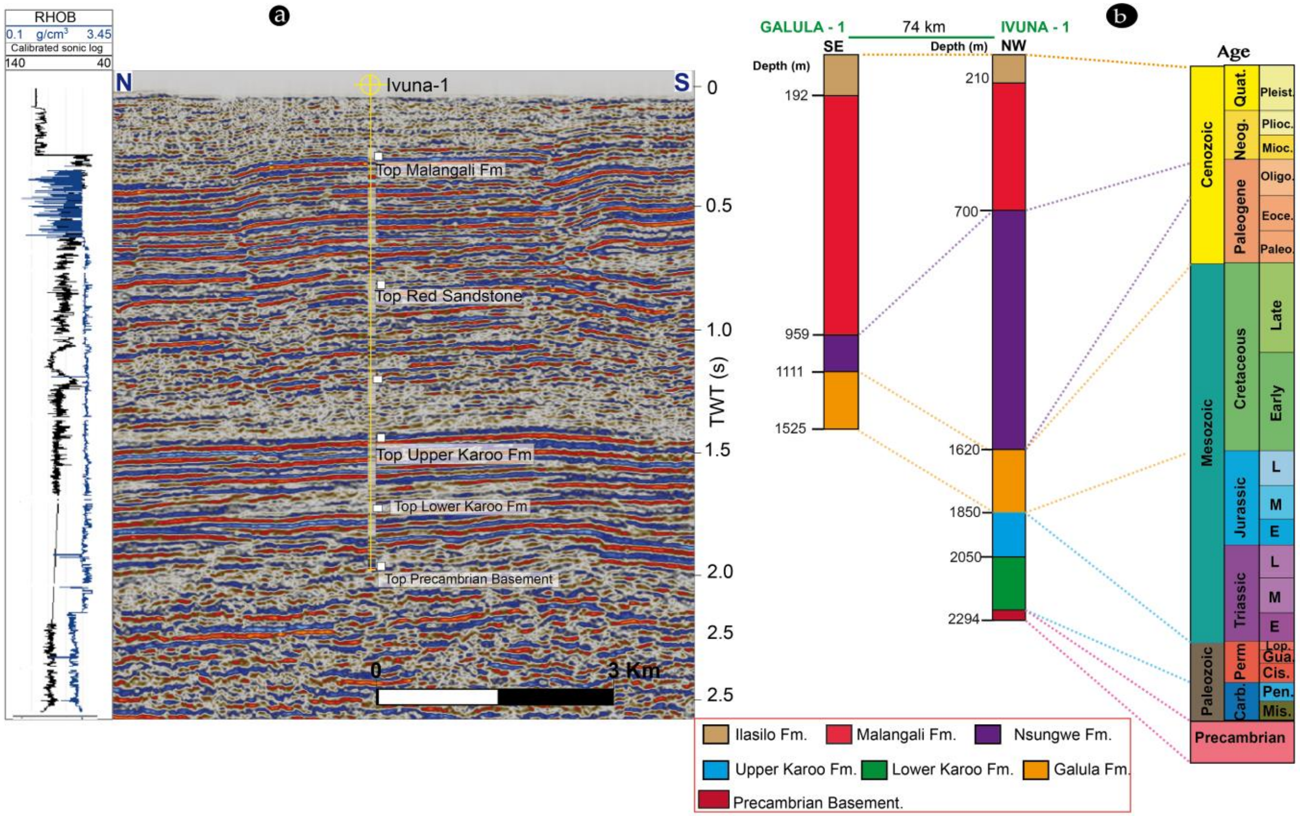

Fig. 3.2. (a) Seismic section showing general stratigraphy of the Rukwa Rift Basin correlated with the major formations (Fm) tops and well logs i.e. the bulk density and acoustic logs from Ivuna-1 tied to seismic section. Stratigraphic data (well tops information) are correlated with high amplitude seismic horizons hence providing confidence and control during interpretation. The ages of key horizons are constrained using previous work by Mtelela. (2016) and references therein. (b) Generalized stratigraphic column of the Galula-1 and Ivuna-1 exploration wells. (Illustrations after Morley et al., 1992; Delvaux et al., 1992; Kilembe and Rosendahl, 1992; Mtelela, 2016; Hilbert-Wolf et al., 2017; Mulaya et al., 2022).

3.3.0 Methods and datasets

3.3.1 Seismic and DEM data

Our study combines Digital Elevation Model created from TanDEM-X 90m data and 2D seismic data tied to wells interpreted using ArcGIS Pro and Schlumberger Petrel software respectively. The TanDEM-X 90m data were acquired by the German Aerospace Center (DLR) in partnership with Airbus Defence and Space between 2010 - 2015 (Wessel, 2016; Rizzoli et al., 2017). The seismic data were released by the Tanzania Petroleum Development Corporation (TPDC) and include (ca. 2450 km) of seismic-reflection profiles acquired by American Oil Company (AMOCO) in the 1980's during petroleum exploration in the region (AMOCO, 1987; Morley et al., 1992). The vertical resolution of the seismic data generally decreases below 5000 - 6000 ms TWT in many seismic lines. These data are stored in SEG - Y format and have not been depth - converted, thus key stratigraphic sequences were identified and mapped in Two Way Travel Time (TWT) along the 2D seismic lines using Schlumberger's Petrel Software v. 2018 (e.g. Fig. 3.3). All the seismic data are displayed with SEG reverse polarity, such that a downward increase in acoustic impedance is represented by a trough (blue) whereas a downward decrease in acoustic impedance is represented by a peak (red) reflection event on a seismic profile (Avseth et al., 2010).

3.3.2 Quality control of seismic data

Quality control of the seismic data involved mapping strong reflectors that display a good continuity across the basin. The major seismic units were mapped in the RRB on the basis of seismic facies, reflector continuity and terminations (e.g. Fig. 3.2a; Fig. 3.3). Consequently, isochron maps and time-thickness maps of the major intervals were generated from the mapped horizons using a convergent interpolation algorithm in Petrel software v. 2018.

3.3.3 Porosity and permeability calculation

Porosity and permeability values were calculated based on petrophysical measurements conducted in the Rock Physics and Geomechanics Laboratory at the University of Aberdeen in the U.K using a Jones Porosimeter/Permeameter instrument. This instrument combines a Coberly-Stevens Boyle's Law porosimeter and a gas permeameter on the same panel. Before conducting petrophysical measurement, four rock samples measuring 1-inch (c. 2.54 cm) diameter of core plugs and average lengths cut between 3.14 cm and 5.11 cm, were prepared using a diamond impregnated core bit. The samples were then oven-dried and petrophysical parameters calculated following the methodology described by Farrell et al. (2014) and Rossetti et al. (2019).

3.4.0 Results

3.4.1 Seismic facies and rifting cycles

Six seismic packages were identified and mapped in the Phanerozoic synrift sedimentary interval above the Precambrian crystalline basement (Fig. 3.4). These packages correspond to different rifting cycles and lithostratigraphic units including the Late Carboniferous-Permian Karoo Supergroup comprising of the Lower and Upper Karoo Formation; the Red Sandstone Group (including the Cretaceous Galula and the Paleogene Nsungwe Formations); and the Late Miocene-Pleistocene Lake Beds Group (including the Malangali and Ilasilo Formations) (Hilbert-Wolf et al., 2017; Mtelela et al., 2017; Mulaya et al., 2022; Fig. 3.3a-b). The tops and bottoms of these major seismic-stratigraphic formations show continuous medium to strong amplitude response across the basin and are distinctly bound by unconformity surfaces. The isochron maps for the entire basin reveal up to 6000ms (TWT) of total sediment package in the hanging wall to the Lupa and the Ufipa border faults (e.g. Mulaya et al., 2022; Fig. 3.4a-b).

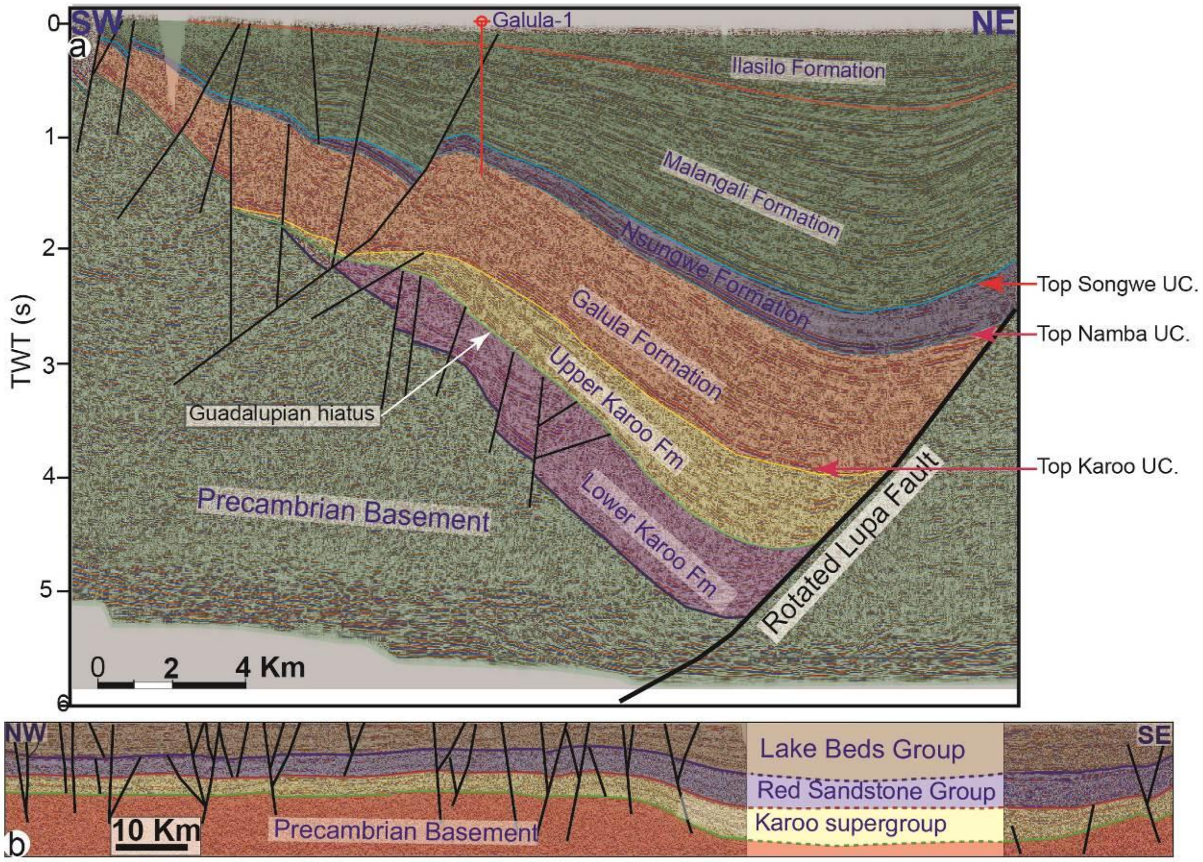

Fig. 3.3. Interpreted seismic sections showing stratigraphic distribution (a) Across the basin (SW-NE section, cf. Mulaya et al., 2022). Note various unconformities (UC.) illustrated (b) Cross section along strike of the border faults.

3.4.2.1 Precambrian tectonic setting

The Top Basement seismic response is characterized by fairly good continuity and variable medium to high amplitude seismic signal, i.e. marked by highly reflective horizon (Fig. 3.3a). The seismic reflection data reveal relatively shallow depths of Precambrian basement ranging between surface exposure (0 ms) over the Ufipa and/Mbozi Block becoming progressively deeper to a maximum of ca. 6000 ms towards the Lupa Fault (Figs. 3.3A, 3.4A(i)). Within the basin, the Precambrian crystalline basement is unconformably overlain by Phanerozoic synrift sedimentary packages. Cross sections show that the top of the basement is intersected by predominantly normal faults and in map view known Precambrian shear zones which align with the overlying rift-related faults (Figs. 3.3A & 3.4B). The seismic sections reveal basement-rooted fault systems extending into the overlying rift sedimentary units (e.g. Figs. 3.3A). A key observation (in map view) shows a unique set of NE-SW to E-W striking faults almost perpendicular to the Chisi shear zone, that are spatially-limited to the location of the Kwera and Saza transfer faults (Fig. 3.4B). The isopach map shows that these NE trending faults occupy a NE-SW striking direction sub-parallel to the Saza shear zones in the central part of the basin (e.g. Mulaya et al, 2022; Fig. 3.4B).

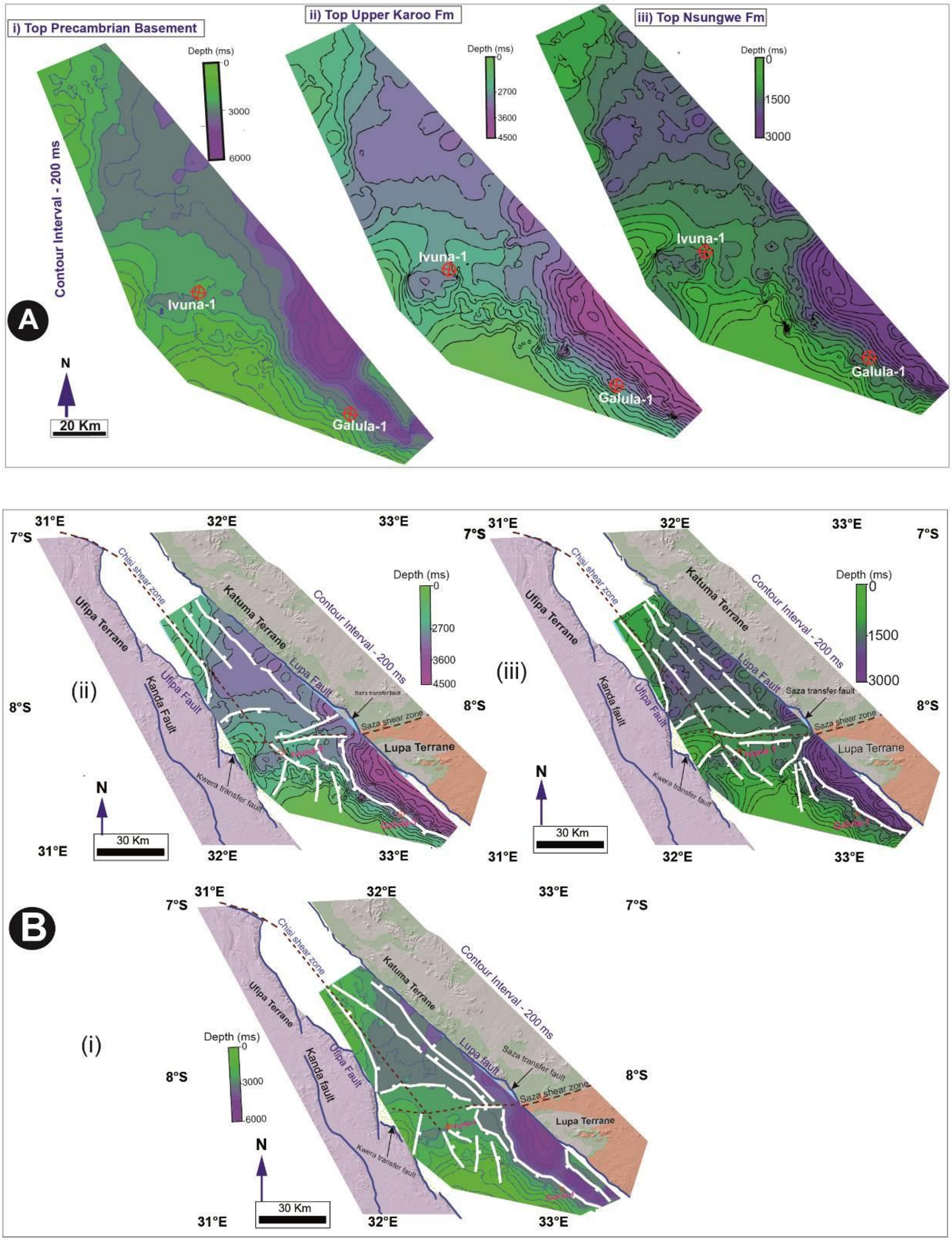

Fig. 3.4. (A) Uninterpreted and (B) interpreted Two-Way-Time (TWT) isochron map for (i) Top Precambrian Basement (ii) Top Upper Karoo Formation (iii) Top Nsungwe Formation with active intrabasin faults and surrounding tectonic terranes traced over the DEM image. Note the Saza and Chisi shear zones shown in Purple

dashed line extending into the basin interpreted from Lemna et al. (2019); Heilman et al. (2019); Mulaya et al. (2022).

3.4.2.2 Late Carboniferous-Early Jurassic (Karoo rifting)

The Late Carboniferous - Early Jurassic period encompasses the first rifting phase (Karoo rifting) and is preserved in the Karoo Supergroup overlying the acoustic basement (e.g. Wopfner, 1993; Figs. 3.2 & 3.3). Seismic sequences of the Karoo facies are characterized by sub-parallel to divergent seismic reflections (e.g. Figs. 3.2 & 3.3). In the northern end of the Mbozi Block, the Karoo seismic facies show variable amplitude within an onlap wedge geometry that pinches out onto the uplifted Mbozi Block (Fig. 3.3A). The thickness of the Karoo succession varies markedly and exhibits various deformation styles across the basin (Figs. 3.2 & 3.3). The inferred thickness for this unit increases significantly towards the Lupa Fault and thins adjacent to the Ufipa and Mbozi terranes (SW end of the section) (Figs. 3.3A). The isochron and thickness map of the whole Karoo Supergroup reveals sediment accumulation to a maximum inferred depth and thickness of 4500 ms and 2200 ms TWT respectively (Figs. 3.4(ii), 3.5A-B). Two horizons with distinctly high amplitudes and structural styles were mapped and subdivide the Karoo Supergroup into two formations i.e. the Lower and Upper Karoo formations which are inferred to correspond to late Carboniferous - early Permian and late Permian times respectively (Mulaya et al., 2022; Fig. 3.3A). The Lower Karoo Formation sequences are characterized by basement rooted fault systems which are truncated at its top whereas the upper strata are relatively undeformed implying an unconformity of mid-Permian age (Fig. 3.3A).

During Karoo rifting, the main depocenter observed south of the RRB had N - S to NW - SE strikes and was located within the hanging walls of a N-S striking normal fault and the Lupa Fault (Fig. 3.5B). The main depocenter widens northward and extends to c. 28 km width south of the Saza shear zones. Its axis lies oblique to the strike of the Lupa Fault until it deviates to a N - S strike and extends 20 km in the direction of NE-end of the Mbozi Block (Fig. 3.5A-B). Further to the south we observe an isolated depocenter (ID) of uniform ~10 km width that is confined laterally by NW-trending normal faults (Fig. 3.5B).

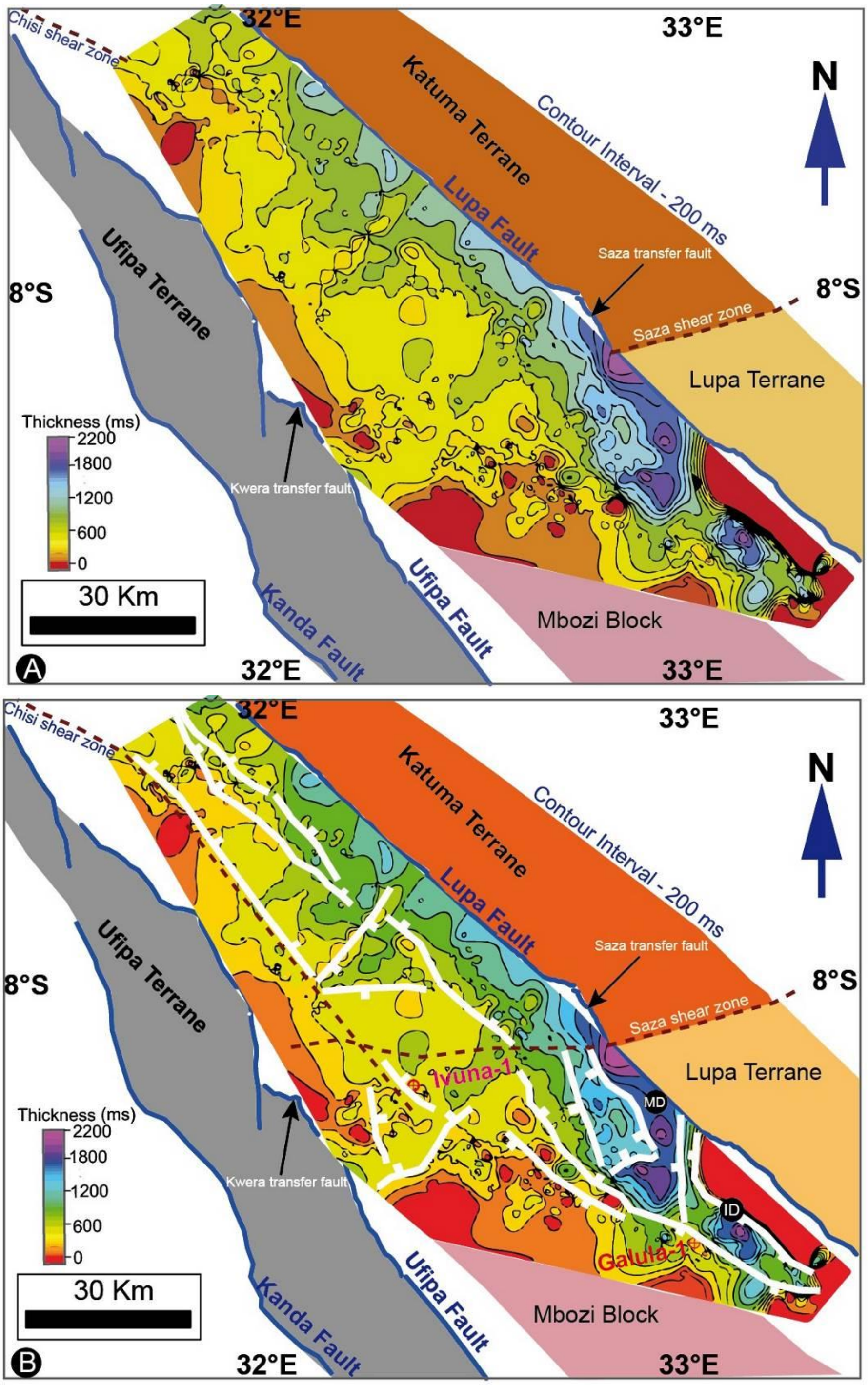

Fig. 3.5. (A) Uninterpreted and (B) Interpreted Time - thickness map for the Karoo Supergroup depositional packages calculated between the Base Lower Karoo Formation and the Top Upper Karoo Formation. Note the main depocenter (indicated as 'MD') with N - S to NW - SE strikes and another isolated depocenter (indicated as 'ID') restricted to the southeast end of the basin.

3.4.2.3 Cretaceous - Paleogene (Post Karoo rifting)

A second rifting phase in the RRB created space for deposition of the Red Sandstone Group across the full extent of the half-graben between the Lupa and the Ufipa faults (Fig. 3.6A-B). These Red Sandstone Group sequences, comprising the Galula and overlying Nsungwe Formations are considered to be of Cretaceous - Paleogene age and are defined by the Top Karoo unconformity at the base and the Songwe unconformity at the top (Delvaux, 2001; Mtelela, 2016; Mulaya et al., 2022). The isochron and time -thickness maps for the Red Sandstone Group reveals deepening and a sediment accumulation increase towards the east and southeast up to inferred thicknesses of 3000 ms TWT and 2200 ms TWT for the Galula and the Nsungwe Formations respectively (Figs. 3.4(iii) & 3.6A-B). During this period both the main depocentre (MD) and the minor independent depocenter (ID) were contiguous in the hanging wall of the Lupa Fault (Fig. 3.6A-B). The MD had a NW-SE strike direction aligning with the general trend of the main Lupa Fault. The eastern margin of the depocenter was defined by the Lupa Fault for 15 km south of the Saza shear zone before it followed the trace of a 15 km long curvilinear fault (Fig. 3.6B). The ID is approximately 5 km wide and located between a N-S striking fault and the Lupa Fault to which it trends obliquely (Fig. 3.6B). The seismic reflection data show distinctly strong reflection (unconformity) continuity across the basin defining a surface between the lowermost Galula Formation and the Nsungwe Formation (cf. Fig. 3.3A). The Cretaceous-aged Galula Formation is relatively thicker than the Nsungwe Formation with maximum thickness up to ~1000 ms TWT formed at its maximum depth ~4500 ms TWT. The Galula Formation is defined at its base by a highly variable reflection response (cf. Figs. 3.2A & 3.3A). This corresponds notably, with the recognised absence of Triassic and all the Jurassic units across much of this basin between the first and second rifting phases. This period of non-deposition and/or erosion is known as Top Namba Unconformity (Mtelela, 2016) and is associated with the persistence of uplifted basement highs and unconformity records.

The uppermost strata of the Red Sandstone Group comprise the Oligocene-aged Nsungwe Formation with maximum thickness measured by two-way-time of c. 400 ms TWT (cf. Fig. 3.3A). The top and bottom horizons of the Nsungwe Formation (cf. Fig. 3.3A) exhibit two unique and prominent seismic reflection responses (previously named as Horizon A and B by Morley et al. (1992). The two seismic horizons most likely form a basin-scale regional unconformity (Top Namba and Top Songwe Unconformity) and are marked by very high amplitudes which are continuous across the basin (Fig. 3.3A). In Domain B of the RRB, these two particular horizons continue until they are offset by the SW-dipping fault with ca. 315 ms TWT of throw (cf. Fig. 3.3A). The reflectors extend across the whole extent of domain B and terminate at the Saza Shear Zone. These distinctive high amplitude reflectors, most likely represent the Top Galula and Base Nsungwe Formations representing we infer, a non-deposition and/or erosion event (Top Namba Unconformity) during the Late Cretaceous and Late Oligocene respectively. We interpret these two prominent horizons represent possible unconformities formed during short-lived Oligocene rifting.

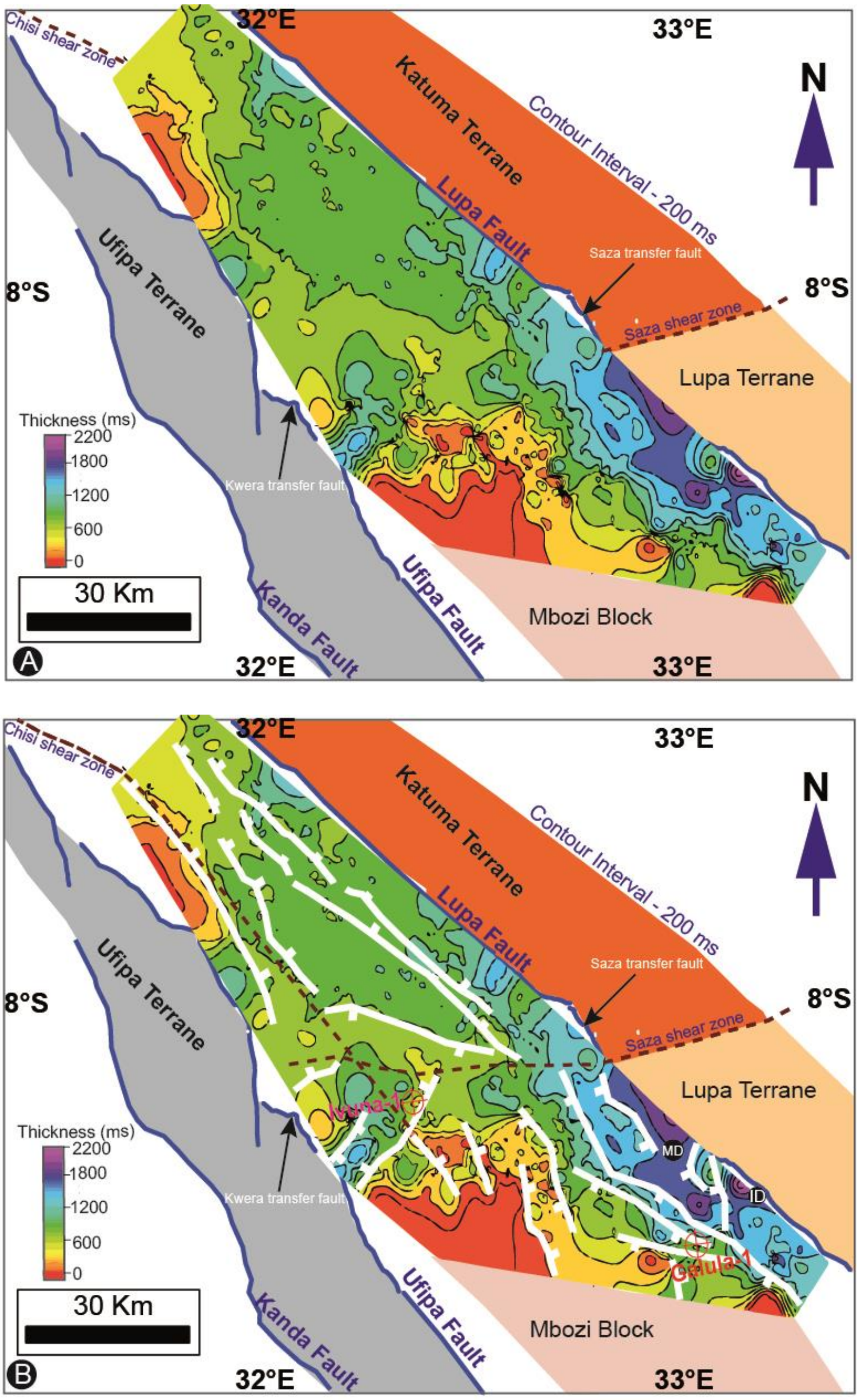

Fig. 3.6. (A) Uninterpreted and (B) Interpreted time - thickness map for the Red Sandstone Group depositional packages calculated between the Base Galula Formation and the Top Nsungwe Formation. To the south of the RRB the main depocenter (indicated as 'MD') with N-S to NW-SE strikes is contiguous with isolated/min-depocenter (indicated as 'ID') restricted to the southeast end of the basin.

3.4.2.4 Late Miocene - Pleistocene (Late Cenozoic rifting)

The Late Miocene to Pleistocene was dominated by the most recent rifting phase which is associated with the youngest sedimentary sequences, that is, the Lake Beds Group. Seismic data show these sequences are characterized by conformable low to high amplitude reflectors exhibiting mild folding (cf. Figs. 3.2A & 3.3A). Our data reveal two unique seismic facies, which are separated by a distinct high amplitude and laterally continuous seismic reflector (cf. Fig. 3.3A). We interpret these two reflectors to define two subdivisions of the Lake Beds Group most likely representing the Malangali Formation and the overlying Ilasilo Formation deposited between the Late Miocene - Pliocene and the Pleistocene times respectively (cf. Fig. 3.3A; Mtelela, 2016). The base of Ilasilo Formation is characterized by a high amplitude seismic horizon representing the beginning of the Pleistocene sequence deposition (e.g. Mtelela, 2016; cf. Figs. 3.2A & 3.3A). The base of the Malangali Formation most likely corresponds to the Top Songwe Unconformity at the top of the Red Sandstone Group (cf. Mtelela, 2016).

The time - thickness map calculated for the Lake Beds Group between the Base Malangali and Top Ilasilo Formation surfaces, records the majority of synrift activity associated with the Late Cenozoic to recent rifting (Fig. 3.7A-B). The seismic records for this phase are characterized by sequences which thicken towards the Lupa Fault with maximum sediment accumulation in the depocenter up to ~2400 ms TWT thick (Fig. 3.7A-B). In the western part of the RRB, the Lake Beds sequences thickness vary between 0 ms TWT and up to 600 ms TWT in the hanging wall of the Ufipa Fault (Fig. 3.7A-B). We observe one main depocenter (~60 km long and ~10 km wide) predominantly trending NW-SE containing ~2400 ms TWT thick of strata bounded by the Lupa Fault and a curvilinear fault trace in the southeast of the basin (Fig. 3.7B). North of the Saza shear zones in Domain A, multiple depocenters ~5 km wide containing ~2200 - 2400 ms thickness appear that are noticeably smaller than depocenters in Domain B (Fig. 3.7A-B). These depocenters are localized mainly along the NW and NNW–striking normal fault systems (Fig. 3.7B).

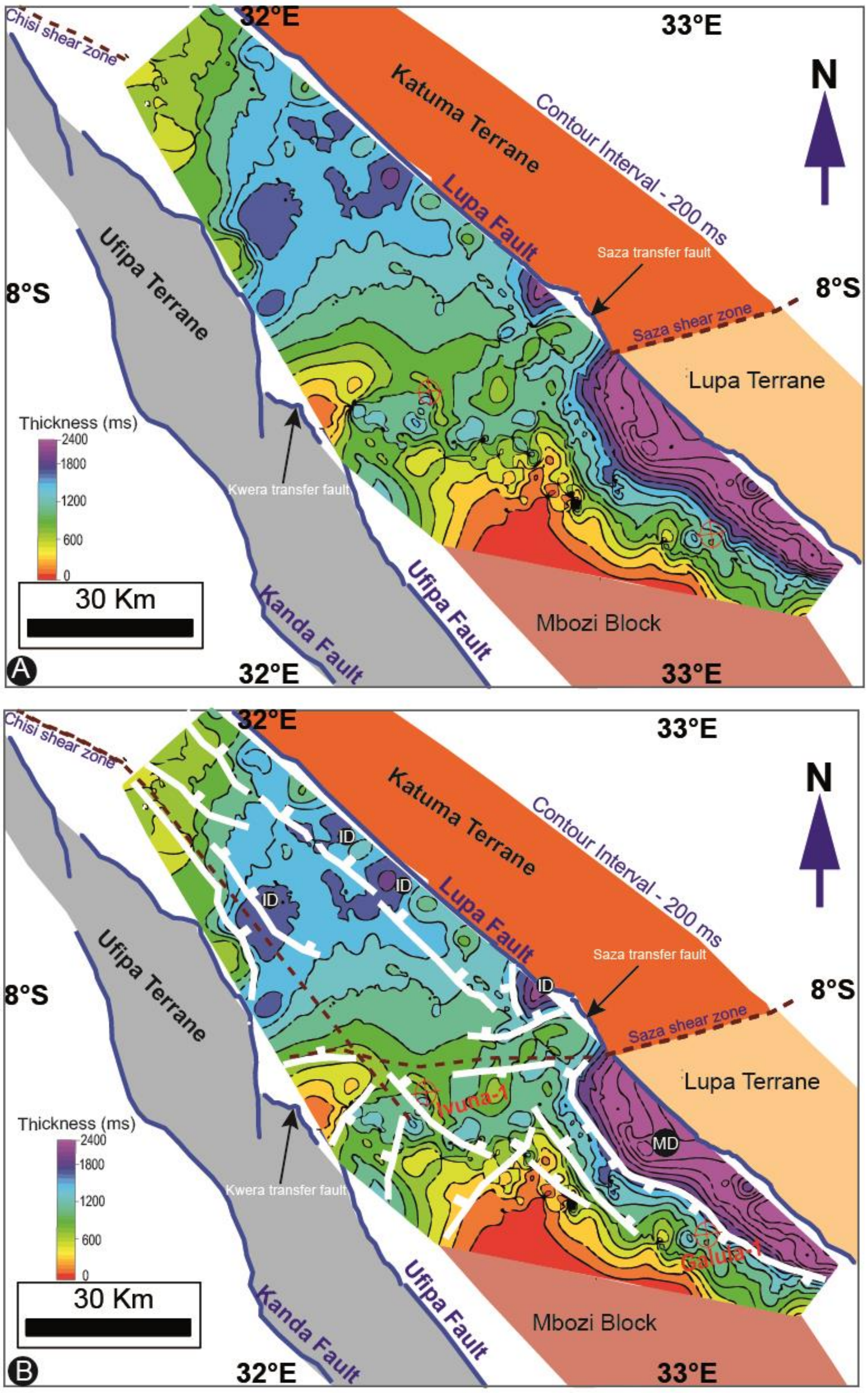

Fig. 3.7. (A) Uninterpreted and (B) interpreted time - thickness map for the Lake Beds Group depositional packages calculated between the Base Malangali and the Top Ilasilo Formation. To the south, the RRB exhibits one main depocenter (indicated as 'MD') bounded by the Lupa Fault and curvilinear fault (in plan view) in the southeast of the basin. Note, north of the Saza shear zone in Domain A the RRB contains multiple min-depocenters (indicated as 'ID') ~5 km wide.

3.4.3 Porosity and permeability of potential helium reservoir rocks

Petrophysical analysis of four outcrop samples shows that sandstones in both the Karoo Supergroup and the Red Sandstone Group are potential helium reservoirs (Fig. 3.8). These sedimentary facies preserve high porosity (26 - 30%) in the sandstone sequences (Table 3.1; Fig. 3.8). In the Lake Beds Group, the porosity ranges between 11 and 24% in tuffaceous mudstone and volcanoclastic sandstones (Fig. 3.8; Table 3.1). The overall permeability of the reservoirs exhibited in sandstone samples are in the range of 272.6 and 660.6 mD for the Karoo Supergroup and Red Sandstone Group respectively (Fig. 3.8; Table 3.1). The permeability for tuffaceous mudstone and volcanoclastic sandstones ranges is lower between 0.4 and 3.2 mD (Fig. 3.8; Table 3.1). Among the various reservoir rocks, the Red Sandstone Group (Galula Formation) exhibit relatively highest quality petrophysical data (sweet spots) followed by the Karoo Supergroup rocks. These petrophysical parameters for potential helium reservoirs are similar to those of the majority of known international siliciclastic reservoirs (Lenhardt and Götz, 2011; Fig. 3.9). Samples from the Lake Beds Group have lower reservoir quality and in places the interval may act as a temporary seal or baffle for helium migration (Fig. 3.9)

Table 3.1. Petrophysical data measured and computed from the cored rock plugs sampled from the major sedimentary sequences of the RRB

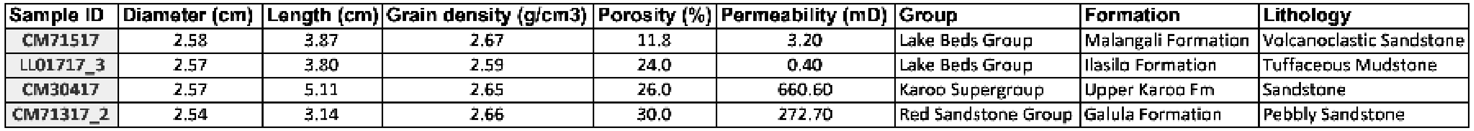

Sample ID	Diameter (cm)	Length (cm)	Grain density (g/cm3)	Porosity (%)	Permeability (mD)	Group	Formation	Lithology
CM71517	2.58	3.87	2.67	11.8	3.20	Lake Beds Group	Malangali Formation	Volcanoclastic Sandstone
LL01717_3	2.57	3.80	2.59	24.0	0.40	Lake Beds Group	Ilasilo Formation	Tuffaceous Mudstone
CM30417	2.57	5.11	2.65	26.0	660.60	Karoo Supergroup	Upper Karoo Fm	Sandstone
CM71317_2	2.54	3.14	2.66	30.0	272.70	Red Sandstone Group	Galula Formation	Pebbly Sandstone

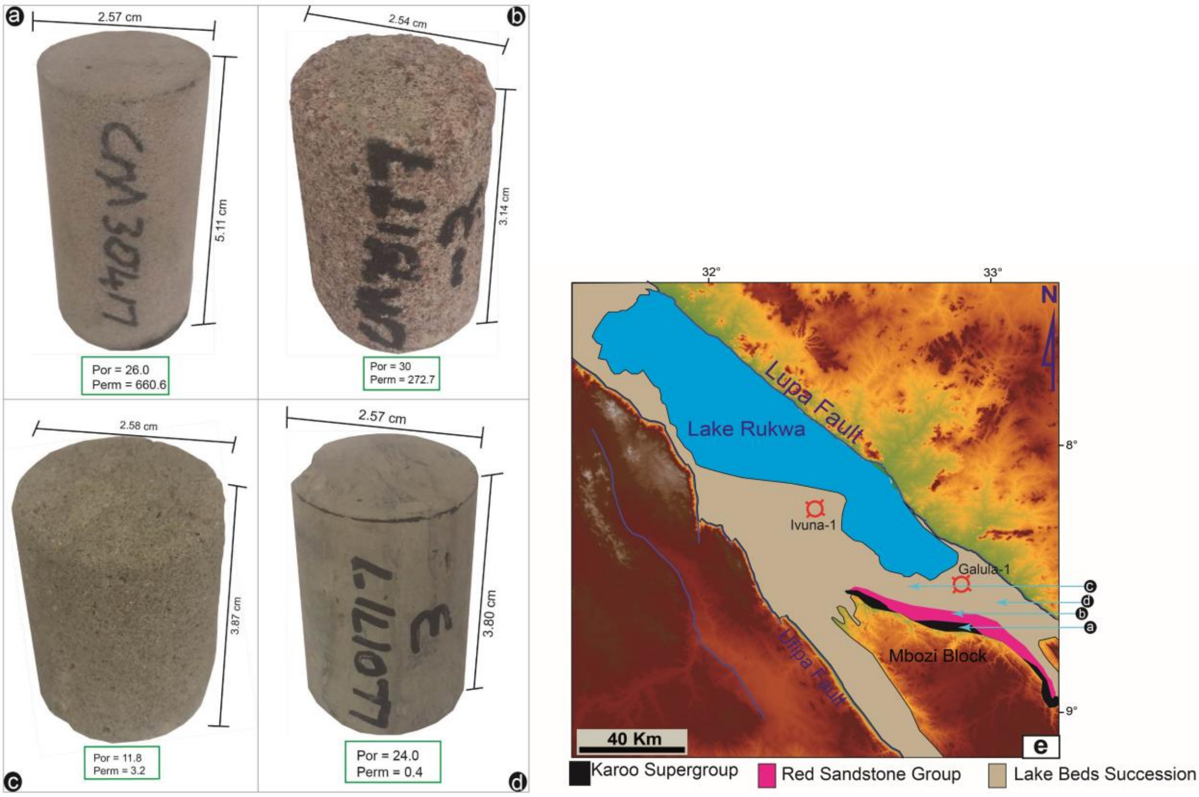

Fig. 3.8. Cored rock plugs measuring c. 2.57 cm average diameter prepared using a diamond-impregnated core bit at the Aberdeen University. The computed porosity and permeability are shown below each sample; (a) Fine- to medium-grained and moderated sorted sandstone, sampled from the Karoo Supergroup. (b) Very coarse-grained sand to pebbles (Pebbly sandstone) moderately sorted; subrounded to rounded texture sampled from the Red Sandstone Group (Galula Formation). (c) Fine- to medium-grained and poorly sorted volcanoclastic sandstone sampled from the Lake Beds Group (Malangali Formation). (d) Gray, tuffaceous mudstone deposits sampled from the Lake Beds Group (Ilasilo Formation). (e) Map showing the location of the outcrop samples with arrows corresponding to samples i.e, a(32°53′, 08°41′), b(32°52′, 08°38′), c(32°42′, 08°32′) and d (33°02′, 08°35′).

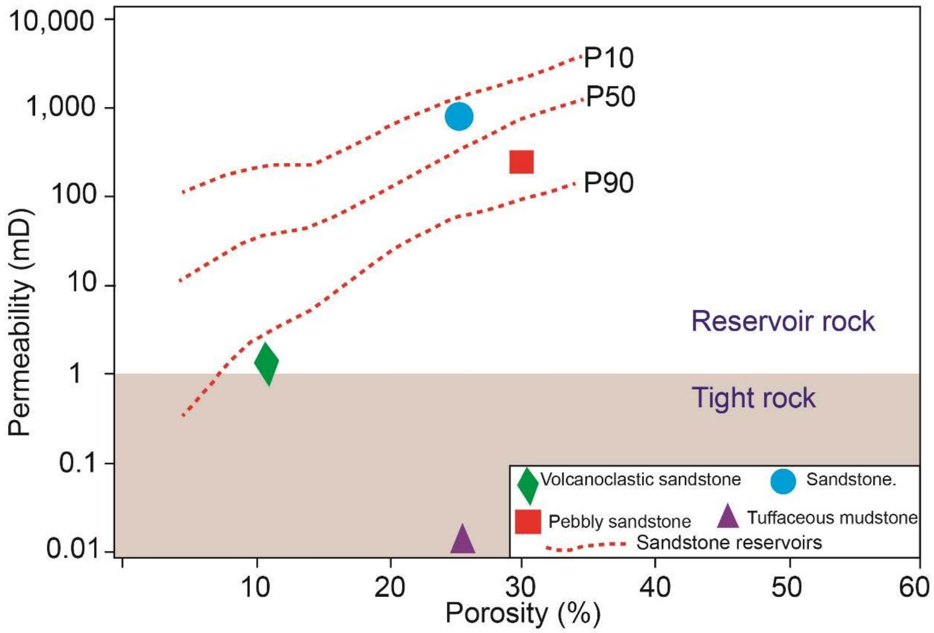

Fig. 3.9. The distribution of porosity and permeability between reservoir and non-reservoir (tight rock) quality of the RRB. P10: represents 10% of international sandstone reservoirs, P50: 50% of international sandstone/carbonate reservoirs, P90: 90% of international sandstone reservoirs adopted from Rossett et al. (2019) and Lenhardt and Götz. (2011).

3.4.4 the current strain fields at the Rungwe Volcanic Province (RVP)

Many border fault structures in the East African Rift System (EARS) have been influenced by pre-existing fabrics to create varied strain field patterns (Lemna et al., 2019; Heilman et al., 2019). In southwest Tanzania, the intersection of the three rift segments, the Rukwa, Malawi and Usangu Rifts is occupied by the Rungwe Volcanic Province (e.g. Harkin, 1960; Fig. 3.10A-B). The transitions between one rift and another show localized uplifts and structural highs covered by volcanic rock (Ebinger et al., 1989; Fig. 3.10A-B). The faults in this region show a radial (spoked) pattern (Fig. 3.10B) with NW–SE strike in the Rukwa Rift, NNW-SSE in the Malawi Rift and NE–SW in the Usangu Rift. The angular relationship between the Usangu Rift shows a T - shape (almost perpendicular) to the Rukwa-Malawi Rift (Fig. 3.10A). Within the Rungwe Volcanic Province the major low - relief volcanic crater (maars) such as Ngozi and Rungwe were mapped and they occur towards the centre of the radial patterns (Fig. 3.10B). Both the Rungwe and Ngozi crater show collinearity with the strike of the Rukwa-Malawi Rift and the Masoko maar occurs in the hanging wall of the NW-trending Livingstone Fault (Fig. 3.10B).

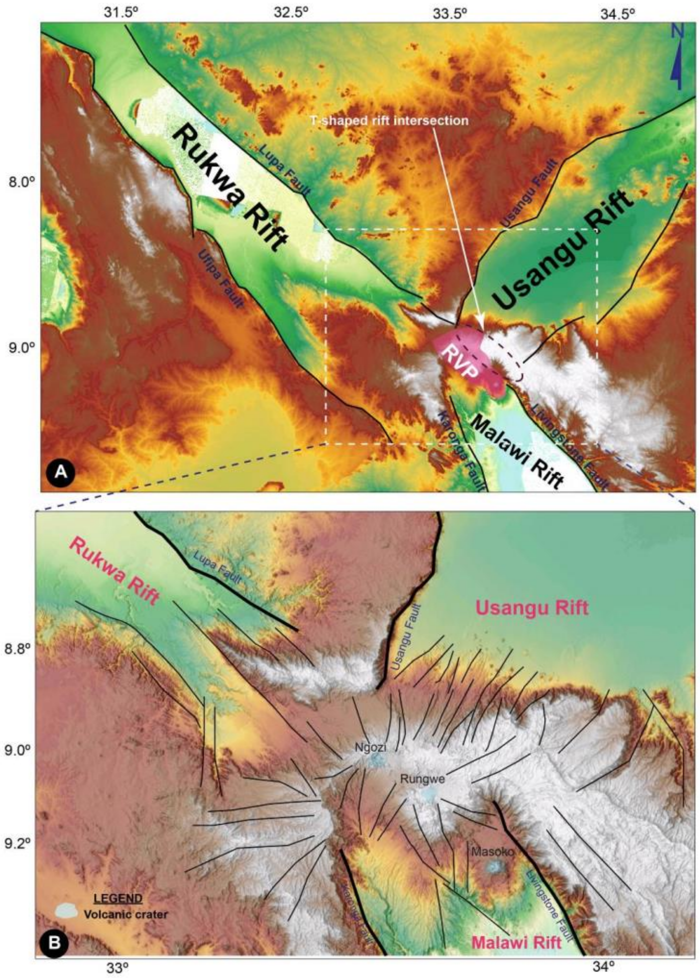

Fig. 3.10. Interpreted fault structures superimposed on (A) colour coded TanDEM- X 90m showing major rifts and border faults intersecting at the Rungwe Volcanic Province (RVP) in the south of the East African Rift System. Note the T-shaped intersection of the Usangu Rift/border faults on the Rukwa-Malawi Rift. (B) Colour-coded hill shade map derived from TanDEM-X 90m data showing fault pattern radiating from the Ngozi and Rungwe volcanic crater while the Masoko maar occurs in the hanging wall of the Livingstone Fault.

3.4.5 Uplift, erosion and unconformity records in the RRB

Seismic stratigraphic records for the Rukwa Rift provide evidence for a number of uplift events. The uplifts events triggered erosion leading to several unconformities, all recorded within the synrift sedimentary packages. Notably, our data reveal a topographic basement high and erosional surface in the west of the RRB adjacent to the Kwera transfer fault (Fig. 3.11B-C). The evidence for uplift formed the erosional surfaces observed on top of the Precambrian basement where Karoo Supergroup is truncated while the Red Sandstone is characterized by significant reduction in stratal thickness and a strong amplitude response over the basement high (Fig. 3.11B). Most likely the stratal truncation reflects the unconformity (Top Karoo Unconformity) which marks the end of the Karoo rifting and sedimentation between the Late Permian and the Early Triassic (Fig. 3.11B). These unconformities form the prominent high amplitude signals including Paleozoic (Top crystalline basement unconformity and Guadalupian hiatus); Mesozoic (Top Karoo unconformity) and Cenozoic (Top Namba and Top Songwe unconformity) that define the stratigraphic section (Mtelela, 2016; Mulaya et al., 2022).

The syn-kinematic record of the uplift events associated with growth fold structures were mapped in the southeast end of the RRB (Figs. 3.11A & C). These records are within the onlaps and stratal thinning that affect synrift sediment packages with the exception of the topmost Ilasilo Formation (Fig. 3.11A). The uppermost Ilasilo Formation displays a kinematic record of onlaps and thinning onto the uplift fold limbs. The synkinematic onlaps constrain key geometrical features of extensional folds associated with uplift kinematics during the Pleistocene (cf. Fig. 3.11A). The recent (Pleistocene) regional uplift observed in the Lake Beds sequences are marked by small-scale but widespread inversion structures (cf. Mulaya et al., 2022). The uplift due to this inversion phase is widely distributed in both northern and southern domains of the Rukwa Rift (cf. Mulaya et al., 2022).

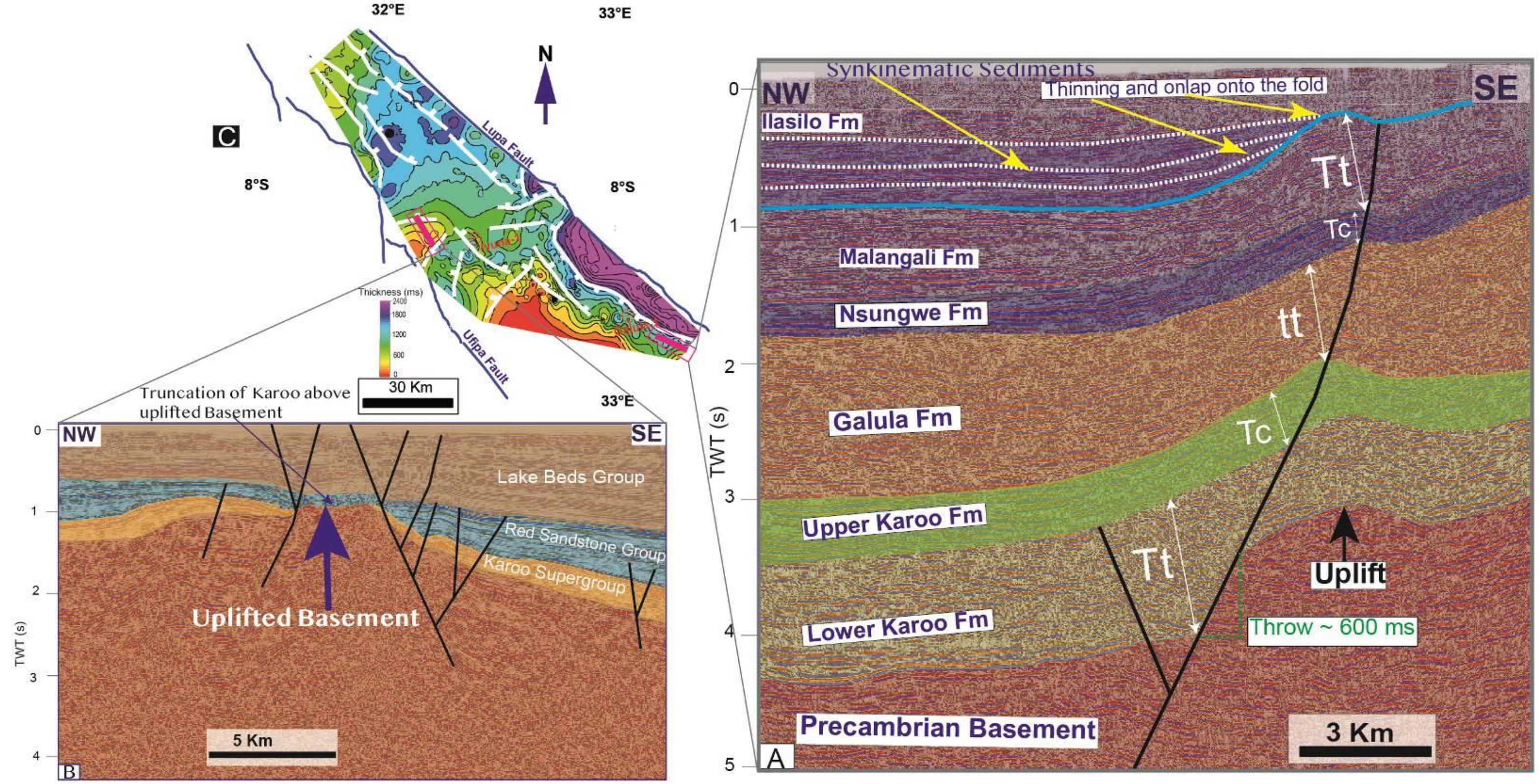

Fig. 3.11. (A) Interpreted seismic section showing the uplift of the whole synrift stratigraphy. The synrift strata alternate between constant thickness (Tc) (relative tectonic quiescence), thinning (tt) and thickening strata (Tt) towards the NW-dipping fault. Note the synkinematic sedimentation shown by intraformational onlaps in the Lake Beds sequences (Ilasilo Formation). (B) Interpreted seismic section illustrating the topographic basement high exhibiting significant thickness reduction of Red Sandstone Group and truncation of the Karoo Supergroup (after Mulaya et al., 2022) (C) time - thickness map for the Lake Beds Group superimposed with active faults showing the location of the seismic lines (see thick red lines) for part (A) and (B) above.

3.5.0 Discussion

3.5.1 Rift physiography and depocenter development

Although the general syn-depositional tectonics in the RRB reveal overall maximum sediment accumulation (~6000 ms TWT) was focused adjacent to the Lupa Fault throughout the basin history, this study reveals that multiple local depocenters were unevenly distributed in the rest of the basin and defined areas of accumulation minima and maxima (e.g. Figs. 3.5-3.7). The seismic data clearly show that the morphology of depocenters in the RRB were remarkably different during the Karoo times compared with the later Cretaceous and Cenozoic time (Figs. 3.5-3.7). Notably, the depocenters in Domain B were initially isolated during Karoo rifting (D1a-b), contiguous during Cretaceous (D2a-b) and finally linked into the main depocenter (D3a) during the later stages of rifting (Late Miocene-Pleistocene) with latest influence from the Rungwe Volcanic Province (Mtelela, 2016; Figs. 3.12A-C). Each depocenter in the RRB displays rift related structural patterns controlling its positioning and morphology owing to cyclicity of tectonic activity from the Late Palaeozoic to Late Cenozoic (Figs. 3.5-3.7; Fig. 3.12A-C; Fig. 3.13A-D). We propose that each depocenter initiation was largely triggered by the onset of normal faulting in response to extensional regimes with alternation of inversion phases associated with uplift, sedimentary loading, tilting and erosional events (e.g. Ge et al., 2020; Mulaya et al., 2022; Fig. 3.13A-D).

Our data reveal that sediment dispersal patterns confined in either isolated (D1a-b), contiguous (D2a-b) or a single main depocenter (D3a) between Karoo and post-Karoo times have implications for helium reservoir distribution (e.g. Jackson et al., 2010; Mulaya et al., 2022; Fig. 3.12A-C). The variation and changes of morphology for these depocenters correspond to different rifting phases (e.g. Fig. 3.13A-D). A change in a trend and morphology of depocenters (e.g. D1a-b, D2a-b and D3a-d) for each rifting phase reflects the spatial and temporal variation in fault activity which affected proportions of sediment concentration and distribution (e.g. Phillips et al., 2019; Fig. 3.12A-C). As a result, the depocenters were shifted progressively in space and time and accommodate sediment deposition (Fig. 3.13A-D). Notably, the synkinematic records during deposition of the Ilasilo Formation near depocenter D3a could imply initiation of confinement of this depocenter due to uplift and fault propagation during Plio-Pleistocene (Fig. 3.11A).

The separation of depocenters with relatively high physiography most likely were related to footwall uplift and grabens that formed during multiphase rifting hence modulating the deposition system and differential erosion in the RRB (Jackson et al., 2010; Figs. 3.11A-B; Fig. 3.13A-D). The development of topographic variations might have influenced the sediment routing (Gawthorpe and Hurst, 1993; Lambiase and Bosworth, 1995; Withjack et al., 2002; Mostafa et al., 2015; Paumard et al., 2020; Mulaya et al., 2022; Fig. 3.13A-D) and thus distribution of potential helium reservoir development in the RRB, i.e. the Karoo and Red Sandstone sequences (Danabalan et al., 2022; Mulaya et al., 2022). The physiographic variations overtime in the basin imply that the basin was subjected to different uplift, erosion, varying sediment sources and sediment accumulation rates during rifting phases modulated by the Saza and the Chisi shear zones (Mulaya et al., 2022; Fig. 3.13A-D). Provenance analysis from previous studies indicate several records of a shift in sedimentary provenance in the RRB from siliciclastic- to volcanoclastic-dominated facies (e.g. Mtelela, 2016; Roberts et al., 2012). Similarly, we infer that extension tectonics exerted significant control on the provenance, direction and location of drainage systems such that clastic sediments were derived most likely via erosion in tributaries that dissected Precambrian rocks that surround the RRB (Fig. 3.12A-D). Equally the Cenozoic volcanoclastic sequences in the Lake Beds Group indicate provenance from draining both rift shoulders and Rungwe volcanism with sediment routing most likely via relay ramps and border fault kinks, near the Saza and Kwera transfer faults (Mostafa et al.2015; Mulaya et al., 2022; Fig. 3.12A-D).

The spatial variation of structures which confine the depocenters along strike gives qualitative constraints on the variation of mechanical processes and rheological properties of lithospheric crust (e.g. Accardo et al., 2020; Fig. 3.12A-C). Differential uplift may have equally promoted differential erosion within the Rukwa Rift and the resulting pattern of topographic highs and lows would have led to lateral offset of depocenters (Fig. 3.12A-C). In addition, the spatial separation and connectivity of depocenters can be attributable to sedimentation rate changes and sediment over-filling (Mtelela, 2016; Phillips et al., 2019). We anticipate that the alternating sediment thickening and thinning versus constant thickness patterns within individual fault block, implies periodic alternation between active tectonics and quiescence during deposition of the Upper Karoo and Malangali Formations (Fig. 3.11A).

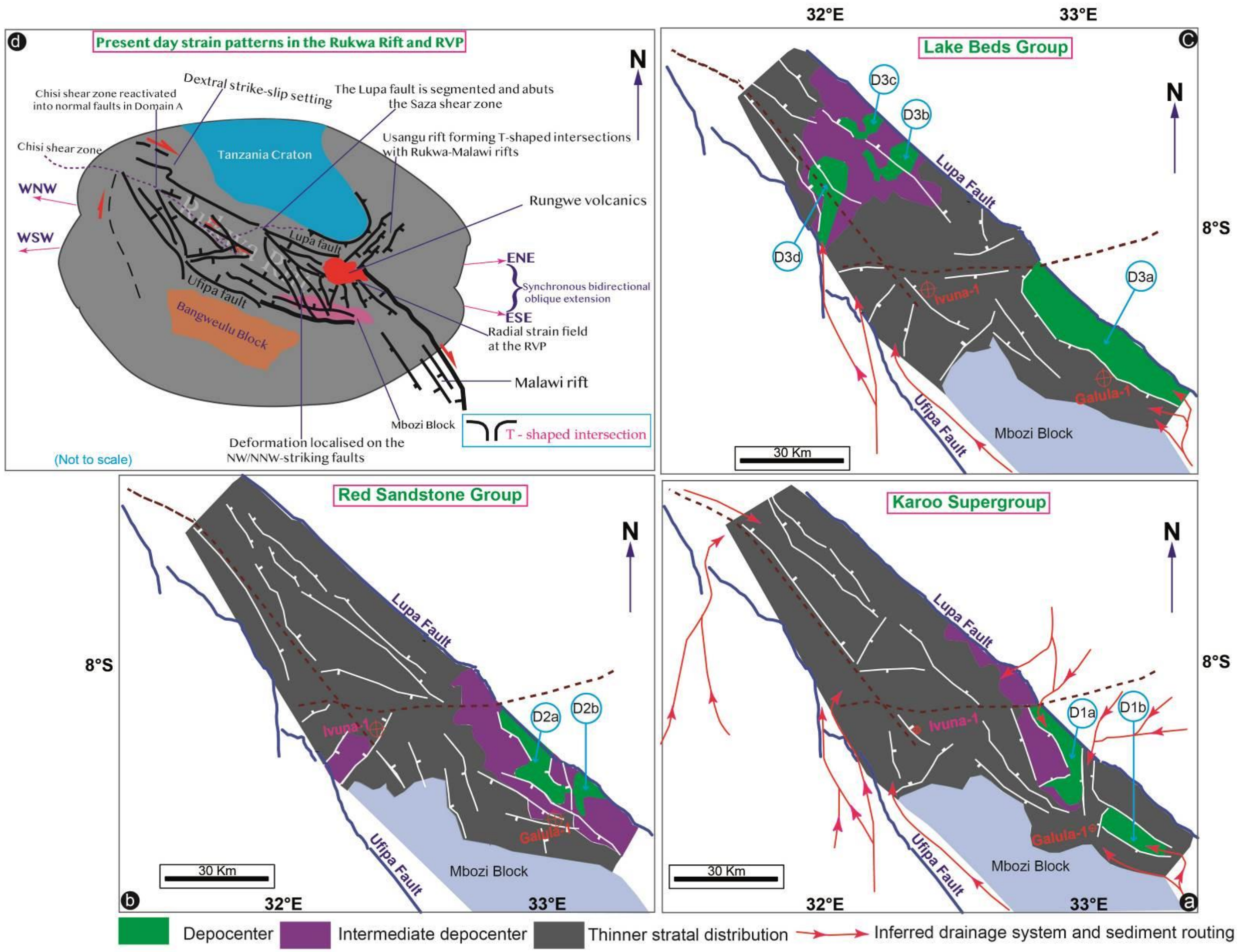

Fig. 3.12. (a) Schematic models showing depocenter evolution i.e. two isolated depocenters during Karoo rifting (indicated as D1a and D1b) bounded with N - S to NW - SE striking faults in Domain B. (b) Interpreted depocenter morphology showing contiguous depocenters (D2a and D2b) restricted to the southeast end of the basin in Domain B. (c) Interpreted depocenter morphology

revealing one main depocenter (D3a) bounded by the Lupa Fault and curvilinear fault (plan view) in Domain B during the Cenozoic time. Note multiple depocenters (D3b, D3c and D3d) ~5 km wide northwest of the basin. (d) 2D- strain model summarizing the present-day strain patterns controlling the sedimentary distribution in the RRB that is, extension dominated normal faults; shear zones and radial strain field at the RVP. Note the Usangu Rift might have preferentially produced T-shaped intersections with the Malawi-Rukwa Rift most likely related to uplift of the Rungwe during Pleistocene. The drainage systems are inferred based on previous provenance analysis and sedimentological studies (Mtelela, 2016; Roberts et al., 2010).

3.5.2 Helium reservoir quality

Our study reveals highly porous and permeable sandstone sequences that are suitable for helium accumulations. However, the validity of these petrophysical parameters of outcrop samples is questionable since the pressure, temperature and diagenetic conditions may change with depth. Nevertheless, we infer that extremely high porosity c. 26 - 30% and permeability c. 272.7 - 660.6 mD in the Karoo and Galula formations may be due to diagenesis (Figs. 3.8 & 3.9; Table 3.1). Other factor may include early helium charging into pores that preserved the primary porosity leading to less cementation in the reservoirs (Gluyas et al., 1993; Zhao et al., 2019). Similar to previous lithological logging, petrographic and field studies (e.g. Roe et al., 1996; Mtelela et al., 2017; Roberts et al., 2010), petrophysical results in this study indicates clear evidence that confirms the presence of less porous and impermeable tuffaceous mudstone and volcanoclastic sandstone that could be potential seal rocks (Fig. 3.8 & 3.9; Table 3.1). The presence of these elements plays a crucial role in trap structures and cap rocks for helium preservation in reservoirs. However, it is noteworthy that high-quality reservoirs are not always a favourable condition for the economical helium accumulations. That is because the helium has the lowest atomic radius hence would likely escape from cap rock even for the lowest calculated permeability ranges reported here (0.4-3.2 mD) and also due to active tectonic activities in the RRB (Mulaya et al., 2022). The lowest permeability being 0.4 mD in the RRB means it might leak helium gas and thus the tuffaceous mudstone might be regarded as a poor cap rock ('tight rock'). Nevertheless, petrophysical parameters may be heterogeneous with a variable proportion of clay mineral content/types and variable pore throats that may attain the quality level of sealing to some degree and potentially impede fluid flows relative to reservoir rocks beneath as a propitious factor for the occurrence of economical helium accumulations (Zhao et al., 2019).

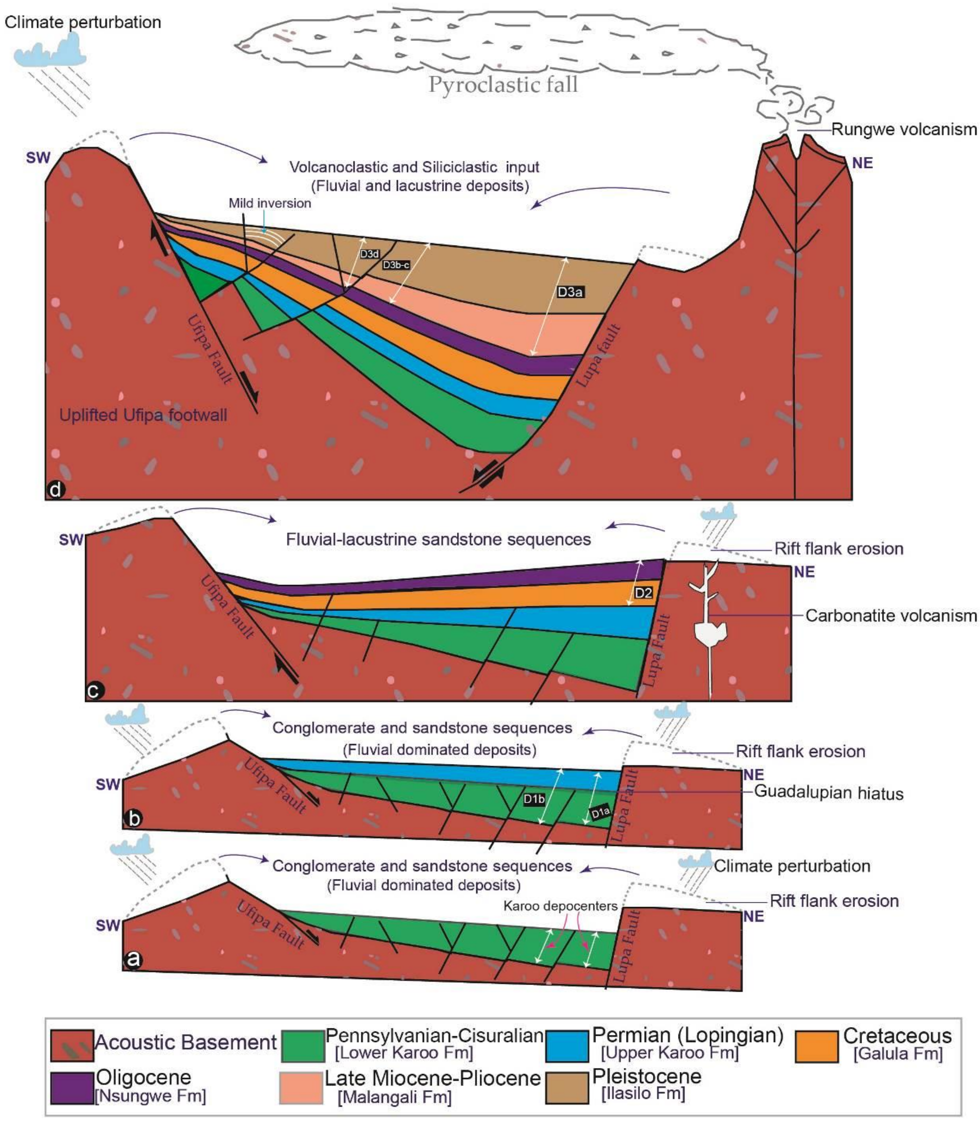

Fig. 3.13. Geological models illustrating the general tectonostratigraphic sequences, depocenter location (represented by white arrows and Ds) are potential reservoirs; (a) early Karoo rifting and depocenter positioning adjacent the Lupa Fault (Pennsylvanian-Cisuralian); (b) continued depocenter positioning (D1a, D1b) adjacent to the Lupa Fault and deposition of conglomerate and sandstone sequences (Lopingian); (c) gently-dipping fluvial-lacustrine sandstone sequences with a depocenter (D2) adjacent to the Lupa Fault (Cretaceous-Oligocene); (d) fluvial and lacustrine deposits influenced by intense Rungwe volcanism (Late Cenozoic). Modified after Mtelela. (2016), Roberts et al. (2010).

3.5.3 Strain controls on stratal dispersal

The main structural patterns interpreted from the time – thickness maps (calculated between Base Malangali and Top Ilasilo Formation) and the DEM reveal an ESE-WNW extension direction for the Rukwa Rift. This produced NW-SE striking faults that form one arm of a radial strain pattern centered at the RVP (Mulaya et al., 2022; Fig. 3.7A-B; Fig. 3.10A-B; Fig. 3.12D). These complex structural patterns control the whole sedimentary sequences in both Domain A and B in the RRB (Mulaya et al., 2022). The radial strain exhibited at the RVP perhaps accommodates simultaneous oblique extension in more than one direction, that is, synchronous bidirectional extension (e.g. Collanega et al., 2020) in the ENE-WSW and ESE-WNW (Figs. 3.10B & 3.12D). The strain patterns that influenced the depositional system and potential reservoirs in the RRB likely resulted from stress and kinematic interactions of the neighboring plate boundaries that is Nubia-Victoria-Rovuma-San plate boundaries (Saria et al., 2014; Lavayssière et al., 2019; Daly et al., 2020; Wedmore et al., 2021; Mulaya et al., 2022). Our local evidence for structural control on sediment distribution in the RRB is consistent with regional evidence provided by previous work (Daly et al., 1989; Ebinger et al., 1989; Theunissen et al., 1996; Delvaux et al., 1992; Morley et al., 1999; Boniface, 2009; Fritz et al., 2013). We propose that the most recent Usangu Rift intersections (T-shaped) with the Rukwa-Malawi rifts could have marked the development of a radial strain field at the Rungwe Volcanic Province most likely during the Pleistocene time hence forming the diagnostic features of synchronous bidirectional extension in the region (Collanega et al., 2020; Figs. 3.10A & 3.12D) rather than polyphase stress regimes and clockwise rotation suggested by Delvaux et al. (1992).

3.6.0 Conclusions

We present the following conclusions;

- The Rukwa Rift Basin comprises multiple local depocenters which thicken towards normal faults and are therefore inferred to have developed during active fault activities thus they provide insights into proportions of accommodation space and potential distribution of helium reservoirs from the Paleozoic to the Cenozoic Era.
- Depositional cycles in the RRB were interrupted by at least three erosional and uplift events leading to unconformities during the Paleozoic, Mesozoic and Cenozoic that are clearly preserved in the synrift strata.
- Anomalously high porosities and permeabilities in sandstones sequences of the RRB provide critical support for potential and commercial helium accumulations with a caveat that the other critical geological factors, such as viable top seals are in place.
- Multiple rifting phases in the RRB controlled the positioning of deposition systems and physiography resulting in areas of sediment accumulation minima and maxima which were modulated by shear zones and fault activity throughout the basin history.
- The depocenters to the south of the Saza shear zone (Domain B) were initially isolated during Karoo rifting, contiguous during Cretaceous and finally linked into a single main depocenter during the latter stages of rifting (Late Miocene-Pleistocene) when the Rungwe volcanics became the dominant influence.

Acknowledgements

The authors would like to thank the Tanzania Petroleum Development Corporation (TPDC) for providing and allowing us to use the seismic dataset. The United Kingdom Commonwealth Scholarship Commission is thanked for funding this study. **European Aid/135375/L/Act/Tz** is thanked for partly funding the petrophysical analysis at the University of Aberdeen in 2017.

References

Accardo, N.J., Gaherty, J.B., Shillington, D.J., Hopper, E., Nyblade, A.A., Ebinger, C.J., Scholz, C.A., Chindandali, P.R.N., Wambura-Ferdinand, R., Mbogoni, G. and Russell, J.B., 2020. Thermochemical modification of the upper mantle beneath the northern Malawi rift constrained from shear velocity imaging. *Geochemistry, Geophysics, Geosystems*, *21*(6), p.e2019GC008843.

Amoco Tanzania Oil Company., 1987. Final well completion report for Galula-1 and Ivuna-1 (Unpublished).

Avseth, P., Mukerji, T. and Mavko, G., 2010. Quantitative seismic interpretation: Applying rock physics tools to reduce interpretation risk. Cambridge university press.

Boniface, N., 2017. Crystal chemistry of pyrochlore from the Mesozoic Panda Hill carbonatite deposit, western Tanzania. *Journal of African Earth Sciences*, *126*, pp.33-44. https://doi.org/10.1016/j.jafrearsci.2016.11.026.

Boniface, N., 2009. Eburnian, Kibaran and Pan-African metamorphic events in the Ubendian belt of Tanzania: Petrology, zircon and monazite geochronology. PhD Thesis, Kiel University.

Chorowicz, Jean, 2005. "The East African rift system". Journal of African Earth Sciences. **43** (1): 379–410. https://doi.org/10.1016/j.jafrearsci.2005.07.019.

Collanega, L., Corti, G., Breda, A., Massironi, M. and Keir, D., 2020. 3D Extension at Plate Boundaries Accommodated by Interacting Fault Systems. *Scientific Reports*, *10*(1), pp.1-12.

Daly, M.C., Chorowicz, J., Fairhead, J.D., 1989. Rift basin evolution in Africa: the influence of reactivated steep basement shear zones. Geological Society, London, Special Publications 44, 309. https://doi.org/10.1144/GSL.SP.1989.044.01.17

Daly, M.C., Green, P., Watts, A.B., Davies, O., Chibesakunda, F. and Walker, R., 2020. Tectonics and landscape of the Central African Plateau and their implications for a propagating Southwestern Rift in Africa. *Geochemistry, Geophysics, Geosystems*, *21*(6), p.e2019GC008746.

Danabalan, D., 2017. Helium: Exploration Methodology for a Strategic Resource. PhD Thesis, Durham University.

Danabalan, D., Gluyas, J.G., Macpherson, C.G., Abraham-James, T.H., Bluett, J.J., Barry, P.H. and Ballentine, C.J., 2021. The principles of helium exploration. *Petroleum Geoscience*.

Delvaux, D., Levi, K., Kajara, R., & Sarota, J., 1992. Cenozoic paleostress and kinematic evolution of the Rukwa–North Malawi rift valley (East African Rift System). Bulletin des Centres de Recherche Exploration-Production ElfAquitaine, 16, 383–406.

Delvaux, D., 2001. Karoo rifting in western Tanzania: Precursor of Gondwana breakup. Contributions to geology and paleontology of Gondwana in honor of Helmut Wopfner: *Cologne, Geological Institute, University of Cologne*, pp.111-125.

Delvaux, D., Kervyn, F., Macheyeki, A. S., & Temu, E. B., 2012. Geodynamic significance of the TRM segment in the East African Rift (W-Tanzania): Active tectonics and paleostress in the Ufipa plateau and Rukwa basin. Journal of Structural Geology, 37, 161–180. https://doi.org/10.1016/j.jsg.2012.01.008

Dypvik, H., Nesteby, H., Ruden, F., Aagaard, P., Johansson, T., Msindai, J. and Massay, C., 1990. Upper paleozoic and Pesozoic sedimentation in the Rukwa-Tukuyu Region, Tanzania. *Journal of African Earth Sciences (and the Middle East)*, *11*(3-4), pp.437-456.

Ebinger, C.J., 1989. Tectonic development of the western branch of East African rift system. Geol. Soc. Am. Bull. 101, 885-903. https://doi.org/10.1130/0016-7606(1989)101%3C0885:TDOTWB%3E2.3.CO;2

Ebinger, C.J., Deino, A.L., Drake, R.E. and Tesha, A.L., 1989. Chronology of volcanism and rift basin propagation: Rungwe volcanic province, East Africa. *Journal of Geophysical Research: Solid Earth*, *94*(B11), pp.15785-15803. https://doi.org/10.1029/JB094iB11p15785

Farrell, N.J.C., Healy, D., Taylor, C.W., 2014. Anisotropy of permeability in faulted porous sandstones. J. Struct. Geol. 63, 50–67. https://doi.org/10.1016/j.jsg.2014.02.008.

Fritz, H., Abdelsalam, M., Ali, K. A., Bingen, B., Collins, A. S., Fowler, A. R., et al. (2013). Orogen styles in the East African Orogen: A review of the Neoproterozoic to Cambrian tectonic evolution. Journal of African Earth Sciences, 86, 65–106. https://doi.org/10.1016/j.jafrearsci.2013.06.004

Gawthorpe, R.L. and Hurst, J.M., 1993. Transfer zones in extensional basins: their structural style and influence on drainage development and stratigraphy. *Journal of the Geological Society*, *150*(6), pp.1137-1152. https://doi.org/10.1144/gsjgs.150.6.1137

Ge, Z., Gawthorpe, R.L., Rotevatn, A., Zijerveld, L., Jackson, C.A.L. and Oluboyo, A., 2020. Minibasin depocentre migration during diachronous salt welding, offshore Angola. *Basin Research*, *32*(5), pp.875-903.

Gluyas, J.G., Robinson, A.G., Emery, D., Grant, S,M. and Oxtoby, N.H. (1993) The link between petroleum emplacement and sandstone cementation In (Ed Parker, J.) Petroleum Geology of NW Europe (Proc. 4th Conference), 1395-1402

Gluyas, J.G. and Swarbrick, R.E., 2021. *Petroleum geoscience*. John Wiley & Sons.

Helium One (2019) Rukwa https://www.helium-one.com/rukwa/ accessed on 29 April 2022

Hilbert-Wolf, H., Roberts, E., Downie, B., Mtelela, C., Stevens, N.J. and O'Connor, P., 2017. Application of U–Pb detrital zircon geochronology to drill cuttings for age control in hydrocarbon exploration wells: A case study from the Rukwa Rift Basin, Tanzania. *AAPG Bulletin*, *101*(2), pp.143-159.

Jackson, C.A., Kane, K.E. and Larsen, E., 2010. Structural evolution of minibasins on the Utsira High, northern North Sea; implications for Jurassic sediment dispersal and reservoir distribution. *Petroleum Geoscience*, *16*(2), pp.105-120.

Harkin, D.A., 1960.The Rungwe volcanics at the northern end of Lake Nyasa. Memoir of the Geological Survey of Tanganyika, 11: 1-172.

Heilman, E., Kolawole, F., Atekwana, E. A., & Mayle, M., 2019. Controls of basement fabric on the linkage of rift segments. *Tectonics*, 38, 1337–1366. https://doi.org/10.1029/2018TC005362.

Katumwehe, A. B., Abdelsalam, M. G., & Atekwana, E. A. (2015). The role of pre-existing Precambrian structures in rift evolution: The Albertine and Rhino grabens, Uganda. Tectonophysics, 646, 117–129. https://doi.org/10.1016/j.tecto.2015.01.022

Kilembe, E. A., & Rosendahl, B. R. ,1992. Structure and stratigraphy of the Rukwa rift. *Tectonophysics*, *209*(1-4), 143-158.

Kolawole, F., Phillips, T.B., Atekwana, E.A. and Jackson, C.A., 2021. Structural inheritance controls strain distribution during early continental rifting, rukwa rift.

Lavayssière, A., Drooff, C., Ebinger, C., Gallacher, R., Illsley-Kemp, F., Oliva, S.J. and Keir, D., 2019. Depth extent and kinematics of faulting in the southern Tanganyika rift, Africa. *Tectonics*, *38*(3), pp.842-862.

Lambiase, J.J. and Bosworth, W., 1995. Structural controls on sedimentation in continental rifts. *Geological Society, London, Special Publications*, *80*(1), pp.117-144. https://doi.org/10.1144/GSL.SP.1995.080.01.06

Lemna, O. S., Stephenson, R., & Cornwell, D. G. (2019). The role of pre-existing Precambrian structures in the development of Rukwa Rift Basin, southwest Tanzania. Journal of African Earth Sciences, 150, 607–625. https://doi.org/10.1016/j.jafrearsci.2018.09.015

Lenhardt, N. and Götz, A.E., 2011. Volcanic settings and their reservoir potential: An outcrop analog study on the Miocene Tepoztlán Formation, Central Mexico. *Journal of Volcanology and Geothermal Research*, *204*(1-4), pp.66-75.

Lenoir, J.L., Liégeois, J.P., Theunissen, K. and Klerkx, J., 1994. The Palaeoproterozoic Ubendian shear belt in Tanzania: geochronology and structure. *Journal of African Earth Sciences*, *19*(3), pp.169-184.

Morley, C. K., R. M. Harper and S. T. Wigger., 1999. Tectonic Inversion in East Africa, in C. K. Morley ed., Geoscience of Rift Systems – Evolution of East African Rift System: AAPG studies in Geology No. 44, p. 193-210.

Morley, C.K., Cunningham, S.M., Harper, R.M. and Wescott, W.A., 1992. Geology and geophysics of the Rukwa rift, East Africa. *Tectonics*, *11*(1), pp.69-81.

Morley, C.K., 1989, Extension, detachments, and sedimentation in continental rifts (with particular reference to East Africa): Tectonics, v. 8, p. 1175–1192.

Mostafa, A., Sehim, A. & Yousef, M. 2015. Unlocking subtle hydrocarbon plays through 3D seismic and well control: A case study from West Gebel El Zeit district, southwest Gulf of Suez, Egypt. Paper presented at the 12th Offshore Mediterranean Conference and Exhibition, March 25–27, Ravenna, Italy.

Mbede, E.I., 1993. Tectonic development of the Rukwa Rift basin in SW Tanzania (Vol. 152). Fachber. Geowiss., TU Berlin.

Mortimer, E., Paton, D.A., Scholz, C.A., Strecker, M.R. and Blisniuk, P., 2007. Orthogonal to oblique rifting: effect of rift basin orientation in the evolution of the North basin, Malawi Rift, East Africa. *Basin Research*, *19*(3), pp.393-407. https://doi.org/10.1111/j.1365-2117.2007.00332.x

Mtelela, C., Roberts, E.M., Hilbert-Wolf, H.L., Downie, R., Hendrix, M.S., O'Connor, P.M. and Stevens, N.J., 2017. Sedimentology and paleoenvironments of a new fossiliferous late Miocene-Pliocene sedimentary succession in the Rukwa Rift Basin, Tanzania. *Journal of African Earth Sciences*, *129*, pp.260-281.

Mtelela, C. (2016). Sedimentology and stratigraphy of the late Cenozoic lake beds succession, Rukwa Rift Basin, Tanzania: implications for hydrocarbon prospectivity (Doctoral dissertation, James Cook University). https://researchonline.jcu.edu.au/47290/

Mtili, K.M., Byrne, D.J., Tyne, R.L., Kazimoto, E.O., Kimani, C.N., Kasanzu, C.H., Hillegonds, D.J., Ballentine, C.J. and Barry, P.H., 2021. The origin of high helium concentrations in the gas fields of southwestern Tanzania. *Chemical Geology*, *585*, p.120542.

Mulaya, E., Gluyas, J., McCaffrey, K., Phillips, T. and Ballentine, C., 2022. Structural geometry and evolution of the Rukwa Rift Basin, Tanzania: Implications for helium potential. *Basin Research*.

Nelson, R.A., Patton, T.L. and Morley, C.K., 1992. Rift-segment interaction and its relation to hydrocarbon exploration in continental rift systems (1). *AAPG bulletin*, *76*(8), pp.1153-1169. https://doi.org/10.1306/BDFF898E-1718-11D7-8645000102C1865D.

Paumard, V., Lang, S., Posamentier, H.W. and Wilson, M.E., 2020. On the value of seismic stratigraphy and seismic geomorphology–Comments on "development patterns of an isolated oligo-mesophotic carbonate buildup, early Miocene, Yadana field, offshore Myanmar" by Teillet et al.(2020). *Marine and Petroleum Geology*, *122*, p.104689.

Phillips, T.B., Fazlikhani, H., Gawthorpe, R.L., Fossen, H., Jackson, C.A.L., Bell, R.E., Faleide, J.I. and Rotevatn, A., 2019. The Influence of Structural Inheritance and Multiphase Extension on Rift Development, the Northern North Sea. *Tectonics*, *38*(12), pp.4099-4126.

Quenell, A.M., McKinlay, A.C. and Aitken, W.G., 1956. Summary of the geology of Tanganyika, part 1. *Geological Surv. Tanganyika Mem*, *126*.

Rizzoli, P., Martone, M., Gonzalez, C., Wecklich, TanDEM-X C., Tridon, D.B., Bräutigam, B., Bachmann, M., Schulze, D., Fritz, T., Huber, M. and Wessel, B., 2017. Generation and performance assessment of the global digital elevation model. *ISPRS Journal of Photogrammetry and Remote Sensing*, *132*, pp.119-139. https://elib.dlr.de/113892/

Roberts, E.M., O'Connor, P.M., Stevens, N.J., Gottfried, M.D., Jinnah, Z.A., Ngasala, S., Choh, A.M. and Armstrong, R.A., 2010. Sedimentology and depositional environments of the Red Sandstone Group, Rukwa Rift Basin, southwestern Tanzania: New insight into Cretaceous and Paleogene terrestrial ecosystems and tectonics in sub-equatorial Africa. *Journal of African Earth Sciences*, *57*(3), pp.179-212. https://doi.org/10.1016/j.jafrearsci.2009.09.002.

Rossetti, L.M., Healy, D., Hole, M.J., Millett, J.M., de Lima, E.F., Jerram, D.A. and Rossetti, M.M., 2019. Evaluating petrophysical properties of volcano-sedimentary sequences: A case study in the Paraná-Etendeka Large Igneous Province. *Marine and Petroleum Geology*, *102*, pp.638-656.

Rosendahl, B.R., Reynolds, D.J., Lorber, P.M., Burgess, C.F., McGill, J., Scott, D., Lambiase, J.J. and Derksen, S.J., 1986. Structural expressions of rifting: lessons from Lake Tanganyika, Africa. Geological Society, London, Special Publications, 25(1), pp.29-43.

Saria, E., Calais, E., Stamps, D. S., Delvaux, D., & Hartnady, C. J. H. , 2014. Present-day kinematics of the East African Rift. Journal of Geophysical Research: Solid Earth, 119, 3584–3600. https://doi.org/10.1002/2013JB010901.

Schlische, R.W., 1991. Half-graben basin filling models: new constraints on continental extensional basin development. *Basin Research*, *3*(3), pp.123-141. https://doi.org/10.1111/j.1365-2117.1991.tb00123.x

Stamps, D.S., Saria, E. and Kreemer, C., 2018. A geodetic strain rate model for the East African Rift System. *Scientific reports*, *8*(1), pp.1-9. DOI:10.1038/s41598-017-19097-w

Theunissen, K., Klerkx, J., Melnikov, A., & Mruma, A., 1996. Mechanisms of inheritance of rift faulting in the western branch of the East African Rift, Tanzania. *Tectonics*, *15*(4), 776-790. https://doi.org/10.1029/95TC03685

Wedmore, L.N., Biggs, J., Floyd, M., Fagereng, Å., Mdala, H., Chindandali, P., Williams, J.N. and Mphepo, F., 2021. Geodetic constraints on cratonic microplates and broad strain during rifting of thick Southern African lithosphere. *Geophysical Research Letters*, *48*(17), p.e2021GL093785. https://doi.org/10.1029/2021GL093785.

Wescott, W.A., W.N. Krebs, D.W. Englehardt, and S.M. Cunningham, 1991, New biostratigraphic age dates from the Lake Rukwa basin in western Tanzania: AAPG Bulletin, v.75, p. 1255–1263.

Wessel, B., 2016. TanDEM-X Ground Segment DEM Products Specification Document. Technical Note 3.1, German Aerospace Center (DLR). https://tandemx-science.dlr.de/

Wheeler, W.H. and Karson, J.A., 1994. Extension and subsidence adjacent to a" weak" continental transform: An example from the Rukwa Rift, East Africa. *Geology*, *22*(7), pp.625-628.

Widlansky, S.J., Clyde, W.C., O'connor, P.M., Roberts, E.M. and Stevens, N.J., 2018. Paleomagnetism of the Cretaceous Galula Formation and implications for vertebrate evolution. *Journal of African Earth Sciences*, *139*, pp.403-420.

Withjack, M.O., Schlische, R.W. and Olsen, P.E., 2002. Rift-basin structure and its influence on sedimentary systems. DOI: 10.2110/pec.02.73.0057.

Wopfner, H., 1993. Structural development of Tanzanian Karoo basins and the break-up of Gondwana. In *Gondwana symposium* (pp. 531-539).

Zhao, J.Z., Li, J., Wu, W.T., Cao, Q., Bai, Y.B. and Er, C., 2019. The petroleum system: a new classification scheme based on reservoir qualities. *Petroleum Science*, *16*(2), pp.229-251.

Zwaan, F., Schreurs, G., Naliboff, J. and Buiter, S.J., 2016. Insights into the effects of oblique extension on continental rift interaction from 3D analogue and numerical models. *Tectonophysics*, 693, pp.239-260. https://doi.org/10.1016/j.tecto.2016.02.036

Chapter 4: Heat flow as a catalyst for radiogenic helium release in the East Africa Rift System

(A manuscript to be submitted in the Chemical Geology Journal)

Heat flow as a catalyst for radiogenic helium release in the East Africa Rift System

Ernest Mulaya[1,2], Jon Gluyas[2], Ken McCaffrey[2], David Byrne[3], Chris Ballentine[4]

[1]School of Mines and Geosciences, University of Dar es Salaam, P.O. Box 35052, Dar es Salaam, Tanzania.

[2]Department of Earth Sciences, Durham University, Durham, UK, DH1 3LE.

[3]*Centre de Recherches P´etrographiques et G´eochimiques, UMR 7358 CNRS—Universit´e de Lorraine, BP 20, F-54501 Vandoeuvre-l`es-Nancy, France*

[4]Department of Earth Sciences, University of Oxford, Oxford, UK, OX1 3AN.

Abstract

The Rukwa Rift section of the East Africa Rift System presents a type setting for radiogenic helium accumulation in a petroleum free basin. As a prerequisite for accumulation, a considerable high heat flow anomaly is required from tectonothermal events to drive the release and circulation of radiogenic helium in the continental crust. Here we apply statistical analysis on geochemical data observed in thermal springs and recorded heat flow to account for crustal helium mass balance for each tectonothermal event in the region.

Our results demonstrate anomalously high heat flow ~64-99 mW/m^2 with a consistent trend of helium isotopic ratio and fluid chemistry in the Rukwa Rift. Mass balance calculation show that the whole crustal volume underlying the East Africa Helium Pool (EAHP) has a capability of producing radiogenic helium of about ∽9.9 x 10^6 mol/yr (∽22 x 10^{-6} mol ^{4}He/m^2 yr) while the total radiogenic helium flux ranges between ∽2.39 x 10^{6}mol/yr and ∽2.68 x 10^9 mol/yr. The Tanzania Craton contributes largely to radiogenic helium releasing up to 50% of the total capacity in the region. The total ^{4}He emission in the Rukwa Rift Basin is about ∽4.45 x 10^5 - 5.01 x 10^8 mol/yr which is thus equivalent to 19-21% of the total production capacity in the region. We suggest that the helium accumulation in the EAHP would have started as early as Palaeproterozoic (2.349 Ga). However, subsequent release has been accelerated

largely by tectonic and volcanic events associated with high heat flow. These results provide a qualitative and quantitative insight to assess both helium and geothermal potentiality in the region.

4.1.0 Introduction

Global supplies of helium have to date been produced as a by-product from natural gas fields. Almost all natural gas accumulations contain traces of helium albeit with different origins i.e. organic (natural gas) versus radiogenic/primordial sources (helium) (Ballentine and Lollar, 2002; Danabalan, 2017; Gluyas, 2019; Danabalan et al., 2022). Despite the serendipitous discovery of helium in giant natural gas provinces e.g. US Mid-west, Canada, Poland, Qatar, Algeria and Australia, the Rukwa Rift Basin (RRB) in the Tanzanian section of the East African Rift System (EARS) presents a rare end-member; a petroleum-free play of radiogenic helium (Gluyas, 2019; Danabalan et al., 2022). The radiogenic helium flux in the Rukwa Rift segments which include the Rukwa Rift Basin (RRB) and the Rungwe Volcanic Province (RVP) is associated with thermal springs along with nitrogen, carbon dioxide and other noble gases (Barry et al., 2013; Danabalan, 2017; Danabalan et al., 2022).

Previous work on the isotopic ratios and gas chemistry from the RRB provide important clues that suggest a binary mixing and degassing model from both mantle and crustal origins (e.g. Barry et al., 2013; Danabalan, 2017; Mtili et al., 2021; Kimani et al., 2021 Danabalan et al., 2022). However, like many other active extensional tectonic regions, the RRB shows a wide range of flux rate and chemical variability associated with potentially high thermal anomalies (Lowenstern et al., 2014; Danabalan et al., 2022; Didas et al., 2022). Although the release of crustal helium depends largely on thermal conditions (e.g. Danabalan et al., 2022), the distribution of the heat flow anomaly in relation to the helium potential in the RRB remains poorly understood.

In this contribution we quantify the mass balance between ^{4}He efflux and production potential of each particular tectonic setting/terrane in the region which we name the East Africa Helium Pool (EAHP) (Fig. 4.1a-b). We account for ^{4}He production capacity of crustal volumes and flux rate through concentrations observed in thermal springs from previous studies in the RRB (e.g. Barry et al., 2013; Lee et al., 2016; Mtili et al., 2021). The calculations assume that each tectonothermal event recorded in the RRB was associated with a heat flow surge (e.g. Torgersen, 2010; Lowenstern et al., 2014). This study provides insights into the timescale of helium production, release and a possible timing of accumulation surge triggered by heat flow anomaly.

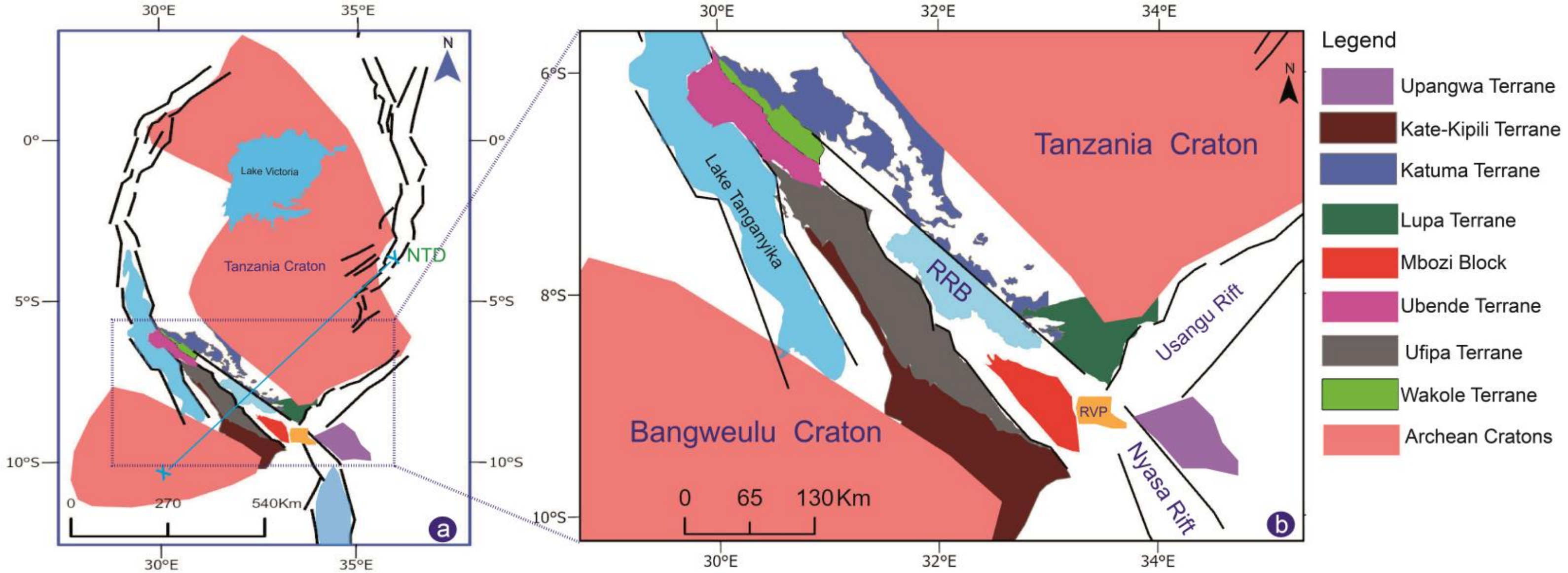

Fig. 4.1 (a) Map showing tectonic terranes which we refer as East Africa Helium Pool (EAHP). (b) Map showing the tectonic terranes surrounding the Rukwa Rift within the Ubendian mobile belt. RRB=Rukwa Rift Basin, RVP=Rukwa Volcanic Province, NTD= North Tanzanian Divergence.

4.2.0 Geological background

4.2.1 Geology and tectonic settings

The tectonics setting and terranes that underlie the East Africa Helium Pool (EAHP) comprises the Tanzania Craton, the Bangweulu Craton and the Ubendian mobile belt (Fig. 4.1a-b). These terranes surround the RRB and influenced its development (Boniface, 2009; Boniface and Schenk, 2012; Fig. 4.1a-b). The Tanzania and Bangweulu cratons comprises mainly granitoids and metamorphic rocks such as granitic gneisses and migmatites (Andersen and Unrug, 1984; Manya and Maboko 2003).

The Ubendian mobile belt consists of uplifted Palaeoproterozoic rocks composed of amphiboles-granulite metamorphic facies (Boniface and Schenk, 2012; Fritz et al., 2013). The Ubendian mobile belt is divided into eight Palaeproterozoic terranes which include; Kate-Kipili, Mbozi, Katuma, Ufipa, Wakole, Ubende, Upangwa and Lupa terranes (Daly, 1988; Lenoir et al., 1994; Theunissen et al., 1996; Fig. 4.1a-b).

The EAHP behaves as a comprehensive closed system comprised of rocks which are rich in helium bearing minerals i.e. uranium and thorium bearing minerals with average crustal density and thickness of ∽2.7 g/cc and ∽42 km respectively (Adams et al, 1959; Burwash and Cumming, 1976; Chaki et al., 2008; René, 2017; Lavayssière, et al., 2019). The uranium concentration in both Tanzania and Bangweulu cratons is ∽18.7 ppm, which is 6-7 times, above the average concentration ∽2.8 ppm recorded over other Precambrian terranes (Manya et al., 2007; Mshiu and Maboko, 2012). The thorium concentrations are 5 times higher in the cratons (∽52.1 ppm) than in other Precambrian terranes (∽10.7 ppm) (Manya et al., 2007; Mshiu and Maboko, 2012).

4.2.2 Tectonothermal events

Several regional tectonothermal events have been previously mapped in the EAHP (e.g. Ebinger et al., 1989; Kilembe & Rosendahl, 1992; Mulaya et al., 2022). Notably, the orogenic event which led to the Ubendian mobile belt dates back to 500Ma

(Tanganyika Orogeny) which involved a collision between the Tanzania Craton and the Bangweulu Craton (Quennell et al., 1956; Lenoir et al., 1994; Boniface, 2009). At least three rifting episodes have been identified in the RRB and Rungwe Volcanic Province (RVP) including Karoo rifting (Late Carboniferous to Triassic), Cretaceous to Oligocene rifting and the Cenozoic rifting (Late Miocene to present) (Ebinger et al., 1989; Kilembe & Rosendahl, 1992; Ebinger and Sleep. 1998; Delveaux, 2001; Boniface, 2017; Mulaya et al., 2022). These events as in many other similar tectonic settings (e.g. Lowernstern 2014) are associated with rifting, orogeny and volcanic activity (Danabalan et al., 2022). All these events were likely associated with heat flow surges that can facilitate fluid mobilization and helium degassing in the active tectonic setting of the RRB (Lowernstern 2014; Danabalan et al., 2022).

4.3.0 Methodology

4.3.1 Defining a closed system for helium production and release

Geochemical and isotope data used in this study were compiled by James, 1967; Barry et al., 2013; Mtili et al., 2021; Kimani et al., 2021 and the mass balance computation (Table 4.1-4.2) follows methods described by Lowenstern et al. (2014). We use these data to compute for helium flux and production models by assuming a closed system where fluids interact mainly with rocks within the tectonic terranes surrounding the RRB (e.g. Lowenstern et al., 2014). We have named the closed system defined in this study as the East Africa Helium Pool (EAHP) (Fig. 4.1a-b) whose areas were calculated from ArcGIS Pro shapefiles (Table 4.1-4.2). The EAHP includes the Ubendian mobile belt ∽114000 km^2, the Bangweulu Craton ∽150000 km^2 (Andersen and Unrug. 1984) and the Tanzania Craton ∽350000 km^2 (Danabalan et al., 2022). The EAHP consist of all terranes which surround the RRB and once had tectonic affiliation with it during geological history (Fig. 4.1a-b).

The total calculated helium production rate per year for the whole EAHP is therefore referred as a Whole-Crust (WC) value against which all the helium fluxes in the system were balanced (Table 4.3). The mass balance computation is based on the fact that ^{4}He can accumulate over time within the EAHP whereas tectonic activity can facilitate degassing and circulation in the region (Ingebritsen and Manning, 2010; Lowenstern et al, 2014; Danabalan et al., 2022).

4.3.2 Statistical modeling of ^{4}He mass balance and heat flow anomaly

Two different cases for the helium flux model were considered for the selected closed system boundary (Table 4.1 & 4.2). The choice of parameters for the two cases is based on previously reported CO_2 flux estimates, of 4.05 and 0.0055 tonnes/day in areas sized 981.5 and 1500 km^2 respectively (Barry et al., 2013; Lee et al., 2016). Previously the lowest and highest end member of crustal and mantle Ra signatures have been reported as 0.02 Ra and 8.0 Ra respectively and hence these values were adopted in this study (Barry et al., 2013; Mtili et al., 2021; Danabalan et al., 2022).

Heat flow data were extracted from previous work by Morley et al. (1999), Njinju et al. (2019) and Didas et al. (2022). The few available isotopic ratios, heat flow and geochemical data from previous studies such as $CO_2/^3He$ and R/Ra (Morley et al., 1999; Barry et al., 2013; Danabalan, 2017; Njinju et al., 2019; Mtili et al., 2021 and Didas et al., 2022) were used for statistical interpolation across the RRB and RVP using ArcGIS Pro.

For the statistical interpolation in ArcGIS Pro, we applied the Inverse Distance Weighting (IDW) method (Geostatistical Analyst Tool) using the available isotope ratio (Ra), CO_2 flux and heat flow data as inputs (assuming output cell size ~0.01, power of ~2 and number of points up to 12) to produce raster images. From the raster images of Ra and $CO_2/^3He$ about 1000 random discrete points were created statistically where a number of random points depends on the resolution required to produce reliable neighbourhoods (Fig. 4.2). These random points surround various locations where data had been previously sampled/computed in the RRB and RVP

(Fig. 4.2). Finally, the cell values from the raster maps were extracted and statistically assigned to those 1000 random points using the Spatial Analyst Tools ('Extract values to points') to represent unique cell values for interpolated Ra and $CO_2/^3He$. The averages of interpolated cell values bounded by each tectonic terrane were used as inputs during mass balance computation (Table 4.1-4.2).

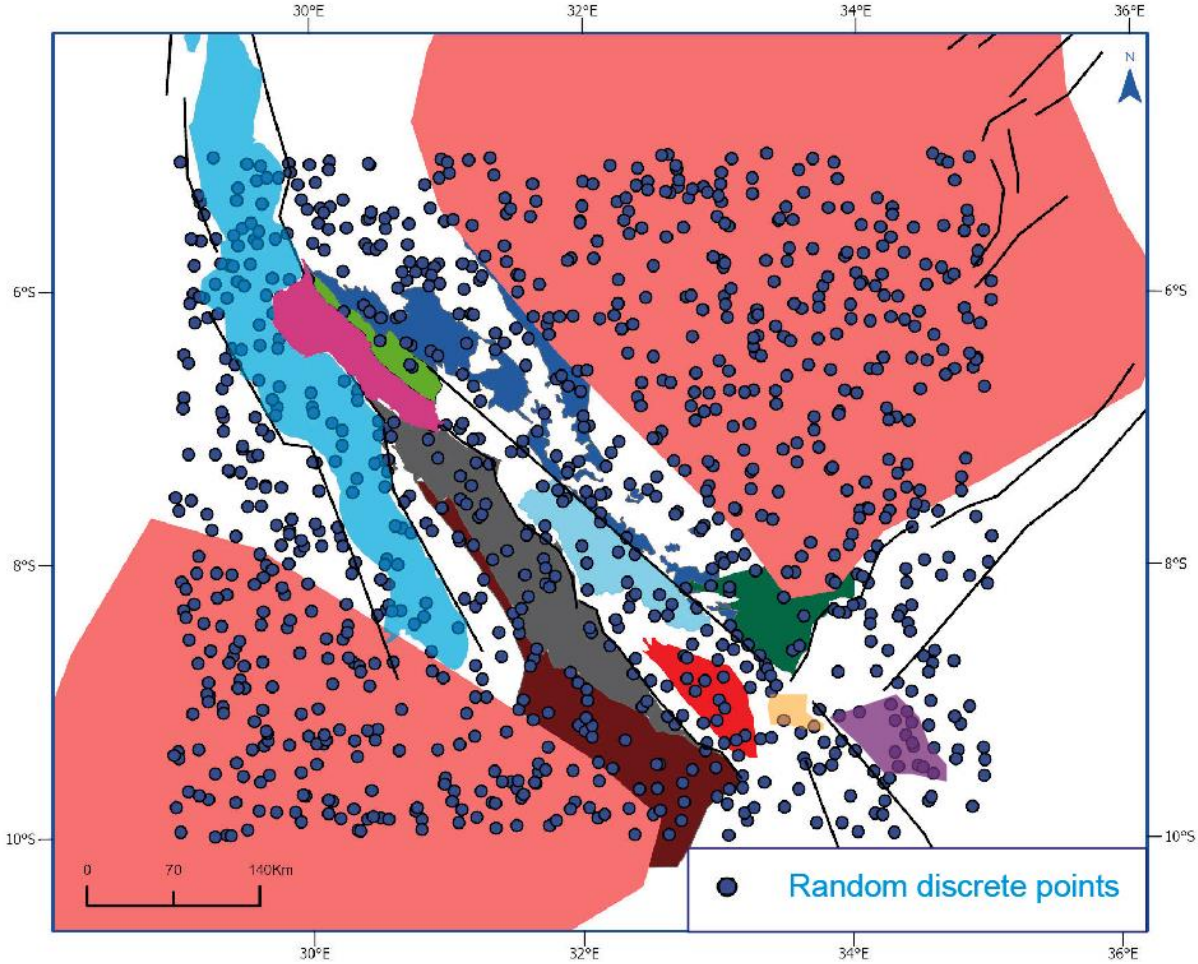

Fig. 4.2 Random discrete points (n=1000) created on which heat flow, $CO_2/^3He$ and $^3He/^4He$ data were interpolated over various tectonic terranes and averaged for use in mass computation and raster mapping (see Fig. 4.1 for legend).

4.4.0 Results

4.4.1 Heat flow distribution in the Rukwa Rift

The distribution of heat flow data in the Rukwa Rift shows a consistent trend i.e. along strike of the Rukwa Rift Basin (RRB) and the Rungwe Volcanic Province (RVP)

(Fig. 4.3a-b). In the RRB the heat flow ranges between 64 mW/m^2 and 86 mW/m^2 above the global average for Mid-Permian Provinces (Fig. 4.3a-b). The heat flow is higher in the Rungwe Volcanic Province up to 99 mW/m^2 and drops sharply towards the Rukwa Rift graben (minimum 64 mW/m^2) (Fig. 4.3a-b). Our model reveals that the heat flow anomaly coincides with changes in topography i.e. higher heat flow up to (99 mW/m^2) observed over the RVP highlands compared with the RRB graben with heat flow as low as ~64 mW/m^2 (Fig. 4.3a-b). Most of the high heat flow values are aligned with faults while others occur in accommodation zones (areas linking rift segments) and volcanically active area i.e. the RVP (Fig. 4.3a). The heat flow decreases significantly towards the distal areas from the RVP where the lowest heat flow up to ~32 mW/m^2 occurs in the Malawi Rift. Notably, further to the northeast of the Rukwa Rift, higher heat flow ~94 mW/m^2 is observed over the Lupa Terrane than any other tectonic terrane within the Ubendian mobile belt (Fig. 4.3a). The high heat flow over the Lupa Terrane is observed near the rift shoulder and horst blocks of both the Rukwa and Usangu rifts and decreases towards the distal areas (Fig. 4.3a).

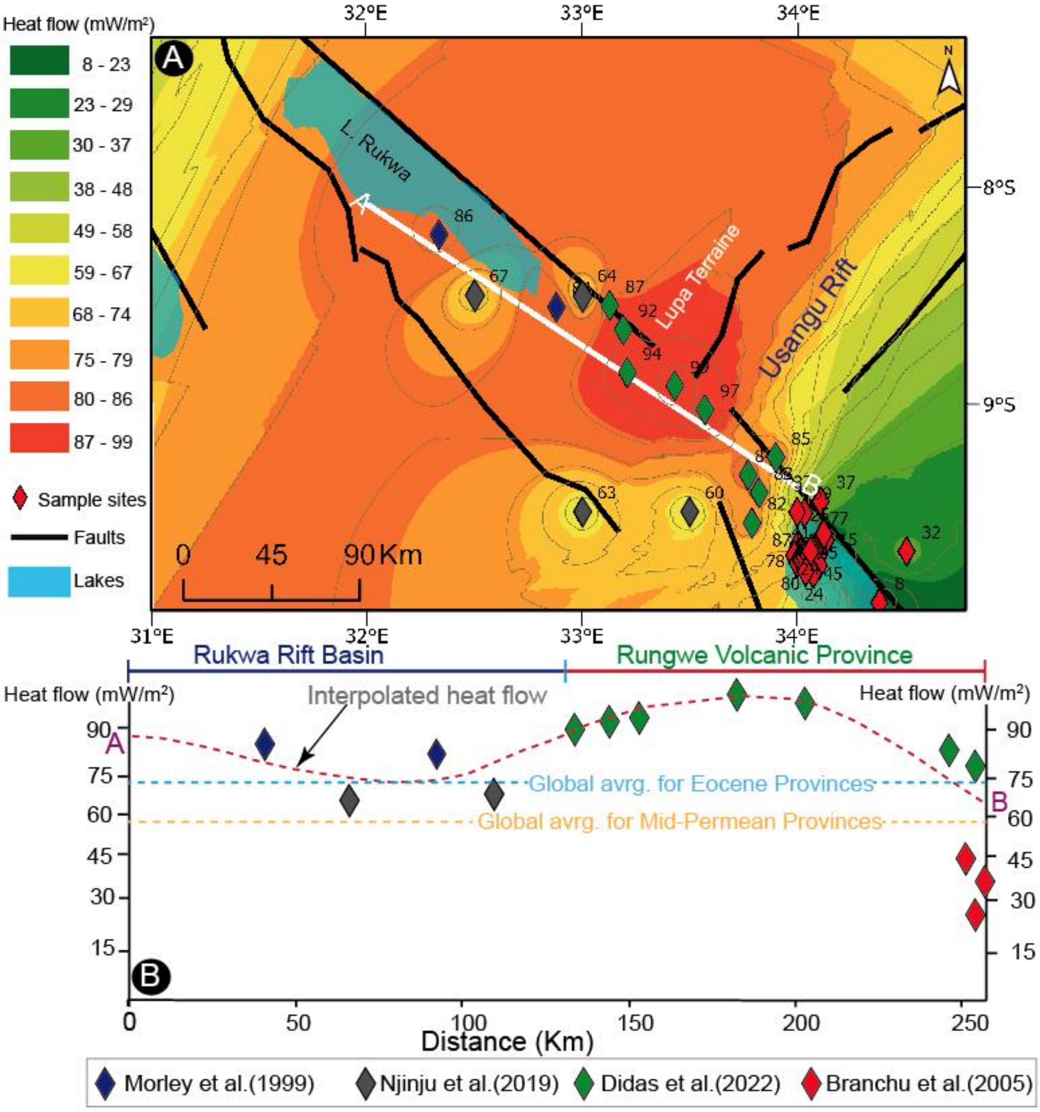

Fig. 4.3 (a) Map showing the distribution of heat flow between RRB and RVP generated from the statistical interpolation at various locations. (b) A profile showing distribution of heat flow values between the RRB and the RVP compared to the global mean heat flow for Mid-Permian and Eocene provinces (after Polyak and Smirnov, 1968; Chapman and Pollack, 1975; Njinju et al., 2019).

4.4.2 Relationship between heat flow and helium isotope ratio

The highest heat flow in the RVP (up to 99 mW/m^2) corresponds to the highest $^3He/^4He$ ratio (3.3-7.10) (Fig. 4.4a-b). In the RRB the lowest heat flow (64mW/m^2) is associated with the lowest $^3He/^4He$ ratio (0.18-0.68) (Fig. 4.4a-b). The changes in a trend of helium isotopic ratio coincide with the changes in topographic profile (Fig. 4.4a-d)

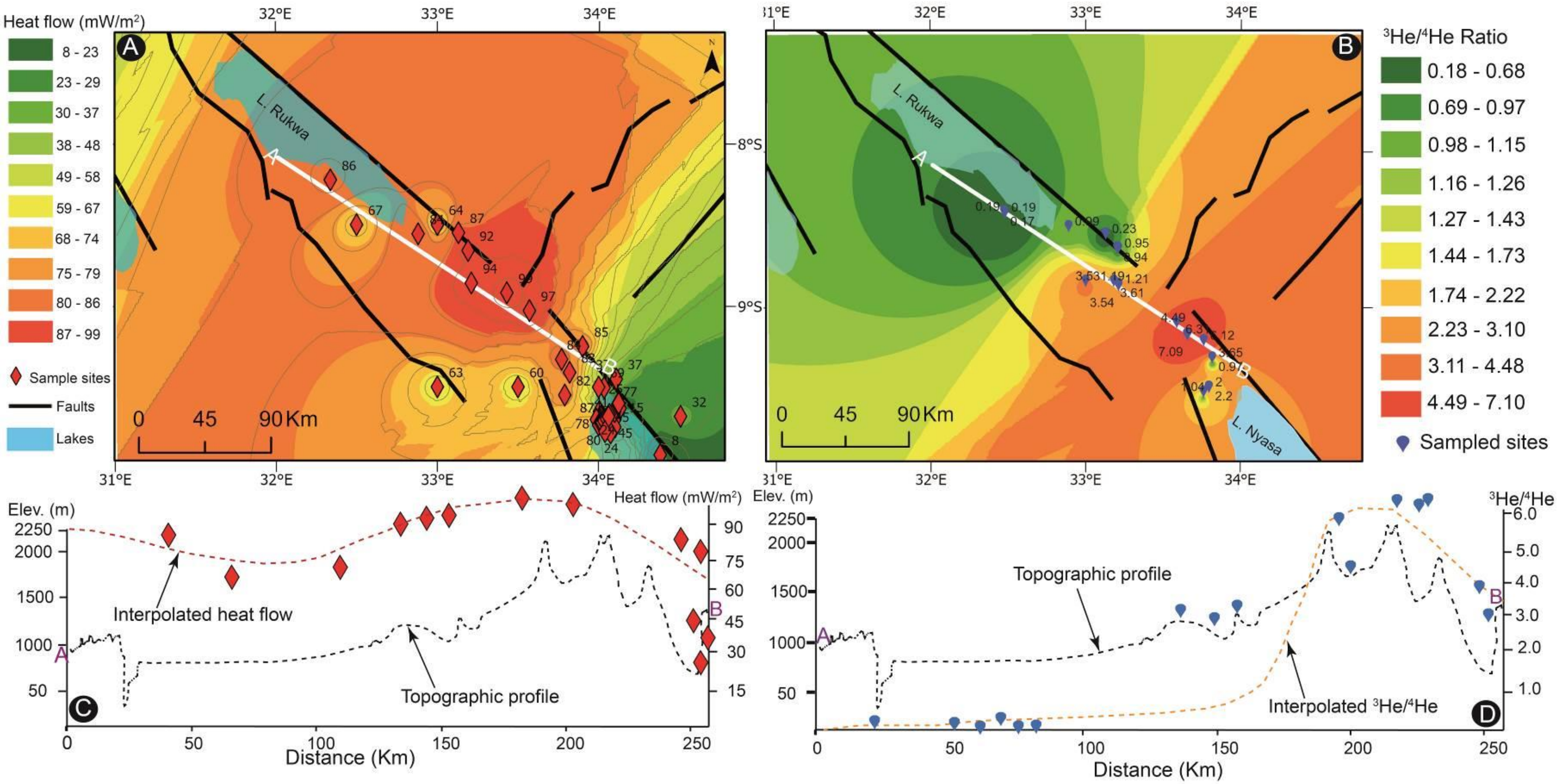

Fig. 4.4. (a) Interpolated heat flow map for the RVP and RRB. The diamond symbols show heat flow values that have been either tested or computed. (b) Raster map showing the distribution of ^{3}He/^{4}He ratios. Areas with available ^{3}He/^{4}He data are shown with blue drop symbols. (c) A profile across the southern part of the RRB and RVP showing distribution of interpolated heat flow against the topographic profile. (d) Section across the southern part of the RRB and RVP showing distribution of interpolated ^{3}He/^{4}He ratio against the topographic profile.

4.4.3 Relationship between heat flow and $CO_2/^3He$ ratio

The general trend of heat flow in relation to $CO_2/^3He$ shows the highest heat flow (~99 mW/m^2) occurring in the RVP characterized by the highest $CO_2/^3He$ (1.4 - 2.9 $x10^{13}$) (Fig. 4.5a-b). The RRB reveals the lowest heat flow (~64 mW/m^2) corresponding to the lowest $CO_2/^3He$ ($0.5x10^{10}$-1.0 $x10^{11}$) (Fig. 4.5a-b). Similar to helium isotopic ratio, the change in $CO_2/^3He$ along strike of the RRB and RVP show corresponding changes with topography (Fig. 4.5a-d; Fig. 4.6a-c).

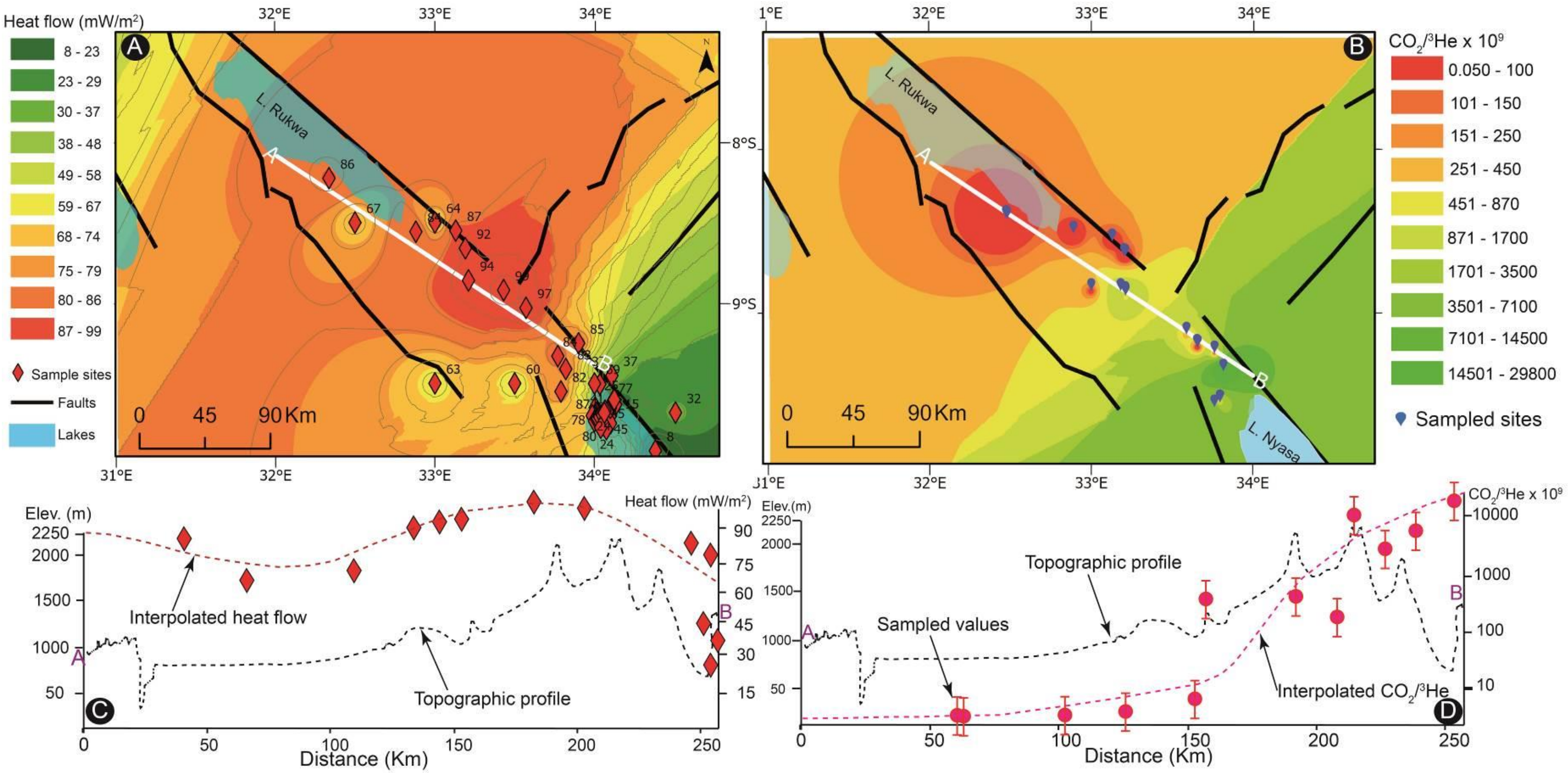

Fig. 4.5 (a) Interpolated heat flow map for the RVP and RRB. The diamond symbols show heat flow values where has been either tested or computed. (b) Raster map created from interpolation of available data to show the distribution of $CO_2/^3He$ ratios. Locations with available $CO_2/^3He$ data are shown with blue drop symbols. (c) A profile across the southern part of the RRB and RVP showing distribution of interpolated heat flow against the topographic profile. (d) A profile across the southern part of the RRB and RVP showing distribution of interpolated $CO_2/^3He$ ratio against the topographic profile.

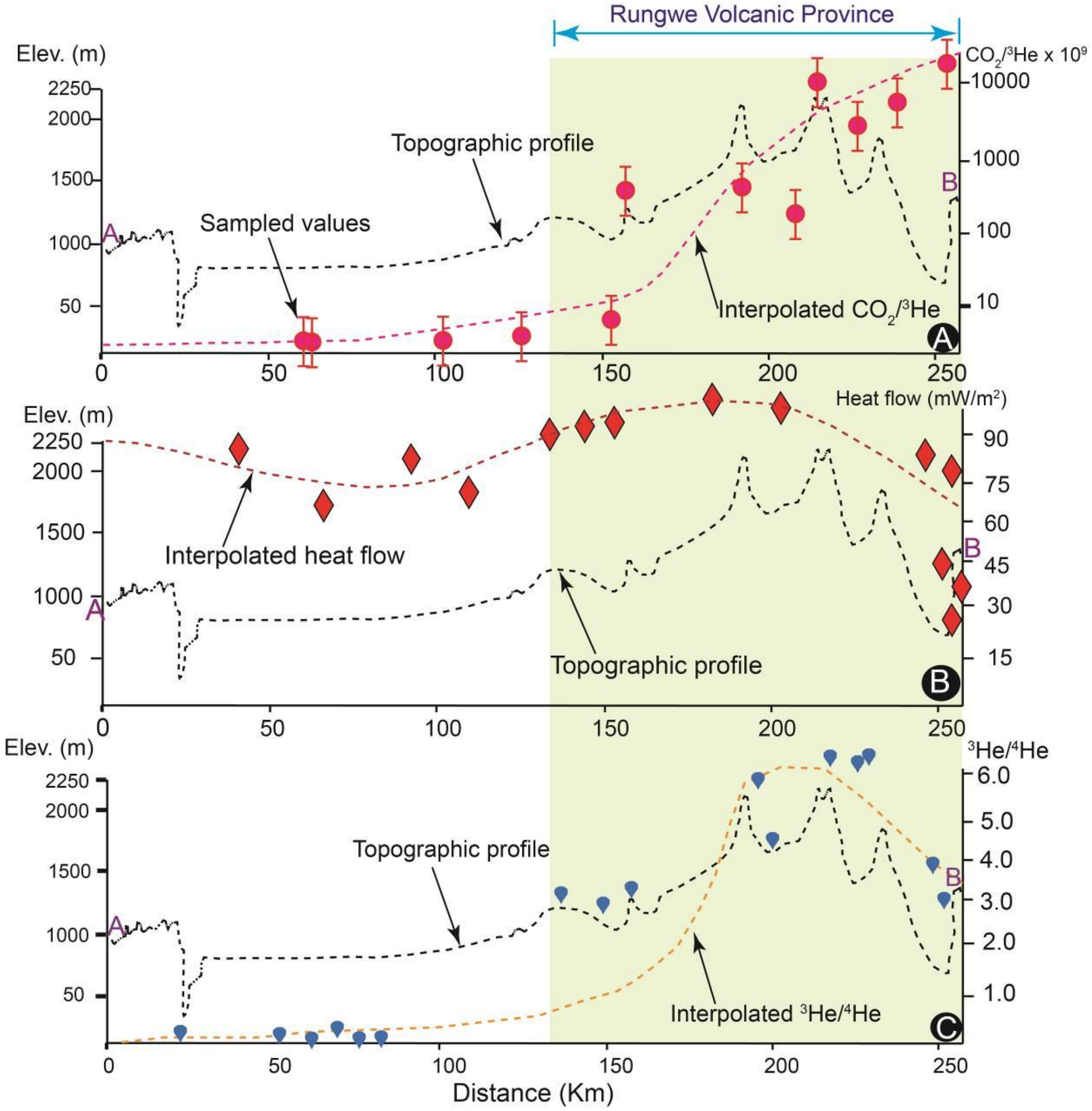

Fig. 4.6 Profile across the RVP and the southern part of the RRB showing distribution of (a) CO$_2$/^{3}He ratio against the topographic profile (b) heat flow against the topographic profile. (c) ^{3}He/^{4}He ratio against the topographic profile. (See Fig. 4.3a for location).

4.4.4 Heat flow anomaly and frequent seismicity in the region

Our observation shows that seismicity swarms occur in areas of high heat flow

(Fig. 4.7). Notably at the junction of border faults between the Rukwa Rift and Usangu Rift, frequent seismicity most likely revealing active tectonic activity and fault reactivation associated with thermal anomalies (Fig. 4.7).

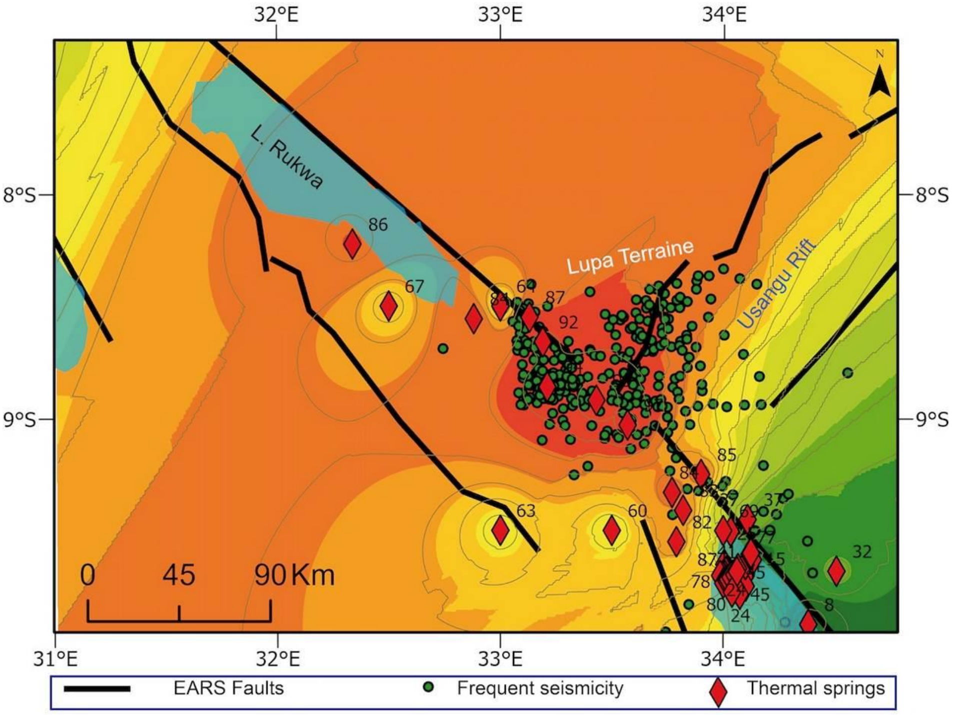

Fig. 4.7. Heat flow map overlain by the distribution of frequent seismicity recorded in the region. Note seismicity clusters occur at the junction between the Usangu Rift and Rukwa Rift.

4.4.5. Helium potential of the East Africa Helium Pool (EAHP)

Helium isotopic ratios (^{3}He/${}_{4}$He), expressed as Ra were interpolated as essential pre-computational values for use in mass balance calculation. The cratons with ~3 to 7 times the average crustal concentration of radioactive elements, have Ra distribution ranging between 1.3 Ra and 1.5 Ra (Table 4.1- 4.2). The RRB presents the lowest Ra ∽0.2 Ra in the system whereas, the Upangwa Terrane, Nyika Terrane and the RVP have the highest Ra ∽3.3- 3.7 Ra. The distribution of Ra in other terranes includes Ufipa ∽1.1 Ra, Ubende ∽1.2 Ra, Katuma ∽1.2 Ra, Wakole ∽1.2 Ra, Mbozi ∽2.6 Ra, Lupa ∽1.9 Ra and Kate Kipili ∽1.6 Ra (Table 4.1- 4.2).

Mass balance computation for degassing and production of radiogenic helium show that the whole 'East African Helium Pool' (EAHP) has a crustal mass of ∽7.0 x 10^{10} megatonnes which includes the Tanzania Craton, Bangweulu Craton and the Ubendian mobile belt (Table 4.3). The tectonic terranes and blocks surrounding the RRB are capable of producing at least 3.3 x 10^{-6} mol ^{4}He/m^2 yr (Table 4.3). In addition, both the Bangweulu and the Tanzania cratons can potentially produce 6 times more than other terranes in the Ubendian mobile belt (∽1.9 x 10^{-5} mol ^{4}He/m^2 yr) making a total helium production rate of at least 2.2 x 10^{-5} mol ^{4}He/m^2 yr in an area of ~614000 km^2 for the Whole-Crust (1WC) under the assumption of a closed system EAHP (Table 4.3).

4.4.5.1 Helium degassing: Case-I

Under this postulate we assume CO_2 flux of 4.05 tonnes/day over an areal extent ∽981.5 km^2 (Lee et al., 2016; Table 4.1). Feasible models under this postulate suggest a total crustal ^{4}He emission of ∽272WC from the EAHP (Table 4.1). The contribution of crustal ^{4}He emissions for each tectonic terrane include 124WC (46%) from the Tanzania Craton, 62WC (22%) from the Bangweulu Craton and 52WC (19%) from the crystalline basement of the RRB. The tectonic terranes in the whole Ubendian mobile belt constitute 36WC (13%) of the helium contribution in the region (EAHP) (Table 4.1).

Case-I shows total radiogenic helium flux ∽2.68 x 10^9 mol/yr in the EAHP with areal extent ∽614000 km^2 (∽4.4 x 10^{-3} mol ^{4}He/m^2 yr) (Table 4.1). Notably, in the RRB the calculated ^{4}He emissions reveal ∽5.01 x 10^8 mol/yr in an area of ∽8890 km^2 (∽5.6 x 10^{-2} mol ^{4}He/m^2 yr (Table 4.1). The ^{4}He emission in the RRB is thus equivalent to 19% of the total WC whereas in the RVP ∽1500 km^2, the ^{4}He emissions are lower ∽2.07 x 10^6 mol/yr (<1%) than in the RRB (Table 4.1).

4.4.5.2 Helium degassing: Case-II

This postulate assumes a CO_2 flux of 0.0055 tonnes/day over an areal extent ∽1500 km^2 (Barry et al., 2013) which results in a crustal helium flux ∽0.24WC (Table 4.2). Similar to Case-1 above, the Tanzania Craton contributes 46% of the crustal ^{4}He emission, Bangweulu Craton (21%), RVP (<1%), the underlying crystalline basement of the RRB (21%) and the Ubendian mobile belt (12%).

Total radiogenic helium flux in the EAHP under Case II results in up to ∽2.39 x 10^{6}mol/yr (∽3.9 x 10^{-6} mol ^{4}He/m^2 yr) (Table 4.2). Similar to Case-1, the calculated ^{4}He emissions under this case reveal ∽4.45 x 10^5 mol/yr from an area of ~8890 km^2 of the RRB (∽5.0 x 10^{-5} mol ^{4}He/m^2 yr). The radiogenic helium degassing in the RRB is thus equivalent to 21% of the WC. In the RVP, the helium emission is lower than in the RRB i.e. ∽1.84 x 10^3 mol/yr (∽1.23 x 10^{-6} mol ^{4}He/m^2 yr) equivalent to <1% (Table 4.2).

Table 4.1. Case-I: CO_2 and He flux for the various tectonic settings of the East Africa Helium Pool (EAHP)

Thermal area	Area (km^2)	QCO_2 (grams/day)	CO_2 (mol/yr)	CO_2/^{3}He	CO2/^{4}He	Q^{4}He (mol/yr)	R/Ra Mantle^2	R/Ra Local	^{3}He/^{4}He	$f_{crustal}$	q^{C}He (mol/yr)	WC	CO_2 Flux (Mt/ yr)	Area of flux	References
Rukwa Basin	8890	1.01E+11	8.34E+11	5.8E+09	1.6E+03	5.1E+08	8.00E+00	0.2	2.8E-07	9.8E-01	5.01E+08	51	4.05	981.5	Lee et al. (2016); Barry et al. (2013); Danabalan et al., 2022
RVP	1500	1.70E+10	1.41E+11	8.7E+09	4.0E+04	3.5E+06	8.00E+00	3.3	4.6E-06	5.9E-01	2.07E+06	0			Mtili et al. (2021); Barry et al. (2013); Danabalan et al., 2022
Ubende Terrane	5275	5.96E+10	4.95E+11	1.0E+10	1.7E+04	2.9E+07	8.00E+00	1.2	1.7E-06	8.5E-01	2.51E+07	3			Interpolation in ArcGIS Pro; Mtili et al. (2021)
Wakole Terrane	2045	2.31E+10	1.92E+11	9.9E+09	1.7E+04	1.2E+07	8.00E+00	1.2	1.7E-06	8.5E-01	9.81E+06	1			Interpolation in ArcGIS Pro; Mtili et al. (2021)
Ufipa Terrane	13978	1.58E+11	1.31E+12	9.2E+09	1.4E+04	9.2E+07	8.00E+00	1.1	1.5E-06	8.6E-01	7.96E+07	8			Interpolation in ArcGIS Pro; Mtili et al. (2021)
Lupa Terrane	6560	7.42E+10	6.15E+11	7.9E+09	2.1E+04	2.9E+07	8.00E+00	1.9	2.7E-06	7.6E-01	2.22E+07	2			Interpolation in ArcGIS Pro; Mtili et al. (2021)
Katuma Terrane	3883	4.39E+10	3.64E+11	9.6E+09	1.6E+04	2.3E+07	8.00E+00	1.2	1.7E-06	8.5E-01	1.93E+07	2			Interpolation in ArcGIS Pro; Mtili et al. (2021)
Upangwa Terrane	11081	1.25E+11	1.04E+12	2.3E+09	1.2E+04	8.7E+07	8.00E+00	3.7	5.2E-06	5.4E-01	4.68E+07	5			Interpolation in ArcGIS Pro; Mtili et al. (2021)
Mbozi Terrane	7887.5	8.92E+10	7.40E+11	2.2E+10	7.9E+04	9.4E+06	8.00E+00	2.6	3.6E-06	6.8E-01	6.34E+06	1			Interpolation in ArcGIS Pro; Mtili et al. (2021)
Kate-Kipili Terrane	42884.1	4.85E+11	4.02E+12	1.2E+10	2.6E+04	1.5E+08	8.00E+00	1.6	2.2E-06	8.0E-01	1.24E+08	13			Interpolation in ArcGIS Pro; Mtili et al. (2021)
Nyika Terrane	10310	1.17E+11	9.67E+11	6.4E+09	3.0E+04	3.2E+07	8.00E+00	3.4	4.8E-06	5.8E-01	1.83E+07	2			Interpolation in ArcGIS Pro; Mtili et al. (2021)

Bangweulu Craton	150000	1.70E+12	1.41E+13	1.1E+10	1.9E+04	7.2E+08	8.00E+00	1.3	1.8E-06	8.4E-01	6.08E+08	62	Interpolation in ArcGIS Pro; Mtili et al. (2021); Andersen and Unrug. (1984)
Tanzania Craton	350000	3.96E+12	3.28E+13	1.0E+10	2.2E+04	1.5E+09	8.00E+00	1.5	2.1E-06	8.1E-01	1.22E+09	124	Interpolation in ArcGIS Pro; Mtili et al. (2021)
Total	**614293.6**										**2.68E+09**	**272.06**	

Table 4.2. Case-II: CO_2 and He flux for the various tectonic settings of the East Africa Helium Pool (EAHP)

Thermal area	Area (km²)	QCO_2 (grams/day)	CO_2 (mol/yr)	$CO_2/^3He$	$CO2/^4He$	Q^4He (mol/yr)	R/Ra Mantle²	R/Ra Local	$^3He/^4He$	$f_{crustal}$	q^CHe (mol/yr)	WC	CO_2 Flux (Mt/yr)	Area of flux	References
Rukwa Basin	8890	8.93E+07	7.41E+08	5810147238	1.63E+03	4.55E+05	8.00E+00	0.2	0.00000028	9.77E-01	4.45E+05	0.05	0.0055	1500	Mtili et al. (2021); Barry et al. (2013); Danabalan et al. (2022)
RVP	1500	1.51E+07	1.25E+08	8669586054	4.01E+04	3.12E+03	8.00E+00	3.3	0.00000462	5.89E-01	1.84E+03	0.00			Mtili et al. (2021); Barry et al. (2013); Danabalan et al. (2022)
Ubende Terrane	5275	5.30E+07	4.39E+08	9983714962	1.68E+04	2.62E+04	8.00E+00	1.2	0.00000168	8.52E-01	2.23E+04	0.00			Interpolation in ArcGIS Pro; Mtili et al. (2021)
Wakole Terrane	2045	2.05E+07	1.70E+08	9913632768	1.67E+04	1.02E+04	8.00E+00	1.2	0.00000168	8.52E-01	8.72E+03	0.00			Interpolation in ArcGIS Pro; Mtili et al. (2021)
Ufipa Terrane	13978	1.40E+08	1.16E+09	9247200474	1.42E+04	8.18E+04	8.00E+00	1.1	0.00000154	8.65E-01	7.07E+04	0.01			Interpolation in ArcGIS Pro; Mtili et al. (2021)
Lupa Terrane	6560	6.59E+07	5.47E+08	7947573838	2.11E+04	2.59E+04	8.00E+00	1.9	0.00000266	7.64E-01	1.98E+04	0.00			Interpolation in ArcGIS Pro; Mtili et al. (2021)
Katuma Terrane	3883	3.90E+07	3.24E+08	9577752101	1.61E+04	2.01E+04	8.00E+00	1.2	0.00000168	8.52E-01	1.71E+04	0.00			Interpolation in ArcGIS Pro; Mtili et al. (2021)
Upangwa Terrane	11081	1.11E+08	9.23E+08	2310542513	1.20E+04	7.71E+04	8.00E+00	3.7	0.00000518	5.39E-01	4.16E+04	0.00			Interpolation in ArcGIS Pro; Mtili et al. (2021)
Mbozi Terranes	7887.5	7.92E+07	6.57E+08	21669463904	7.89E+04	8.33E+03	8.00E+00	2.6	0.00000364	6.77E-01	5.64E+03	0.00			Interpolation in ArcGIS Pro; Mtili et al. (2021)
Kate-Kipili Terrane	42884.1	4.31E+08	3.57E+09	11611227264	2.60E+04	1.37E+05	8.00E+00	1.6	0.00000224	8.02E-01	1.10E+05	0.01			Interpolation in ArcGIS Pro; Mtili et al. (2021)
Nyika Terrane	10310	1.04E+08	8.59E+08	6393470310	3.04E+04	2.82E+04	8.00E+00	3.4	0.00000476	5.76E-01	1.63E+04	0.00			Interpolation in ArcGIS Pro; Mtili et al. (2021)
Bangweulu Craton	150000	1.51E+09	1.25E+10	10672146767	1.94E+04	6.43E+05	8.00E+00	1.3	0.00000182	8.40E-01	5.40E+05	0.05			Interpolation in ArcGIS Pro; Mtili et al. (2021)

Tanzania Craton	350000	3.52E+09	2.92E+10	10415137036	2.19E+04	1.33E+06	8.00E+00	1.5	0.0000021	8.15E-01	1.09E+06	0.11	Interpolation in ArcGIS Pro; Mtili et al. (2021); Danabalan et al. (2022)
Total	**114293.6**										**2.39E+06**	**0.24**	

Table 4.3. Radiogenic helium production models

Location	**U Conc. (ppm)**	**Th Conc. (ppm)**	**J^4He Prod (atoms/g/yr)**	**Crustal ϱ g/cc**	**Total Area (cm^2)**	**Thickness (cm)**	**Mass (g)**	**Mass/NA (gmol)**	**Q^C4He (molyr^{-1})**	**References**
Cratons	18.7	52.1	1.0E+08	2.7	5.0E+15	4.2E+06	5.67E+22	9.4E-02	9.5E+06	Danabalan et al. (2022); Chaki et al. (2008); Lavayssière, et al. (2019)
Other terranes	2.8	10.7	1.7E+07	2.7	1.1E+15	4.2E+06	1.29609E+22	2.2E-02	3.7E+05	Manya et al. (2007); Mshiu and Maboko. (2012); Danabalan et al. (2022); Chaki et al. (2008); Lavayssière, et al. (2019)

Table 4.4. Postulate-I: Helium emissions and accumulation models for various tectonothermal events in the Rukwa Rift Basin.

Note the models highlighted in green show realistic cases.

CASE - I	Accumulation Time (Myr)	Initial Production (at least)
MODEL - I: Assuming similar 4He emissions were discharged since onset of East African rifting coeval with magmatism (8.6 Ma- Harkin, 1960; Ebinger, 1989) via the whole region	2.34E+03	2349 Palaeoproterozoic
MODEL - II: Assuming similar 4He emissions were discharged during the onset of East African rifting coeval with magmatism (8.6 Ma- Harkin, 1960; Ebinger, 1989) via only Rukwa Basin and RVP	4.E+02	409 Ma (Early Devonian)
MODEL - III: Assuming similar 4He emissions were discharged since onset of Karoo rifting via the whole region (Late Carboniferous 300 Ma-Delvaux, 2001)	8.16E+04	
MODEL - IV: Assuming similar 4He emissions were discharged since onset of Karoo rifting via the Rukwa Rift (Late Carboniferous 300 Ma-Delvaux, 2001)	1.52E+04	
MODEL - V: Assuming similar emissions were discharged since Cretaceous Carbonatite magmatism (120 Ma) via whole region	3.26E+04	
MODEL - VI: Assuming g similar emissions were discharged since Cretaceous Carbonatite magmatism (120 Ma) via Rukwa Rift	6.E+03	

Table 4.5. Postulate 2: Helium emissions and accumulation models for various tectonothermal events in the Rukwa Rift Basin

CASE - II	Accumulation Time (Myr)	Initial Production (at least)
MODEL - I: Assuming similar 4He emissions were discharged during onset of East African rifting coeval with magmatism (8.6 Ma- Harkin, 1960; Ebinger, 1989) via the whole region	2.08E+00	10.68 Ma (Miocene)
MODEL - II: Assuming similar ^{4}He emissions were discharged since onset of East African rifting coeval with magmatism (8.6 Ma- Harkin, 1960; Ebinger, 1989) via only Rukwa Basin and RVP	3.89E-01	389 Ka (Quaternary)
MODEL - III: Assuming similar 4He emissions were discharged since onset of Karoo rifting via the whole region (Late Carboniferous 300 Ma-Delvaux, 2001)	7.25E+01	372.5 Ma (Late Devonian)
MODEL - IV: Assuming similar ^{4}He emissions were discharged since onset of Karoo rifting via the Rukwa Rift (Late Carboniferous 300 Ma-Delvaux, 2001)	1.36E+01	313.6 Ma (Pennsylvanian)
MODEL - V: Assuming similar emissions were discharged since Cretaceous Carbonatite magmatism (120 Ma) via whole region	2.90E+01	149 Ma (Late Jurassic)
MODEL - VI: Assuming similar emissions were discharged since Cretaceous Carbonatite magmatism (120 Ma) via Rukwa Rift conduits	5.43E+00	125.43 Ma (Early Cretaceous)

4.4.6 Radiogenic residence time in the Rukwa Rift

Residence time are calculated using geochemical data, i.e. resolved radiogenic isotopes ^{4}He and ^{40}Ar from uranium and thorium that were quantitatively recovered from fluids by Danabalan et al. (2022), Mtili et al. (2021) and Kimani et al. (2021). The calculations assume that these daughter isotopes were produced in situ and accumulated within the hydrological closed system of the Rukwa Rift, i.e. the Rukwa Rift Basin and Rungwe Volcanic Province. Therefore, the residence time refers to the period since isolation of a daughter isotope and interaction with a hydrological system within either crystalline basement or overlying sedimentary units i.e. Ubendian Basement, Karoo Supergroup, Red Sandstone Group and Lake Beds Group.

We calculate the radiogenic noble gas concentration of noble gas per volume of water using Gas-Water ratios (Vg/Vw). The assumptions made for reference Air Saturated Water (ASW), initial pore fluid composition and salinity are adopted from Mtili et al., 2021. The ASW also assumes that the groundwater has undergone little or no changes i.e. phase separation since last equilibration with the atmosphere (Holland et al., 2013; Warr et al., 2018). We further assume that all radiogenic noble gases were produced in situ either within sedimentary settings or from the deeper crust of the Rukwa Rift and accumulated in the stratigraphic sequences controlled dominantly by vertical diffusive migration (cf. Holland et al., 2013; Cheng et al., 2021). For instance, at Ivuna mudpots locality the average Vg/Vw of 0.0075 shown in equation (1);

$$\frac{\mathrm{V_g}}{\mathrm{V_w}}(36_{\mathrm{Ar}}) = 0.0075\,. \tag{1}$$

This can be rewritten in equation (2) as;

$$\frac{V_g}{V_w}(36_{Ar}) = \frac{1}{133.3}\,. \tag{2}$$

This means that at the Ivuna mudpots 1 cm$^{3\ \text{at}}$ Standard Temperature and Pressure (STP) of ^{36}Ar can be stripped out by 133.3 cm^{3} of water in the subsurface. Since ^{4}He/^{20}Ne ratio in the Rukwa Rift ranges from 1- 15000 (Mtili et al., 2021), therefore the atmospheric contribution in the hydrologic closed system of the Rukwa Rift is either little or negligible.

Given the average concentrations of the ^{40}Ar/^{36}Ar ratio =726 and ^{40}Ar = 16175 x 10^{-6} cm^{3}/cm^{3} at Ivuna mudpots.

The concentration of ^{36}Ar in equivalent volume of water is the concentration of ^{40}Ar ÷ ^{40}Ar/^{36}Ar ratio, i.e. 16175 x 10^{-6} cm^{3} /cm^{3} ÷ 726 = 2.2 10^{-5}cm^{3} /cm^{3} ^{36}Ar.

4.4.6.1 Noble gases accumulation in the hydrologic system of the Rukwa Rift: Case study of Ivuna mudpots

Since 1 cm^{3} STP of ^{36}Ar can be stripped out by 133.3 cm^{3} of water in the subsurface (Equation 2), therefore groundwater ^{36}Ar concentration of 2.2 10^{-5}cm^{3} /cm^{3} will require 2.97 x 10^{-3} cm^{3} of subsurface water i.e. the total volume of water that the noble gases have interacted with beneath the Ivuna mudpots. This amount of water can therefore be used to compute the concentration of other radiogenic noble gases per equivalent volume of water sampled from the same locality.

Using the equivalent volume of water i.e. 2.97 x 10^{-3} cm^{3}, the concentration of ^{40}Ar = 16175 x 10^{-6} cm^{3}/cm^{3} per volume of water will be 5.45 cm^{3}/cm^{3} H_20. Similar algorithms can be applied for the resolved ^{4}He concentration.

In order to calculate the noble gas concentration per gram of host rock we consider the reasonable estimate of the rock matrix density and measured porosity based on assumptions made also by Warr et al., 2018 (Equation 3);

$$\text{Conc. } 40_{\text{Ar}}\left[\frac{\text{cm3}}{\text{gram}}\text{ of host rock}\right] = 40_{\text{Ar}}\left[\frac{\text{cm3}}{\text{cm3}}\text{ of water}\right]\text{x Porosity} \div \text{Density.} \tag{3}$$

Where density = 2.7 g/cc and porosity measurements are 11.8% for the Lake Beds Group, 30% for the Red Sandstone Group, 26% Karoo Supergroup (refer Chapter 2) and Precambrian Basement is 0.64% (Chaki et al., 2008).

Substituting Equation (3) into the radiogenic dating Equation (4) described by Warr et al., 2018 and references therein.

$$\text{Conc. } 40_{\text{Ar}} \left[\frac{\text{cm3}}{\text{gram}} \text{ of host rock}\right] = 0.105 \text{ x } 40_{\text{K}} \text{ x } [e^{\lambda_{40} t} - 1]. \tag{4}$$

Solving for residence time ‘t’ for K-Ar equation will lead to Equation (5);

$$t = \frac{\ln\left[\frac{40\text{Ar} + (0.105 \text{ x } 40\text{Ar}}{0.105 \text{ x } (40\text{K})}\right]}{\lambda_{40}} \tag{5}$$

Similarly solving for radiogenic residence time ‘t’ for U-Th/He Equation (6) will lead to a solution shown in Equation (7);

$$4_{\text{He}} = 8 \text{ x } (238_{\text{U}}) \text{ x } [e^{\lambda_{238} t} - 1]) + 7 \text{ x } (235_{\text{U}}) \text{ x } [e^{\lambda_{235} t} - 1] + 6 \text{ x } (232_{\text{Th}}) \text{ x } [e^{\lambda_{232} t} - 1]. \tag{6}$$

$$t = \left[\frac{\frac{\ln[(4_{\text{He}}) \text{ x } 8 \text{ x } (238_{\text{U}}) \text{ x } 7 \text{ x } (235_{\text{U}}) \text{ x } 6 \text{ x } (232_{\text{Th}})]}{\ln[8 \text{ x } (238_{\text{U}}) \text{ x } 7 \text{ x } (235_{\text{U}}) \text{ x } 6 \text{ x } (232_{\text{Th}})]}}{\lambda_{238} + \lambda_{235} + \lambda_{232}}\right]. \tag{7}$$

Where ^{238}U, ^{235}U, ^{232}Th and ^{40}K are elemental concentrations in the host rock, i.e.U-238 (2.8ppm), U-235 (2.8ppm), U-232 (10.7 ppm) (Manya et al., 2007; Mshiu and Maboko, 2012) and K-40 (2%) (Warr et al., 2018) respectively. The decay constants per year with values in parenthesis are as λ_{238} (0.155125 x 10^{-9} yr^{-1}), λ_{235} (0.98485 x 10^{-9} yr^{-1}), λ_{232} (0.049475 x 10^{-9} yr^{-1}) (Brevart et al., 1982 and references therein) and λ_{40} (0.557 × 10^{-10}

yr^{-1}) (Wetherill et al., 1956). The results for these radiogenic ages are as shown in Table 4.6 & 4.7).

Table 4.6. Average radiogenic ages for each sampling locality based on the ^{40}K-^{40}Ar Equation relating radiogenic isotopes where average residence times are calculated using bulk porosity (**Φ)** of each lithostratigraphic units in the Rukwa Rift Basin i.e. Lake Beds Group (LKB), Red Sandstone Group (RSS), Karoo and Basement. Concentrations of ^{40}Ar isotopes expressed per cm^3 of pore water (degassed water volume) of respective lithology using Vg/Vw after Mtili et al. (2021), Warr et al. (2018), Holland et al. (2013). For each level both individual samples and an average concentration is presented.

Sample Location	**[Vg/Vw] ^{36}Ar**	**^{40} Ar [cm^3 STP/cm^3]**	**^{40}Ar [cm^3/cm^3 H_20]**	**Φ [LKB]**	**Φ [RSS]**	**Φ [Karoo]**	**Φ [Basement]**	**Density (g/cc)**	**^{40}K ppm**	**λ_{40} Yr-1**	**Ages [LKB]**	**Ages [RSS]**	**Ages [Karoo]**	**Ages [Basement]**
Ivuna mudpots	7.50E-03	1.62E-02	5.45	0.118	0.3	0.26	0.0064	2.7	2.00E+04	5.57E-11	2.0E+06	5.17E+06	4.48E+06	1.10E+05
Itumbula salt pond	4.83E-02	9.59E-03	38.40	0.118	0.3	0.26	0.0064	2.7	2.00E+04	5.57E-11	1.4E+07	3.64E+07	3.16E+07	7.78E+05
Kajundu spring	4.40E-02	3.99E-03	13.90	0.118	0.3	0.26	0.0064	2.7	2.00E+04	5.57E-11	5.2E+06	1.32E+07	1.14E+07	2.81E+05
Tete spring	6.20E-02	3.10E-03	18.50	0.118	0.3	0.26	0.0064	2.7	2.00E+04	5.57E-11	6.9E+06	1.75E+07	1.52E+07	3.75E+05
Ibaya spring	4.32E+00	8.13E-05	1450.00	0.118	0.3	0.26	0.0064	2.7	2.00E+04	5.57E-11	5.3E+08	1.32E+09	1.15E+09	2.93E+07
Ngwilo spring	2.61E-01	1.37E-03	94.40	0.118	0.3	0.26	0.0064	2.7	2.00E+04	5.57E-11	3.5E+07	8.95E+07	7.76E+07	1.91E+06
Nanyara spring	3.88E+00	7.35E-05	1400.00	0.118	0.3	0.26	0.0064	2.7	2.00E+04	5.57E-11	5.2E+08	1.28E+09	1.12E+09	2.83E+07
Songwe river	2.05E+01	1.69E-05	6420.00	0.118	0.3	0.26	0.0064	2.7	2.00E+04	5.57E-11	2.3E+09	5.25E+09	4.63E+09	1.30E+08

Table 4.7. Average radiogenic ages for each sampling locality based on equation relating radiogenic uranium, thorium and helium isotopes. The average residence times are calculated using bulk porosity (**Φ)** of each lithostratigraphic units in the Rukwa Rift Basin i.e. Lake Beds Group (LKB), Red Sandstone Group (RSS), Karoo and Basement. Generally, the age ranges in Neo-Mesoproterozoic period (See description in text).

Sample Location	**^{4}He [cm^{3}STP/cm^{3}]**	**^{4}He [cm^{3}/cm^{3}H$_{2}$O]**	**^{4}He [cm^{3}/gm Rock]**	**[Vg/Vw] ^{36}Ar**	**^{238}U[ppm]**	**^{232}Th [ppm]**	**λ_{238} Yr^{-1}**	**λ_{235} Yr-1**	**λ_{232} Yr^{-1}**	**Ages [LKB]**	**Ages [RSS]**	**Ages [Karoo]**	**Ages [Basement]**
Ivuna mudpots	4.7E-02	1.58E+01	6.9E-01	0.0075	2.8	10.7	1.55E-10	9.85E-10	4.95E-11	8.1E+08	8.9E+08	8.8E+08	5.7E+08
Itumbula salt pond	3.4E-02	1.36E+02	6.0E+00	0.04825	2.8	10.7	1.55E-10	9.85E-10	4.95E-11	9.9E+08	1.1E+09	1.1E+09	7.5E+08
Kajundu spring	2.0E-04	6.95E-01	3.0E-02	0.044	2.8	10.7	1.55E-10	9.85E-10	4.95E-11	5.5E+08	6.3E+08	6.2E+08	3.1E+08
Tete spring	8.0E-03	4.77E+01	2.1E+00	0.062	2.8	10.7	1.55E-10	9.85E-10	4.95E-11	9.0E+08	9.8E+08	9.7E+08	6.6E+08
Ibaya spring	1.0E-04	1.78E+03	7.8E+01	4.32	2.8	10.7	1.55E-10	9.85E-10	4.95E-11	1.2E+09	1.3E+09	1.3E+09	9.6E+08
Ngwilo spring	1.1E-03	7.23E+01	3.2E+00	0.2605	2.8	10.7	1.55E-10	9.85E-10	4.95E-11	9.4E+08	1.0E+09	1.0E+09	7.0E+08
Nanyara spring	2.0E-05	3.76E+02	1.6E+01	3.8825	2.8	10.7	1.55E-10	9.85E-10	4.95E-11	1.1E+09	1.1E+09	1.1E+09	8.3E+08
Songwe river	7.8E-07	2.97E+02	1.3E+01	20.4935	2.8	10.7	1.55E-10	9.85E-10	4.95E-11	1.1E+09	1.1E+09	1.1E+09	8.1E+08

4.5.0 Discussion

4.5.1 Crustal radiogenic helium 'kitchen'

Our models reveal that the entire rock volume of the Tanzania Craton contributes to 46 – 50% (∽124WC) of ^{4}He flux in the EAHP (Table 4.1). The estimated average helium production potential in the whole EAHP sums to ~22 x 10^{-6} mol ^{4}He/m^2 yr including the cratons ~ 19 x 10^{-6} mol ^{4}He/m^2 yr and the Ubendian mobile belt ~3.3x 10^{-6} mol ^{4}He/m^2 yr (Table 4.1- 4.2). These values are generally greater (up to ~9 times) than the global statistical averages calculated for major sedimentary basins which are up to ~1.74 - 2.2 x 10^{-6} - mol ^{4}He/m^2 yr (Torgersen, 2010; Cheng et al., 2021). Elsewhere previous studies have reported helium flux from continental crust settings such as the Paris Basin ~0.2-7.9 x 10^{-6} mol ^{4}He/m^2 yr and the Great Artesian Basin~0.9-1.6 x 10^{-6} mol ^{4}He/m^2 yr, Saskatchewan lakes ~0.2-52 x 10^{-6} mol ^{4}He/m^2 yr and Williston Basin ~0.29-1.34 x 10^{-6} mol ^{4}He/m^2 yr which are inline with this study (Torgersen, 2010; Torgersen et al., 1992) (Torgersen, 2010; Torgersen et al., 1992); Cheng et al., 2021).

Such a significant amount of ^{4}He flux in the EAHP would require massive impingement of high heat flow triggering helium release most likely related to a mantle plume beneath the Tanzania Craton (Pik et al., 2016; Ebinger and Sleep, 1998; Danabalan et al., 2022). For the Tanzania Craton, a thermal surge has been previously evidenced from thermal springs, seismic tomography and diamond kimberlitic rocks which serve as unique proxy for metasomatism and heat flow aspects in the region (e.g. Bulanova et al., 2004; Stiefenhofer and Farrow, 2004; Park and Nyblade, 2006; Brown et al., 2012; Ebinger et al., 2013). Since the Tanzania Craton has the highest contribution to ^{4}He flux (∽124 WC), it is likely that cratonic foundering and metasomatic weakening facilitates ^{4}He release and circulation over large distances throughout the region (e.g. Shirey et al., 2013; Danabalan, 2017; Table 4.1). Due to the fact that the crustal thickness in the region varies (Kachingwe et al., 2015; Didas et al., 2022), it is possible that the asymmetric geometry of a cratonic 'keel' associated with lithospheric-scale faults, may deflect the mantle plume unevenly between the two branches of East Africa Rift System (Koptev et al., 2015; Fig. 4.8). Similar to suggestions by Koptev et al. (2015), the variation of isotopic ratios and heat flow observed in this study over the RRB and the RVP may also support the asymmetrical i.e. magmatic and non-magmatic nature of the East African Rift System.

Since the helium production is a continuous process, several degassing models in this study (e.g. Table 4.4 – 4.5) could suggest that the ^{4}He mass balance is largely affected by degassing surges triggered by transient tectonothermal regimes. However, since the heat flow decay in the continental crust takes up to ~800 Myrs (e.g. Sclater et al., 1980; Hu et al., 2000), each successive tectonothermal event recorded in the Rukwa Rift (Mulaya et al., 2022), implies transient degassing surges followed by a hiatus of crustal stability and tectonic quiescence associated with normal degassing under a steady-state thermal regime. We postulate that heat transfer from the plume magmatism makes a significant contribution to the conductive and convective heat flow recharge, injection and fluid dynamics in the region (e.g. Lysak, 1992; Ebinger and Sleep, 1998; Pik et al., 2016; Fig. 4.8). Notably high heat flow up to 99 mW/m^2 for the Rungwe Volcanic Province reflects a local thermal anomaly associated with tectonics and suggests a possible mechanism for continual heat flow recharge in the EAHP (e.g. Njinju et al., 2019; Fig. 4.8). However, a tectonothermal event related to a mantle plume may not necessarily be the only thermal source as radiogenic heat production and intra-crustal magma chambers may contribute to the heat surge in the region (Sclater et al., 1980; Pollack, 1982). The assumption made for degassing and migration of crustal ^{4}He may equally depend on other factors in place such as the intensity of crustal opening i.e. fracturing, efficiency of release from the helium bearing minerals and concentration of other carrier fluids (Haliford et al., 2022; Danabalan et al., 2022).

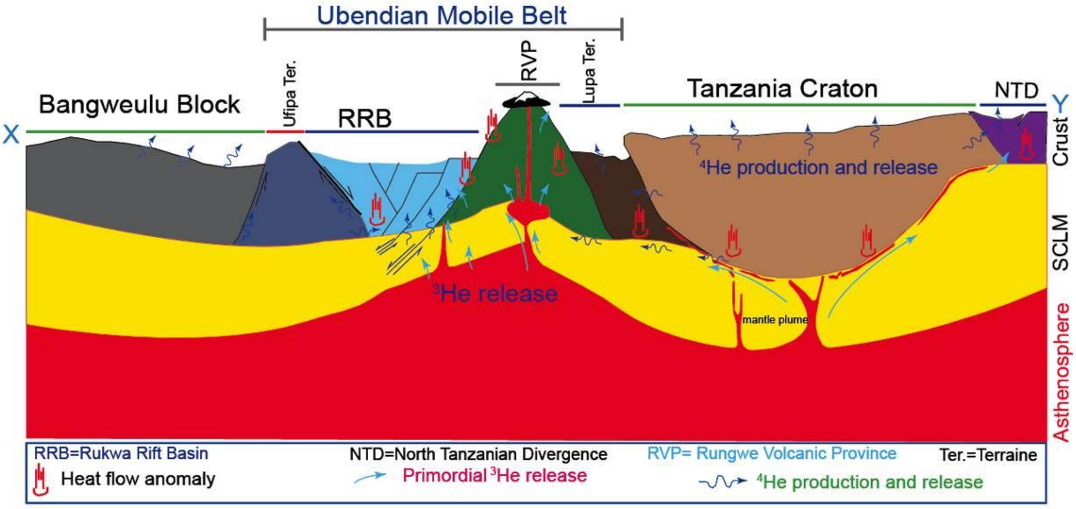

Fig. 4.8. Conceptual model showing the heat flow distribution for the EAHP related to plume magmatism. The heat flow anomaly triggered by the tectonothermal event is essential for releasing radiogenic helium from the continental crust. NTD=North Tanzanian Divergence; RRB= Rukwa Rift Basin; RVP=Rungwe Volcanic Province (refer Fig. 4.1a for map location) (After Koptev et al., 2015; Mtili et al., 2021; Kimani et al., 2021; Danabalan et al., 2022).

4.5.2 Implication of heat flow anomalies for helium potential

The occurrence of heat flow anomalies in the Rukwa Rift marked by corresponding changes in the topographic profile coincides with notable changes in isotopic ratios (Fig. 4.4d; Fig. 4.6b). This relationship can be observed on a profile across the RRB and the RVP where the changes in isotopic ratios $CO_2/^3He$ and $^3He/^4He$ coincide with changes in topography (Fig. 4.6a-c). Pronounced high topography over the RVP up to ~2250 m is associated with anomalously high heat flow (~99 mW/m^2) and isotopic ratios i.e. high $CO_2/^3He$ ~1.4 -2.9 x10^{13} and high $^3He/^4He$ ~3.3-7.0 (Fig. 4.6a-c). The topographic high in the RVP may be related to crustal uplift due to a thermo-kinematic anomaly contributing to regional stress fields reflecting extension tectonics and doming in the region (Mareschal and Gliko, 1991; Negredo et al., 1995).

The anomalies of heat flow and isotopic ratio in some places coincide with tectonically active fault networks in the RRB and RVP most likely due to increased porosity and deep-rooted fracture/fault permeability (Lysak, 1992; Mulaya et al., 2022; Halford et al., 2022; Fig. 4.8). The evidence of the heat flow anomaly occurring along/proximal to faults and accommodation zones in the Rukwa Rift reveal tectonic strain and permeable conduit systems which may facilitate fluid migration in the region (e.g. Lowenstern et al., 2014; Haliford et al., 2022; Mulaya et al., 2022). The fact that the seismicity record and geodetic studies show high frequency of earthquakes with significant magnitude (e.g. Stamps et al., 2018; Fig. 4.7) implies heat flow anomaly is associated with active tectonics which could influence fluid migration. Thermal anomalies in active tectonics have been associated with circulation of hydrothermal fluid and seismicity in the region (e.g. Wilks et al., 2017).

More than 50% of the $CO_2/^3He$ ratios in this study range between ∽$0.5x10^{10}$ and 2.9 $x10^{13}$ (Fig. 4.5a-b; Fig. 4.6a) that implies a binary source between crust and mantle signatures in the Rukwa Rift as suggested by Barry et al. (2013) and Danabalan. (2017). The observed spatial variation of geochemical anomalies and heat flow along the strike of the Rukwa Rift segments may be attributable to a bimodal crustal thickness distribution ∽29 and 42 km previously reported in the region (e.g. Last et al., 1997; Plasman et al., 2017; Borrego et al., 2018). This lithospheric thickening and thinning profile may have caused a variable rifting intensity and fluid dynamics (e.g. Lysak, 1992; Lemna et al., 2019; Kolawole et al., 2021; Kimani et al., 2021; Mtili et al., 2021; Mulaya et al., 2022). Similarly, the variation of active strain patterns mostly inherited from Karoo fabrics may equally modulate the heat flow i.e. deflect thermal weakening effects within individual rifts (Bellahsen et al., 2013; Kolawole et al., 2019; Mulaya et al., 2022;).

Along the East Africa Rift System, heat flow has been reported to vary considerably depending on the stages of rifting with highest heat flow recorded in the Afar Rift (∽150 - 250 mW/m^2) while the lowest is in the Malawi Rift ∽ 8-24 mW/m^2 (Lysak, 1992; Jones, 2020; Fig. 4.3a). However, the heat flow values in the RRB and RVP are higher than both the average value for continental provinces ∽49 mW/m^2 (Sclater, 1980) and the global average for Mid-Permian provinces (∽58 mW/m^2) during deposition of Karoo sediments (Polyak and Smirnov, 1968; Chapman and Pollack, 1975; Kilembe & Rosendahl, 1992; Njinju et al., 2019; Fig. 4.3b). Most of the heat flow data values are also above the global average for recent Eocene Provinces ∽72 mW/m^2 and differs by 10 - 18% (Polyak and Smirnov, 1968; Chapman and Pollack, 1975; Fig. 4.3a-b).

4.5.2 Reconstructing helium accumulation models

A number of feasible closed system models for various terranes surrounding the RRB provide insights into the mass balance between helium production and flux in the EAHP. These models are considered under two major postulates (Postulate 1 & 2) which correspond to the two cases of helium flux model (Case I & II) through specific area/terrane of conduits. Each postulate reveals fluid dynamics during certain tectonothermal events which acted as a 'catalyst' for helium production and release surge i.e. assuming 100% efficiency of helium release in the region. The tectonothermal events which have been previously mapped include; initiation of the Karoo rifting (∽300) (Kilembe & Rosendahl, 1992; Delvaux, 2001); carbonatite volcanism (∽120 Ma) (Boniface, 2017) and the recent East African rifting coeval with magmatism (8.6 Ma); (Ebinger et al., 1989; Ebinger and Sleep. 1998).

4.5.2.1 Postulate - 1

We illustrate six helium accumulation and degassing models based on helium degassing Case-I and in relation to tectonothermal events recorded in the RRB (e.g. Danabalan et al., 2022; Mulaya et al., 2022). Although six models were considered (Table 4.1), only two models can explain feasibly the volume of ^{4}He emissions from the EAHP;

(1) MODEL - I: Assuming constant ^{4}He emissions were discharged since the onset of East African rifting coeval with magmatism to date (8.6 Ma- Harkin, 1960; Ebinger et al., 1989) via the whole region (EAHP) (Table 4.4; Fig. 4.9a). This model shows unmatched mass balance between helium production and helium flux. In order to account for this unbalanced scenario, the whole rock volume under the EAHP must have started ^{4}He production since at least the Palaeoproterozoic (2.349 Ga) with residence/accumulation time of at least 2340 Myr (Table 4.4). This timing coincides with the previously reported last phase of metamorphism in the Tanzania Craton at 2.4 Ga which serves as a proxy for high heat flow in the region (Pinna et al., 1994; Weeraratne et al., 2003; Danabalan et al., 2022).

(**2) MODEL - II**: Assuming ^{4}He emissions similar to those we observe today were discharged during the onset of East African rifting coeval with magmatism (8.6 Ma- Harkin, 1960; Ebinger, 1989) via the Rukwa Basin and RVP which serve as the main conduits only. This degassing model can only be explained if the ^{4}He production had started since the Early Devonian (409 Ma) and accumulated for at least 400 Myr (Table 4.4; Fig. 4.9b).

Under Postulate-1, the mass balance calculations show that four models (Model-III-VI) out of six do not provide reasonable values since the degassing yields more radiogenic helium (hundred to thousand times) than the production capacity of the underlying crust. The assumption of a closed system model does not apply here since the accumulation time would extend far beyond the age of the Earth (beyond 4.6 Gyr). Therefore, the unbalanced mass computation between ^{4}He flux and production for these models may otherwise imply an open system involving an exogenous source rather than a closed a system within the EAHP only (e.g. Haliford et al., 2022).

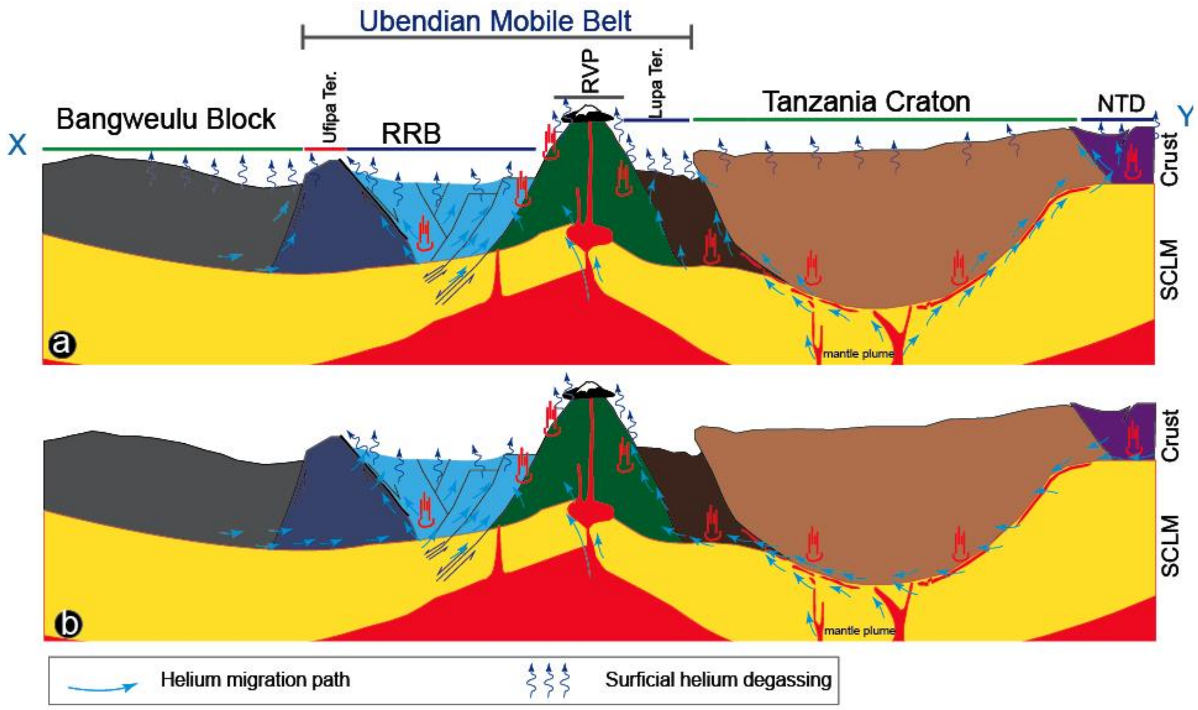

Fig. 4.9. Conceptual model showing the current helium migration and degassing model for the whole East Africa Helium Pool (a) radiogenic degassing via the whole EAHP region (b) degassing via the Rukwa Rift Basin (RRB) and the Rungwe Volcanic Province (RVP). Note the arrowhead indicates a proposed direction of regional migration.

4.5.2.2 Postulate – 2

Mass balance results based on the assumption of the helium degassing model for Case II illustrated above and six plausible models for the helium production and release. These models assume 100% for both production and release efficiency from the source rocks within the EAHP.

(1) **MODEL - I:** Assuming ^{4}He emissions similar to those we observe today were discharged during the onset of East Africa rifting and coeval with magmatism (8.6 Ma- Harkin, 1960; Ebinger et al., 1989) via the whole region (EAHP). This model suggests that the production capacity of the EAHP crustal rock volume would take 2.08 Myr to accumulate crustal ^{4}He in the region. The helium production would have therefore started in the Miocene (10.8 Ma) to account

for the current flux rate observed in the region (Barry et al., 2013; Lee et al., 2016; Table 4.5; Fig. 4.9a).

(2) **MODEL- II:** This model is similar to Model-I above except that we assume the conduits of fluid flow to include both the Rukwa Basin and the RVP. The combined conduit areas over ^{4}He emission would therefore be smaller than the volume of rock and helium production capacity in the EAHP. The accumulation minimum time would therefore be reduced to helium released recently since the Quaternary (389 Ka) (Table 4.5; Fig. 4.9b).

(3) **MODEL- III:** In this model we postulate that the tectonothermal event during Karoo rifting i.e. Late Carboniferous 300Ma (Delvaux, 2001) would have paved a way for crustal instability and break up associated with helium release in the region. We therefore assume similar ^{4}He emissions observed today were discharged since onset of Karoo rifting where the helium was vented off through the whole region (EAHP). This model suggests that production of helium must have been started since the Late Devonian (372.5 Ma) having potentially accumulated for at least 72.5 Myr (Table 4.5).

(4) **MODEL - IV:** This model is similar to Model-III except the ^{4}He was vented through the Rukwa Rift only. To account for this emission, the helium production would have started since the Pennsylvanian time (313.6 Ma) and accumulated for 13.6 Myr (Table 4.5).

(5) **MODEL - V:** Assuming similar emissions we observe today were discharged since the Cretaceous (120 Ma) during carbonatite magmatism via the whole region (EAHP). Under this model, helium production would have initiated during the Late Jurassic (149 Ma) for the residence period of at least 29 Myr (Table 4.5).

(6) **MODEL - VI:** We assume similar conditions to Model-V except that the conduits for ^{4}He emissions were discharged via the Rukwa Rift. The time for helium release and accumulation would be 5.43 Myr which started during the Early Cretaceous (125.43 Ma). This timing coincides with the previously

reported carbonatite volcanism in the Rukwa Rift hence implying the influence of heat flow surge associated with rifting associated with volcanic diking events hence contributing to helium release. During this time the Red Sandstone sequences were simultaneously depositing whereas the Karoo sequences had already deposited with Top Karoo unconformity in place (Mulaya et al., 2022). Therefore this timing could have favored accumulation of radiogenic helium in the Karoo sedimentary sequences. The petrophysical analysis of the Karoo sequences has been analyzed previously as 660.6 mD permeability and 26% porosity hence making it potential reservoir for helium accumulation (see Chapter 3).

The estimate of radiogenic ages for noble gases sampled in the Rukwa Rift show a bimodal cluster of noble gas release surges i.e. during recent East Africa Rift System and Pan-African orogenic cycles respectively (Fig. 4.10). The two episodes are known to have been associated with magmatism and metamorphism respectively (Ebinger et al., 1989; Boniface, 2009). We infer that although helium has been continually generated from basement since the Precambrian to date, the release surges were during the Pan-African orogenic cycles and the recent East Africa Rift System. The mechanism of migration of released radiogenic noble gases most likely involved mainly vertical diffusion followed by petrophysical entrapment in pore fluids of the lithostratigraphic sequences in the Rukwa Rift (e.g. Cheng et al., 2021; Cheng et al., 2022). However, for each method applied i.e. K-Ar and U-Th/He methods, some of the computed ages from the same locality show a disparity in the radiogenic ages. Age disparity between calculated and known ages of lithostratigraphic units most likely imply an exogenous source for radiogenic noble gases via vertical diffusion of helium within a closed system i.e. overlying sedimentary units supplied by Precambrian Basement (e.g. Cheng et al., 2021). Disparities of radiogenic ages may also imply interplay of other factors e.g. assumptions made in each method and history path of radiogenic minerals, i.e. slow cooling of rocks, alteration and recrystallization of clock minerals which can not be ruled out in this study (e.g. Curtis and Reynolds., 1958; Lippolt et al., 1994; Taylor and Aitken.,1997).

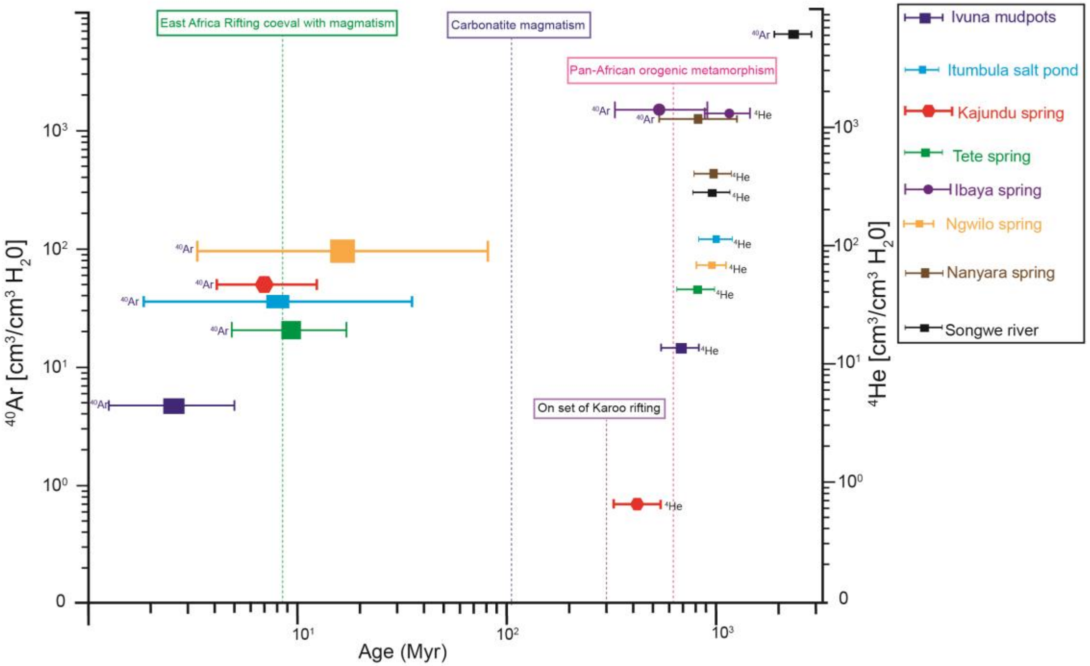

Fig. 4.10. Distribution of average radiogenic ages given in Ma based on ^{40}Ar and ^{4}He for eight (N=8) sampling locality in the Rukwa Rift (adopted from Warr et al., 2018 The observed uncertainty in ages is due to variation of porosities as discrete inputs in calculation of radiogenic ages, i.e. 11.8% (Lake Beds Group), 30% (Red Sandstone Group), 26% (Karoo Supergroup) and 0.64% (Precambrian Basement) based on petrophysical analysis (Mulaya, 2022 In Press; Chaki et al., 2008). Note the two clusters of radiogenic helium release during the Precambrian Pan-African orogenic cycles and the recent East Africa Rift System. Major regional geological events are based previous publications (Ebinger et al., 1989; Kilembe & Rosendahl, 1992; Delvaux, 2001; Boniface, 2009).

4.6.0 Conclusions

This study concludes the following

- Mass balance computation suggest that a comprehensive closed system of the East Africa Helium Pool (EAHP) has a crustal mass of ∽7.0 x 10^{10} megatonnes and has the capability of producing ^{4}He of about∽9.9 x 10^6 moles per year.
- The Tanzania Craton contributes largely to radiogenic helium production and release contributing up to 50% in the region.
- The changes of heat flow anomalies in the Rukwa Rift between 64-99 mW/m^2 are marked by corresponding changes in topographic profile.
- The helium accumulation in the EAHP would have started since the Paleoproterozoic. However, subsequent release has been accelerated largely by episodic tectonothermal events in the region.
- The RRB is a potential setting for radiogenic helium accumulation, however, the presence of other factors such as trapping and preservation of the accumulated helium is crucial for a potential helium resource.
- Apart from the helium potentiality in the EAHP, heat flow anomaly can be used as a proxy for geothermal energy targets.

References

Adams, J.A.S., Osmond, J.K. and Rodgers, J.J.W. (1959) The geochemistry of uranium and thorium, Physics and Chemistry of the Earth, 3, 298-348.

Andersen, L.S. and Unrug, R., 1984. Geodynamic evolution of the Bangweulu Block, northern Zambia. *Precambrian Research*, *25*(1-3), pp.187-212.

Ballentine, C.J., Sherwood Lollar, B., 2002. Regional groundwater focusing on nitrogen and noble gases into the Hugoton-Panhandle giant gas field. USA. Geochim. Cosmochim. Acta 66, 2483–2497. https://doi.org/10.1016/S0016-7037(02)00850- 5.

Ballentine, C. J.&Burnard, P. G., 2002. Production, release and transport of noble gases in the continental crust. Rev. Mineral. Geochem. 47, 481–538.

Barry, P.H., Hilton, D.R., Fischer, T.P., De Moor, J.M., Mangasini, F. and Ramirez, C., 2013. Helium and carbon isotope systematics of cold “mazuku” CO2 vents and hydrothermal gases and fluids from Rungwe Volcanic Province, southern Tanzania. *Chemical Geology*, *339*, pp.141-156.

Bellahsen, N., Husson, L., Autin, J., Leroy, S., d'Acremont, E., 2013. The effect of thermal weakening and buoyancy forces on rift localization: field evidence from the Gulf of Aden oblique rifting. Tectonophys 607, 80–97Boniface, N., 2017. Crystal chemistry of pyrochlore from the Mesozoic Panda Hill carbonatite deposit, western Tanzania. *Journal of African Earth Sciences*, *126*, pp.33-44. https://doi.org/10.1016/j.jafrearsci.2016.11.026

Boniface, N., 2017. Crystal chemistry of pyrochlore from the Mesozoic Panda Hill carbonatite deposit, western Tanzania. *Journal of African Earth Sciences*, *126*, pp.33-44. https://doi.org/10.1016/j.jafrearsci.2016.11.026.

Boniface, N., 2009. Eburnian, Kibaran and Pan-African metamorphic events in the Ubendian belt of Tanzania: Petrology, zircon and monazite geochronology. PhD Thesis, Kiel University.

Boniface, N. and Schenk, V., 2012. Neoproterozoic eclogites in the Paleoproterozoic Ubendian Belt of Tanzania: evidence for a Pan-African suture between the Bangweulu Block and the Tanzania Craton. *Precambrian Research*, *208*, pp.72-89.

Borrego, D., Nyblade, A.A., Accardo, N.J., Gaherty, J.B., Ebinger, C.J., Shillington, D.J., Chindandali, P.R., Mbogoni, G., Ferdinand, R.W., Mulibo, G. and O'Donnell, J.P., 2018. Crustal structure surrounding the northern Malawi rift and beneath the Rungwe Volcanic Province, East Africa. *Geophysical Journal International*, *215*(2), pp.1410-1426.

Bulanova GP, Muchemwa E, Pearson DG, Griffin BJ, Kelley SP, Klemme S, Smith CB (2004) Syngenetic inclusions of yimengite in diamond from Sese Kimberlite (Zimbabwe); evidence for metasomatic conditions of growth. Lithos 77:181-192, doi:10.1016/j.lithos.2004.04.002

Branchu, P., Bergonzini, L., Delvaux, D., De Batist, M., Golubev, V., Benedetti, M. and Klerkx, J., 2005. Tectonic, climatic and hydrothermal control on sedimentation and water chemistry of northern Lake Malawi (Nyasa), Tanzania. *Journal of African Earth Sciences*, *43*(4), pp.433-446

Brevart, O., Dupré, B. and Allegre, C.J., 1982. Metallogenic provinces and the remobilization process studied by lead isotopes; lead-zinc ore deposits from the southern Massif Central, France. *Economic Geology*, *77*(3), pp.564-575.

Brown, R.J., Manya, S., Buisman, I., Fontana, G., Field, M., Mac Niocaill, C., Stuart, F.M., 2012. Eruption of Kimberlite magmas: physical volcanology, geomorphology and age of the youngest kimberlitic volcanoes known on earth (the upper Pleistocene/ Holocene Igwisi Hills volcanoes, Tanzania). Bull. Volcanol. 74 (7), 1621–1643. https://doi.org/10.1007/s00445-012-0619-8.

Burwash, R.A. and Cumming, G.L. 1976. Uranium and thorium in the Precambrian basement of western Canada. I. Abundance and distribution, Canadian Journal of Earth Sciences,13(2): 284-293

Chaki, S., Takarli, M. and Agbodjan, W.P., 2008. Influence of thermal damage on physical properties of a granite rock: porosity, permeability and ultrasonic wave evolutions. *Construction and Building Materials*, *22*(7), pp.1456-1461.

Chapman, D.S., Pollack, H.N., 1975. Global heat flow: a new look. Earth Planet. Sci. Lett. 28 (1), 23–32.

Curtis, G.H. and Reynolds, J.H., 1958. Notes on the potassium-argon dating of sedimentary rocks. *Geological Society of America Bulletin*, *69*(2), pp.151-160.

Daly, M.C., 1988. Crustal shear zones in Central Africa: a kinematic approach to Proterozoic tectonics. *Episodes Journal of International Geoscience*, *11*(1), pp.5-11.

Danabalan, D. (2017). Helium: Exploration methodology for a strategic resource, PhD thesis, Durham University, UK, 1-293.

Danabalan, D., Gluyas, J.G., Macpherson, C.G., Abraham-James, T.H., Bluett, J.J., Barry, P.H. and Ballentine, C.J., 2022. The principles of helium exploration. *Petroleum Geoscience*, *28*(2), pp.petgeo2021-029.

Davis, W.J., and Villeneuve, M.E., 2001. Evaluation of the ^{232}Th decay constant by empirical cross-calibration of ^{208}Pb/^{232}Th and ^{207}Pb/^{235}U systematics in monazites. (Abs. #3838) 11th Annual V.M. Goldschmidt Conference, Hot Springs, Virginia, USA (2001)

Delvaux, D. (2001). Karoo rifting in western Tanzania: precursor of Gondwana break-up. Contributions to geology and paleontology of Gondwana in honor of Helmut Wopfner (pp. 111–125). Geological Institute, University of Cologne.

Didas, M.M., Armadillo, E., Hersir, G.P., Cumming, W. and Rizzello, D., 2022. Regional thermal anomalies derived from magnetic spectral analysis and 3D gravity inversion: Implications for potential geothermal sites in Tanzania. *Geothermics*, *103*, p.102431.

Ebinger, C. J., Deino, A. L., Drake, R. E., & Tesha, A. L. (1989). Chronology of volcanism and rift basin propagation: Rungwe volcanic province, East Africa. Journal of Geophysical Research: Solid Earth, 94(B11), 15785–15803. https://doi.org/10.1029/JB094 iB11p 15785

Ebinger, C., & Sleep, N. H. (1998). Cenozoic magmatism in central and east Africa resulting from impact of one large plume. Nature, 395, 788–791.

Ebinger, C.J., Shillington, D.J., et al., 2018. Crustal structure surrounding the northern Malawi rift and beneath the Rungwe Volcanic Province, East Africa. Geophys. J. Int. 215, 1410–1426. https:// doi.org/10.1093/gji/ggy331

Ebinger, C.J., van Wijk, J., Keir, D. and Bickford, M.E., 2013. The time scales of continental rifting: Implications for global processes. *Geol. Soc. Am. Spec. Pap*, *500*, pp.371-396.

Fritz, H., Abdelsalam, M., Ali, K. A., Bingen, B., Collins, A. S., Fowler, A. R., Ghebreab, W., Hauzenberger, C. A., Johnson, P. R., Kusky, T. M., Macey, P., Muhongo, S., Stern, R. J., & Viola, G. (2013). Orogen styles in the East African Orogen: A review of the neoproterozoic to cambrian tectonic evolution. Journal of African Earth Sciences, 86, 65–106. https://doi.org/10.1016/j. jafre arsci.2013.06.004

Gluyas, J.G. (2019a) The emergence of the helium industry: the history of helium exploration, part 1 of 2, American Association of Petroleum Geologists Explorer, January 2019,16-17

Gluyas, J.G. (2019b) Helium shortages and emerging helium rovinces: the history of helium exploration part 2, American Association of Petroleum Geologists Explorer, February 2019, 18-22

Halford, D.T., Karolytė, R., Barry, P.H., Whyte, C.J., Darrah, T.H., Cuzella, J.J., Sonnenberg, S.A. and Ballentine, C.J., 2022. High helium reservoirs in the Four Corners area of the Colorado Plateau, USA. *Chemical Geology*, *596*, p.120790.

Holford, S.P., Hillis, R.R., Hand, M., Sandiford, M., 2011. Thermal weakening localizes intraplate deformation along the southern Australian continental margin. Earth Planet. Sci.Lett. 305 (1–2), 207–214.

Harkin, D.A., 1960. The Rungwe Volcanics at the Northern End of Lake Nyasa.

Hu, S., He, L., Wang, J., 2000. Heat flow in the continental area of China: a new data set. Earth Planet. Sci. Lett. 179 (2), 407–419.

Ingebritsen, S.E. and Manning, C.E., 2010. Permeability of the continental crust: dynamic variations inferred from seismicity and metamorphism. *Geofluids*, *10*(1-2), pp.193-205.

James, T. C. (1967a). Thermal springs in Tanzania. Institution of Mining and Metallurgy, Transactions/Section B (Applied Earth Science), 76, B1–B18. In Macheyeki, A. S., Delvaux, D., De Batist, M., & Mruma, A. (2008). Fault kinematics and tectonic stress in the seismically active Manyara–Dodoma Rift segment in Central Tanzania–Implications for the East African Rift. Journal of African Earth Sciences, 51(4), 163–188.

James, T. C. (1967b). Thermal springs in Tanzania—discussions and conclusions. Institution of Mining and Metallurgy, Transactions/Section B (Applied Earth Science), 76, B168–B174. In Macheyeki, A. S., Delvaux, D., De Batist, M., & Mruma, A. (2008). Fault kinematics and tectonic stress in the seismically active Manyara–Dodoma Rift segment in Central Tanzania–Implications for the East African Rift. Journal of African Earth Sciences, 51(4), 163–188.

Jones, D.J.R., 2020. A summary of the East Africa Rift Temperature and Heat flow model (EARTH). BGS Open Report, OR/20/006

Last, R., Nyblade, A., Langston, C., Owens, T., 1997. Crustal structure of the east African plateau from receiver functions and Rayleigh wave phase velocities. J. Geophys. Res. Solid Earth 102, 24469–24483. https://doi.org/10.1029/97JB02156.

Lemna, O.S., Stephenson, R. and Cornwell, D.G., 2019. The role of pre-existing Precambrian structures in the development of Rukwa Rift Basin, southwest Tanzania. *Journal of African Earth Sciences*, *150*, pp.607-625.

Kachingwe, M., Nyblade, A., Julia, J., 2015. Crustal structure of Precambrian terranes in the southern African subcontinent with implications for secular variation in crustal genesis. Geophys. J. Int. 202, 533–547. https://doi.org/10.1093/gji/ggv136.

Kilembe, E. A., & Rosendahl, B. R. (1992). Structure and stratigraphy of the Rukwa Rift. Tectonophysics, 209(1–4),143–158.https://doi.org/10.1016/0040-1951(92)90016–Y

Kimani, C.N., Kasanzu, C.H., Tyne, R.L., Mtili, K.M., Byrne, D.J., Kazimoto, E.O., Hillegonds, D.J., Ballentine, C.J. and Barry, P.H., 2021. He, Ne, Ar and CO2 systematics of the Rungwe Volcanic Province, Tanzania: Implications for fluid source and dynamics. *Chemical Geology*, *586*, p.120584.

Kolawole, F., Phillips, T.B., Atekwana, E.A. and Jackson, C.A.L., 2021. Structural inheritance controls strain distribution during early continental rifting, rukwa rift. *Frontiers in Earth Science*, p.670.

Koptev, A., Calais, E., Burov, E., Leroy, S. and Gerya, T., 2015. Dual continental rift systems generated by plume–lithosphere interaction. *Nature Geoscience*, *8*(5), pp.388-392.

Lee, H., Muirhead, J.D., Fischer, T.P., Ebinger, C.J., Kattenhorn, S.A., Sharp, Z.D., Kianji, G., 2016. Massive and prolonged deep carbon emissions associated with continental rifting. Nat. Geosci. 9, 145–149. https://doi.org/10.1038/ngeo2622.

Lenoir, J.L., Li´egeois, J.P., Theunissen, K., Klerkx, J., 1994. The Palaeoproterozoic Ubendian shear belt in Tanzania: geochronology and structure. J. Afr. Earth Sci. 19, 169–184. https://doi.org/10.1016/0899-5362(94)90059-0.

Lavayssière, A., Drooff, C., Ebinger, C., Gallacher, R., Illsley-Kemp, F., Oliva, S.J. and Keir, D., 2019. Depth extent and kinematics of faulting in the southern Tanganyika rift, Africa. *Tectonics*, *38*(3), pp.842-862.

Lowenstern, J.B., Evans, W.C., Bergfeld, D. and Hunt, A.G., 2014. Prodigious degassing of a billion years of accumulated radiogenic helium at Yellowstone. *Nature*, *506*(7488), pp.355-358.

Lysak, S.V., 1992. Heat flow variations in continental rifts. Tectonophysics 208 (1–3),309–323.

Manya, S., Maboko, M.A. and Nakamura, E., 2007. The geochemistry of high-Mg andesite and associated adakitic rocks in the Musoma-Mara Greenstone Belt, northern Tanzania: possible evidence for Neoarchaean ridge subduction?. *Precambrian Research*, *159*(3-4), pp.241-259.

Mareschal, J.C., Gliko, A., 1991. Lithospheric thinning, uplift, and heat flow precedingrifting. Tectonophysics 197 (2–4), 117–126.

Morley, C.K.,Wescott,W.A., Harper, R.M., Cunningham, S.M., 1999. Geology and Geophysics of the Rukwa Rift, in C.K.Morley ed., Geoscience of Rift Systems—Evolution of East Africa. AAPG Stud. Geol. 44, 91–110.

Mshiu, E.E. and Maboko, M.A., 2012. Geochemistry and petrogenesis of the late Archaean high-K granites in the southern Musoma-Mara Greenstone Belt: Their influence in evolution of Archaean Tanzania Craton. *Journal of African Earth Sciences*, *66*, pp.1-12.

Mtili, K.M., Byrne, D.J., Tyne, R.L., Kazimoto, E.O., Kimani, C.N., Kasanzu, C.H., Hillegonds, D.J., Ballentine, C.J. and Barry, P.H., 2021. The origin of high helium concentrations in the gas fields of southwestern Tanzania. *Chemical Geology*, *585*, p.120542.

Mulaya, E., Gluyas, J., McCaffrey, K., Phillips, T. and Ballentine, C., 2022. Structural geometry and evolution of the Rukwa Rift Basin, Tanzania: Implications for helium potential. *Basin Research*, *34*(2), pp.938-960.

Negredo, A.M., Fernandez, M. and Zeyen, H., 1995. Thermo-mechanical constraints on kinematic models of lithospheric extension. *Earth and Planetary Science Letters*, *134*(1-2), pp.87-98. https://doi.org/10.1016/0012-821X(95)00107-N

Njinju, E.A., Kolawole, F., Atekwana, E.A., Stamps, D.S., Atekwana, E.A., Abdelsalam, M.G. and Mickus, K.L., 2019. Terrestrial heat flow in the Malawi Rifted Zone, East Africa: Implications for tectono-thermal inheritance in continental rift basins. *Journal of Volcanology and Geothermal Research*, *387*, p.106656.

Park, Y. and Nyblade, A.A., 2006. P-wave tomography reveals a westward dipping low velocity zone beneath the Kenya Rift. *Geophysical Research Letters*, *33*(7).

Parsons-Davis, T., Wimpenny, J., Keller, C.B., Thomas, K., Samperton, K.M., Renne, P.R., Mundil, R., Moody, K., Knight, K., Kristo, M.J. and Williams, R., 2018. New measurement of the 238U decay constant with inductively coupled plasma mass spectrometry. *Journal of Radioanalytical and Nuclear Chemistry*, *318*(1), pp.711-721.

C. Patterson, "Age of Meteorites and the Earth," Geochim. Cosmochim. Acta **10**, 230 (1956)

Pik, R., Marty, B. and Hilton, D.R., 2006. How many mantle plumes in Africa? The geochemical point of view. *Chemical Geology*, *226*(3-4), pp.100-114.

Polyak, B.G., Smirnov, Y.B., 1968. Relationship between terrestrial heat flow and the tectonics of continents. Geotect. 4, 205–213.

Pollack, H.N., 1982. The heat flow from the continents. Annual Rev. Ear. Planet. Sci. 10,459–481.

Pinna, P., Calvez, J.Y., Abessolo, A., Angel, J.M., Mekoulou-Mekoulou, T., Mananga, G. and Vernhet, Y., 1994. Neoproterozoic events in the Tcholliré area: Pan-African crustal growth and geodynamics in central-northern Cameroon (Adamawa and North Provinces). *Journal of African Earth Sciences*, *18*(4), pp.347-353.

Plasman, M., Tiberi, C., Ebinger, C., Gautier, S., Albaric, J., Peyrat, S., Gama, R., 2017. Lithospheric low-velocity zones associated with a magmatic segment of the Tanzanian Rift, East Africa. Geophys. J. Int. 210, 465–481. https://doi.org/10.1093/gji/ggx177.

Quennell, A. M., McKinlay, A. C., & Aitken, W. G. (1956). Summary of the geology of Tanganyika, part 1 (p. 126). Geological Surv. Tanganyika Mem.

René, M. 2017. Nature, sources, resources and production of thorium, Chapter 8 in, Descriptive Inorganic Chemistry Researches of Metal Compounds, IntechOpen, DOI:10.5772/intechopen.68304

Shirey, S.B., Cartigny, P., Frost, D.J., Keshav, S., Nestola, F., Nimis, P., Pearson, D.G., Sobolev, N.V. and Walter, M.J., 2013. Diamonds and the geology of mantle carbon. *Reviews in Mineralogy and Geochemistry*, *75*(1), pp.355-421.

Stamps, D.S., Saria, E. and Kreemer, C., 2018. A geodetic strain rate model for the East African Rift System. *Scientific reports*, *8*(1), pp.1-9.

Stiefenhofer, J., Farrow, D.J., 2004. Geology of the Mwadui kimberlite, Shinyanga district, Tanzania. Lithos 76, 139–160. https://doi.org/10.1016/j. lithos.2004.04.017

Sclater, J.G., Jaupart, C., Galson, D., 1980. The heat flow through oceanic and continental crust and the heat loss of the Earth. Rep. Geophys. Space Phys. 18, 269–311.

Taylor, R.E. and Aitken, M.J. eds., 1997. *Chronometric dating in archaeology* (Vol. 2). Springer Science & Business Media.

Theunissen, K., Klerkx, J., Melnikov, A., & Mruma, A. (1996). Mechanisms of inheritance of rift faulting in the western branch of the East African Rift. Tanzania. Tectonics, 15(4), 776–790.https://doi.org/10.1029/95TC0 3685

Torgersen, T., 2010. Continental degassing flux of 4He and its variability. *Geochemistry, Geophysics, Geosystems*, *11*(6).

Warr, O., Lollar, B.S., Fellowes, J., Sutcliffe, C.N., McDermott, J.M., Holland, G., Mabry, J.C. and Ballentine, C.J., 2018. Tracing ancient hydrogeological fracture network age and compartmentalisation using noble gases. *Geochimica et Cosmochimica Acta*, *222*, pp.340-362.

Wedepohl, K.H., 1995. The composition of the continental crust. *Geochimica et cosmochimica Acta*, *59*(7), pp.1217-1232.

Weeraratne, D.S., Forsyth, D.W., Fischer, K.M. and Nyblade, A.A., 2003. Evidence for anupper mantle plume beneath the Tanzanian craton from Rayleigh wave tomography. *Journal of Geophysical Research: Solid Earth*, *108*(B9).

Wetherill, G.W., Wasserburg, G.J., Aldrich, L.T., Tilton, G.R. and Hayden, R.J., 1956. Decay Constants of K 40 as Determined by the Radiogenic Argon Content of Potassium Minerals. *Physical Review*, *103*(4), p.987.

Wilks, M., Kendall, J.M., Nowacki, A., Biggs, J., Wookey, J., Birhanu, Y., Ayele, A. and Bedada, T., 2017. Seismicity associated with magmatism, faulting and hydrothermal circulation at Aluto Volcano, Main Ethiopian Rift. *Journal of Volcanology and Geothermal Research*, *340*, pp.52-67.

Chapter 5: Assessing Helium Potential from Geothermally Active Settings

(A manuscript to be submitted in the Journal of African Earth Sciences)

Assessing Helium Potential from Geothermally Active Settings

Ernest Mulaya[1,2], Jon Gluyas[2], Ken McCaffrey[2], Chris Ballentine[3]

[1]School of Mines and Geosciences, University of Dar es Salaam, P.O. Box 35052, Dar es Salaam, Tanzania.

[2]Department of Earth Sciences, Durham University, Durham, UK, DH1 3LE.

[3]Department of Earth Sciences, University of Oxford, Oxford, UK, OX1 3AN.

Abstract

Global and society is faced with significant shortages of helium supply. Helium is primarily produced from granitic crustal basement and migrates into sedimentary basins. Therefore, successful exploration for helium resources requires a thorough understanding of a wide range of suitable geologic settings including a broader understanding of transport processes of basement fluids into sedimentary sequences. Geothermally active regions are the critical sources of high heat flow required for helium release in this system unlike their 'dry' helium-rich lithospheric counterparts. However, definitive examples of geological settings on a global scale where similar helium components occur collectively is still proven challenging. Here we describe the similarities and differences between three provinces all located within geothermally active regions; Bakreswar-Tantloi (India), Yellowstone (USA) and the Rukwa Rift (Tanzania).

Combining of geological, geochemical and structural evidence from these three regions shows that most of the sites with high helium concentration content above the economic threshold of 0.3% occur along deep-rooted fault systems which suggest the possibility of such faults being the main migration conduits for hydrothermal fluids and helium from Precambrian basement. Most likely the migration is dominated by diffusive transport and advection to charge both proximal and distal potential reservoirs in the surrounding region.

We find that these regions also exhibit high heat flow ~>99 mW/m^2 and geothermal gradient ~>39 °C/km. The anomalous thermal conditions in these provinces are sufficient to trigger helium release from the underlying Precambrian basements and enhance migration of deep crustal fluids containing helium. This study presents the evidence that it is not the extreme thermal conditions which matter to release radiogenic helium but the attainment of thermal condition above closure conditions for most helium-retentive minerals. Therefore, these findings provide an innovative approach to understanding and assessing the helium potential in similar tectonic settings elsewhere in the world.

5.1.0 Introduction

Radiogenic helium generated within the continental crust serves as a crucial societal resource albeit currently in short supply in the world (Danabalan, 2017; Gluyas, 2019a; Gluyas, 2019b; Cheng et al., 2021; Danabalan et al., 2022). Since the generation processes require slow, deep time in geological terms, ancient crust is likely to have generated most helium. Thus, an understanding the global distribution of Precambrian continental crust is therefore a key component of an assessment of where economic reserves of radiogenic helium (^4He) will be found (Ballentine and Sherwood-Lollar, 2002; Danabalan et al 2017; Fig. 5.1). A release and migration model of ^4He, liberated from the decay of uranium, thorium and potassium, from Precambrian basement is mainly dominated by vertical diffusive transport, dissolution and subsequent exsolution in overlying sedimentary systems (Cheng et al., 2021). In addition, the regional distribution of radiogenic helium may be modified by advective lateral flow particularly in more permeable lithologies and structural networks (e.g. Mulaya et al., 2022). The migrated radiogenic helium may be trapped in pore spaces in stratigraphic sequences where it potentially concentrates to form an economic reserve (Danabalan, 2017).

Geochemical analysis of gases seeping from the ground in the Rukwa Rift within the western branch of the East African Rift Systems (EARS) contain up to 10% of ^{4}He (James, 1967; Danabalan, 2017). This rift exhibits all the prerequisites for the generation, accumulation and preservation of ^{4}He in the sedimentary sequences (Mulaya et al., 2022; Danabalan et al., 2022). The radiogenic helium which diffuses into overlying sedimentary sequences in the Rukwa Rift Basin is sourced from the surrounding Precambrian rocks; Archean-aged Tanzania Craton and other Proterozoic rocks (Fig. 5.2a-b). A plausible release model for ^{4}He shows that the heat anomaly generated during recent rifting and volcanism in the region triggered ^{4}He release from previously quiescent continental crust (Danabalan, 2017; Danabalan et al., 2022). Elsewhere, the Bakreswar-Tantloi (India) and the Yellowstone (USA) settings are geothermally active areas which exhibit similar significantly high heat flow similar to the Rukwa Rift (Morgan et al., 1977; Shanker, 1988; Hurwitz et al., 2012; Chaudhuri et al., 2015). High heat flow conditions are required as most helium-retentive minerals such as apatite, zircon, and uraninite will release helium above their closure temperatures and initiate diffusive transport (Danabalan et al., 2022). However, the question of whether these three geologic settings can be linked and assessed for helium prospectivity in a similar way remains open. Therefore, in this study we use a common approach to assess the helium potentials of the Rukwa Rift (Tanzania), the Bakreswar-Tantloi province (India) and the Yellowstone province (USA). We review and assess the play elements for generation, migration and accumulation potential of these regions. Thus, our study provides a method for qualitative and quantitative comparison into the radiogenic helium potential in similar tectonic settings elsewhere in the world.

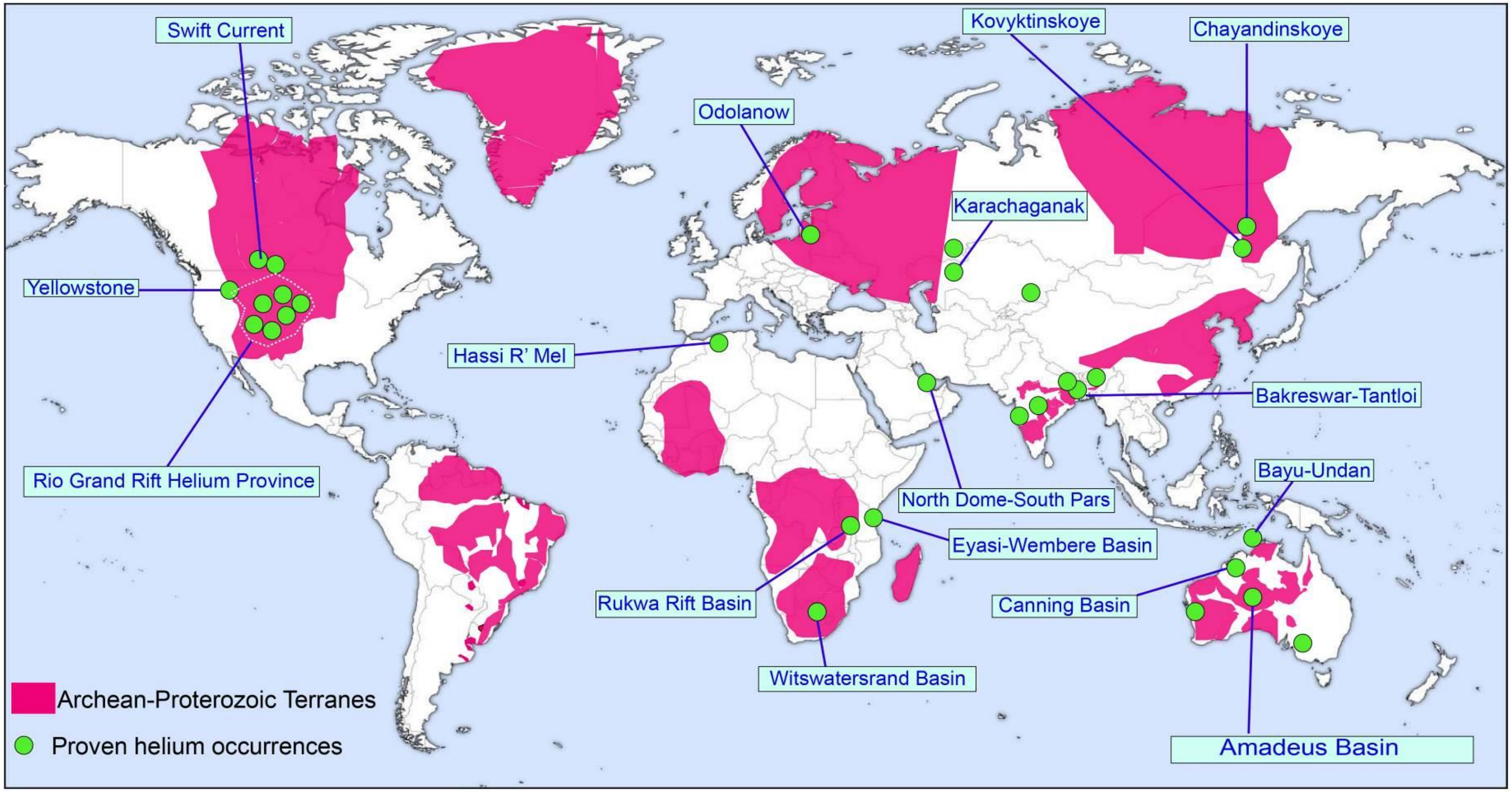

Fig. 5.1. Map showing global distribution of the Archean and the Proterozoic terranes along with sites which have been documented with significant helium occurrences i.e. both producing sites and sites under investigation (Modified after www.freeworldmaps.net; Cordani and Sato, 1999; Yuan and Romanowicz, 2010; Van Hinsbergen et al., 2011; Dulfer et al., 2016; Danabalan, 2017; Dey and Moyen, 2020).

5.1.1 Background of the Rukwa Rift

The Rukwa Rift section of the western branch of the East African Rift System (EARS) in Tanzania is regarded as active example of a cratonic rift zone (Ebinger, 2005; Mulaya et al., 2022). The Rukwa Rift Basin (RRB) lies within the NW-trending Paleoproterozoic Ubendian orogenic belt at the southwestern margin of Tanzania between the Tanzanian Archean-aged Craton and the Archean-Paleoproterozoic Bangweulu Block (Lenoir et al., 1994; Kilembe and Rosendahl, 1992; Figs. 5.2a-b). The Ubendian belt is subdivided into eight terranes, which are separated by ductile shear zones such as the Mughese shear zone, the Mutose shear zones, Saza shear zone and the Chisi shear zone (Boniface et al., 2012; Delvaux et al., 2012; Lemna et al., 2019; Mulaya et al., 2022; Fig. 5.2b). The Precambrian rocks in each terrane such as granitic intrusions are potentially rich in uranium, thorium and potassium hence capable of producing helium. Radiogenic helium from these Precambrian terranes migrates into the sedimentary sequences of the RRB (Danabalan, 2017). The migration of deep helium-rich fluids in the RRB is triggered by recent tectonic and volcanic activities associated with the East African Rift System (Barry et al., 2013; Danabalan et al, 2017; Mulaya et al., 2022). Previous studies which combine geochemical data, structural and geological evidence suggest radiogenic helium seeps out of the RRB mainly via deep-rooted fault, lithology contacts and fracture networks (Mulaya et al., 2022).

Potential reservoirs and trap geometry for radiogenic helium occurs within the stratigraphic sequences of the RRB (Mulaya et al., 2022). These stratigraphic sequences include three major sedimentary packages overlying Precambrian basement namely; the Permian Karoo Supergroup; the Oligocene and Cretaceous Red Sandstone Group; and the Neogene to Quaternary Lake Bed Group (Quennell et al., 1956; Wescott et al., 1991; Morley et al., 1992; Roberts et al., 2010 Mtelela et al., 2016). The dominant lithostratigraphic composition is mainly clastic sedimentary rocks such as mudstone, siltstone and sandstone which are controlled by structural geometry (Roberts et al., 2010; Mtelela et al., 2016; Mulaya et al., 2022). All these components are ideal for a potential helium resource in the RRB, whose findings can be used as basis of comparison with other similar geological settings elsewhere in the world.

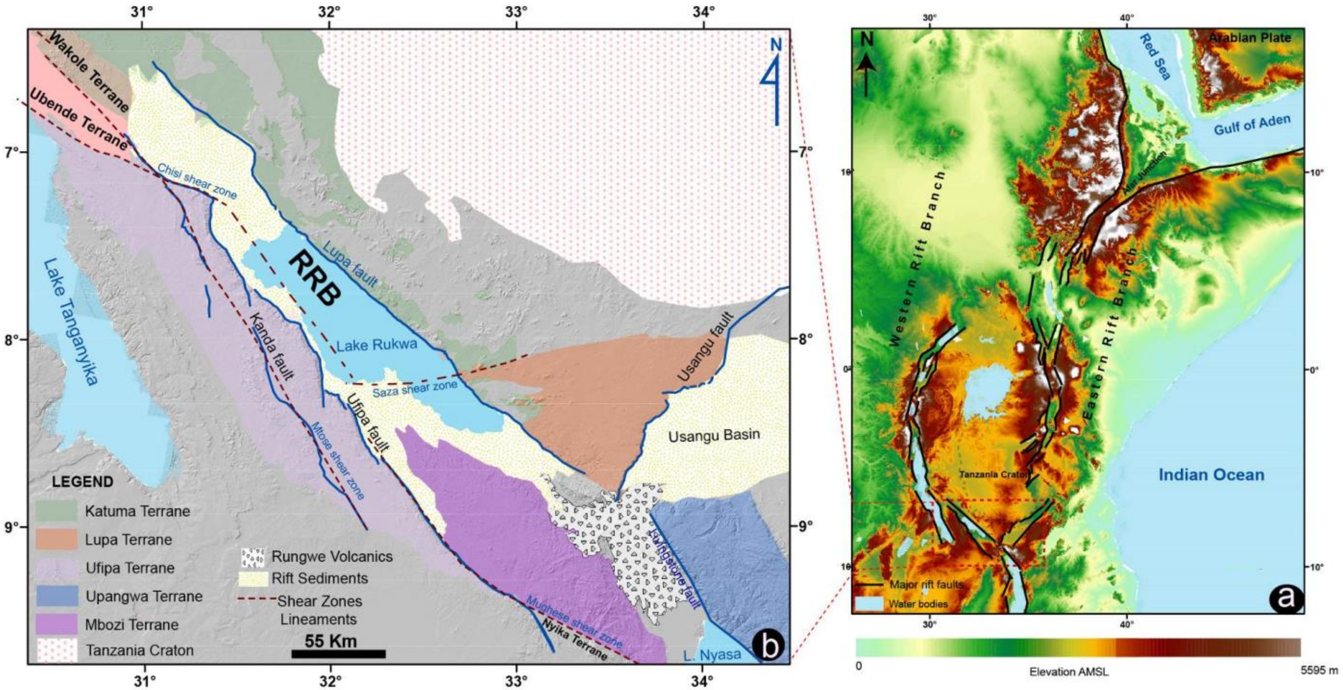

Fig. 5.2 (a) Shaded relief of the Eastern and Western branches of the East Africa Rift System showing major rifts including the Rukwa Rift. (B) Regional geologic settings surrounding the Rukwa Rift Basin (RRB) superimposed on hill shaded TanDEM-X 90m data showing Precambrian terranes and shear zones (modified after Theunissen et al., 1996; Lemna et al., 2019; Mulaya et al., 2022).

5.1.2 Geology and helium potential of India

The India subcontinent comprises five major Archean (~3.3 - 2.5 Ga) cratonic provinces which include, the Bastar, Meghalaya, Aravalli, Bundelkhand, Dharwar and Singhbhum cratons (Ramakrishna and Vaidyanadhan 2008; Jain et al., 2020; Fig. 5.3). These Archean cratons are in most cases associated with one or more Precambrian mobile belts which are in places occupied by sedimentary basins (Jain et al., 2020).

The Indian subcontinent has several geothermal provinces, each associated with significant areas of elevated heat flow (Chaudhuri et al., 2015). A number of these geothermal provinces of the country co-exist with potential sites for helium occurrences (Oldham, 1883; Shanker and GSI, 1991). Just like the Rukwa Rift in Tanzania, significant amount of radiogenic helium in India emanates from thermal springs (Das et al., 2005; Chaudhuri et al., 2015). These thermal springs are at three locations; (1) Eastern and northeastern India including Bakreswar-Tantloi, (2) west coast of India and (3) Northern India in the Himalayan Belt (Shanker, 1988; Shanker and GSI, 1991; Das et al., 2005; Fig. 5.4). Many of the sampled sites show significant helium concentration ranging from ~1-7% v/v (Chaudhuri et al., 2015; Chaudhuri et al., 2019; Brown, 2021; Fig. 5.3; Fig. 5.4). These significant radiogenic helium concentrations are above the average value ~0.3% used in the USA as a benchmark for an economic helium accumulation (Danabalan, 2017; Danabalan et al., 2022). The most developed helium prospects in India include the geothermal sites of Bakreswar (West Bengal) and Tantloi (Jharkhand) referred in this study as Bakreswar-Tantloi province (Das et al., 2005; Fig. 5.3; Fig. 5.4). This geothermal province occurs within the West Bengal Basin in the eastern Indian shield that formed from Gondwana rifting (Ghose et al., 2002). The potential source for radiogenic helium is Archean metamorphic and igneous rock i.e. gneiss and schist belonging to the Chotanagpur Gneissic Complex (Shanker and GSI, 1991; Chaudhuri et al., 2015).

Precambrian terranes of the India Subcontinent

The India subcontinent is a rigid shield which formed largely during the Archean time (3.3 - 2.5 Ga) (Ramakrishna and Vaidyanadhan, 2008; Meert et al., 2010; Meert and Pandit, 2015). The Precambrian cratons such as Bastar, Aravalli, Bundelkhand, Dharwar and Singhbhum are known rich sources of helium due to concentrations of uranium and thorium that are up to 7 times higher than average continental crust (Meert and Pandit, 2015; Danabalan et al., 2022; Fig. 5.3). The cratons may contain up to ∽18.7 ppm U and ∽52.1 ppm Th which is sufficient to decay and produce significant radiogenic helium (Manya et al., 2007; Mshiu and Maboko, 2012; Danabalan, 2017). Several provinces in India are underlain by the Archean-Proterozoic aged metamorphic-granitic complexes and thus are potentially rich in U and Th (Ramakrishna and Vaidyanadhan, 2008). The India subcontinent contains more than 300 thermal springs with the highest recorded concentration of up to ~7.0 % ^{4}He v/v (Oldham, 1883; Chaudhuri et al., 2015; Brown, 2021; Fig. 5.4). Such high concentration is significantly far above the minimum value required for an economic helium reserve of ~0.3% (Danabalan, 2017).

The helium prospectivity of the adjacent Proterozoic mobile belts is similar to the Archean cratons. Notable Proterozoic mobile belts in the Indian subcontinent include: Aravalli–Delhi, Satpura, Pandyan, Eastern Ghats and Singhbhum mobile belt (Ramakrishna and Vaidyanadhan, 2008; Jain et al., 2020). The Proterozoic mobile belts separate different tectonic terranes and are characterized by high-grade metamorphic rocks, Precambrian volcanic rocks, and major faults and shear zones (Jain et al., 2020). Notable structures include the Great Boundary Fault (GBF) which separates the Aravalli Banded Gneiss Complex (BGC) from the Bundelkhand Craton in the north-central region (Meert and Pandit, 2015). The Western Margin Fault divides the Aravalli Cratons from the Delhi-Fold Belt. The Central Indian Tectonic Zone sits between the Aravalli-Bundelkhand Craton and the Bastar-Singhbhum

Craton (Naqvi and Rogers 1987; Meert et al. 2010). These geologic settings support a number of sedimentary basins in the Indian Subcontinent, for example the Purana Basins which may provide potential conditions for helium generation, migration conduits and accumulation.

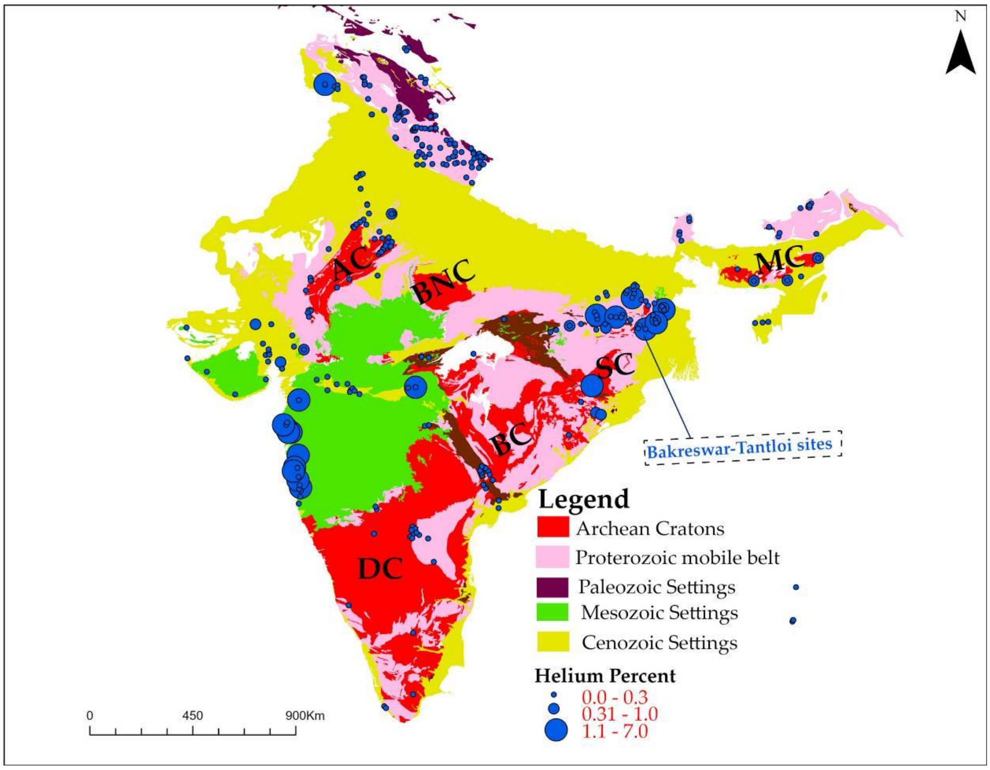

Fig. 5.3. Geological map of India showing helium concentration over major Archean Craton, Proterozoic mobile belt and major structures. DC-Dharwar Craton, BC-Bastar Craton, BNC- Bundelkhand Craton, AC-Aravalli Craton, MC- Meghalaya Craton, SC-Singhbhum Craton, (After Meert and Pandit 2015; Jain et al., 2020; Brown, 2021).

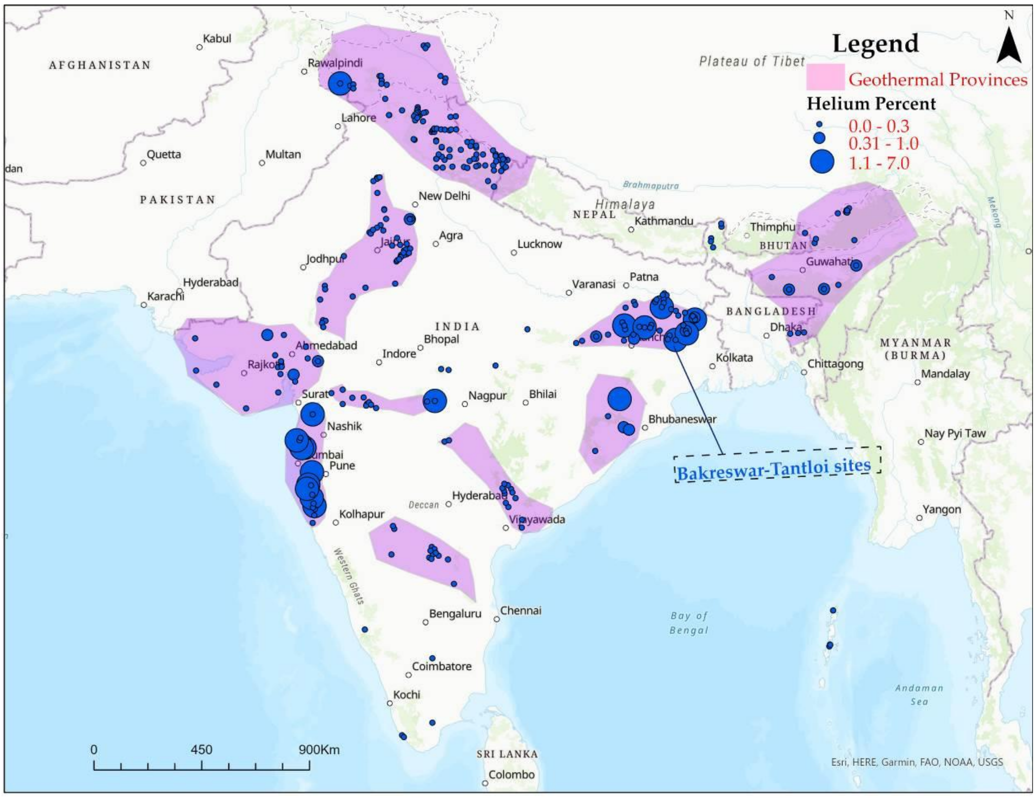

Fig. 5.4. Map showing distribution of thermal springs and the helium potential of the India subcontinent (modified after Oldham, 1883; Chaudhuri et al., 2015; Maji et al., 2021; Brown, 2021).

5.1.3 Yellowstone province

The Yellowstone province is one of the most famous active geothermal hot spots on Earth (Lowenstern et al., 2014; Fig. 5.5). The thermal springs at the Yellowstone are highly rich in radiogenic helium (low R/Ra< 2.5), i.e. R= $^{3}He/^{4}He$ in sample, $^{3}He/^{4}He$ in air (1.39×10^{-6}) (Lowenstern et al., 2014). Yellowstone is characterized by a caldera with several geothermal sites such as the Heart Lake Geyser Basin; Mud Volcano; Hot Spring Basin, Roaring Mountain, Norris GB, Brimstone Basin (Lowenstern et al., 2014; Fig. 5.5). The geologic setting comprises Precambrian igneous and metamorphic rocks (~3.5 - 2.7 Ga) of the Beartooth-Bighorn Province and the Montana sedimentary provinces overlying the Wyoming Craton (Mueller and Frost, 2006; Mueller et al., 2008; Lowenstern et al., 2015). Precambrian metamorphic rocks occur to the north of Yellowstone province which border the Palaezoic-Mesozoic formations to the west. Palaezoic-Mesozoic formations also occurs in the south where it is bordered to the east by the Absaroka Volcanics which extends along the whole eastern edge of the Yellowstone province. Pre-caldera rhyolite encircles the outside area of the caldera rim while post-caldera rhyolite occurs inside the caldera rim (Fig. 5.5).

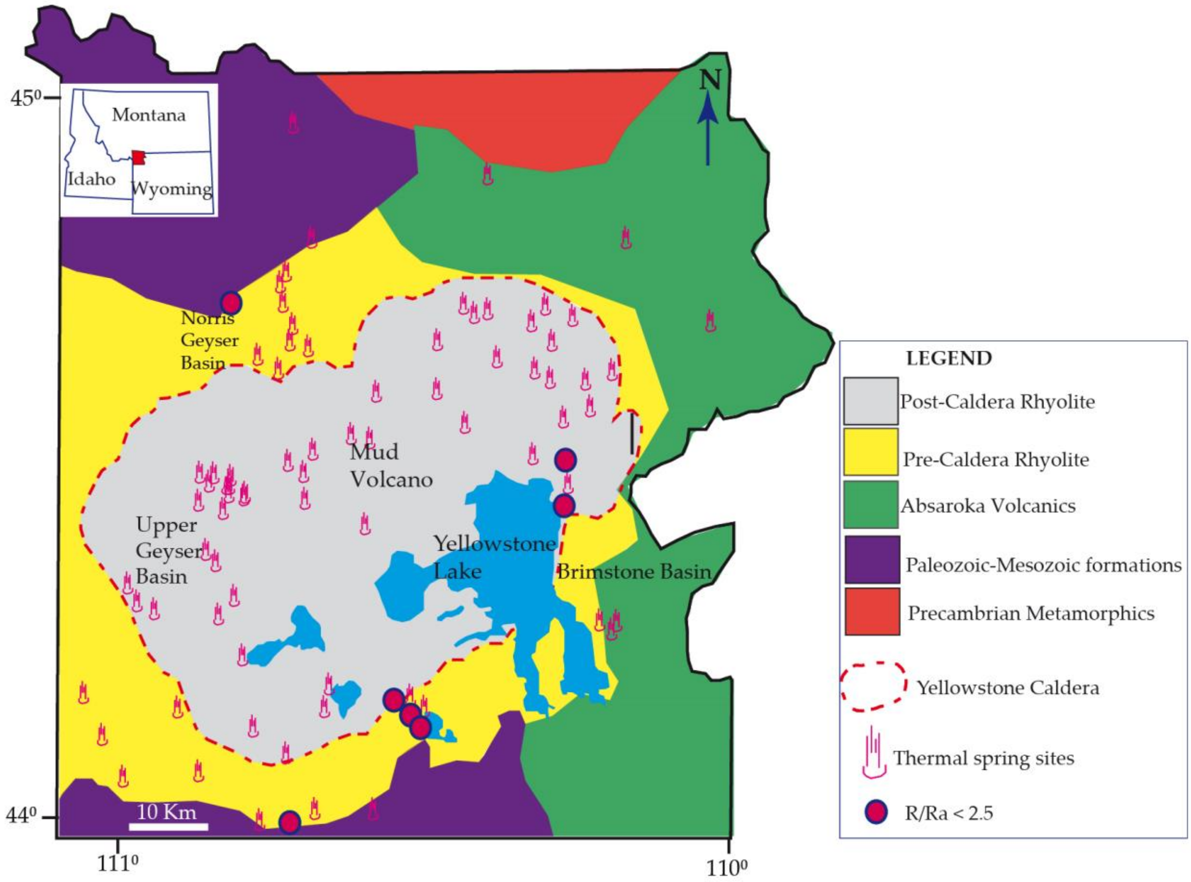

Fig. 5.5. Map showing a general geological map of the Yellowstone province and distribution of thermal springs around the Yellowstone Caldera (after Morgan et al., 1977; Lowenstern et al., 2014; Lowenstern et al., 2015).

5.2.0 Methods

Geological and geochemical data used in this study were extracted from previous investigations, that is existing maps and geological information as cited in the text. ArcGIS data (shapefiles) for India were downloaded from the Bhukosh database created by the Geological Survey of India (GSI) (Bhukosh, 2022). Geological, structural and geochemical data related to helium occurrences at the Yellowstone, Rukwa Rift and Bakreswar – Tantloi province were reviewed from existing publications. These data were then collated in Microsoft Excel and exported into ArcGIS Pro to create shapefiles. Manipulation and analysis of these shapefiles and imported Microsoft Excel data were compiled using ArcGIS Pro v.2018 to create maps. The comparison of various helium systems was interpreted and shown in maps, tables, graphs and ternary plots.

5.3.0 Results

5.3.1 Helium source and generation potential of the Bakreswar-Tantloi province

The India subcontinent exhibits significantly high helium concentration up to ~ 7%v/v which occurs within the geothermal provinces (Fig. 5.3; Fig. 5.4). We identified four potential areas with the highest helium concentration ~1-7% associated with high uranium-lead ratios ~200-300 (Fig. 5.3; Fig. 5.4; Fig. 5.6). These provinces include the west coast, northern provinces south of Himalaya and a northeast province which includes the Bakreswar-Tantloi province (Fig. 5.3; Fig. 5.4). The Bakreswar-Tantloi province comprises over 60 thermal spring sites in an area of ~2500 km^2 (Chaudhuri et al., 2015; Fig. 5.3; Fig. 5.4). Geochemical data for the Bakreswar-Tantloi province shows average radiogenic helium content up to 3.0% (Fig. 5.4). Helium seepage in the Bakreswar-Tantloi province occurs preferentially in proximity to deep-rooted faults which seem likely to be the main migration conduits (Fig. 5.7). Helium migration conduits may also include fissures, fractures and along faulted contacts of Gondwana sediments (Ghose et al., 2002; Fig. 5.7).

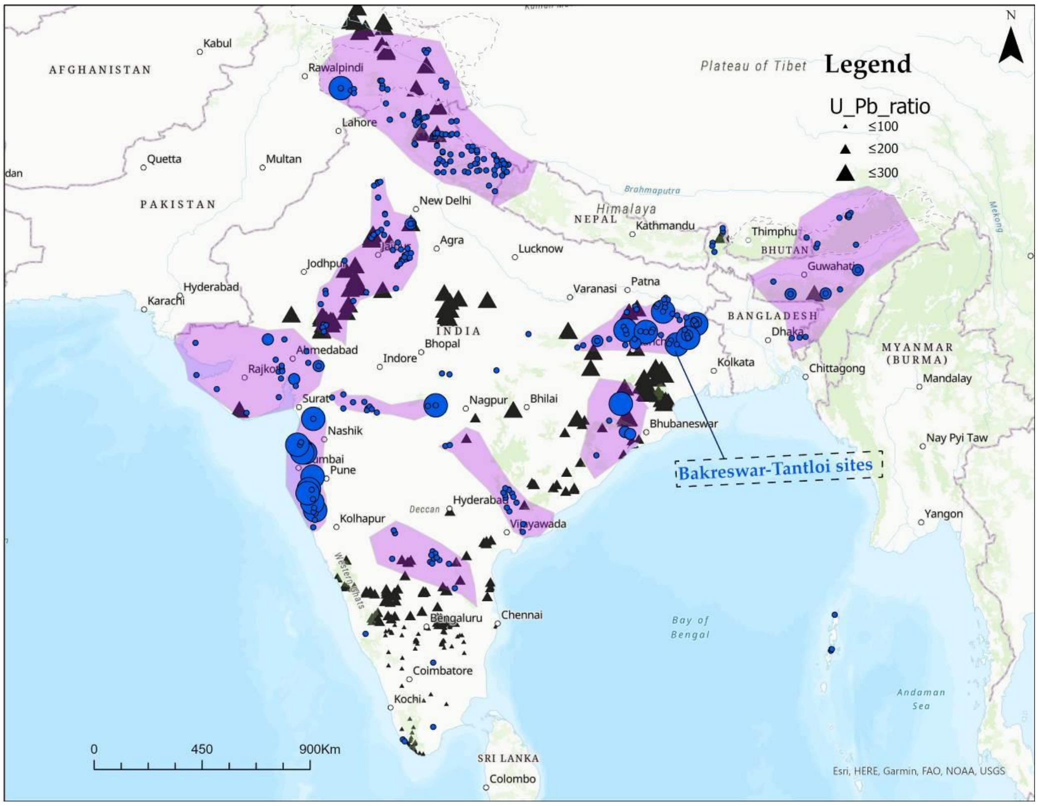

Fig. 5.6. India map showing distribution of helium potential areas along with uranium lead ratio and geothermal provinces. Note location of the Bakreswar-Tantloi in the map of India (modified after Oldham, 1883; Chaudhuri et al., 2015; Maji et al., 2021).

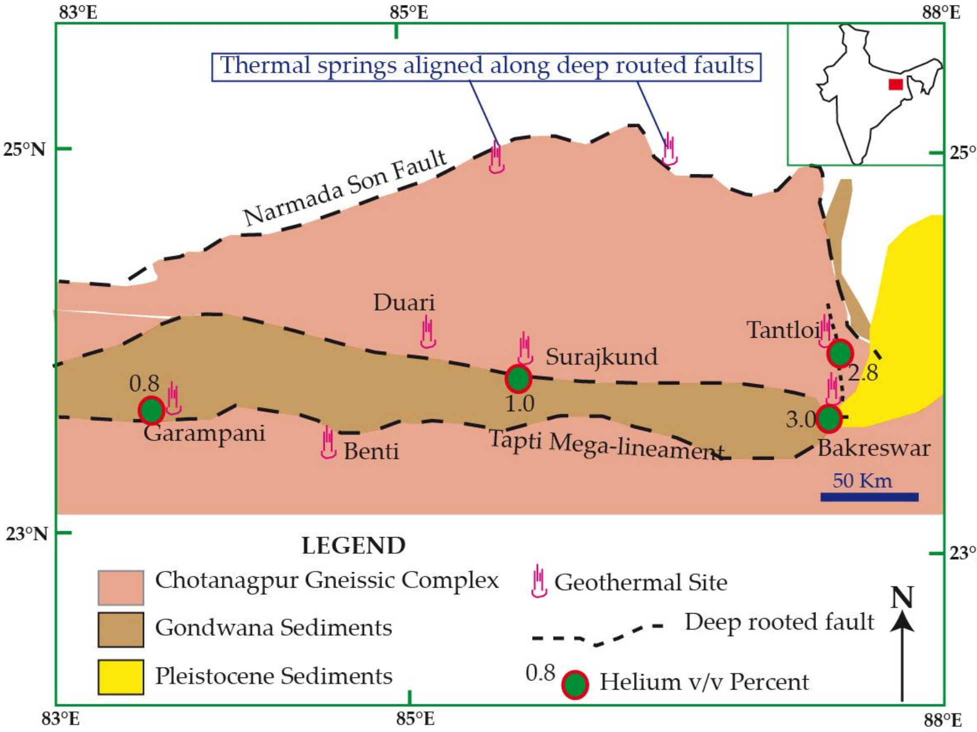

Fig. 5.7. Geological and structural map showing spatial relationship with thermal springs and helium potential in the Bakreswar-Tantloi provinces (after Chaudhuri et al., 2015; Maji et al., 2021).

5.3.2 Helium source, generation and release at the Yellowstone province

The Yellowstone province displays high radiogenic helium concentration and low isotopic ratio ~2.5 Ra (Lowenstern et al., 2014; Fig. 5.8). Most of the analysed sites show high helium concentration occurring along fault systems which abut Yellowstone Caldera (Fig. 5.8). High helium concentration is observed at sites which are outside the caldera realm particularly at the contact between Paleozoic-Mesozoic formations (Fig. 5.8).

Like the Tanzanian Archean Craton (Fig. 5.9; Fig. 5.10), the underlying Wyoming Craton at the Yellowstone possibly contain anomalous concentration of uranium, potassium and thorium. Yellowstone fulfills two crucial prerequisites for the generation and release of radiogenic helium. Firstly, the Yellowstone area has been underlain by long quiescent old rocks, an Archean craton ~2.5 Ga which with time has been capable of producing significant radiogenic helium. Secondly, a recent, tectonic perturbation has occurred (~2Ma) dominated by crustal metamorphism and magmatic underplating/hotspot (Christiansen, 2001; Lowenstern et al., 2014). The supervolcano has been heating the Archean Wyoming Craton (~2.8 Ga) hence increasing distributed heat flow (Lowenstern et al., 2015). High heat flow (~100 - 300 mW/m^2) (outside caldera) and 600-700 mW/m^2 (inside caldera) facilitates the release of accumulated radiogenic helium via deep hydrothermal systems which manifest as widely distributed thermal springs and fumarolic vents across the region (Morgan et al., 1977; Hurwitz et al., 2012; Danabalan et al., 2015; Fig. 5.8; Table 5.1).

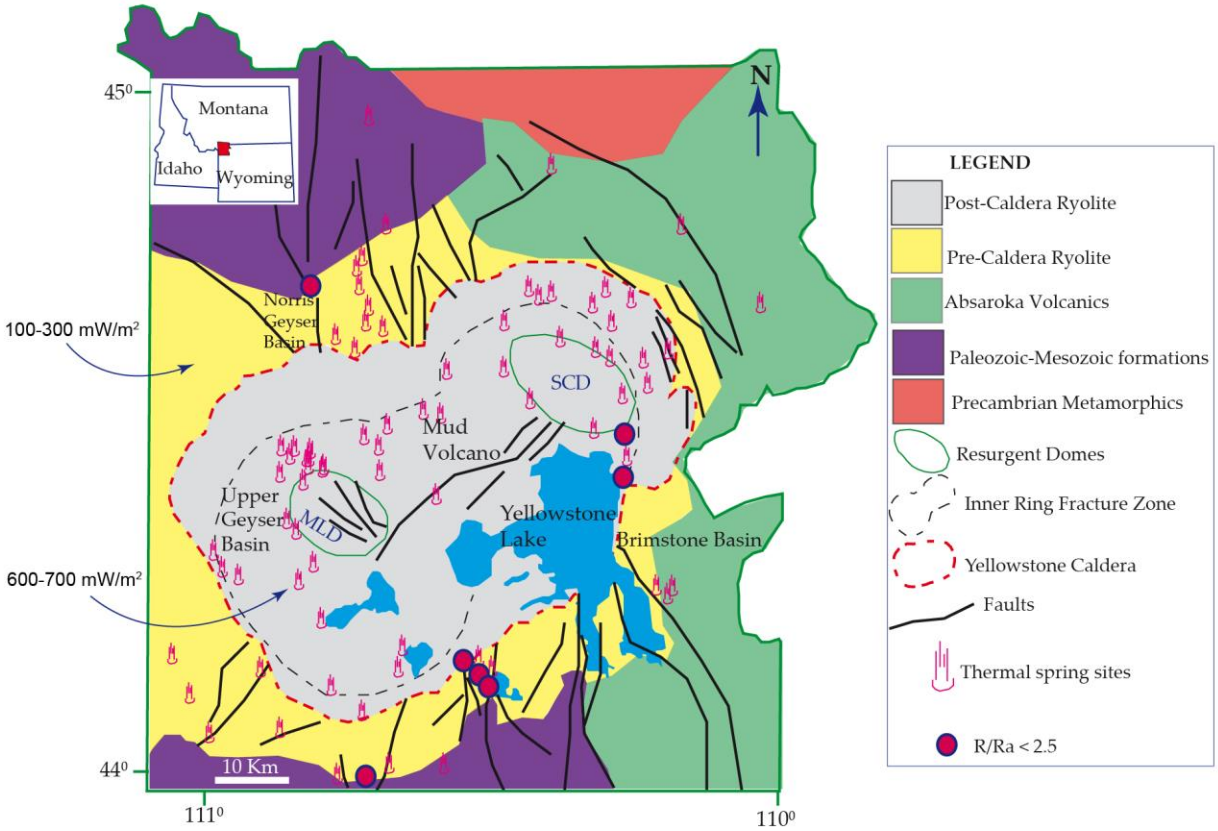

Fig. 5.8. Geological and structural map showing spatial relationship with thermal springs and helium potential at the Yellowstone province. MLD – Mallard Lake Dome, SCD- Sour Creek Dome. Note higher heat flow ~600-700mW/m^2 inside the caldera than outside ~100-300mW/m^2 (after Morgan et al., 1977; Hurwitz et al., 2012; Lowenstern et al., 2014; Lowenstern et al., 2015).

5.3.3 Helium occurrences and geothermal sites of the Rukwa Rift

The Rukwa Rift exhibits significantly wide range of ^{3}He/^{4}He ratio, i.e. from the lowest ~<0.3 to the highest ~ >1.0 occurring within or proximal to the geothermal sites characterized by hot springs (Fig. 5.9). We identified four geothermal sites which include the Lupa and Songwe sites which exhibit lower ^{3}He/^{4}He ratios (<1.0) than the Rungwe and Mampulo sites with ^{3}He/^{4}He ratios (~>1.0) (Fig. 5.9). The highest helium concentration up to 10%v/v at Itumbula and Ivuna areas are within or proximal to deep-rooted faults, fissures, fractures which seem likely to be the main migration conduits (Mulaya et al., 2022; Fig. 5.10).

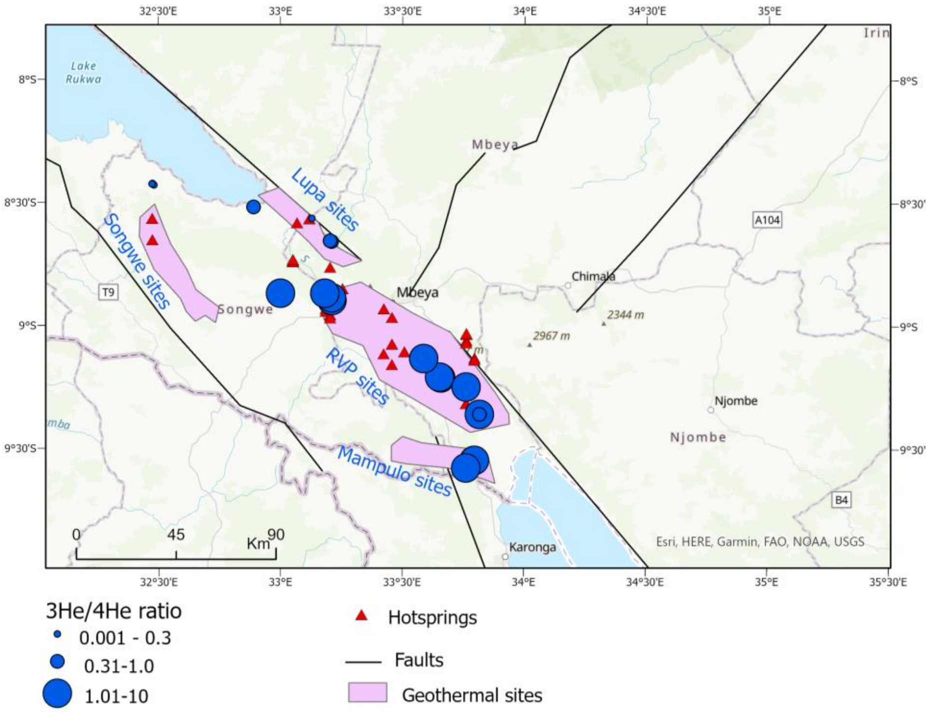

Fig. 5.9. Map showing distribution of thermal springs and the helium potential of the Rukwa Rift (after Danabalan, 2017; Mulaya et al., 2022).

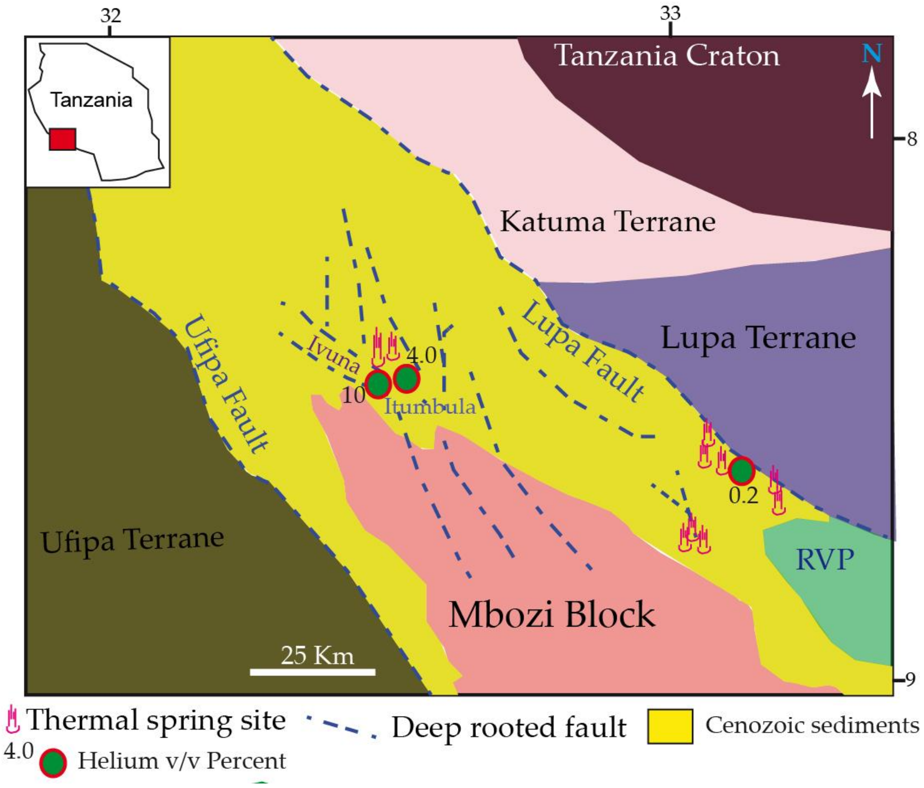

Fig. 5.10. Geological and structural map showing spatial relationship with thermal springs and helium potential at the Rukwa Rift (after Danabalan, 2017; Mulaya et al., 2022).

5.3.4 Comparison of the Bakreswar-Tantloi, Yellowstone and Rukwa Rift

The Yellowstone, Rukwa Rift and the Bakreswar-Tantloi reveal comparable geologic settings, geothermal conditions, isotopic ratios and compositions (Table 5.1). These provinces exhibit high heat flow and geothermal gradient i.e. ~100 - 700 mW/m^2, ~700-1000°C/km at Yellowstone; ~99 mW/m^2, ~39°C/km at Rukwa Rift Basin and ~200 mW/m^2, ~80°C/km at Bakreswar-Tantloi (Njinju et al., 2019; Shanker, 1988; Chaudhuri et al., 2015; Morgan et al., 1977; Hurwitz et al., 2012; Table 5.1). Based on Bakreswar-Tantloi, Yellowstone and Rukwa Rift data we observe a negative correlation between helium concentration and heat flow (Fig. 5.11). Our initial hypothesis to explain this relationship is that high helium concentration depends largely on deep faults which are basement-rooted rather than heat flow (Fig. 5.10; Fig. 5.11). Despite the requirement of high heat flow for releasing helium, close proximity to the volcanic centers increases dilution of the helium system with CO_2 (Fig. 5.11).

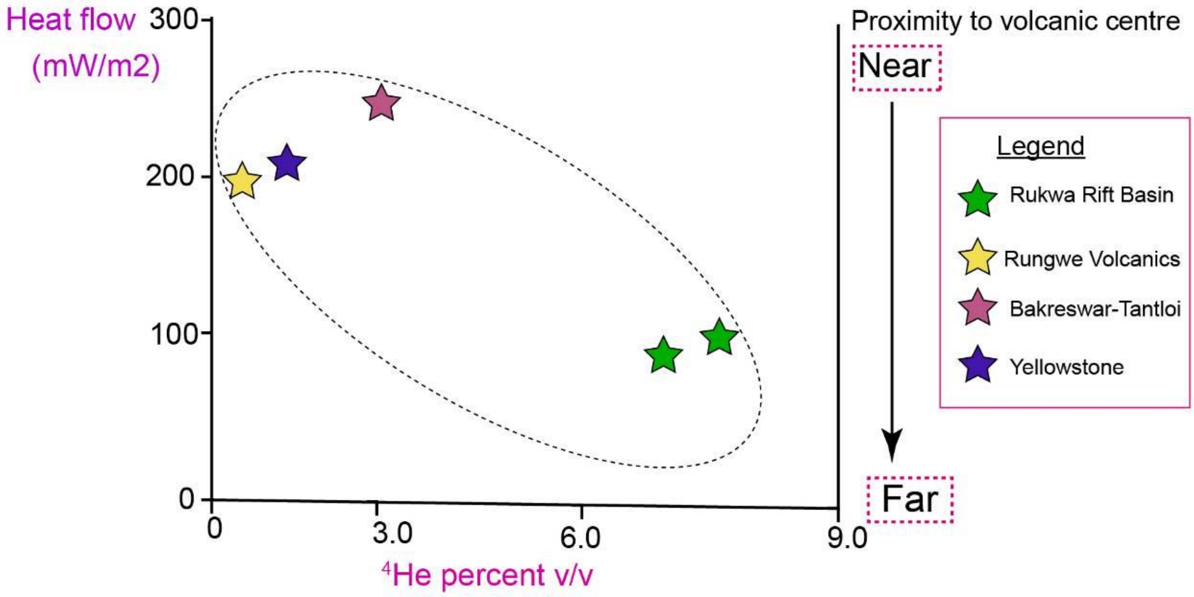

Fig. 5.11. Relationship between heat flow and helium concentration. We hypothesise that near the province to volcanic centre the more the dilution from CO_2 hence low helium concentration and vice versa (after Lowenstern et al., 2014; Chaudhuri et al., 2015; Danabalan et al., 2022).

Table 5.1. A summary showing comparisons for the Yellowstone (USA), Bakreswar-Tantloi (India) and Rukwa Rift (Tanzania).

Feature/element	**Yellowstone Province (USA)**	**Rukwa Rift (Tanzania)**	**Bakreswar-Tantloi (India)**
Location	Located within the Yellowstone Plateau Volcanic Field (Lowenstern et al., 2015)	Located in the vicinity of the Rungwe Volcanic Province (Mulaya et al., 2022)	Located near the extinct Rajmahal volcanic Trap (Sarangi, 2003)
Composition	Dominated by Archean rocks (3.5 - 2.5 Ga)	Surrounded by Archean to	Dominated by Archean

		Proterozoic rocks (2.7- 1.7 Ga)	metamorphic and igneous rocks
Crustal thickness	Crustal thinned ~18-20 km (Yuan et al., 2010)	Crustal thickness thinned ~32 to 42 km (Lavayssière et al., 2019)	Crustal thinned ~24 - 36km (Ghose et al., 2002)
Volcanic events	Recent (Cenozoic) magmatic activity ~2.0 Ma (Lowenstern et al., 2014)	Recent (Cenozoic) volcanic activity ~ < 8.7 Ma (Ebinger et al., 1989)	Volcanic activity over the Kerguelen hotspot in the early Cretaceous **(**Courtillot, 2002)
Thermal spring temperature	Magma-hydrothermal system from high-temperature interaction with buried rhyolites at temperatures 150 to 275 °C (Fournier, 1989).	Thermal spring temperature at surface ~36 – 71°C (Barry et al., 2013)	Thermal spring temperature at surface ranges 40-72° C (Chaudhuri et al., 2015).
Gaseous composition	CO$_2$-rich up to 99.5% (Allen and Day 1935; Werner and Brantley 2003; Lowenstern et al., 2015)	-CO2 ~80% rich near Rungwe volcanics -Nitrogen rich ~90% in Rukwa Basin (Barry et al., 2013; Danabalan, 2017)	Nitrogen rich ~90 (Chaudhuri et al., 2019)
Geothermal gradient	Geothermal gradient ~700-1000°C per kilometer (Fournier 1989)	Geothermal gradient of 39 °C per kilometer (Roe et al.,	Geothermal gradient ~80 °C/km (Chaudhuri et

		1996)	al., 2015)
Heat flow	High heat flow up to ~100-300 mW/m^2) (outside caldera) and 600-700 mW/m^2 (inside caldera) (Morgan et al., 1977; Hurwitz et al., 2012)	High heat flow up to (~99 mW/m^2) (Njinju et al., 2019; Mulaya et al., 2022 in Chapter 3)	High heat flow up to (~200 mW/m^2) (Shanker, 1988; Chaudhuri et al., 2015).
Fluid conduits	Thermal springs emerge via fractures and deep-rooted faults	Thermal springs emerge via fractures, porous sediments, and deep-rooted faults	Thermal springs emerge via deep rooted faults, folds and fissures (Ghose et al., 2002; Chaudhuri et al., 2015)
Cold spring occurrences	No cold springs observed	Cold springs observed at Kafwira Njuni (Harkin, 1960)	Cold spring recorded at the neighbor site at Salbardi (Maharashtra)
Fluid source	Isotopic studies show binary mix i.e magmatic and radiogenic signal (Lowenstern, 2014)	Isotopic studies show binary mix i.e magmatic and radiogenic signal (Danabalan, 2017)	No thorough isotopic studies
Helium isotopic ratios	^{3}He/^{4}He ranges <1.1 to 17Ra (Lowenstern et al., 2014)	^{3}He/^{4}He ranges 0.16 to 14.9Ra (Barry et al., 2013)	No thorough isotopic studies
Helium concentration	Helium concentration	Helium	Helium

	above minimum economic concentration ~0.3%.	concentration up to ~10% (Danabalan, 2017)	concentration up to ~3.0% (Chaudhuri et al.,2015)
Sediment sequences	Little cover sequences. Was not part of Gondwana	Gondwana sediments in place e.g. Karoo Supergroup (Mulaya et al., 2022)	Gondwana sediments in place (Maji et al., 2021)

5.4.0 Discussion

5.4.1 Effects of thermal conditions on helium occurrences

The Rukwa Rift (Tanzania), Bakreswar-Tantloi (India) and Yellowstone (USA) presents potential structural and thermal conditions for the occurrences of helium (Fig. 5.5; Fig. 5.7; Fig. 5.9; Fig. 5.10). These provinces are commonly dominated by crustal-scale faults that root in the Precambrian basement rocks (Fig. 5.7; Fig. 5.10; Fig. 5.12a-c). These faults may act as the main conduits for hydrothermal fluids containing radiogenic helium. Most likely the migration is dominated by diffusive transport and advection associated with high thermal conditions (Cheng et al., 2021). Such high thermal conditions are sufficient to trigger helium release from the underlying Precambrian basement and enhance migration of deep crustal fluids to form economic accumulation (Danabalan et al., 2022). As the current global helium reserves dwindles and more worsened by Russia curtailed production since the war in Ukraine, searching for new economic helium resources is of utmost importance. The dependency of helium production from oil fields such as Hassi R'mel in Algeria and South Pars in Qatar is highly dependent on the demand and geopolitics of petroleum products. Concerted efforts to cut green house gases to prevent global warming may indeed force for new source of helium from geothermally active settings whose helium concentration is higher (> 0.3 %) than the trace concentrations in the oil fields (0.05% He on average) (Danabalan, 2017).

High heat flow and temperature associated with volcanic centres, for instance, the supervolcano at the Yellowstone is required to elevate the temperature of the Precambrian rocks i.e. the Wyoming Craton to promote a primary release of ^{4}He from source minerals. However, proximity to the volcanic centers may dilute the helium accumulation by plumbing magmatic CO_2 into helium system (e.g. Lowenstern et al., 2015; Danabalan, 2017; Fig. 5.11). Although there may be geochemical similarity of high ^{3}He/^{4}He ratios across Yellowstone caldera which in many cases correlate to high CO_2, a location of flux and volcanic center still remain critical, that's high CO_2 is expected in inside the caldera rim rather than outside (Griesshaber et al., 1992). This spatial relationship can be displayed in Fig. 5.11 where the Rukwa Rift Basin located relatively farther from volcanic center has higher helium concentration ~>6% than the Yellowstone, Rungwe Volcanics and Bakreswar-Tantloi with average concentration ~<3%. However, the volcanic dilution effects of CO_2 may be complicated by a nature of tectonic activity and resulting structural compartmentalization which controls a type and extent area of fluid circulation in the region (Weinlich et al., 1999).

We argue that it is not the extreme heat flow and temperature which matters for the release of radiogenic helium rather a minimum heat flow and temperature above closure conditions for most helium-retentive minerals (Danabalan et al., 2022; Fig. 5.8). This hypothesis can explain why at the Yellowstone low isotopic ratios <2.5 Ra and high helium concentrations are observed outside the caldera with moderate heat flow ~100-300 mW/m^2 e.g. at Heart Lake Geyser Basin. Inside the caldera, however, there is extremely high heat flow 600-700 mW/m^2 and high geothermal gradients ~700-1000°C/km but low helium concentration i.e. high isotopic ratio ~7.5- 17 Ra associated with CO_2 rich fluids (Morgan et al., 1977; Hurwitz et al., 2012; Lowenstern et al., 2014; Fig. 5.8). Similarly, in the Rukwa Rift, the highest heat flow >100 mW/m^2 and low helium concentration 0.2% (>6.0 Ra) is observed within ~20 kms diameter from the Rungwe volcanic centre while in the Rukwa Rift Basin located more than 60 kms from the centre there is low heat flow <70 mW/m^2 and high radiogenic helium concentration > 1% (<1.0 Ra) (Njinju et al., 2019; Danabalan et al., 2022; Fig. 5.10). We suggest that a location of the helium prospects relative to either volcanic centres, coal beds or metamorphic provinces will determine the composition of other fluids within the helium system, that is whether the system is either nitrogen or carbon dioxide rich (Fig. 5.13).

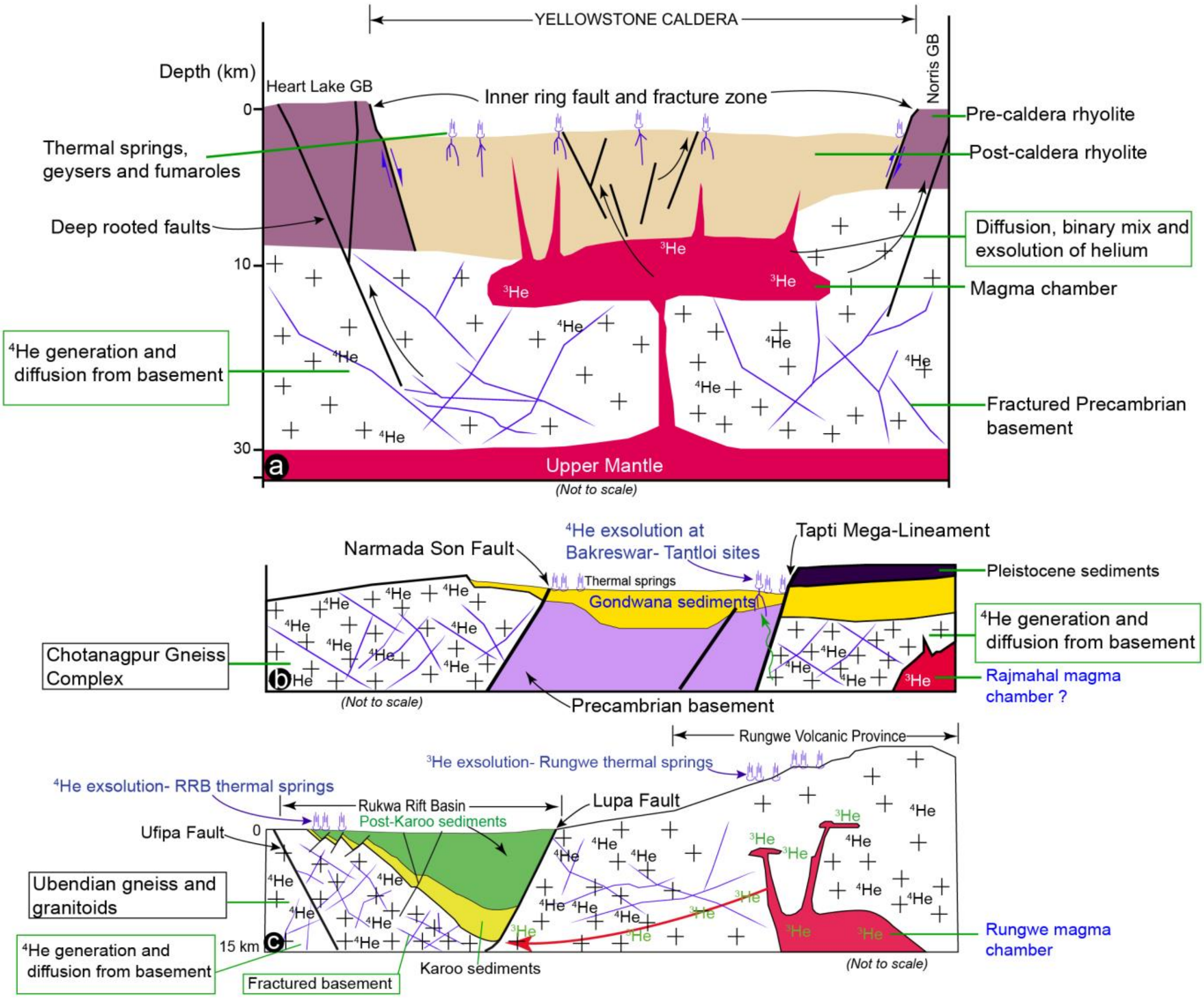

Fig. 5.12. Conceptual model showing helium generation and release model for helium via deep structural network and hydrothermal fluid at (a) Yellowstone (USA) (after Lowenstern et al., 2014; Lowenstern et al., 2015) and (b) Bakreswar-Tantloi province in India (after Chaudhuri et al., 2015; Valdiya and Sanwal, 2017) and (c) Rukwa Rift (Tanzania) (after Mulaya et al., 2022).

5.4.2 Geologic setting of India and helium release at the Bakreswar-Tantloi province

The India subcontinent exhibits the prerequisites for ^{4}He resources with identified generation to accumulation elements in various geological settings that are somewhat similar in nature to the Rukwa Rift in Tanzania (see Table 5.1; Fig. 5.4; Fig.

5.9; Fig. 5.10; Fig. 5.12b-c). As Danabalan (2017) suggested, these prerequisites include: (1) Abundance of substantial Precambrian cratons associated with mobile belts to provide source rocks for helium generation (Jain et al., 2020). (2) Recent tectonic events associated with heat flow perturbation and crustal opening; basement-rooted faulting produced by rifting and/or uplift to pave a way for release and migration of generated helium (e.g. Chaudhuri et al., 2015). (3) Timely formation of adjacent sedimentary basins which are likely to contain reservoir rocks, seals and trapping structures capable of accumulating helium and preserving them over geological time periods. All these geologic components are potentially suited to creating play fairways for helium system.

High helium concentration at the Bakreswar-Tantloi province is potentially favored by geothermal activity associated with high heat flow (Table 5.1; Fig. 5.12b). The Bakreswar-Tantloi province lies within a geologically complex region, near the dynamic frontal part of the Indo-Australian and Eurasian plate boundary (Das et al., 2015). These recent tectonic activities are potentially associated with deep-seated tectonism which controls the distribution of geothermal provinces and sediments deposition as potential settings for helium accumulation (Jain et al., 2020).

Previous studies show crustal stretching thinning from 36 to 24 km across the Bakreswar - Tantloi thermal springs within the West Bengal Basin (Mukhopadhyay et al 1986; Ghost et el., 2002). A combination of crustal stretching, uplifted mantle and heat transfer beneath the West Bengal Basin accounts for high heat flow (~200mW/m^2) and elevated geothermal gradient (~80°C/km) hence leading to thermal conditions above closure for helium - retentive minerals (Shanker, 1988; Ghose et al., 2002; Singh et al., 2004; Chaudhuri et al., 2015; Danabalan et al., 2022). The crustal-scale structures associated with residual heat flow most likely from Rajmahal volcanism and/or radiogenic heat production in the crust, plays a significant role in the consistent high heat recharge into the region (Sarangi, 2003;

Fig. 5.12b). The heat flow is a very critical component for heating the crust and facilitates fracturing of rocks which enables migration of helium from crust (e.g. Torgersen and Clarke, 1985; Etiope and Martinelli, 2002; Brown, 2021; Danabalan et al., 2022; Table 5.1). We suggest that high heat flow potentially triggers helium flux and thermal release of deep fluids from the Chotanagpur Gneissic Complex hence leading to an optimal helium play fairway we observe at the Bakreswar - Tantloi province (Fig. 5.5b; Fig. 5.7b). The rocks in this area have been documented to be highly sheared, brecciated and mylonitized hence adding more porosity and permeability for helium migration (Maji et al., 2021).

Elsewhere within the India Subcontinent, notable geothermal provinces found on the west coast, east coast and Himalayan belt exhibit high heat flow up to 230 mW/m^2 (Chaudhuri et al., 2019; Fig. 5.4; Table. 5.1). Such high heat flow may equally promote the deep convective circulation of fluids hence accounting for the anomalous helium concentration observed widely at more than 300 sites across the country (Chaudhuri et al., 2019; Fig. 5.12b).

5.4.3 Potential helium charge at the Yellowstone and Bakreswar - Tantloi province

The helium charge mechanism at the Yellowstone and Bakreswar-Tantloi provinces is still not well understood. Previous studies in the Yellowstone geothermal province suggest that the loss of helium is due to thin sedimentary packages and a lack of traps suitable for helium accumulation (Lowenstern et al., 2015; Danabalan, 2017). Although a large volume of radiogenic helium is lost to atmosphere, we argue that the Yellowstone may still serve as a potential helium source i.e., a source to charge into the neighbouring prospects via migration (Fig. 5.12a). In proximity, the Yellowstone is surrounded with Cretaceous shale and sandstone sequences at Mount Everts whereas Montana sedimentary provinces and volcanoclastic sequences of the Absaroka Supergroup (Eocene Epoch) can be potential provinces for radiogenic helium accumulation (Smedes and Prostka, 1972; Ruppel, 1982;

Malone, 1995; Lowenstern et al., 2015). However, the question of trap integrity and efficiency remains open.

Similarly, there is still little understanding on helium trap integrity and sealing efficiency at the Bakreswar-Tantloi province. However, we suggest that both deep diffusive transport from fracture basement and shallow gas phase from exsolution above bubble point may dominate the migration of ^{4}He followed by long-lateral migration into neighboring potential reservoirs (Cheng et al., 2021; Fig. 5.12b). The potential reservoirs may either be located either within or in proximity to these sites (Danabalan, 2017).

It appears that both the Rukwa Rift and Bakreswar-Tantloi are characterized by similar Gondwana sediments which suggest similar settings linked to disaggregation of the Gondwana Supercontinent (Meert and Pandit, 2015; Jain et al., 2020; Fig. 5.7; Fig. 5.9; Fig. 5.10; Fig. 5.12 b-c). The Gondwana sediments also known as Karoo Supergroup in the Rukwa Rift Basin serves as one of the potential reservoirs for helium overlying the Precambrian Ubendian basement (Mulaya et al., 2022; Fig. 5.12c). We suggest that the lateral migration of helium may continue via optimal conduits, i.e. faults over tens of kilometres until entrapped and accumulation occurs in distal settings. However, the preservation requires efficient seal rocks such as evaporites which are out of scope for this study. Further study on seal efficiency and trap analysis is recommended to confirm effective helium sealing in respective to stratigraphic sequences.

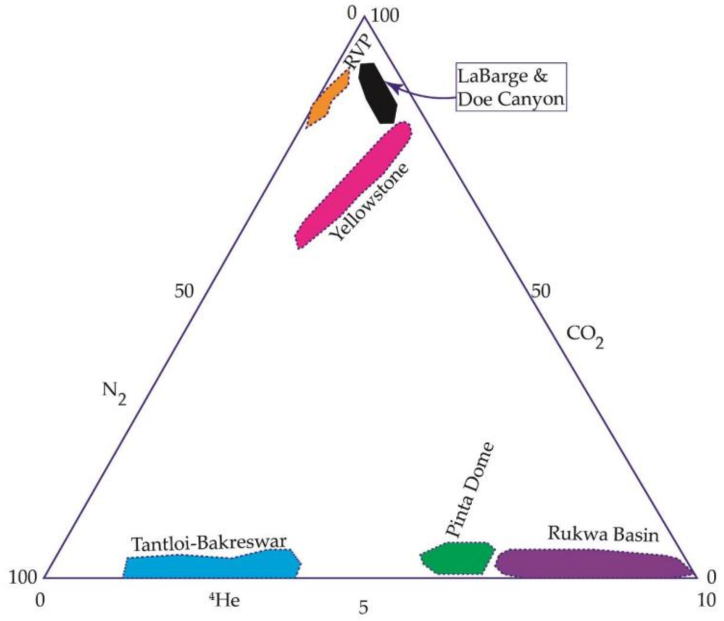

Fig. 5.13. Ternary plot showing relative elemental composition of thermal spring gases in helium system for Bakreswar - Tantloi (India), Rukwa Rift (Tanzania) and Yellowstone (USA). Note RVP - Rungwe Volcanic Province (After Chaudhuri et al., 2015; Mtili et al., 2022).

5.4.4 Fluid migration model at the Yellowstone province

The Yellowstone province is an area of active tectonics that paves a way for helium release from the basement rocks triggered by elevated heat flow (Torgersen and Clarke, 1985; Etiope and Martinelli, 2002; Danabalan et al., 2022; Fig. 5.12a). Migration of deep crustal fluids is facilitated through deep-rooted faulting connecting to thermal springs and fumarolic vents as the main conduits (Danabalan, 2017; Lowenstern et al., 2015; Fig. 5.8; Fig. 5.12a). Most likely the migration is dominated by diffusive transport and advection aided by sufficient hydrothermal plumbing associated with high heat flow (Lowenstern et al., 2015; Cheng et al., 2021; Fig. 5.12a). The high heat flow from the supervolcano which heats up the Wyoming Craton may potentially promote a primary release of ^{4}He from source minerals (e.g. Lowenstern et al., 2014). The geochemistry and isotopic studies exhibit a binary mix of radiogenic (^{4}He) and primordial (mantle) derived ^{3}He (Lowenstern et al., 2014 and references therein). Abundance of magmatic fluids rich in CO$_2$ up to 99 % may play a vital role in the dissolution and exsolution of other fluids including the accumulation rate of helium gas phase (Cheng et al., 2021; Fig. 5.12a).

5.5.0 Conclusions

In this contribution we conclude the following:

- The Rukwa Rift (Tanzania), the Bakreswar-Tantloi (India) and the Yellowstone (USA) present unique geological and structural conditions with proven occurrences of high helium concentration above minimum economic concentration ~0.3%.
- The Yellowstone, Rukwa Rift and Bakreswar-Tantloi exhibit anomalous heat flow and geothermal gradients which are sufficient to trigger helium release from helium-retentive minerals such as apatite, zircon, uraninite and initiate diffusive transport.
- High helium concentration up to 3% that is ten times minimum economic concentration in geothermally active provinces of the India Subcontinent present potential interest for further helium exploration.
- High helium occurrences in the India subcontinent are associated with high uranium lead ratio.
- Despite the occurrences of high helium concentration in the Yellowstone and Bakreswar – Tantloi provinces, trap integrity may still be of a challenge
- Migration of great volumes of helium at sites such as the Yellowstone and Bakreswar-Tantloi provinces may be dominated by diffusive transport, exsolution and advection aided by sufficient hydrothermal plumbing associated with high heat flow.
- Despite the requirement of high heat flow for releasing helium, close proximity to the volcanic centers may increase dilution of the helium system with CO_2.

References

Allen, E.T., Day, A.L., 1935. Hot Springs of the Yellowstone National Park 466. Carnegie Institute of Washington Publication (525 pp.).

Ballentine, C.J., Sherwood Lollar, B., 2002. Regional groundwater focusing on nitrogen and noble gases into the Hugoton-Panhandle giant gas field. USA. Geochim. Cosmochim. Acta 66, 2483–2497. https://doi.org/10.1016/S0016-7037(02)00850- 5.

Barry, P.H., Hilton, D.R., Fischer, T.P., De Moor, J.M., Mangasini, F. and Ramirez, C., 2013. Helium and carbon isotope systematics of cold "mazuku" CO2 vents and hydrothermal gases and fluids from Rungwe Volcanic Province, southern Tanzania. *Chemical Geology*, *339*, pp.141-156.

Boniface, N., Schenk, V., & Appel, P. (2012). Paleoproterozoic eclogites of MORB-type chemistry and three Proterozoic orogenic cycles in the Ubendian Belt (Tanzania): Evidence from monazite and zircon geochronology, and geochemistry. Precambrian Research, 192, 16–33. https://doi.org/10.1016/j.precamres.2011.10.007.

Bhukosh, 2022: https://bhukosh.gsi.gov.in/Bhukosh/Public accessed on 5th March 2022.

Brown, A. J. (2021). Screening the helium opportunity of India for future exploration and production. Undergraduate project, University of Southampton, UK, 1-21.

Chaudhuri, H., Sinha, B. and Chandrasekharam, D., 2015. Helium from geothermal sources. Proc World Geotherm Congr.

Chaudhuri, H., Seal, K., Maji, C., Pal, S. and Mandal, M.K., 2019. The unrevealed facts on helium resources of India. *Arabian Journal of Geosciences*, *12*(6), pp.1-19.

Cheng, A., Lollar, B.S., Warr, O., Ferguson, G., Idiz, E., Mundle, S.O., Barry, P.H., Byrne, D.J., Mabry, J.C. and Ballentine, C.J., 2021. Determining the role of diffusion and basement flux in controlling 4He distribution in sedimentary basin fluids. *Earth and Planetary Science Letters*, *574*, p.117175.

Christiansen, R.L., 2001. *The quaternary and pliocene Yellowstone Plateau volcanic field of Wyoming, Idaho, and Montana* (Vol. 729). US Department of the Interior, US Geological Survey.

Cordani, U.G. and Sato, K., 1999. Crustal evolution of the South American Platform, based on Nd isotopic systematics on granitoid rocks. *Episodes Journal of International Geoscience*, *22*(3), pp.167-173.

Courtillot, V., 2002. *Evolutionary catastrophes: the science of mass extinction*. Cambridge University Press.

Danabalan, D. (2017). Helium: Exploration methodology for a strategic resource, PhD thesis, Durham University, UK, 1-293.

Danabalan, D., Gluyas, J.G., Macpherson, C.G., Abraham-James, T.H., Bluett, J.J., Barry, P.H. and Ballentine, C.J., 2022. The principles of helium exploration. *Petroleum Geoscience*, *28*(2), pp.petgeo2021-029.

Das, N.K., Bhandari, R.K., Sen, P. and Sinha, B., 2005. The helium potential of India. *Current Science*, *88*(12), pp.1883-1888.

Delvaux, D., Kervyn, F., Macheyeki, A. S., & Temu, E. B. (2012). Geodynamic significance of the TRM segment in the East African Rift (W-Tanzania): Active tectonics and paleostress in the Ufipa plateau and Rukwa basin. Journal of Structural Geology, 37, 161–180. https://doi.org/10.1016/j.jsg.2012.01.008

Dey, S. and Moyen, J.F., 2020. Archean granitoids of India: windows into early Earth tectonics–an introduction. *Geological Society, London, Special Publications*, *489*(1), pp.1-13.

Dulfer, H., Milligan, P.R., Coghlan, R., Czarnota, K., Highet, L.M., Champion, D.C. and Skirrow, R.G., 2016. *Potential for intrusion-hosted Ni-Cu-PGE sulfide deposits in Australia: a continental-scale analysis of mineral system prospectivity*. Geoscience Australia.

Ebinger, C. (2005). Continental break-up: The East African perspective. Astronomy and Geophysics, 46(2), 2.16–2.21. https://doi.org/10.1111/j.1468-4004.2005.46216.x

Ebinger, C. J., Deino, A. L., Drake, R. E., & Tesha, A. L. (1989). Chronology of volcanism and rift basin propagation: Rungwe volcanic province, East Africa. Journal of Geophysical Research: Solid Earth, 94(B11), 15785–15803. https://doi.org/10.1029/JB094 iB11p 15785

Etiope, G. and Martinelli, G., 2002. Migration of carrier and trace gases in the geosphere: an overview. *Physics of the earth and planetary interiors*, *129*(3-4), pp.185-204.

Fournier, R.O., 1989. Geochemistry and dynamics of the Yellowstone National Park Hydrothermal System. Ann. Rev. Earth Planet. Sci. 17, 13–53.

Ghose, D., Chowdhury, D.P. and Sinha, B., 2002. Large-scale helium escape from earth surface around Bakreswar–Tantloi geothermal area in Birbhum district, West Bengal, and Dumka district, Jharkhand, India. *Current Science*, pp.993-996.

Gluyas, J.G. (2019a). The emergence of the helium industry: the history of helium exploration, part 1 of 2, American Association of Petroleum Geologists Explorer, January 2019,16-17

Gluyas, J.G. (2019b) Helium shortages and emerging helium provinces: the history of helium exploration part 2, American Association of Petroleum Geologists Explorer, February 2019, 18-22.

Griesshaber E., O'Nions R. K., and Oxburgh E. R. (1992). Helium and carbon isotope systematics in crustal fluids from the Eifel, the Rhine Graben and Black Forest, F.R.G. Chem. Geol. 99, 213–235.

Harkin, D.A., 1960. The Rungwe Volcanics at the Northern End of Lake Nyasa, Geological Survey of Tanganyika, Dodoma. 172 pp.

https://www.freeworldmaps.net accessed on 26th October 2022.

Hurwitz, S., Harris, R.N., Werner, C.A. and Murphy, F., 2012. Heat flow in vapor dominated areas of the Yellowstone Plateau Volcanic Field: Implications for the thermal budget of the Yellowstone Caldera. *Journal of Geophysical Research: Solid Earth*, *117*(B10).

James, T. C., 1967. Thermal springs in Tanzania. Institution of Mining and Metallurgy, Transactions/Section B (Applied Earth Science), 76, B1–B18. In Macheyeki, A. S., Delvaux, D., De Batist, M., & Mruma, A. (2008). Fault kinematics and tectonic stress in the seismically active Manyara–Dodoma Rift segment in Central Tanzania–Implications for the East African Rift. Journal of African Earth Sciences, 51(4), 163–188.

Jain, A.K., Banerjee, D.M. and Kale, V.S., 2020. *Tectonics of the Indian subcontinent*. Springer Nature.

Jain, A.K. and Banerjee, D.M., 2020. The Indian subcontinent: its tectonics. *Proceedings of the Indian National Science Academy*, *86*, pp.775-875.

Kilembe, E. A., & Rosendahl, B. R. (1992). Structure and stratigraphy of the Rukwa rift. Tectonophysics, 209(1–4), 143–158. https:// doi.org/10.1016/0040-1951(92)90016 -Y

Lavayssière, A., Drooff, C., Ebinger, C., Gallacher, R., Illsley-Kemp, F., Oliva, S.J. and Keir, D., 2019. Depth extent and kinematics of faulting in the southern Tanganyika rift, Africa. *Tectonics*, *38*(3), pp.842-862.

Lemna, O. S., Stephenson, R., & Cornwell, D. G. (2019). The role of pre-existing Precambrian structures in the development of Rukwa RiftBasin, southwest Tanzania. Journal of African Earth Sciences, 150, 607–625. https://doi.org/10.1016/j.jafrearsci.2018.09.015

Lenoir, J. L., Li.geois, J. P., Theunissen, K., & Klerkx, J. (1994). The Palaeoproterozoic Ubendian shear belt in Tanzania: Geochronology and structure. Journal of African Earth Sciences, 19(3), 169–184. https://doi.org/10.1016/0899-5362(94)90059-0

Lowenstern, J.B., Evans, W.C., Bergfeld, D. and Hunt, A.G., 2014. Prodigious degassing of a billion years of accumulated radiogenic helium at Yellowstone. *Nature*, *506*(7488), pp.355-358.

Lowenstern, J.B., Bergfeld, D., Evans, W.C. and Hunt, A.G., 2015. Origins of geothermal gases at Yellowstone. *Journal of Volcanology and Geothermal Research*, *302*, pp.87-101.

Maji, C., Chaudhuri, H. and Khutia, S., 2021. Quantitative approximation of geothermal potential of Bakreswar geothermal area in eastern India. In *Geothermal Energy*. IntechOpen.

Malone, D.H., 1995. Very large debris-avalanche deposit within the Eocene volcanic succession of the northeastern Absaroka Range, Wyoming. *Geology*, *23*(7), pp.661-664.

Manya, S., Maboko, M.A. and Nakamura, E., 2007. The geochemistry of high-Mg andesite and associated adakitic rocks in the Musoma-Mara Greenstone Belt, northern Tanzania: possible evidence for Neoarchaean ridge subduction? *Precambrian Research*, *159*(3-4), pp.241-259.

Meert, J.G., Pandit, M.K., Pradhan, V.R., Banks, J., Sirianni, R., Stroud, M., Newstead, B. and Gifford, J., 2010. Precambrian crustal evolution of Peninsular India: a 3.0-billion-year odyssey. *Journal of Asian Earth Sciences*, *39*(6), pp.483-515.

Meert, J.G. and Pandit, M.K., 2015. The Archaean and Proterozoic history of Peninsular India: tectonic framework for Precambrian sedimentary basins in India. *Geological Society, London, Memoirs*, *43*(1), pp.29-54.

Morgan, P., Blackwell, D.D., Spafford, R.E. and Smith, R.B., 1977. Heat flow measurements in Yellowstone Lake and the thermal structure of the Yellowstone caldera. *Journal of Geophysical Research*, *82*(26), pp.3719-3732.

Morley, C. K., Day, R. A., Lauck, R., Bosher, R., Stone, D. M., Wigger, S. T., Wescott, W. A., Haun, D., Bassett, N., & Bosworth, W. (1999b). Geology and geophysics of the Anza Graben. In C.K. Morley (Ed.), Geoscience of rift systems—Evolution of East Africa: AAPG studies in geology no. 44 (pp. 67–90).

Mshiu, E.E. and Maboko, M.A., 2012. Geochemistry and petrogenesis of the late Archaean high-K granites in the southern Musoma-Mara Greenstone Belt: Their influence in evolution of Archaean Tanzania Craton. *Journal of African Earth Sciences*, *66*, pp.1-12.

Mtelela, C., Roberts, E. M., Downie, R., & Hendrix, M. S. (2016). Interplay of structural, climatic, and volcanic controls on late quaternary lacustrine–deltaic sedimentation patterns in the Western Branch of the East African Rift System, Rukwa Rift Basin. Tanzania. Journal of Sedimentary Research, 86(10),1179–1207. https://doi.org/10.2110/jsr.2016.73

Mtili, K.M., Byrne, D.J., Tyne, R.L., Kazimoto, E.O., Kimani, C.N., Kasanzu, C.H., Hillegonds, D.J., Ballentine, C.J. and Barry, P.H., 2021. The origin of high helium concentrations in the gas fields of southwestern Tanzania. *Chemical Geology*, *585*, p.120542.

Mueller, P.A. and Frost, C.D., 2006. The Wyoming Province: a distinctive Archean craton in Laurentian North America. *Canadian Journal of Earth Sciences*, *43*(10), pp.1391-1397.

Mueller, P.A., Mogk, D.W., Henry, D.J., Wooden, J.L. and Foster, D.A., 2008. Geologic evolution of the Beartooth Mountains: Insights from petrology and geochemistry. *Northwest Geology*, *37*, pp.5-20.

Mukhopadhyay, M., Verma, R.K. and Ashraf, M.H., 1986. Gravity field and structures of the Rajmahal Hills: Example of the Paleo-Mesozoic continental margin in eastern India. *Tectonophysics*, *131*(3-4), pp.353-367.

Mulaya, E., Gluyas, J., McCaffrey, K., Phillips, T. and Ballentine, C., 2022. Structural geometry and evolution of the Rukwa Rift Basin, Tanzania: Implications for helium potential. *Basin Research*, *34*(2), pp.938-960.

Naqvi, S.M. and Rogers, J.J.W., 1987. Precambrian geology of India: Oxford University Press. *New York*.

Njinju, E.A., Kolawole, F., Atekwana, E.A., Stamps, D.S., Atekwana, E.A., Abdelsalam, M.G. and Mickus, K.L., 2019. Terrestrial heat flow in the Malawi Rifted Zone, East Africa: Implications for tectono-thermal inheritance in continental rift basins. *Journal of Volcanology and Geothermal Research*, *387*, p.106656.

Oldham, R. D.: Geology of Jaunsar, Rec. Geol. Surv. India, XVI, (1883), 193-196.

Quennell, A. M., McKinlay, A. C., & Aitken, W. G. (1956). Summary of the geology of Tanganyika, part 1 (p. 126). Geological Surv.Tanganyika Mem.

Ramakrishna, M. and Vaidyanadhan, R., 2008. Geology of India, Vol. 1. *Geological Society of India, Bangalore*, *556*(3).

Roberts, E. M., O'Connor, P. M., Stevens, N. J., Gottfried, M. D., Jinnah, Z. A., Ngasala, S., Choh, A. M., & Armstrong, R. A. (2010). Sedimentology and depositional environments of the Red Sandstone Group, Rukwa Rift Basin, southwestern Tanzania: New insight into Cretaceous and Paleogene terrestrial ecosystems and tectonics in sub-equatorial Africa. Journal of African Earth Sciences, 57(3), 179–212.https://doi.org/10.1016/j.jafre arsci.2009.09.002

Roe, E., Dypvik, H., & Kilembe, E. (1996). Sedimentological analysis of the logs and cuttings from the wells Ivuna #1 and Galula #1, the Rukwa Rift valley, Western Tanzania—A progress report, (unpublished).

Ruppel, E.T., 1982. Geology of pre-Tertiary rocks in the northern part of Yellowstone National Park. In: Reid, S.G., Foote, D.J. (Eds.), Geology of the Yellowstone Park Area. Wyoming Geological Association 33rd Annual Field Conference Guidebook, pp. 111–137.

Sarangi, A.K., 2003. Grade control in Jaduguda uranium mine, Jharkhand. *The transactions, the Mining Geological and Metallurgical institute of India*, *99*(1), pp.2002-03.

Singh, A.P., Kumar, N. and Singh, B., 2004. Magmatic underplating beneath the Rajmahal Traps: gravity signature and derived 3-D configuration. *Journal of Earth System Science*, *113*(4), pp.759-769.

Shanker, R. and Geological Survey of India (GSI)., 1991 *Geothermal atlas of India*. Geological Survey of India.

Shanker, R., 1988. Heat-flow map of India and discussions on its geological and economic significance. *Indian Minerals*, *42*(2), pp.89-110.

Smedes, H.W. and Prostka, H.J., 1972. *Stratigraphic framework of the Absaroka volcanic supergroup in the Yellowstone National Park region* (No. 729-C).

Theunissen, K., Klerkx, J., Melnikov, A., & Mruma, A., 1996. Mechanisms of inheritance of rift faulting in the western branch of the East African Rift, Tanzania. *Tectonics*, *15*(4), 776-790. https://doi.org/10.1029/95TC03685

Torgersen, T. and Clarke, W.B., 1985. Helium accumulation in groundwater, I: An evaluation of sources and the continental flux of crustal 4He in the Great Artesian Basin, Australia. *Geochimica et Cosmochimica Acta*, *49*(5), pp.1211-1218.

Yuan, H. and Romanowicz, B., 2010. Lithospheric layering in the North American craton. *Nature*, *466*(7310), pp.1063-1068.

Yuan, H., Dueker, K. and Stachnik, J., 2010. Crustal structure and thickness along the Yellowstone hot spot track: Evidence for lower crustal outflow from beneath the eastern Snake River Plain. *Geochemistry, Geophysics, Geosystems*, *11*(3).

Weinlich, F.H., Bräuer, K., Kämpf, H., Strauch, G., Tesař, J. and Weise, S.M., 1999. An active subcontinental mantle volatile system in the western Eger rift, Central Europe: Gas flux, isotopic (He, C, and N) and compositional fingerprints. *Geochimica et Cosmochimica Acta*, *63*(21), pp.3653-3671.

Werner, C., Brantley, S., 2003. CO2 emissions from the Yellowstone volcanic system. Geochem. Geophys. Geosyst. 4 (no. 7) (http://dx.doi.org/10.1029/2002GC000473).

Wescott, W. A., Krebs, W. N., Englehardt, D. W., & Cunningham, S. M. (1991). New biostratigraphic age dates from the Lake Rukwa Basin in western Tanzania. AAPG Bulletin, 75, 1255–1263.

Van Hinsbergen, D.J., Buiter, S.J., Torsvik, T.H., Gaina, C. and Webb, S.J., 2011. The formation and evolution of Africa from the Archaean to Present: introduction. *Geological Society, London, Special Publications*, *357*(1), pp.1-8.

Valdiya, K.S. and Sanwal, J., 2017. Satpura Horst and Narmada–Tapi Grabens. In *Developments in Earth Surface Processes* (Vol. 22, pp. 237-247). Elsevier.

Chapter 6: Conclusions and future research

6.1.0 Summary and implication of findings

A study in the Rukwa Rift Basin (RRB) suggests a typical half-graben geometry containing a gently dipping wedge of synextensional sedimentary packages up to a maximum thickness of ~6000 ms TWT. The overall geometry was modulated by shear zones and fault activity throughout the basin history. The resulting basin architecture is due to multiple rifting phases from the Paleozoic to the Cenozoic Era which controlled the positioning of deposition systems and physiography resulting in areas of sediment accumulation minima and maxima. These structures particularly basement-rooted faults and associated sedimentary sequences accommodate ESE-WNW directed oblique divergence which exert control on occurrences of thermal springs rich in helium-nitrogen that are manifest at the surface regionally. Similarly, extensional tectonics exerted significant control on the provenance, differential erosional patterns, drainage system and sediment routing in the Rukwa Rift.

The Saza Shear Zone (SSZ) was mapped for the first time in this study, and it lies sub-parallel to the extension direction of the Rukwa Rift crosscutting the NW-trending Chisi Shear Zone (CSZ) almost perpendicularly. The SSZ is inferred to have been provided an earlier strain shadow and partitioning which controlled segmentation of the Rukwa Rift into two structural domains A (north) and B (south). Similarly, segmentation of the Rukwa Rift inhibited an even distribution of regional stresses between the two structural domains, hence partitioning the extension rate and strains in the two domains. Therefore, the SSZ, CSZ and deep-rooted faults such as the Lupa Fault presents the main structures modulating the RRB tectonics and also may equally play the role of fluid migration and partitioning.

This study suggests remarkable inherited fabrics due to multiphase rifting tectonics of the Rukwa Rift. The earlier dominant fault orientations e.g. Precambrian basement fabrics are collinear with the recent mapped faults e.g. Cenozoic faults (Fig. 6.1a-c). The seismic sections reveal several zones of inherited basement fabrics where similar orientation of faults systems connect from the basement extending to the overlying sedimentary sequences (Fig. 6.1a-c). The combination of these faults into the basin likely implies two plausible explanations; either reactivation of the pre-existing fabrics (Precambrian) in controlling rift basin development and geometry (e.g. Peace et al., 2018; Heilman et al., 2019) or these faults are of post-Karoo ages (Permian) that extended down into the basement as they grew with time. These suggestions are largely in agreement with earlier conclusions from aeromagnetic studies by Heilman et al. (2019), Lemna et al. (2019) and field documentation (cf. Theunissen et al. 1996; Delvaux et al., 2012).

Interpretation of seismic reflection data reveal two phases of inversion which resulted in different fold styles in the RRB; multifaulted anticlinal Karoo inversion during the Early Jurassic and a mild inversion during the Pleistocene which gave rise to both symmetrical and asymmetrical open anticlines. We hypothesize that the earlier was likely attributable to a compressional pulse associated with uplift during initiation of Gondwana rifting while the later was short-lived inversion due to either (1) kinematic interactions of the Nubia-Victoria-Rovuma-San plates and associated tectonic boundaries; (2) variation of resultant local strains on intrabasinal faults inherited from basement fabrics, or (3) thermo-kinematic anomalies from the East African mantle plumes. However, we observe no inversion structures within the Kwera-Saza Accommodation Zone (KSAZ) which suggests that this area formed a strain shadow, as commonly observed in transfer zones (cf. Mulaya et al., 2022).

Isochron and time-thickness maps illustrate that the depocenters to the south of the RRB might have been isolated initially during Karoo rifting, contiguous during Cretaceous and possibly linked into a single main depocenter during the latter stages of rifting (Late Miocene -Pleistocene). The distribution of multiple depocenters in space and time which thicken towards normal faults, are inferred to have developed during active fault activities hence providing insights into proportions of accommodation space and potential distribution of helium reservoirs.

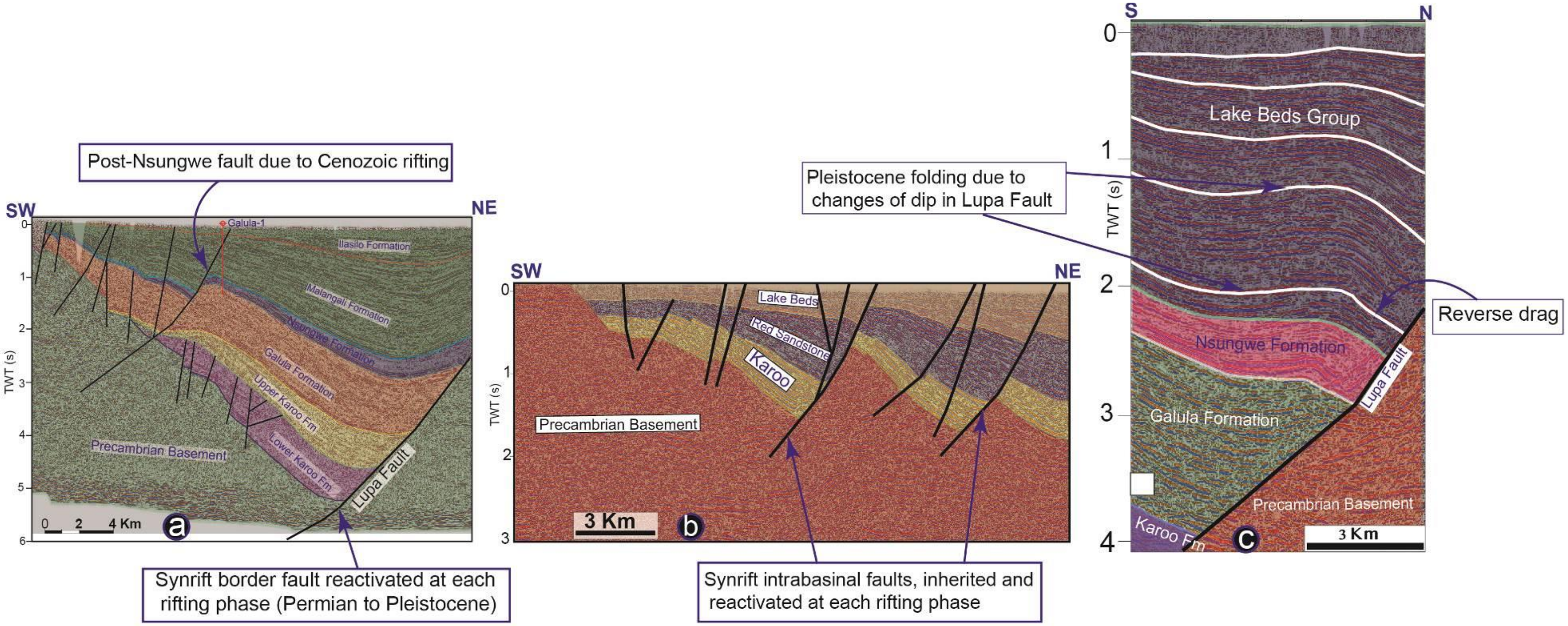

Fig. 6.1. Geoseismic section showing a typical example of fault reactivation, fabric inheritance, fault growth and timing in the history of the RRB. (a) Lupa fault reactivation from Permian to Pleistocene and SW-dipping intrabasinal fault during Cenozoic rifting (b) Basement faults inherited into intrabasinal faults throughout the basin history of the RRB (c) Pleistocene folding leading to reverse drag onto the Lupa Fault due to changes in the geometry of the Lupa Fault downdip (modified after Mulaya et al., 2022).

The gas composition data and statistical analysis of heat flow from the Rukwa Rift show significantly high radiogenic helium content above the economic threshold of 0.3% from sites which exhibit high heat flow ~64 - 99 mW/m^2. The anomalous thermal conditions show a geothermal gradient of ~40°C/km and temperature in Ivuan-1 well of >100°c (Fig. 6.2). These thermal conditions are sufficient to trigger helium release from Precambrian basement rich in radioactive elements such as uranium and thorium. High heat flow and geothermal gradient enhance migration of deep crustal fluids containing helium primarily via basement fractures and basement-rooted faults. Most likely the migration is dominated by diffusive transport and advection to charge both proximal and distal potential reservoirs in the surrounding region (Fig. 6.3a-b). We conclude that it is not the extreme thermal conditions which matter to trigger the release of radiogenic helium but fulfillment of thermal conditions that are above closure conditions for most helium-retentive minerals to account for the high concentrations of observed helium.

A mass balance calculation shows that the whole crustal volume underlying the East Africa Helium Pool (EAHP) has a capability of producing radiogenic helium of about ∽9.9 x 10^6 mol/yr (∽22 x 10^{-6} mol ^{4}He/m^2 yr) while the total radiogenic helium flux ranges between ∽2.39 x 10^6mol/yr and ∽2.68 x 10^9 mol/yr. The total ^{4}He emission in the RRB is about ∽4.45 x 10^5 - 5.01 x 10^8 mol/yr which is thus equivalent to 19-21% of the total production capacity in the EAHP region. The helium accumulation in the EAHP would have started since the Paleoproterozoic. However, subsequent release has been accelerated largely by episodic tectonothermal events in the region. These results provide a qualitative and quantitative insight to assess helium and other similar settings elsewhere in the world such as Yellowstone (USA) and Bakreswar - Tantloi (India).

Burial history curves of layers in the RRB shows that deposition and subsidence of the Rukwa Rift Basin dates back to 300 My based on Ivuna-1 well (Fig. 6.2). Initially the Karoo Supergroup was at a surface (depth = 0 m) 300 My ago and since then, other new layers including Red Sandstone and Lake Beds Group have been deposited above it. The Karoo layer has thus been buried to greater and greater depths so that the layer is currently at present ca. 2300 m below the surface. At the deepest depth of the Ivuna-1 well the temperature is greater than 100°c, high enough to trigger helium release from helium bearing minerals. Gradients of the burial history curve with gentle gradients of the burial history curves show medium rates of subsidence and burial of sedimentary sequences between the Permian to Oligocene whereas steep gradients reveal a rapid rate of burial and subsidence between the late Miocene and Plio-Pleistocene epochs. The study shows two uplift events in the rift (1) the Mesozoic uplift which was associated with compressional pulse during initiation of Gondwana rifting and (2) the Cenozoic uplift due to the short-lived stress reversal and widespread inversion in the Rukwa Rift (Mulaya et al., 2022, Fig. 6.2).

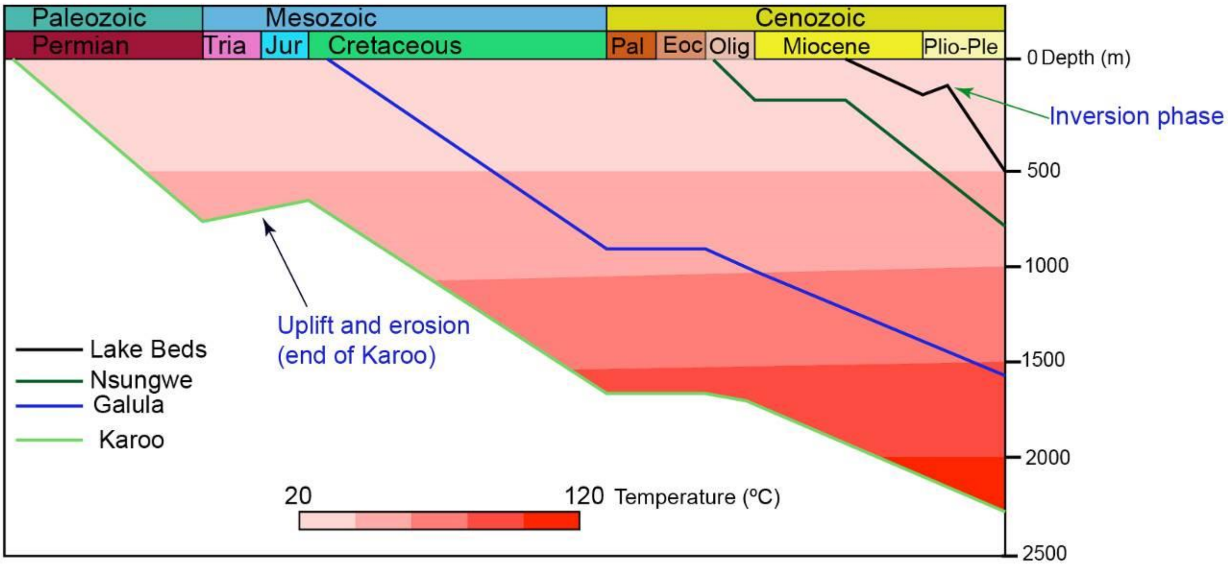

Fig. 6.2. A diagram summarising burial history curves for the major formations in the RRB based on Ivuna-1 well i.e. the depth of burial due to subsidence curve versus the timing of major tectonic events, including the estimated temperatures as a critical component for helium release from minerals and migration. The calculated temperature history is based on assumption of geothermal gradient of 40°C/km and surface temperature of 20°C (after Mulaya et al., 2022, Chapter 4 & 5 in this thesis).

Similar to hydrocarbon systems elsewhere, the potential traps for helium in the RRB exhibit stratigraphic, structural or a combination of both. Notable trapping mechanism includes; juxtaposition of stratal sequences, inversion folds, extensional folds and fault traps widely distributed in the RRB (Fig. 6.3a-b). Petrophysical analysis on outcrop samples which are mainly sandstone sequences from Karoo and Red Sandstone Formation show anomalously high porosity and permeability ranges c. 26-30% and 272.7-660.6 mD respectively. Notable sequences in the stratigraphy includes shales and/or carbonates that have been documented in the Lake Beds strata (Mtelela, 2016) and Nsungwe Formation (Chapter 2) hence implying the presence of effective seals for helium. Altogether these prerequisites elements are appropriate for economic accumulation of radiogenic helium hence their confirmation add a significant value and improve chances of success for helium exploration.

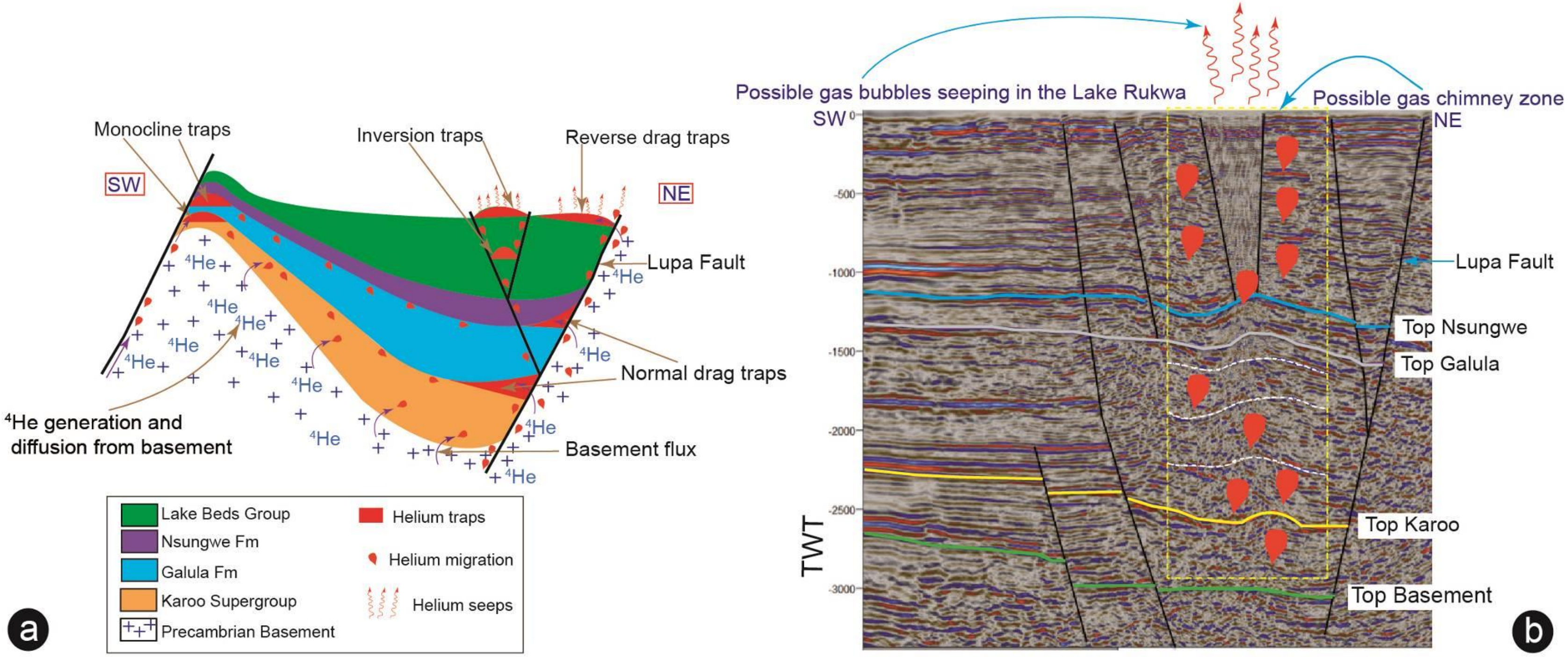

Fig. 6.3. (a) A SW-NE geological section showing helium generation, migration and accumulation model in the RRB. (b) Geoseismic section (X-line TXZ-09/TXZ-46) interpreted as a possible zone of gas chimney.

6.2.0 Recommendations for future research

The coupling of geological, geochemical and structural evidence in this work provides an innovative approach to understanding and assessing the helium potential in the Rukwa Rift section of the East Africa Rift System and other similar tectonic settings elsewhere in the world. However, despite definitive conclusions made in this thesis, we recommend the following as basis for future research which would make significant contributions to our understanding of helium prospectivity.

Interpretation in this study is based on 2-D seismic reflection data which have limited resolution to some extent hence adding uncertainties in our findings. Future research to resolve these uncertainties and possible pitfalls in this work would require additional data particularly additional 3-D seismic reflection datasets (when they become available) tied to well data covering a wide area of the basin. This would enable a detailed understanding of the structural and stratigraphic complexes in the RRB thus improving this work.

Another way to resolve uncertainties of this work would be creating a detailed geochemical and geophysical database integrated through numerical simulations to develop an initial dynamic helium model of the subsurface. Numerical models may include fluid migration, external sources of helium in an open system model and sensitivity testing of the comprehensive model to optimize the available helium resources and quantify uncertainty in the Rukwa Rift.

The mass balance calculation shown in this work can be constrained with further quantitative understanding of post-generation processes such as CO_2 flux estimates, phase separation, groundwater residence time, ^4He flux and migration loss within each different lithological units in the stratigraphic sequences of the RRB.

Many thermal spring sites in the Rukwa Rift are devoid of significant radiogenic helium concentration (e.g. Barry et al., 2013), possibly due to lack of fluid connectivity spatially, i.e. hydrothermal circulation of fluid carrying radiogenic helium and variability of crustal-scale open-system behaviour (e.g. Lowenstern et al., 2014). Sampling of hydrogeological fracture network for fluid age analysis and structural compartmentalization using noble gases would improve our understanding on the relationship between fluid and various structure patterns.

Although seismicity and geodetic observation reveal a complex kinematic interplay of the Nubia-Somalia-Rovuma-San plates as a source of far-field stresses to Rukwa Rift (e.g. Saria et al., 2014; Stamps et al., 2018; Daly et al., 2020; Mulaya et al., 2022), extensive work on numerical and sandbox models may help constrain understanding of the mechanical and rheological complexities involved in inversion episodes within an extensional dominated rift. With this study it is difficult to discern an exclusive single factor which caused inversion and explains its distribution in the region.

This study observes no inversion in the KSAZ due faults acting as a buttress to far field regional and other resultant local forces as observed in other basins (e.g. Walsh et al., 2001; Reilly et al., 2017; Phillips et al., 2020). Understanding of micro structural patterns with steep dips, short wavelength folds and high density faulting not visible in 2-D seismic reflection data may improve our findings and resolve uncertainties in this work.

Anomalously high porosities and permeabilities of outcrop sandstones sequences documented in the RRB reveal potentially good reservoirs for commercial accumulations of helium. However, the presence of other factors such as trap integrity and preservation of the accumulated helium may still be a challenge. Therefore, further research on other critical geological factors, such as good top seal constrained through drilling would improve our understanding on seal rock efficiency. Given small atomic radius of helium (e.g. Danabalan et al., 2022) and multiphase deformation in the RRB (Chapter 2), future work on both stratal seal and fault seal analysis would add further value on petrophysical parameters as important inputs during helium resource estimation.

The Saza Shear Zone mapped for the first time in this work is based on 2-D seismic reflection data and Digital Elevation Model (DEM). Detailed field study in the area is recommended to improve our geological and structural understanding of the proposed shear zone.

Although this work infers a role for thermogenic reaction of organic rich shale and liptinitic coal in the Karoo sequences in producing nitrogen gas in the RRB, future work on testing of this hypothesis by isotopic studies is highly recommended.

References

Barry, P. H., Hilton, D. R., Fischer, T. P., De Moor, J. M., Mangasini, F., & Ramirez, C., 2013. Helium and carbon isotope systematics of cold “mazuku” CO2 vents and hydrothermal gases and fluids from Rungwe Volcanic Province, southern Tanzania Chemical Geology, 339, 141-156. https://doi.org/10.1016/j.chemgeo.2012.07.003

Cheng, A., Lollar, B.S., Warr, O., Ferguson, G., Idiz, E., Mundle, S.O., Barry, P.H., Byrne, D.J., Mabry, J.C. and Ballentine, C.J., 2021. Determining the role of diffusion and basement flux in controlling 4He distribution in sedimentary basin fluids. *Earth and Planetary Science Letters*, *574*, p.117175.

Daly, M.C., Green, P., Watts, A.B., Davies, O., Chibesakunda, F. and Walker, R., 2020. Tectonics and landscape of the central African Plateau and their implications for a propagating Southwestern Rift in Africa. *Geochemistry, Geophysics, Geosystems*, *21*(6), p.e2019GC008746.

Danabalan, D., Gluyas, J.G., Macpherson, C.G., Abraham-James, T.H., Bluett, J.J., Barry, P.H. and Ballentine, C.J., 2022. The principles of helium exploration. *Petroleum Geoscience*, *28*(2), pp.petgeo2021-029.

Delvaux, D., Kervyn, F., Macheyeki, A. S., & Temu, E. B., 2012. Geodynamic significance of the TRM segment in the East African Rift (W-Tanzania): Active tectonics and paleostress in the Ufipa plateau and Rukwa basin. Journal of Structural Geology, 37, 161–180. https://doi.org/10.1016/j.jsg.2012.01.008

Heilman, E., Kolawole, F., Atekwana, E. A., & Mayle, M., 2019. Controls of basement fabric on the linkage of rift segments. *Tectonics*, 38, 1337–1366. https://doi.org/10.1029/2018TC005362.

Lemna, O. S., Stephenson, R., & Cornwell, D. G. (2019). The role of pre-existing Precambrian structures in the development of Rukwa RiftBasin, southwest Tanzania. Journal of African Earth Sciences, 150, 607–625.

Lowenstern, J.B., Evans, W.C., Bergfeld, D. and Hunt, A.G., 2014. Prodigious degassing of a billion years of accumulated radiogenic helium at Yellowstone. *Nature*, *506*(7488), pp.355-358.

Mtelela, C. (2016). Sedimentology and stratigraphy of the late Cenozoic lake beds succession, Rukwa Rift Basin, Tanzania: implications for hydrocarbon prospectivity (Doctoral dissertation, James Cook University). https://researchonline.jcu.edu.au/47290/

Mulaya, E., Gluyas, J., McCaffrey, K., Phillips, T. and Ballentine, C., 2022. Structural geometry and evolution of the Rukwa Rift Basin, Tanzania: Implications for helium potential. *Basin Research*, *34*(2), pp.938-960.

Peace, A., McCaffrey, K., Imber, J., van Hunen, J., Hobbs, R. and Wilson, R., 2018. The role of pre-existing structures during rifting, continental breakup and transform system development, offshore West Greenland. *Basin Research*, *30*(3), pp.373-394. https://doi.org/10.1111/bre.12257

Phillips, T., Jackson, C. A. L., and Norcliffe, J., 2020. Pre-inversion normal fault geometry controls inversion style and magnitude, Farsund Basin, offshore southern Norway. *Solid Earth*. https://doi.org/10.5194/se-11-1489-2020

Reilly, C., Nicol, A. and Walsh, J., 2017. Importance of pre-existing fault size for the evolution of an inverted fault system. *Geological Society, London, Special Publications*, *439*(1), pp.447-463. https://doi.org/10.1144/SP439.2

Saria, E., Calais, E., Stamps, D. S., Delvaux, D., & Hartnady, C. J. H. , 2014. Present-day kinematics of the East African Rift. Journal of Geophysical Research: Solid Earth, 119, 3584–3600. https://doi.org/10.1002/2013JB010901.

Stamps, D.S., Saria, E. and Kreemer, C., 2018. A geodetic strain rate model for the East African Rift System. *Scientific reports*, *8*(1), p.732.

Theunissen, K., Klerkx, J., Melnikov, A., & Mruma, A., 1996. Mechanisms of inheritance of rift faulting in the western branch of the East African Rift, Tanzania. *Tectonics*, *15*(4), 776-790. https://doi.org/10.1029/95TC03685

Walsh, J.J., Childs, C., Meyer, V., Manzocchi, T., Imber, J., Nicol, A., Tuckwell, G., Bailey, W.R., Bonson, C.G., Watterson, J. and Nell, P.A., 2001. Geometric controls on the evolution of normal fault systems. *Geological Society, London, Special Publications*, *186*(1), pp.157-170. https://doi.org/10.1144/GSL.SP.2001.186.01.10

Appendix

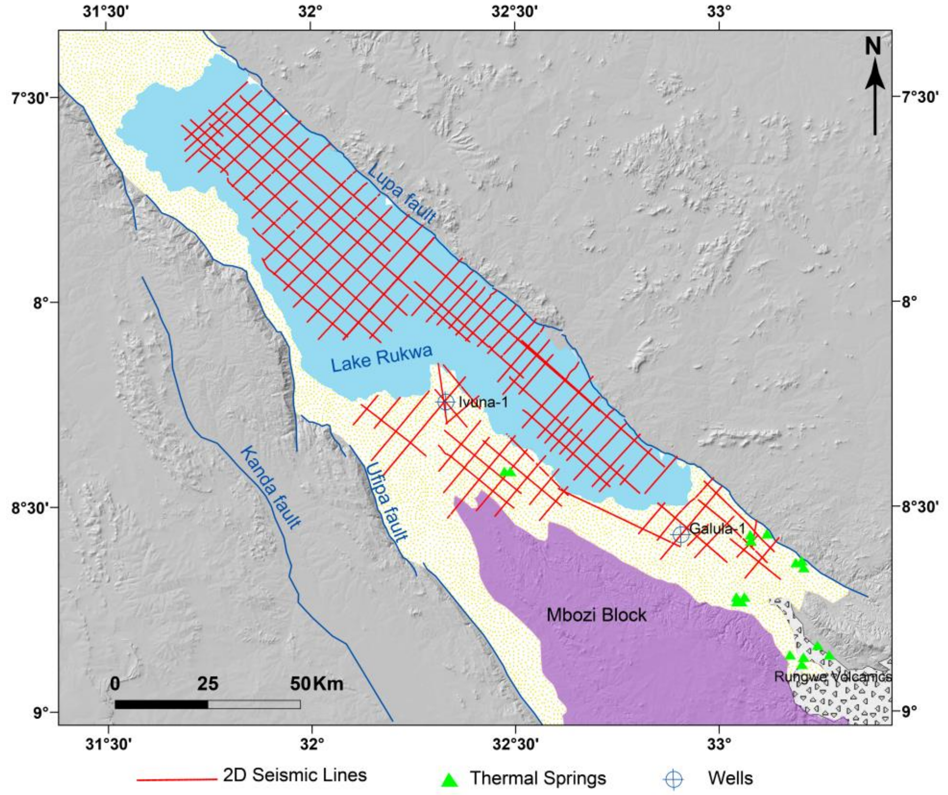

Appendix 1: Map showing the distribution of the 2D seismic lines in the Rukwa Rift